

First-principles Approaches for Accurate Predictions of Nanostructured Materials

by

Qing Zhao

B.S., Mechanical Engineering, Shanghai Jiao Tong University (2012)

B.S., Mechanical Engineering, Purdue University (2012)

S.M., Mechanical Engineering, Massachusetts Institute of Technology (2014)

Submitted to the Department of Mechanical Engineering
in Partial Fulfillment of the Requirements for the Degree of
Doctor of Philosophy in Mechanical Engineering and Computation
at the

MASSACHUSETTS INSTITUTE OF TECHNOLOGY

February 2019

© Massachusetts Institute of Technology. All rights reserved

Signature redacted

Author _____

Qing Zhao

Department of Mechanical Engineering

October 16, 2018

Signature redacted

Certified by _____

Heather J. Kulik

Assistant Professor, Department of Chemical Engineering

Thesis Supervisor

Signature redacted

Certified by _____

Yang Shao-Horn

Professor, Department of Mechanical Engineering Materials Science and Engineering

Thesis Committee Chair

Signature redacted

Accepted by _____

Nicolas Hadjiconstantinou

Professor, Department of Mechanical Engineering

Chairman, Department Committee on Graduate Students

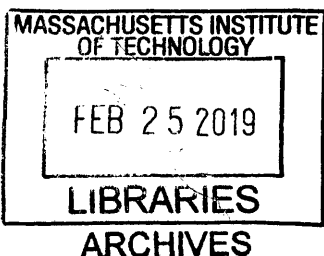
Signature redacted

Accepted by _____

Youssef Marzouk

Associate Professor, Department of Aeronautics and Astronautics

Co-Director, Computational Science and Engineering Program



First-principles Approaches for Accurate Predictions of Nanostructured Materials

by

Qing Zhao

Submitted to the Department of Mechanical Engineering
on October 16, 2018, in Partial Fulfillment of the
Requirements for the Degree of
Doctor of Philosophy in Mechanical Engineering and Computation

Abstract

Nanostructured materials have attracted increasing interest in recent years due to their unusual mechanical, electrical, electronic and optical properties. First-principles electronic structure calculations (e.g., with density functional theory or DFT) provide unique insights into the structure-property relationships of nanostructured materials that can enable further design and engineering. The favorable balance between efficiency and accuracy of DFT has led to its wide application in chemistry, solid-state physics and biology. However, DFT still has limitations and suffers from large pervasive errors in its predicted properties. For small systems, more accurate methods are available but challenges remain for studying nm-scale materials. In the solid-state, unique challenges arise from both the strong sensitivity of correlated transition metal oxides on approximations in DFT and the periodic boundary condition. Therefore, a greater understanding of approximations inherent in DFT is needed for nanostructured materials.

In this thesis, we study nanostructured semiconducting materials, where conventional DFT can be expected to perform well. We develop methods for sampling amorphous materials, rationalizing periodic table dependence in material stability for materials discovery of ordered materials, and bring a surface reactivity perspective to understanding growth processes during materials synthesis. Within the challenging cases of transition metal oxides, we explore how common approximations (e.g., DFT+U and hybrids) affect key nanoscale properties, such as the nature of density localization, and as a result, key observables such as surface stability and surface reactivity. Observation of divergent behavior between these two methods highlights the limited interchangeability of DFT+U and hybrids in the solid-state community. Finally, leveraging the understanding developed in the first two parts of the thesis, we employ a multiscale approach to systematically tailor DFT functional choice for challenging condensed phase systems using accurate reference data from higher level methods. The combination of large-scale electronic structure modeling with state-of-the-art methodology will provide important, predictive insight into tailoring the nanoscale properties of useful materials, and further development in approximate DFT.

Thesis Supervisor: Heather J. Kulik
Assistant Professor of Chemical Engineering, MIT

Acknowledgements

First and foremost, I would like to thank my advisor Professor Heather J. Kulik for her bringing me into the field of computational materials, insightful guidance and continuous support for the past four years. When I first joined the group, I knew nothing about this field, it is Heather's patience, encouragement, motivation and inspiration that helped me build confidence, establish interest in my research, discover the beauty of science, and make the decision to enter academia in the future. She always inspired me to think deeply in the research, provided me the most opportunity in exploring research, patiently instructed me how to give good presentations, how to write papers, and pointed out my weakness for future career. I learnt a lot from Heather, in addition to all the scientific knowledge she passed to me, her love of science and insist on long-term exploration, her patience to all students, serve as the best example to us. No matter how busy, Heather is always there to help me with anything I need, and she always put us at the first position. I feel so lucky to have Heather as my Ph.D. advisor, and coming to MIT to do my graduate work with her is one of the best decisions I have ever made.

Many thanks to my great thesis committee members, Professor Yang Shao-Horn, Professor Alexie Kolpak, Professor Betar Gallant, and Professor Nicolas Hadjiconstantinou. Their insightful suggestions from both views of experiments and theories during committee members and individual meetings have led to improvements of my thesis.

I gratefully acknowledge the following funding resources that support my study at MIT, from National Science Foundation under grant number ECCS-1449291 and Robert Bosch, LLC. Part of the simulation work was carried out using computational resources from the Extreme Science and Engineering Discovery Environment (XSEDE).

It has been a great time working with the members, both present and past, the students and the postdoctoral researchers in the Kulik group. Dr. Efthymios I. Ioannidis, Dr. Lisi Xie, Natasha Seelam, and Dr. Niladri Patra helped me a lot when I started my PhD in the group. During my first semester, I collaborated with Dr. Lisi Xie on the InP quantum dots projects and she helped me start fast and build knowledge in this area. We had so many great discussions, and her passion towards science always motivated me. I learned how to coding with the coding expert in the group, Dr. Efthymios I. Ioannidis. I learned from Helena Qi how to make figures and she provided critical readings for my manuscripts. I enjoyed discussing research with Dr. Jeong Yun Kim, and her suggestions in my projects inspired me. And many thanks to Jon Paul Janet for providing me useful suggestions in machine learning, to Terry Z. H. Gani for discussions in density localization work, to Akash Bajaj for the collaborations in ionization potential project, to Fang Liu for discussions of delocalization error work and help me implementing TeraChem code, to Zhongyue Yang and Tzuhsing Yang for discussions that help me improve my thesis. I would also like to thank the undergraduate students and high school students that I have been working with: Stanley S. H. Ng, Shouping Chen, Naomi Bright, and Yu Jin. Many thanks to other group members, Yusu Liu, Jing Yang, Chenru Duan, Rimsha Mehmood, Aditya Nandy, and Mengyi Wang.

I would like to thank my parents for their continuous support, encouragement and love throughout my life. My parents raised me with a love of science and supported me in

all my pursuits. I can feel their love and care every moment, though the long distance between China and US. My parents-in-law also care me and support me during my PhD life. My dog, DouDou is also an important member of my family, and many thanks for her accompany and the happiness she brought to me. I also would like to thank all my friends here at MIT and Boston. They made my PhD life more colorful.

Finally, I would like to thank my husband, Xi Rong, who is also a PhD student at Mechanical Engineering department at MIT and graduated last year. He is the first person that introduced the area of density functional theory to me and helped me identify the best area for my PhD. During the past four years, I am surrounded with his encouragement, accompany, care, support and love without which I cannot finish the study. He always stayed by my side during my most difficult time, and he is also always the person that I can share my success and happiness with. Thanks for all the things you did for me.

Contents

Chapter 1 Introduction	13
1.1 Nanostructured materials	14
1.1.1 Quantum dots	15
1.1.2 Heterogeneous catalysis.....	15
1.2 Computational work.....	16
1.3 Thesis outline	18
Chapter 2 Theory and Methodology	21
2.1 Hartree-Fock theory	22
2.2 Density functional theory.....	23
2.3 Exchange correlation functionals.....	25
2.3.1 LDA and GGA	25
2.3.2 Delocalization error	26
2.3.3 Hybrid functionals	27
2.4 DFT+U method	29
2.5 Electronic structure analysis	30
2.5.1 Quantum theory of atoms in molecules (QTAIM)	30
2.5.2 Natural bond orbital (NBO)	31
2.5.3 Mayer bond order.....	33
2.6 Nudged elastic band for transition state search.....	33
2.7 Ab initio molecular dynamics	34
Chapter 3 Discovering Amorphous Nanostructures	37
3.1 Introduction	38
3.2 Computational details	40
3.3 AIMD sampling for cluster generation	42
3.4 Generalizing the sampling approach.....	45
3.4.1 Different sized clusters	45
3.4.2 Alternative starting configurations	48
3.5 Accelerating cluster structure generation.....	49
3.6 Comparing properties of clusters	52
3.7 Conclusions.....	59
Chapter 4 Stability of Fullerene Allotropes.....	61
4.1 Introduction	62
4.2 Computational details	63
4.3 Energetics and electronic properties of $A_{36}B_{36}$ fullerenes.....	65
4.4 Comparison of $A_{28}B_{28}$, $A_{30}B_{30}$, and $A_{36}B_{36}$ fullerenes	70
4.5 Conclusions.....	77
Chapter 5 Growth Mechanism of III-V Quantum Dots.....	79
5.1 Introduction	80
5.2 Model curation and computational details	82
5.2.1 InP clusters.....	82
5.2.2 Elementary steps of InP QD Growth	83
5.2.3 Computational details	85

5.3 Bond cleavage energies.....	87
5.3.1 Rigid ligand dissociation energies	87
5.3.2 In-O bond cleavage	90
5.4 PH ₃ addition	91
5.4.1 Thermodynamics.....	91
5.4.2 A model for QD-size dependent reactivity	94
5.4.3 Kinetics	98
5.5 Conclusion	99
Chapter 6 Density Localization and Surface Properties in the Solid State	101
6.1 Introduction.....	102
6.2 Computational details	104
6.2.1 Hybrid calculations	104
6.2.2 DFT+U.....	106
6.2.3 Structure preparation and post-processing.....	107
6.3 Charge localization in transition metal oxides	108
6.3.1 Transition metal oxides	108
6.3.2 Density of states	113
6.3.3 Ligand diffuseness	115
6.4 Charge localization in open-framework solids and extracted transition metal complex analogues.....	118
6.4.1 Open-framework solids.....	118
6.4.2 Extracted transition metal complex analogues	121
6.5 Surface properties in the solid-state	124
6.5.1 Surface science.....	124
6.5.2 Computational details	125
6.5.3 Surface formation energy.....	126
6.5.4 Adsorption energy.....	128
6.5.5 Surface stability vs. reactivity.....	130
6.5.6 Occupation matrix in DFT+U.....	131
6.5.7 Electron density	133
6.6 Comparison with experimental data	135
6.7 Conclusion	136
Chapter 7 Ionization Potential in Polymer Electrolyte	139
7.1 Introduction.....	140
7.2 IP by reduced-scaling correlated wavefunction theory	141
7.3 IP tuning in gas phase	143
7.4 IP tuning in polarizable continuum model	145
7.5 Dynamics of IP sampling	147
Chapter 8 Summary and Outlook	149
8.1 Summary	150
8.2 Outlook	152
References	154

List of Figures

Figure 2-1. Delocalization error in DFT	27
Figure 3-1. Representative InP clusters as starting configurations for high temperature <i>ab initio</i> molecular dynamics	41
Figure 3-2. Average distances over time from <i>ab initio</i> molecular dynamics	42
Figure 3-3. Initial configurations in the <i>ab initio</i> molecular dynamics simulations	45
Figure 3-4. Relative energy of InP clusters as a function of system size	47
Figure 3-5. Flowchart schematic for accelerating sampling approach	50
Figure 3-6. Relative energy of amorphous InP clusters obtained from <i>ab initio</i> molecular dynamics sampling	53
Figure 3-7. Radial distribution functions of all InP amorphous clusters	55
Figure 3-8. Representative configurations of In and P atoms with large coordination number	56
Figure 3-9. Distribution of partial charges for In and P atoms in InP clusters	57
Figure 3-10. Relative energy of amorphous clusters against crystalline models	58
Figure 4-1. Structures of fullerene allotropes and studied elements	65
Figure 4-2. Relative energy of $A_{36}B_{36}$ fullerenes	67
Figure 4-3. Relationship between relative energy and properties of $A_{36}B_{36}$ fullerenes	68
Figure 4-4. HOMO-LUMO gaps of $A_{36}B_{36}$ fullerenes	70
Figure 4-5. Relative energy of $A_{28}B_{28}$ and $A_{30}B_{30}$ fullerenes	72
Figure 4-6. Simplified models to study four-, five-, six-membered rings	73
Figure 4-7. Relationship between $A_{30}B_{30}$ fullerene stability and energy penalty derived from simplified models	75
Figure 4-8. Relationship between all fullerene allotrope stability and a descriptor	76
Figure 5-1. Structures of InP clusters and elementary reaction steps	83
Figure 5-2. Dissociation energies on the MSC with different ligands	88
Figure 5-3. Correlation between In-O bond cleavage and rigid ligand dissociation energies	91
Figure 5-4. a) Relative reaction energies for PH_3 addition. b) Correlation of relative reaction energies versus surface In ⁺ -In separation on MSC	93
Figure 5-5. Surface In ⁺ -In separation versus In-O Mayer bond order for bridging ligands on MSC and a simplified model	95
Figure 5-6. Distributions of surface In ⁺ -In separation on the ESC, MSC, and QD	96
Figure 5-7. a) Activation energy versus reaction energy on ESC b) Absolute ESC PH_3 addition reaction coordinate	98
Figure 6-1. Structures of transition metal compounds	108
Figure 6-2. Dependence of shift of transition metal partial charge with percentage of HF exchange and U for rutile-type MO_2	109
Figure 6-3. Electron density difference for the rutile type TiO_2 and PtO_2	113
Figure 6-4. Projected density of states for PtO_2 and TiO_2	115
Figure 6-5. Ti GGA reference partial charges and Ti partial charge sensitivity to changes in U and HF exchange	117
Figure 6-6. Dependence of shift of transition metal partial charge for $M(OH)_2$	119
Figure 6-7. Structures of open-framework solid $K_3Fe(CN)_6$ and extracted transition metal complex $Fe(CN)_6$	122

Figure 6-8. Fe partial charge sensitivities for solids and complexes	123
Figure 6-9. Fe magnetic or spin-state ordering sensitivity for solids and complexes.....	124
Figure 6-10. MO_2 structures for surface formation energy and oxygen adsorption energy	127
Figure 6-11. MO_2 surface formation energy GGA references and sensitivity to tuning U and HF exchange.....	127
Figure 6-12. MO_2 oyxygen adsorption energy GGA references and sensitivity tuning U and HF exchange.....	129
Figure 6-13. TiO_2 surface formation energy versus TiO_2 oxygen adsorption energy for α_{HF} tuning the PBE0 global hybrid functional, α_{HF} -tuning, or ω -tuning the HSE06 range-separated hybrid (RSH) functional	131
Figure 6-14. Occupation matrix fractionality differences between the pristine surface and bulk structure or between O-atom adsorbed surfaces and pristine surfaces	132
Figure 6-15. Effect of HF exchange on electron density difference of TiO_2 between the pristine surface and bulk structure and between O-atom adsorption and the pristine surface.....	134
Figure 7-1. IP calculated by DLPNO-CCSD(T), CCSD(T), and experimental values for 24 organic molecules	142
Figure 7-2. Structures of one TFSI anion covered with neutral glyme molecules	143
Figure 7-3. IP with optimally tuned ω PBEh, and IP with optimally tuned ω PBEh, and comparison between IP and $-\text{HOMO}$ in gas phase	144
Figure 7-4. Comparison between IP and $-\text{HOMO}$ in PCM.....	145
Figure 7-5. Comparison of IP by ω PBEh and by DLPNO-CCSD(T) in PCM	146
Figure 7-6. Structures of PF_6^- anion icovered by 14 neutral glyme molecules and variations in $-\text{HOMO}$ in the 10 ps AIMD sampling.....	147
Figure 7-7. Correlation between HOMO of the full configuration and the maximum HOMO of individual solvent molecule in AIMD sampling	148

List of Tables

Table 4-1. Relative energy penalties of four-membered, and five-membered rings with respect to six-membered rings in kcal/mol for III-V and II-VI materials.....	73
Table 6-1. Band gaps of TiO ₂ and PtO ₂ with HF exchange and DFT+U.	114
Table 6-2. Comparison of partial charges at different levels of theory for representative solids.	121
Table 7-1. Comparison of IP calculated by DLPNO-CCSD(T) and CCSD(T).....	142

Chapter 1 Introduction

1.1 Nanostructured materials

Nanostructured materials¹⁻¹¹ are materials with a microstructure of clusters, molecules, or crystallites of which the characteristic length scale is on the order of nanometers, typically 1 to 100 nanometers. The development of nanostructured materials in both academia and industry exploded over the past decade due to their unusual and remarkable mechanical¹²⁻¹⁵, electrical^{9, 16-18}, electronic¹⁹⁻²¹, magnetic²²⁻²⁵ and optical^{8, 26-27} properties that can be achieved. Nanostructured materials have unique properties that are significantly different and considerably improved compared with their coarser-grained counterparts. The changes in properties come from their relatively small grain sizes, leading to large percentage of the atoms in the grain boundary environments and the increased interactions between the grains.

More importantly, the properties of nanostructured materials are highly sensitive to their sizes and shapes²⁸⁻³⁰. The simple reason behind this is the surface to volume ratio can be simply altered with particle size and shape, and a high percentage of surface atoms may introduce many size- or shape-dependent physical- and chemical-related phenomena. Therefore ideally, the properties of nanostructured materials can be tuned base on our demands. However, assembling nanoparticles to form a certain nanostructure is a very complex process and numerous scientists are working on different synthetic strategies to find economically affordable ways for synthesizing demanding nanostructures.

Nanostructured materials can be classified based on the dimensions of the confined size effect. A representative nanostructured material of zero-dimensional is quantum dots, in which the spatial distributions of the excited electron-hole pairs are confined within a small volume, resulting in the enhanced electronic and optical properties. Nanotubes and nanowires are the most common one-dimensional nanomaterials, in which the electrons can only move freely in one direction. Carbon nanotubes are the most successful and widely applied nanotubes and have potential applications in many areas, including composite materials, energy storage, mechanical and optical devices. Thin films are representative two-dimensional nanomaterials and can be used as coatings in various areas, such as decorative coatings, optical coatings protective coatings, and electrically operating coatings, as well as thin-film photovoltaic

cells or thin-film batteries. Three-dimensional nanostructured materials are built of nanoparticles as building blocks and have nanometer-sized grains. Unique properties of three-dimensional nanostructured materials can be achieved by controlling the chemical composition, the grain size and the orientations of building block in interfaces.

Quantum dots and heterogeneous catalysis are particular focus of this thesis and will be introduced in details below.

1.1.1 Quantum dots

Colloidal semiconducting nanocrystals (i.e., quantum dots or QDs)³¹⁻³³ have attracted significant attention in the scientific community due to its unique size- and shape-dependent electronic and optical properties. Typical QDs consist of two different parts: an inorganic crystalline core with diameters of several nanometers and capping ligands that stabilize the inorganic cores on the surface. The quantum confinement effects of QDs enable their size- and shape-dependent electronic and optical properties. In general, larger QDs emit longer wavelengths and smaller QDs emit shorter wavelengths, and thus the emission colors can be tuned by their size. The highly tunable properties of QDs make them have a broad range of applications including fluorescence labeling for biotechnology^{31, 34}, light-emitting diodes³⁵⁻³⁶, solar cells³⁷⁻³⁸, and lasers³⁹⁻⁴⁰.

The historical focus of the QDs community is on the synthesis of II-VI quantum dots, particularly of CdSe⁴¹ due to its scalable and size-tunable synthesis approaches. CdSe QDs haven even been commercialized as lighting and display materials. However, cadmium containing QDs are inherent toxic and may pose risks to human health and biological environment. Thus, many researchers have focused on the development of cadmium-free QDs, such as III-V and IV-VI QDs. Some examples are InP⁴², InAs⁴³, PbSe⁴⁴, PbS⁴⁵ and ZnS⁴⁶ QDs. Among them, InP QDs have emerged as an attractive alternative to CdSe because of their ability to emit over the same range of visible wavelengths.

1.1.2 Heterogeneous catalysis

Catalyst is designed to help accelerate chemical reactions by making the reactions kinetically accessible, as well as avoiding undesirable side reactions to eliminate further

expensive product separation steps. Heterogeneous catalysis⁴⁷ is a type of catalysis in which the catalyst occupied a phase, usually solid, different from the reactants and products. The advantage of using heterogeneous catalyst is the relative ease of separation from the product and better tolerance of extreme reaction conditions. Development of heterogeneous catalysis improves chemical reactions in many different areas, from energy applications including fuel cells, electrochemistry and biofuel production, to pollution control including CO₂ reduction and limit emission of noxious gas from automobiles, to medical applications and food production. It indeed benefits our community in all aspects.

Most compelling heterogeneous catalysis contains transition metals since their outmost *d* orbitals are incompletely filled with electrons and increased the opportunities for accepting and donating electrons. For example, Pd and Pt-Rh are the best catalysts for NO removal⁴⁸, while Co, Fe, and Ru are more widely used as Fischer-Tropsch catalysts⁴⁹, and Pt, Pd, and Ag are more popular among oxidation reactions⁵⁰, and Ru and Fe are the best ammonia synthesis catalysts⁵¹.

1.2 Computational work

The historical advances of nanostructured materials technology in the past 20th century are mostly based on experimental discovery. With the rapid development of computer technology in the past decade, computer simulations based on a quantum-mechanical description of the interactions between electrons and atomic nuclei have had an increasingly important impact on the study of nanostructured materials, not only in fundamental understanding of the structure-property relationships⁵²⁻⁵³, but also with a strong emphasis toward materials design⁵²⁻⁵⁴ for future technologies. A breakthrough in these computational efforts is the development of Kohn-Sham DFT⁵⁵⁻⁵⁶ that solving the Schrödinger equation based on non-interacting electron density and exchange correlation functionals. Since then, many efficient algorithms aimed to solve the Kohn-Sham DFT equations have been implemented in numerous codes, boosting the applications of DFT in studies of nanostructured materials in many different research areas across physics, chemistry, materials science, and biology.

Computational work with DFT allows an accurate prediction of different properties in nanostructured materials. For example, DFT method can be used to predict mechanical properties of crystals, such as elastic coefficients and moduli, theoretical strength, mechanical stability, intrinsic hardness, intrinsic brittleness and ductility, and thermal conductivity. For semiconducting materials, DFT allows the direct calculations of more important electronic properties, such as band gaps, band structures, and defect states. For magnetic materials, with the help of DFT, we can study spin crossover systems, evaluating exchange coupling constants, calculating magnetic anisotropy parameters, and predicting transport through magnetic molecules. In surface science, DFT helps with elucidating atomic-scale mechanisms for chemical reactions on surfaces and to quantitatively describe the rates of heterogeneous catalysis reactions with a combination of thermodynamics.

Given the success of DFT calculations in various properties of nanostructured materials in an efficient manner, it enables high throughput materials design to rapidly screen for new materials. It can highly reduce the investment of both time and expense in high-cost and time-consuming procedures of experimental discovery. The idea of high throughput materials design is based on computational quantum mechanical approaches, such as with DFT, and techniques rooted in database construction and intelligent data mining. The procedure is simple, creating a large database containing both existing and hypothetical materials containing different element identity and different structural properties, calculating the target properties of these materials, and then intelligently interrogate the database in the search of materials with desired properties.

The efficiency of DFT also enables performing of very many energy and gradient calculations to study its time evolution of a system. DFT-based molecular dynamics (MD), i.e., ab initio molecular dynamics, have enjoyed a rapid development with the increasing efficiency of DFT calculations. Though classical MD simulations based on inexpensive empirical force fields have long been applied in biological systems, ab initio MD have added more benefits that it allows a more realistic description of the chemical process with breaking or forming of chemical bonds, and thus mimicking actual experimental conditions more closely.

For larger biological systems, a hybrid method⁵⁷ that describes the central part of the large system using quantum mechanical (QM) methods, whereas the surroundings are described by classical molecular mechanics methods (MM), i.e., QM/MM methods have been widely used to keep the accuracy of the central important region with reasonable efficiency.

1.3 Thesis outline

In this thesis, we study nanostructured materials by using density functional theory, and aim to provide important insight into tailoring the nanoscale properties of useful materials, and into the further development of approximate DFT. For the first part, we study nanostructured semiconducting materials, where conventional DFT can be expected to perform well. We develop methods for sampling amorphous materials, rationalizing periodic table dependence in material stability for materials discovery of ordered materials, and bring a surface reactivity perspective to understanding growth processes during materials synthesis. For the second part, we focus on understanding the inherent approximations of DFT in the challenging cases of the solid-state transition metal oxides, where periodic boundary condition needs much higher computational cost and the properties are more sensitive on DFT approximations. We explore how common approximations (e.g., DFT+U and hybrids) affect key nanoscale properties, such as the nature of density localization, and as a result, key observables such as surface stability and surface reactivity. Finally, we use the understanding developed in the first two parts of the thesis, and employ a multiscale approach to systematically tailor DFT functional choice for challenging condensed phase systems using accurate reference data from higher level methods.

Chapter 2 reviews the fundamental theory and methodology employed in this thesis to study nanostructured materials including density functional theory, the currently widely used approximate exchange correlation functionals, and the delocalization errors presented in approximate DFT. Motivated by eliminating energetic delocalization errors, two commonly used methods to address delocalization errors have been introduced, the hybrid functionals and DFT+U method. In addition, methods to perform electronic structure analysis on nanostructures are also discussed, including quantum theory of

atoms in molecules, natural bond orbitals and bond order calculations. We also discuss transition state search method to study the kinetic stability of nanostructured growth process, as well as ab initio molecular dynamics for amorphous structure sampling.

Chapter 3 introduces high temperature ab initio molecular dynamics as a robust method to generate amorphous nanostructures. We use semiconducting indium phosphide nanoparticles as an example to generate amorphous nanostructures and this sampling approach can be generalized to other materials. We discuss the sensitivities of this sampling approach to different initial configurations, alternative methods to accelerate the sampling approaches. We also investigate the relative stabilities, structural properties, and electronic properties of these sampled amorphous materials.

Chapter 4 discusses a systematic study of the role of elemental identity in determining electronic, energetic, and geometric properties of representative III-V and II-VI fullerene allotropes.

Chapter 5 explores the growth mechanism of indium phosphide quantum dots with large-scale electronic structure calculations to understand the synthesis process. A first-principles-derived model that unifies InP QD formation from isolated precursor and early stage cluster reactions to 1.3-nm magic size clusters has been developed, and has been used to rationalize experimentally-observed properties of full sized > 3 nm QDs. We also discuss the surface-dependent reactivity for all elementary growth process steps including In-ligand bond cleavage and P precursor addition.

Chapter 6 focuses on transition metal oxides in the solid state by exploring how common approaches to address the delocalization errors in approximate DFT (e.g., DFT+U and hybrids) affect the density localizations. In addition to transition metal oxides, we also study open-framework solids in which the metal is coordinated by molecular ligands, and extracted molecular analogues from open-framework solids to directly compare the effects on molecular system and periodic system. In addition to electron density property, we also discuss the effects of approximations on key observables relevant to heterogeneous catalysis, such as surface stability through evaluation of surface formation energy and surface reactivity through calculation of adsorption energy in the solid state. The results have been interpreted in terms of electron

delocalization in approximate DFT and compared with the observations on transition metal surfaces with modifying exchange correlation functionals.

Chapter 7 introduces a multiscale approach to systematically tailor DFT functional choice for challenging condensed phase systems using accurate reference data from high level correlated wavefunction theory. An interesting observation related to understanding the dynamic process of key electronic properties is also discussed in this chapter.

Chapter 8 summarizes the work in this thesis and provides an outlook for potential future work based on the understanding in this thesis.

Chapter 2 Theory and Methodology

Electronic structure calculations aims to numerically solve many-body Schrödinger equation, and they are first-principles in nature. It is different from other methods in a way that no external parameters are used other than the most basic description of the system, thus it enables study of the systems without reference to experiment. However, the numerical solution of Schrödinger equation remains a difficult task. Exact solutions of the equation are, in general, only solvable for the smallest and simplest systems. The treatment of electron-electron repulsion is the principal source of the difficulty and it couples the Hamiltonian for each electron, making them intractable to solve and necessitating major approximations. Many different approximations have been introduced to reduce the equations to a simplified form that can be solved within reasonable time, but at the penalty of losing accuracy of the predicted properties.

2.1 Hartree-Fock theory

Hartree-Fock (HF) theory is the fundamental to electronic structure calculations. To introduce Hartree-Fock method, we start with time-independent Schrödinger equation,

$$\hat{H}\Psi = E\Psi \quad (2.1)$$

As usual in many-body electronic structure calculations, the nuclei of the studied systems are assumed be fixed that the motion of nuclei and electrons can be separated, which is known as Born-Oppenheimer approximation. Under this assumption, the Hamiltonian operator, \hat{H} , is simplified to,

$$\hat{H} = \hat{T}_e + \hat{V}_{ne} + \hat{V}_{ee} = \sum_i \left(-\frac{\nabla_i^2}{2} \right) + \sum_{i,I} \left(-\frac{Z_I}{|\mathbf{R}_I - \hat{r}_i|} \right) + \frac{1}{2} \sum_{i \neq j} \frac{1}{|\hat{r}_i - \hat{r}_j|} \quad (2.2)$$

including kinetic energy of electrons, Coulomb attraction between electrons and nuclei, and the Coulomb repulsion between electrons.

To solve the time-independent many-body Schrödinger equation, Hartree-Fock theory assumes that the overall electron wavefunction can be described by a modified form of Hartree Product that satisfies the anti-symmetry principle, known as the Slater determinant with the generalized form of N electrons as,

$$\Psi = \frac{1}{\sqrt{N!}} \begin{vmatrix} \chi_1(\mathbf{r}_1) & \chi_2(\mathbf{r}_1) & \cdots & \chi_N(\mathbf{r}_1) \\ \chi_1(\mathbf{r}_2) & \chi_2(\mathbf{r}_2) & \cdots & \chi_N(\mathbf{r}_2) \\ \vdots & \vdots & \ddots & \vdots \\ \chi_1(\mathbf{r}_N) & \chi_2(\mathbf{r}_N) & \cdots & \chi_N(\mathbf{r}_N) \end{vmatrix} \quad (2.3)$$

Each component in the above Slater determinant represents an individual electron wavefunction and the assumption that the electrons are described by an anti-symmetric product is equivalent to the assumption that each electron moves independently of all the others. It can also be shown that the use of Slater determinant to describe the wavefunction is equivalent to assuming that each electron moves in an electric field that is averaged from the Coulomb repulsion of all other electrons.

Due to the nature of the anti-symmetry of the determinant, Hartree-Fock theory provides exact treatment of Coulomb repulsion and exchange for a wavefunction. However, the exact treatment of exchange in Hartree-Fock theory is unfortunately paired with an absence of direct treatment of short-range, dynamics correlation. To address this problem, there are some post-HF methods, such as coupled cluster and Møller-Plesset perturbation theory, which have been used to study systems with limited number of electrons due to the high computational cost.

2.2 Density functional theory

Density functional theory (DFT) is the most popular and successful electronic structure method to study a wide range of nanostructured materials in physics, chemistry and materials science. It balances well between computational efficiency and accuracy. Similarly as in HF theory, it is also assumed fixed nuclei and the motion of nuclei and electrons can be separated. In practice, the many-body wavefunction, which needs to be minimized, is of $3N$ -dimensions, where N is the number of particles. In order to make the problem tractable, Hohenberg and Kohn⁵⁵ demonstrated that the external potential is a unique functional of the electron density only. Thus the Hamiltonian, and hence all ground state properties, are determined solely by the electron density. Instead of solving many-body wavefunction of N electrons, density functional theory treats the electron density that depends on only three spatial coordinates as the central variable, and thus

leads to a remarkable reduction in difficulty. The many-body Hamiltonian \hat{H} fixes the ground state of the studied system, i.e., it determines the ground state many-body wavefunction, Ψ , and thus the Hohenberg and Kohn theorem ensures that it is also a unique functional of the ground state density. Consequently, the electron kinetic energy and the electron-electron interaction energies will be functional of electron density $n(\mathbf{r})$. Therefore we define the functional $F[n(\mathbf{r})]$ as,

$$F[n(\mathbf{r})] = \langle \Psi | \hat{T}_e + \hat{V}_{ee} | \Psi \rangle \quad (2.4)$$

This functional $F[n(\mathbf{r})]$ is a universal functional in the sense that it has the same dependence on the electron density for any system, independent of the external potential concerned. The exact density dependence of this functional is, however, unknown. Using this functional, we can then define, for a given external potential $v(\mathbf{r})$, the total energy is

$$E[n(\mathbf{r})] = \int v(\mathbf{r}) n(\mathbf{r}) d\mathbf{r} + F[n(\mathbf{r})] \quad (2.5)$$

In order to define useful approximations to $F[n(\mathbf{r})]$ which yield accuracy of predicted properties, Kohn and Sham⁵⁶ made further simplification by mapping the original system of interacting electrons onto a fictitious system of non-interacting electrons that has the same density. For a system of non-interacting electrons, the ground-state charge density is representable as a sum over one-electron orbitals (the *KS orbitals*), $\psi_i(\mathbf{r})$,

$$n(\mathbf{r}) = \sum_i |\psi_i(\mathbf{r})|^2 \quad (2.6)$$

The energy functional then becomes,

$$E[n(\mathbf{r})] = T_s[n(\mathbf{r})] + E_H[n(\mathbf{r})] + E_{xc}[n(\mathbf{r})] + \int v(\mathbf{r}) n(\mathbf{r}) d\mathbf{r} \quad (2.7)$$

The first term is the kinetic energy of non-interacting electrons,

$$T_s[n(\mathbf{r})] = \sum_i -\frac{1}{2} \int \psi_i^*(\mathbf{r}) \nabla^2 \psi_i(\mathbf{r}) d\mathbf{r} \quad (2.8)$$

The second term, Hartree energy, contains the electrostatic interactions between clouds of charge. The third term is the exchange-correlation energy includes all of the many-body effects not present in the rest of the functional due to the approximations. Qualitatively speaking, exchange-correlation energy contains four parts: the kinetic energy correction, which is difference between the true kinetic energy of real interacting electrons and the

kinetic energy of the non-interacting electrons; the exchange energy, which is a result of the requirement that the many-body wavefunction must be antisymmetric to the exchange of any two electrons; the correlation energy, which is the energy recovered by allowing the movements of the electrons in the system to be fully correlated; and the correction of self-interaction error, which correct for the fact an electron is allowed to interact with itself. However, the exact exchange-correlation term remains unknown and a great effort in the density functional theory community is focused on developing more accurate exchange-correlation functional.

2.3 Exchange correlation functionals

2.3.1 LDA and GGA

In contrast with Hartree-Fock thoery, DFT provides explicit inclusion of short-range correlation. However, this treatment of electron correlation in practice unfortunately results in a trade-off effect that the Coulomb repulsion energy is estimated as an integral of each single particle orbital with the density of the rest of the system, resulting in what is known as self-interaction error (SIE). Exchange term in DFT must simultaneously reduce repulsion of same-spin electrons as in Hartree-Fock theory and reduce the self-interaction error.

The simplest approximation to the exchange correlation functional is the local density approximation (LDA). It assumes the electron density behave locally and derived from a homogeneous electron gas with constant density. In general, for a spin-unpolarized system, a local-density approximation for the exchange-correlation energy is written as,

$$E_{xc}^{\text{LDA}}[n(\mathbf{r})] = \int n(\mathbf{r}) \varepsilon_{xc}(n(\mathbf{r})) d\mathbf{r} \quad (2.9)$$

where $n(\mathbf{r})$ is the electron density and ε_{xc} is the exchange-correlation energy of approximated homogeneous electron gas of density $n(\mathbf{r})$. The local spin-density approximation (LSDA) is to generalize of LDA to include electron spin,

$$E_{xc}^{\text{LDA}}[n(\mathbf{r})] = \int n(\mathbf{r}) \varepsilon_{xc}(n(\mathbf{r})_{\uparrow}, n(\mathbf{r})_{\downarrow}) d\mathbf{r} \quad (2.10)$$

LDA performs well for systems with slowly varying electron densities, and chemical trends are well reproduced. Because the LDA assumes that the density is the same everywhere, the LDA has a tendency to underestimate the exchange energy and overestimate the correlation energy. The errors due to the exchange and correlation parts tend to compensate each other.

On the basis of LDA, the exchange-correlation functional is significantly improved by taking the inhomogeneity of the electron density into account and incorporating the electron density gradient. This improvement is referred to as generalized gradient approximations (GGA) and have the following form,

$$E_{xc}^{\text{GGA}}[n(\mathbf{r})_{\uparrow}, n(\mathbf{r})_{\downarrow}] = \int n(\mathbf{r}) \epsilon_{xc}(n(\mathbf{r})_{\uparrow}, n(\mathbf{r})_{\downarrow}, \nabla n(\mathbf{r})_{\uparrow}, \nabla n(\mathbf{r})_{\downarrow}) d\mathbf{r} \quad (2.11)$$

There are many different GGA exchange-correlation functionals. The exchange term in DFT must simultaneously reduce repulsion of same-spin electrons as in Hartree-Fock theory and reduce the self-interaction error. The most popular exchange functional includes Perdew-Burke-Ernzerhof functional (PBE)⁵⁸, Beck88 exchange⁵⁹, and PW91 functional⁶⁰. Correlation functional includes the correlation effect of interaction between electrons in the electronic structure and it is a measure of how much the movement of one electron is influenced by the presence of all other electrons. Electron correlation energy is sometimes divided into short-range dynamic correlation and long-range static correlation. Dynamic correlation is the correlation of the movement of electrons. Some popular correlation functional includes the Lee-Yang-Parr correlation functional (LYP)⁶¹, Perdew-Burke-Ernzerhof functional (PBE)⁵⁸, and PW91 functional⁶⁰.

Meta-GGA functionals further incorporate the second derivative of the electron density or equivalently the kinetic energy density. This more flexible form holds broad promise for reducing errors in approximate DFT by including higher order terms of the density⁶²⁻⁶³.

2.3.2 Delocalization error

All of these approximated exchange correlation functionals are well known to suffer from self-interaction error, that each electron lives in the field of all electrons including itself and thus can be potentially interacted with itself. Self-interaction error is

also referred to as delocalization error (DE). DE⁶⁴⁻⁶⁶ has a quantitative energetic definition as the deviation from linearity with respect to exact piecewise linear behavior⁶⁷, which also requires a derivative discontinuity⁶⁸⁻⁷¹, with fractional addition or removal of an electron. Pure exchange correlation functionals in approximate DFT (e.g., LDA or GGA) exhibits a convex deviations⁷²⁻⁷³ from piecewise-linearity (Figure 2-1).

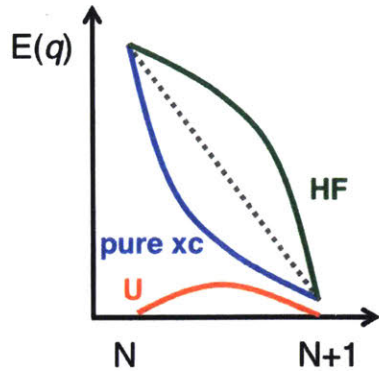


Figure 2-1. Comparison of the dependence of the energy in a practical exchange-correlation functional (e.g., LDA or GGA), or Hartree-Fock calculation (green lines) as the charge is varied between integer points (blue lines) along with representative correct piecewise linear behavior (gray dashed line). An example +U correction is shown in the atomic limit (red line).

Delocalization error in approximate DFT gives rise to many well-known problems in predicting dissociation energies⁷⁴⁻⁷⁸, barrier heights⁷⁹, band gaps⁸⁰⁻⁸¹, and electron affinities⁸²⁻⁸⁴. Open shell transition metal complexes and solids are particularly sensitive to imbalances in DE, which leads to strongly xc-dependent predictions of spin-state^{63, 85-89} or magnetic ordering⁹⁰⁻⁹² and thus electronic properties.

2.3.3 Hybrid functionals

Hartree-Fock (HF) theory conversely overlocalizes electrons and exhibits concave deviations⁷²⁻⁷³ from piecewise linearity (Figure 2-1). The observations motivate incorporation of a portion of HF exchange from HF theory with the rest of the pure exchange correlation functional to address the delocalization errors in approximate DFT, which is the so-called hybrid functionals. The major shortcoming of the hybrid functionals is the percentage of mixing HF exchange is unknown and is empirically determined by comparing with available experimental data. One of the most widely used

B3LYP^{59, 61, 79} hybrid functional includes GGA exchange functional, LDA exchange functional, HF exchange, GGA correlation functional and LDA correlation functional,

$$E_{xc}^{\text{B3LYP}} = E_x^{\text{LDA}} + a_0(E_x^{\text{HF}} - E_x^{\text{LDA}}) + a_x(E_x^{\text{GGA}} - E_x^{\text{LDA}}) + E_c^{\text{LDA}} + a_c(E_c^{\text{GGA}} - E_c^{\text{LDA}}) \quad (2.12)$$

where $a_0 = 0.20$, $a_x = 0.72$, and $a_c = 0.81$. The other widely used PBE0 hybrid functional mixes GGA exchange functional and HF exchange, along with the full GGA correlation functional,

$$E_{xc}^{\text{PBE0}} = a_0 E_x^{\text{HF}} + (1-a_0) E_x^{\text{PBE}} + E_c^{\text{PBE}} \quad (2.13)$$

where $a_0 = 0.25$.

Since the HF exchange interaction exhibits the correct asymptotic decay, an alternative approach to improve approximate DFT functional is preserving GGA exchange at short range while activating HF exchange asymptotically to achieve correct asymptotic behavior, via a range-separated hybrid functional. A distance-dependent Coulomb repulsion operator is introduced,

$$\frac{1}{r_{12}} = \frac{1 - [\alpha + \beta \text{erf}(\omega r_{12})]}{r_{12}} + \frac{\alpha + \beta \text{erf}(\omega r_{12})}{r_{12}} \quad (2.14)$$

where the first term is the short-range term that decays on a $1/\omega$ length-scale, and the second term is a long-range term with correct $1/r$ asymptotic behavior for $\alpha+\beta=1$. If HF exchange is only introduced in the long-range portion (i.e., $\alpha=0$, $\beta=1$), the Coulomb operator of short-range (SR) and long-range (LR) components becomes,

$$\frac{1}{r_{12}} = \frac{1 - \text{erf}(\omega r_{12})}{r_{12}} + \frac{\text{erf}(\omega r_{12})}{r_{12}} \quad (2.15)$$

where the first term is the short-range component and the second term is the long-range component, and ω is an adjustable parameter. A commonly used long-range corrected hybrid functional is LRC- ω PBEh⁹³ with the form,

$$E_{xc}^{\text{LRC-}\omega\text{PBEh}} = a E_x^{\text{HF,SR}}(\omega) + (1-a) E_x^{\text{PBE,SR}}(\omega) + E_x^{\text{HF,LR}}(\omega) + E_c^{\text{PBE}} \quad (2.16)$$

where range separation parameter $\omega=0.2$ bohr⁻¹, and short-range HF exchange $a = 0.2$.

In solids, short-range hybrids that only incorporate HF exchange in the short range are more often applied since effects in the solid are more sensitive to descriptions of dynamic correlation and exchange dominate over the accuracy recovered through

correct description of the computationally costly long-range, static correlation. A popular short-range hybrid in the solid community is HSE06⁹⁴ with the form,

$$E_{xc}^{\text{HSE06}} = aE_x^{\text{HF,SR}}(\omega) + (1-a)E_x^{\text{PBE,SR}}(\omega) + E_x^{\text{PBE,LR}}(\omega) + E_c^{\text{PBE}} \quad (2.17)$$

where range separation parameter $\omega=0.11$ bohr⁻¹, and short-range HF exchange $a = 0.25$.

2.4 DFT+U method

The general form of DFT+U energy functional includes three contributions: 1) energy from a standard exchange correlation approximation (E_{DFT}), 2) Hubbard model Hamiltonian correction (E_{Hub}), and 3) a double counting term approximately removes the effect of corrections present in the other two terms (E_{DC}),

$$E_{\text{DFT+U}}[n(\mathbf{r})] = E_{\text{DFT}}[n(\mathbf{r})] + E_{\text{Hub}}[\{n_m^{l\sigma}\}] - E_{\text{DC}}[\{n^{l\sigma}\}] \quad (2.18)$$

There will be an E_{Hub} and E_{DC} contribution for each Hubbard atom and subshell identified. Most commonly, the double counting term is obtained within the fully localized limit,

$$E_{\text{DC}}[\{n^{l\sigma}\}] = \frac{1}{2}Un(n-1) - \frac{1}{2}J[n^\uparrow(n^\uparrow-1) + n^\downarrow(n^\downarrow-1)] \quad (2.19)$$

where the total number of electrons is denoted n , and spin up or spin down electrons are denoted as n^\uparrow or n^\downarrow , respectively.

Typically, a frequent simplifying assumption is to treat same-spin and opposite-spin electrons equivalently with,

$$U_{\text{eff}} = U - J \quad (2.20)$$

and we thus obtain an expression for the DFT+U energy as,

$$E^{\text{DFT+U}} = E^{\text{DFT}} + \frac{1}{2} \sum_{I,\sigma} \sum_{nl} U_{nl}^I [\text{Tr}(\mathbf{n}_{nl}^{l\sigma} (1 - \mathbf{n}_{nl}^{l\sigma}))] \quad (2.21)$$

There is a “+U” correction for each nl subshell of atom I to which a U_{nl}^I is applied. The elements of the $\mathbf{n}_{nl}^{l\sigma}$ occupation matrix are obtained as a projection of the molecular state at k-point k onto localized atomic orbitals on an atom I ,

$$n_{mm'}^{l\sigma} = \sum_{k,v} \langle \psi_{k,v} | \phi_{m'}^I \rangle \langle \phi_m^I | \psi_{k,v} \rangle \quad (2.22)$$

The “+U” correction is incorporated self-consistently with a modification to the potential as

$$V^U = \sum_{I,nl} \sum_m \frac{U_{nl}^I}{2} (1 - 2n_{nl,m}^{I\sigma}) |\phi_{nl,m}^I\rangle \langle \phi_{nl,m}^I| \quad (2.23)$$

where the shifts are a maximum $U/2$ or minimum $-U/2$ for molecular orbitals that project fully onto the atomic orbitals that are empty of filled, respectively.

The Hubbard U corresponds to the difference between the ionization potential (IP) and electron affinity (EA) of electrons on atom I in subshell nl with respect to the rest of the system,

$$U_{nl}^I = \text{IP}_{nl}^I - \text{EA}_{nl}^I = E(n_{nl}^I + 1) + E(n_{nl}^I - 1) - 2E(n_{nl}^I) \quad (2.24)$$

which may be recognized as a finite difference approximation to the second derivative of the energy,

$$U_{nl}^I = \frac{\partial^2 E}{\partial(n_{nl}^I)^2} \quad (2.25)$$

The DFT+U method has been recently demonstrated⁹⁵ that it can recover piecewise linearity in transition metal chemistry. It has been showed⁹⁵ that this piecewise linearity is not recovered at a calculated self-consistent⁸⁵, linear-response⁹⁶⁻⁹⁷ U but at one determined by the semi-local DFT deviation from linearity⁹⁸.

2.5 Electronic structure analysis

2.5.1 Quantum theory of atoms in molecules (QTAIM)

The quantum theory of atoms in molecules⁹⁹ proposed by Bader is a topology analysis technique to describe atoms and bonds in studied system. In topology analysis, the points at where gradient norm of function value is zero (except at infinity) are called as critical points (CPs). Similarly, in QTAIM, molecular structure is revealed by the stationary points of the electron density together with the gradient paths of the electron density that originate and terminate at these points. Critical points can be classified into four types based on the number of negative eigenvalues of Hessian matrix of real space function, such as identifying the nuclear positions, bond critical point, center of ring

system, and center of cage system. In this thesis, we apply properties related to bond critical point to reveal bond strength, and bond critical point is associated with two negative eigenvalues of Hessian matrix.

Another important concept in QTAIM is basin, which can be defined for any real space function, such as electron density, molecular orbital, and electrostatic potential. A real space function generally has one or more maxima, which are referred to as attractors. Each basin is a subspace of the whole space, and uniquely contains an attractor. The basins are separated by interbasin surfaces, which are defined as the zero-flux surface of the real space functions,

$$\nabla f(\mathbf{r}) \cdot \mathbf{n}(\mathbf{r}) = 0 \quad (2.26)$$

where $\mathbf{n}(\mathbf{r})$ is the unit normal vector of the surface at position \mathbf{r} .

For electron population analysis, electron density can be used to define the basins. Electron population numbers can thus be obtained by integrating electron density in the basin.

2.5.2 Natural bond orbital (NBO)

Natural orbitals Θ_k are the reduced form of a wavefunction ψ and defined as the eigenorbitals of the first-order reduced density operator Γ ,

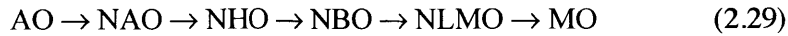
$$\Gamma\Theta_k = p_k\Theta_k \quad (2.27)$$

where the eigenvalue p_k represents the population of the eigenfunction Θ_k for the molecular electron density operator Γ of ψ , and can be evaluated as,

$$p_k = \langle \Theta_k | \Gamma | \Theta_k \rangle \quad (2.28)$$

The density operator is the 1-electron projection of the full N-electron probability distribution of the total wavefunction ψ . Thus, natural orbitals are based on wavefunction ψ only and form a complete orthonormal set.

The natural bond orbitals (NBO) are one of a sequence of natural localized orbitals that includes natural atomic orbitals (NAO), natural hybrid orbitals (NHO), natural bond orbitals (NBO), and natural semi-localized molecular orbitals (NLMO). These natural localized orbitals are intermediate between atomic orbitals (AO) and molecular orbitals (MO):



The initial AO to NAO transformation is based on two criterions, the “maximum resemblance” criterion that defines Löwdin’s original symmetric orthogonalization algorithm with the “maximum occupancy” criterion that defines intrinsic natural character.

NHOs h_A are optimized linear combination of NAOs on the given center,

$$h_A = \sum_k a_k \Theta_k^A \quad (2.30)$$

The NHOs also form a complete orthonormal set that spans the full basis space.

NBOs are localized 1-center or 2-center, but occasionally more-center orbitals that describe the Lewis-like molecular bonding pattern of electron pairs (or of individual electron in open-shell calculations) in optimally compact form. More precisely, NBOs are an orthonormal set of localized “maximum occupancy” orbitals whose leading $N/2$ (or N terms in open-shell calculations) terms give the most accurate possible Lewis-like description of the total N -electron density. The NBO analysis searches over all possible ways of defining the bonds and lone pairs for the variationally optimal bonding environment to place maximum occupancy in the leading $N/2$ Lewis-type NBOs. The Lewis-type NBOs determine the localized Natural Lewis Structure (NLS) representation of the wavefunction, while the remaining non-Lewis-type NBOs complete the span of the basis and describe the residual effects. In this construction, the general idea of NBO is a valence bond-type description of the wavefunction and the only input to the NBO analysis is the molecular wavefunction Ψ . The 1-center orbitals are lone pairs, and is each composed of a single NHO,

$$n_A = h_A \quad (2.31)$$

The 2-center orbitals are bonds and are normalized linear combinations of two bonding NHOs, h_A, h_B ,

$$\Omega_{AB} = a_A h_A + a_B h_B \quad (2.32)$$

The coefficients a_A, a_B satisfying,

$$a_A^2 + a_B^2 = 1 \quad (2.33)$$

An NBO bond is covalent when a_A and a_B has identical values, while the bond exhibits more ionic property when one value is close to 1 and the other is close to 0.

2.5.3 Mayer bond order

The Mayer bond order between two atoms A and B can be defined in terms of their density matrix and the overlap density matrix,

$$I_{AB} = I_{AB}^\alpha + I_{AB}^\beta = 2 \sum_{a \in A} \sum_{b \in B} [(P^\alpha S)_{ba} (P^\alpha S)_{ab} + (P^\beta S)_{ba} (P^\beta S)_{ab}] \quad (2.34)$$

where P^α and P^β are alpha and beta density matrix and S is the overlap density matrix. If total density matrix $P = P^\alpha + P^\beta$ and spin density matrix $P^S = P^\alpha + P^\beta$ are used, the above equation can be rewritten as,

$$I_{AB} = \sum_{a \in A} \sum_{b \in B} [(PS)_{ba} (PS)_{ab} + (P^S S)_{ba} (P^S S)_{ab}] \quad (2.35)$$

In closed-shell calculations, the spin density matrix term is zero and the equation becomes,

$$I_{AB} = \sum_{a \in A} \sum_{b \in B} (PS)_{ab} (PS)_{ba} \quad (2.36)$$

Total valence of an atom, which measures atomic bonding capacity, is defined as the sum of its related bond orders,

$$V_A = \sum_{B \neq A} I_{AB} \quad (2.37)$$

2.6 Nudged elastic band for transition state search

An important problem in theoretical chemistry is to identify the minimum energy path (MEP) for a chemical reaction. Any point along MEP is at an energy minimum in all directions perpendicular to this path. The energy maximum along the MEP is the saddle point and gives the activation energy barrier, and the corresponding structure is referred to as a transition state (TS). Nudged elastic band (NEB) is a method to find the TS between the initial (reactant) and the final (product) configurations, both of which are local energy minima on the potential energy surface. NEB is based on chain-of-states method, in which the reaction pathway is described by a string of images. These configurations are connected by spring forces to ensure equal spacing along the reaction

pathway. NEB method usually starts from linear interpolation between the initial and final configurations. The images along the NEB path are relaxed to the MEP through a force projection scheme in which potential forces act perpendicular to the band, and spring forces act along the band. The combined NEB forces on image i contains two independent components,

$$\mathbf{F}_i^{\text{NEB}} = \mathbf{F}_i^{\perp} + \mathbf{F}_i^{\parallel} \quad (2.38)$$

where the first term is the force due to the potential perpendicular to the band and the second term is the spring force. The potential force has the form,

$$\mathbf{F}_i^{\perp} = -\nabla(\mathbf{R}_i) + \nabla(\mathbf{R}_i) \cdot \hat{\tau}_i \hat{\tau}_i \quad (2.39)$$

where \mathbf{R}_i is the position of the image i and τ_i is the unit vector to the higher energy neighboring image of image i . The spring force is,

$$\mathbf{F}_i^{\parallel} = k(|\mathbf{R}_{i+1} - \mathbf{R}_i| - |\mathbf{R}_i - \mathbf{R}_{i-1}|) \hat{\tau}_i \quad (2.40)$$

Overall, the combined potential forces and string forces will drag the band towards the MEP.

2.7 Ab initio molecular dynamics

Molecular dynamics (MD) is used to model physical movements of atoms and molecules. The atoms and molecules interact with each other, and the resulting forces allow the dynamic evolution of the whole system. In order to update positions and velocities within each fixed time period, Verlet algorithm is often used. The new position of a particle after a fixed time period Δt ,

$$x(t + \Delta t) = x(t) + v(t)\Delta t + \frac{1}{2}a(t)\Delta t^2 \quad (2.41)$$

where $x(t)$ is the current position, $v(t)$ is the current velocity and $a(t)$ is the current acceleration computed from all forces on it. New force on the particle at new position $x(t+\Delta t)$ can then be re-evaluated. Based on the force at t and force at $t+\Delta t$, new velocity can be obtained as,

$$v(t + \Delta t) = v(t) + \frac{a(t) + a(t + \Delta t)}{2} \Delta t \quad (2.42)$$

The error in both position and velocity is $O(\Delta t^2)$, and thus the time step needs to be carefully selected based on balance between accuracy and efficiency.

There are different constraint conditions in MD simulations, such as the microcanonical ensemble (NVE) in which number of particles, volume and energy of system are kept constant, canonical ensemble (NVT) in which number of particles, volume and temperature are kept constant, and isothermal-isobaric ensemble (NPT) in which number of particles, temperature and pressure are kept constant. To keep constant temperature in the MD sampling, thermostat needs to be added. Some popular methods to control temperature include velocity rescaling, the Nosé-Hoover thermostat, the Andersen thermostat and Langevin dynamics. The idea of velocity rescaling is to rescale the velocities at each step so that the kinetic energy gives the desired temperature. However, velocity rescaling schemes do not strictly follow the canonical ensemble and do not allow temperature fluctuations which are present in real systems. Anderson thermostat introduces a stochastic element to the temperature by having random collisions of molecules with an imaginary heat bath at the desired temperature. Nosé-Hoover thermostat introduces heat bath as part of the system consisting of only one imaginary particle. Langevin dynamics introduces a small damping force to control the system temperature.

One of the most challenging aspects of MD simulations is to capture accurate interatomic forces. In classical MD simulations, the interactions are computed from empirical potential functions, which have been parametrized to reproduce experimental or accurate ab initio data of small model systems. The limitations of classical MD simulations include the non-transferability of force field to different systems, incapable of predicting chemical bonding processes, and failures to model changes in electronic structure. Therefore, ab initio molecular dynamics based on first principles methods become popular to remove the limitations of classical MD simulations and the interatomic forces are calculated with electronic structure calculations, such as DFT. Two commonly used ab initio MD approaches are Car-Parrinello MD and Born-Oppenheimer MD. In Born-Oppenheimer MD, the time-independent Schrödinger equation is directly solved at each MD step with the Born-Oppenheimer assumption. The nuclear degree of freedom is then propagated using ionic forces.

Chapter 3 Discovering Amorphous Nanostructures

This chapter has been published in

Q. Zhao, L. Xie, H. J. Kulik, *J. Phys. Chem. C*, 119 (40), 23238-23249 (2015).¹⁰⁰

3.1 Introduction

Nanostructured materials exhibit unique properties with respect to their bulk counterparts, and first-principles simulation can provide valuable insight into their unusual structure-property relationships. Semiconducting quantum dots (QDs) in particular have drawn the attention of a broad scientific community because they exhibit unique size- and shape- dependent electronic and optical properties¹⁰¹. QDs have demonstrated their technological relevance in a broad number of applications including in fluorescence labeling for biotechnology^{31, 34}, light-emitting diodes³⁵⁻³⁶, solar cells³⁷⁻³⁸, and lasers³⁹⁻⁴⁰. Although CdSe QDs were the first to be developed with controllable size¹⁰² in large quantity with emission across the visible range¹⁰³, alternative QDs have been sought due to the high toxicity¹⁰⁴ of cadmium. InP QDs have since been identified as one of the most promising alternatives to CdSe both because of their broader emission color range and lack of intrinsic toxicity^{42, 105-106}. Nevertheless, preparation of high-quality InP QDs has remained challenging, despite ongoing efforts to understand and direct the nucleation and growth mechanisms during synthesis^{42, 106-109}.

Several groups have carried out semi-empirical, tight-binding¹¹⁰ and DFT¹¹¹⁻¹¹⁵ studies of InP nanowires¹¹¹⁻¹¹³ and the related core-shell InAs/InP nanowires¹¹⁴⁻¹¹⁵ as well as studies of bulk InP surfaces¹¹⁶⁻¹¹⁸ both pristine and in the presence of water. InP QDs are comparatively less well studied with only a few semi-empirical, tight-binding¹¹⁹⁻¹²⁰ or hybrid DFT¹²¹ studies. In some of these cases, the surface has been passivated with neutral¹¹¹ or partially charged^{112, 121} hydrogen atoms, oxygen atoms¹¹¹, or methyl groups¹²⁰, while in other cases an unpassivated surface^{111, 119} is studied. Regardless of passivation approach, typically the experimental bulk crystal structure geometry is used¹¹³ and at most a local geometry optimization¹²¹ is carried out on the experimental starting structure. Studies of bulk crystal models and geometry optimized models have also been carried out on QDs comprised of CdSe¹²²⁻¹²⁴, PbSe¹²³⁻¹²⁴, and PbS¹²⁵ both with^{122, 125} and without¹²³⁻¹²⁵ ligand passivation. A key challenge for studying InP nanostructures is that InP QDs have been characterized with a crystalline core but relatively disordered, partially oxidized amorphous shell that appears to limit further growth of InP QDs⁴². Part of the amorphous shell is attributed to the breakdown and reaction of the carboxylate ligands used in precursors to synthesize InP QDs, and the full extent of the structure of

the surface of these QDs is not known. No attempts have been made to model or sample potential amorphous structures of InP QD surfaces.

Despite the lack of study of amorphous InP surfaces, a great deal of computational effort has been dedicated to obtaining low energy configurations of other types of nanostructures. One of the most popular approaches is the coalescence kick method, in which atoms are randomly placed far apart and then pushed towards the center of mass until they coalesce into a cluster that is roughly the size of the pairwise sums of known covalent radii. This search is repeated many times, and the most stable structure after optimization with DFT is hypothesized to be the global minimum¹²⁶. This approach has been fruitfully applied to small clusters such as Pt₈¹²⁷, Mg₁₇¹²⁸, AlB₃H_{2n} (n=0-6)¹²⁹, and Ge₁₀¹³⁰. High computational demands and large numbers of possible random structures have limited the kick method to small, mostly single element clusters of less than 20 atoms. Low energy structures of similarly sized metallic (e.g. Au₂₀¹³¹) and bimetallic¹³² clusters have been obtained using genetic algorithms combined with DFT to evaluate energies and carry out geometry optimizations¹³¹⁻¹³³.

Minimum hopping methods, in which minima are sought and then propagated away from dynamically with a history list used to avoid revisiting the same minima, that are carried out primarily with tight-binding, have been carried out on small clusters (e.g. 19 atoms of silicon)¹³⁴. Similarly sized clusters, e.g. Si16, have been accessible with metadynamics¹³⁵. In a related approach known as Basin-hopping Monte Carlo, configurations are geometry optimized after the Monte Carlo move, have permitted study of larger 55 atom clusters of Ag and Ag/Pd mixtures when combined with a simplified Lennard-Jones force field¹³⁶ or around 33 atom Pt-alloy clusters when a mixture of tight-binding, semi-empirical approaches and DFT are used¹³⁷. Simulated annealing molecular dynamics, in which systems are heated and then slowly-cooled, combined with semi-empirical or classical molecular dynamics has permitted study of larger 50 atom gold clusters¹³⁸ or up to 160 atoms of stoichiometric ZnS¹³⁹.

In light of the uncertainty regarding the shell structure around InP QDs, we were interested in identifying whether we could discover possible low-energy structures of indium phosphide clusters that have order distinct from the bulk crystal structure. Our goal is to identify candidate surface and cluster structures that are likely to be accessible

depending on synthesis conditions, not necessarily identify the global energy minimum for our structures. By not mandating a global minimum search, we may study larger clusters and identify whether alternative structures can be competitive with crystalline order. Our initial inspiration for this approach comes from a recent study¹⁴⁰ in which graphene spontaneously reorganized to form fullerenes during molecular dynamics simulations. Here, we instead employ high-temperature *ab initio* molecular dynamics on models of crystalline InP, e.g. of the InP(111) surface that contains hexagonal bonding structure similar to graphene, and we will demonstrate that this approach encourages reorganization to low energy structures.

3.2 Computational details

All *ab initio* molecular dynamics (AIMD) simulations and geometry optimizations¹⁴¹ were carried out with TeraChem¹⁴²⁻¹⁴³. AIMD simulations were performed with the Hartree-Fock (HF) method and the 3-21G basis set¹⁴⁴. Geometry optimizations were carried out using density functional theory (DFT) with the hybrid B3LYP^{59, 61, 145} exchange-correlation functional and the composite LACVP* basis set. The LACVP* basis set corresponds to an LANL2DZ effective core potential basis for the indium atom and 6-31G* basis for the phosphorus atom. The default B3LYP definition in TeraChem uses the VWN1-RPA form¹⁴⁶ for the local density approximation component of the correlation. In the AIMD simulations, we employ a 0.5 fs timestep and keep a constant temperature of 1000 K with a Langevin thermostat. Resulting trajectories range from 20,000 to 50,000 time steps (10 to 25 ps) in length.

Initial configurations for the AIMD simulations were obtained from models of the experimental zinc blende InP crystal structure. Experimental parameters for the InP structure¹⁴⁷ were obtained from the Crystallography Open Database (COD)¹⁴⁸, which provides a Crystallographic Information File (CIF) that contains the InP unit cell geometry, space group, and lattice parameter. The super cell builder function in Avogadro¹⁴⁹ was then used to build models of crystallographic planes (InP(111), InP(011), InP(001)) and spherical cuts of the bulk (In_7P_{17} , $\text{In}_{12}\text{P}_{12}$, $\text{In}_{13}\text{P}_{13}$, $\text{In}_{22}\text{P}_{22}$) by removing unneeded atoms from super cells (see Figure 3-1). These initial structures ranged in size from 6 atoms to 32 atoms.

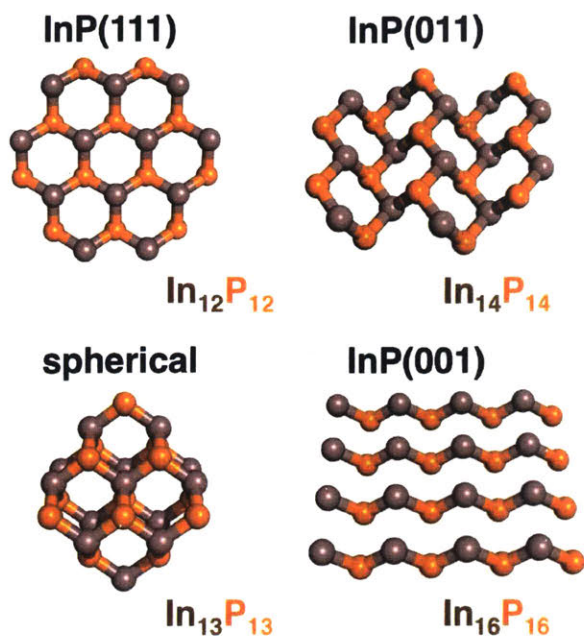


Figure 3-1. Representative ball and stick models of zinc blende InP clusters, which are starting configurations for high temperature *ab initio* molecular dynamics: single layer models of the InP(111) ($\text{In}_{12}\text{P}_{12}$, top left), InP(011) ($\text{In}_{14}\text{P}_{14}$, top right), InP(001) ($\text{In}_{16}\text{P}_{16}$, bottom right) surfaces as well as a spherical cut of bulk ($\text{In}_{13}\text{P}_{13}$, bottom left). Indium atoms are brown and phosphorus atoms are indicated in orange.

Coordination numbers of individual atoms are assigned based on rescaled covalent radii of indium and phosphorus, which are 1.42 Å and 1.07 Å¹⁵⁰, respectively. The cutoff for an In-P bond was assigned as:

$$d_{\text{cut}}(\text{A-B}) = 1.25 * (r_{\text{cov}}(\text{A}) + r_{\text{cov}}(\text{B})) , \quad (3.1)$$

which is 3.1 Å when A=In and B=P for the In-P bond. For comparison, the nearest-neighbor In-P distance in the experimental zinc blende InP structure is 2.54 Å^{139, 147}. Since our cutoff distance for coordination is somewhat arbitrary, we also analyzed the sensitivity of coordination number trends to variations in the distance cutoff of about 10% (that is, ± 0.3 Å). When coordination numbers of In by P or vice versa are reported in the results, these analyses are based on $d_{\text{cut}}(\text{In-P}) = 3.1$ Å, with results obtained at $d_{\text{cut}}(\text{In-P}) = 2.8$ Å and = 3.4 Å in parentheses. Similarly, coordination of phosphorus by another phosphorus atom is identified by P-P distances within $d_{\text{cut}}(\text{P-P}) = 2.7$ Å.

Partial charges of atoms were obtained from the TeraChem interface with the Natural Bond Orbital (NBO) v6.0 package¹⁵¹. NBO calculates the natural atomic orbitals

(NAOs) for each atom by computing the orthogonal eigenorbitals of the atomic blocks in the density matrix, and the NBO partial charge on an atom is obtained as the difference between the atomic number and the total population for the NAO on the atom.

3.3 AIMD sampling for cluster generation

We have performed high-temperature (1000 K) *ab initio* molecular dynamics (AIMD) on a 24 atom model of a single layer of the InP(111) surface. The model InP(111) structure has a slightly non-planar, hexagonal shape due to tetrahedral bond angles around In and P (Figure 3-1). We note that our simulation temperature is lower than the experimental melting point (1343 K) for crystalline InP¹⁵², but it is above the typical temperature for InP quantum dot synthesis (450 K)^{42, 107-109}. Since our simulation only includes indium and phosphorus atoms, rearrangements of the InP(111) model in the AIMD trajectory are completely defined by average instantaneous In-P, In-In, and P-P distances (Figure 3-2). During the very initial stages of the high temperature MD run (Figure 3-2), all average distances briefly increase before they plateau and then decrease substantially. While InP(111) surface atoms are tetrahedral with three-fold coordination in-plane of In and P, the isolated sheet first becomes planar, increasing average distances. Following this initial increase, the layer then buckles, with edge atoms folding inward to form a second layer of InP where the fold has occurred. More local folding events occur until the structure becomes globular.

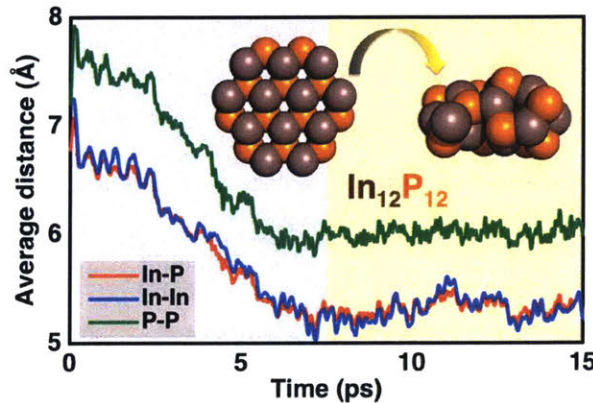


Figure 3-2. Average distances of In-P (red line), In-In (blue line), and P-P (green line) for the $\text{In}_{12}\text{P}_{12}$ cluster over time from *ab initio* molecular dynamics. The average distances for all bond types have a region of monotonic decline (gray shaded region) followed by a leveling off with small oscillations (orange region). A representative initial and final

structure of $\text{In}_{12}\text{P}_{12}$ is indicated in inset (indium atoms are brown van der Waals spheres and phosphorus atoms are orange van der Waals spheres).

The formation of the three-dimensional cluster leads to rapid, approximately linearly, decreasing average distances over the first 7.5 ps of the AIMD trajectory. A linear best fit to obtain the rate of change of average distances between In and P atoms is obtained as:

$$d_{\text{avg}}(\text{In-P}) = -0.25t + 6.90 , \quad (3.2)$$

where $d_{\text{avg}}(\text{In-P})$ is the average distance in Å and the simulation time, t , is in ps. Similarly, the time evolution of the average In-In distances may be obtained with the same -0.25 Å/ps slope but with a larger intercept of 6.97 Å. These two relationships may be compared to the time evolution of the average distance of all phosphorus atoms:

$$d_{\text{avg}}(\text{P-P}) = -0.29t + 7.83 , \quad (3.3)$$

where $d_{\text{avg}}(\text{P-P})$ is in Å and t is in ps. The larger P-P intercept is due to larger initial increases in P-P distances, which is then compensated by a slightly steeper slope (-0.29 Å/ps). Once the coalescence period has completed, all average distances stabilized for the remainder of the simulation (an additional 7.5 ps), with constant averages $d_{\text{avg}}(\text{In-In})=5.3$ Å, $d_{\text{avg}}(\text{In-P})=5.3$ Å, and $d_{\text{avg}}(\text{P-P})=6.0$ Å. Instantaneous fluctuations (~ 0.1 Å) in average distances between time steps are nearly the same in the coalescence and in the stabilized regimes. Phosphorus atoms on the surface show the single largest variations in position during the simulation, while In atoms both in the core and on the surface exhibit smaller variations.

We then verified that unchanging average distances corresponded to fluctuations about a single energy minimum with geometry optimizations of five isolated snapshots 1.5 ps apart from the 7.5 ps stabilized regime. Geometry optimizations are carried out with B3LYP/LACVP*, and they lead to a reduction in total energy of 77-105 kcal/mol for each snapshot, partially due to corrections in differences between HF/3-21G (used for AIMD) and B3LYP/LACVP* preferred geometries. The final energies of the five geometry optimizations vary by no more than 0.2 kcal/mol, confirming the stabilized regime corresponds to fluctuations around a single minimum energy basin.

The initial layer of InP(111) was roughly a circle with a 12.7 Å diameter, while

the new globular cluster is ellipsoidal with dimensions of 11.9 Å, 7.9 Å, and 5.9 Å. The change in size corresponds to a reduction in surface area of 193 Å², as determined by van der Waals radii, and a ~250 kcal/mol reduction in energy after geometry optimization. We repeated the high-temperature AIMD at 700 K and 500 K in order to identify whether simulation temperature had a significant effect on energetics. Final energies of the 700 K and 500 K clusters were within 1-2 kcal/mol of the 1000 K structure, but coalescence time increased from 7.5 ps at 1000 K to 15 ps at 700 K and 20 ps at 500 K, motivating continued use of 1000 K for AIMD.

The average coordination number (CN) in the optimized cluster is 2.8 ($d_{\text{cut}} = 2.8$ Å; 2.7; $d_{\text{cut}} = 3.4$ Å; 2.8) for In and 3.0 (2.8; 3.0) for P, which is an increase from CN=2.5 for the initial single-layer InP(111) structure. The maximum CN is 3 (3; 3) for In and 4 (3; 4) for P, and 10-11 of the 12 In and P atoms have CN 3 or higher. The minimum CN is 2 (0; 2) for In and 2 (2; 2) for P atoms, and only 1-2 In or P atoms have this low coordination. While the presence of undercoordinated atoms is surprising when associated with a large reduction in surface area, overall higher average CN outweighs the energy penalty of the few undercoordinated species observed.

Comparison of NBO charges for the optimized clusters reveals average In and P charges (q) of +1.14 and -1.14, which are larger than +1.01 and -1.01 for the initial InP(111) model. Under-coordinated atoms are more neutral with charges of +0.71 and +1.06 (CN=2) for In atoms and -0.99 (CN=2), -0.76/-0.71 (CN=3) for P atoms. Since In-P bonds are fairly ionic, the degree of In-P charge separation appears to correlate roughly to the strength of bonding. For the initial InP(111) structure, CN=2 boundary indium atoms had a charge of 0.93, while boundary phosphorus atom charges were -0.87. These results suggest that in some cases the CN=2 coordinated atoms in the cluster are in a higher effective coordination environment than the edge atoms in the initial InP(111) cluster. The two outlying CN=3 phosphorus atoms ($q = -0.76, -0.71$) are in a unique configuration in which one of the three coordinating atoms for each atom is the other phosphorus atom. Phosphorus-phosphorus bonds are covalent, explaining the lower net charge on these P atoms. The two phosphorus atoms form a dimer with a P-P distance of 2.3 Å, which is elongated with respect to the 1.9 Å¹⁵³ bond in a gas phase phosphorus dimer due to bonding of the P atoms with other cluster atoms.

3.4 Generalizing the sampling approach

3.4.1 Different sized clusters

It is interesting to identify whether these AIMD-driven rearrangements are strongly size-dependent by repeating the procedure for 6-28 atom single-layer models of InP(111). The initial configurations range from highly symmetric to more elongated (see Figure 3-3), where elongated structures (e.g., In_5P_5 , In_7P_7 , $\text{In}_{11}\text{P}_{11}$, and $\text{In}_{13}\text{P}_{13}$) are 4.9 Å wide (7.6 Å for $\text{In}_{13}\text{P}_{13}$) and 1.7x, 2.5x, or 4.2x longer (2.5x for $\text{In}_{13}\text{P}_{13}$). The smallest models have nearly 4 times as many two-coordinated atoms as three-coordinated ($\text{CN}_{\text{avg}}=2$ in In_3P_3 and In_4P_4), but this ratio decreases to 1.2 in the largest asymmetric model ($\text{In}_{12}\text{P}_{12}$, $\text{In}_{13}\text{P}_{13}$, $\text{In}_{14}\text{P}_{14}$ all have $\text{CN}_{\text{avg}}=2.5$). The In_3P_3 , In_8P_8 , In_9P_9 , and $\text{In}_{10}\text{P}_{10}$ models are relatively symmetric with comparable widths and lengths, and the $\text{In}_{14}\text{P}_{14}$ model is of intermediate symmetry between $\text{In}_{12}\text{P}_{12}$ and $\text{In}_{13}\text{P}_{13}$. While all other structures are generated from repeating hexagonal patterns, to satisfy the stoichiometry of In_4P_4 and In_6P_6 , single atoms were added to In_4P_4 and a bridge was introduced between two hexagons in In_6P_6 .

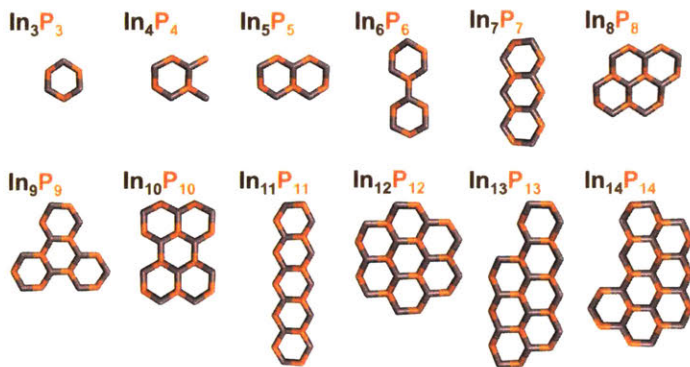


Figure 3-3. Initial configurations in the size range of In_3P_3 to $\text{In}_{14}\text{P}_{14}$ for *ab initio* molecular dynamics simulations from one layer of InP(111).

For nearly all InP(111) structures considered, the high-temperature AIMD simulations exhibit the same rapid, monotonic decrease in average distances corresponding to formation of a globular cluster followed by a leveling off and stabilization of average distances as in $\text{In}_{12}\text{P}_{12}$ (see Figure 3-2). The In_3P_3 , In_5P_5 , In_8P_8 , and In_9P_9 clusters required the shortest times (2.5 ps) to reach the stable regime, though the

two smaller clusters (In_3P_3 and In_5P_5) did not strictly rearrange to form a globular structure. For the smallest cluster (In_3P_3), large fluctuations in average distances were observed without any rapid decline. Instead, the evenly distributed In-P-In and P-In-P angles in the cyclic structure rearranged to acute In-P-In angles and very obtuse P-In-P angles. The rearrangement for In_5P_5 was similar with an additional breaking of the central link in the originally bicyclic compound and formation of acute In-P-In and obtuse P-In-P angles. The most asymmetric $\text{In}_{11}\text{P}_{11}$ layer required the longest time (15 ps) to reach the stable region. Counter to expectations, low-CN atoms on the In_4P_4 model did not accelerate the dynamics, but the singly coordinated atoms in In_4P_4 initiated a second layer in the structure, more closely mimicking nanoparticle-like clusters than In_3P_3 and In_5P_5 . Fluctuations of average distances in the stable regime ($\sim 0.05\text{--}0.1 \text{ \AA}$) did not show dependence on the cluster size except for larger fluctuations (up to 0.16 \AA) in the three smallest clusters.

The commonality of behavior in AIMD simulations over a wide range of system sizes motivates future work in automating this approach for generating cluster structures from other elements, stoichiometry, and size ranges. The signatures of coalescence and stabilization during the AIMD trajectory provide a path for an automatic method. Coalescence will be identified as follows: after the first 3,000 steps, a running average is computed over 1,000 steps, and a finite difference slope is compared every 500 steps. When the finite difference slope is reduced, zero, or positive twice, the simulation is identified as being in the stabilized regime. The simulation is then continued until the slope remains near zero for 1 ps. We have implemented this automatic method and are currently employing it in ongoing study of other materials.

The energetic properties of the resulting 6-28 atom clusters we generate exhibit a strong size-dependence (Figure 3-4). In order to examine how the energy depends on cluster size, we define a relative energy per pair of In, P atoms referenced against the energy of the smallest cluster size studied (In_3P_3):

$$E_{\text{per pair}}(n) = \frac{E(\text{In}_n\text{P}_n)}{n} - \frac{E(\text{In}_3\text{P}_3)}{3}, \quad (3.4)$$

where $E(\text{In}_n\text{P}_n)$ is the energy of cluster In_nP_n and n is the number of In, P pairs. In each case, relative energies are obtained from five optimized snapshots obtained 0.5-2.5 ps

apart, as for $\text{In}_{12}\text{P}_{12}$. The relative energy decreases rapidly from In_3P_3 to In_8P_8 and levels off for the larger sized clusters (In_9P_9 to $\text{In}_{14}\text{P}_{14}$). This energetic dependence is fit with an exponential trend line of the form:

$$E_{\text{per pair}}(n) = 210(2n)^{-1.05} - 30.5 \quad , \quad (3.5)$$

with a residual of 20.3 kcal/mol. The asymptotic relative energy per pair is -30.5 kcal/mol, and clusters $\text{In}_{81}\text{P}_{81}$ in size or larger are predicted to be within 1 kcal/mol of the asymptote.

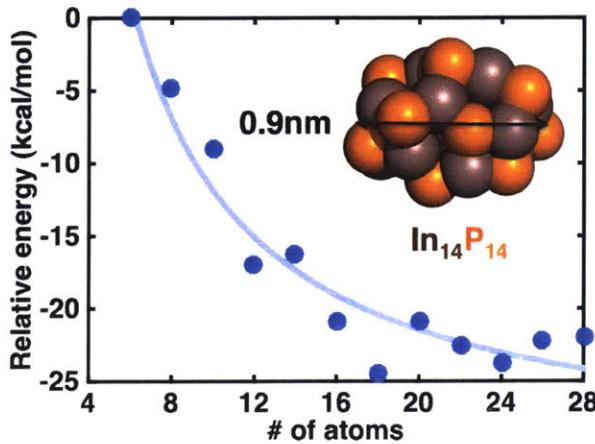


Figure 3-4. Relative energy per pair of InP atoms (blue dots) as a function of system size referenced against the In_3P_3 cluster. Energies are obtained from averages of geometry optimizations from several snapshots obtained from high temperature *ab initio* molecular dynamics on single layers of the InP(111) surface. The resulting structure of one representative cluster ($\text{In}_{14}\text{P}_{14}$) is shown in inset along with its corresponding size (indium atoms shown as brown van der Waals spheres and phosphorus atoms are orange van der Waals spheres). An exponential best fit line (light blue) is also shown.

Overall, the diameters of the structures are reduced by 24-37% from the initial InP(111) structures with the diameter reduction increasing with increasing cluster size, corresponding to an increase in CN as well. Average In CN for the clusters range from 2.0 (2.0; 2.0) for In_3P_3 and In_5P_5 to 3.5 (3.0; 3.5) for $\text{In}_{10}\text{P}_{10}$ and 3.3 (3.2; 3.5) for $\text{In}_{13}\text{P}_{13}$ with CN increasing as cluster size increases especially from In_3P_3 to $\text{In}_{10}\text{P}_{10}$. As CN averages level off, so do the energies of the clusters. The average P coordination numbers range from 2.0 (2.0; 2.0) for the small clusters (In_3P_3 and In_5P_5) to 3.5 (3.4; 3.6) for larger structures ($\text{In}_{10}\text{P}_{10}$, $\text{In}_{11}\text{P}_{11}$, and $\text{In}_{13}\text{P}_{13}$).

Of the subset of high-CN atoms, we identify buried atoms as CN=4 or higher that

are at least one covalent radius (r_{cov}) closer to the center of mass than the average radius of the cluster ($r_{\text{cluster,avg}}$):

$$r_{\text{buried}} < r_{\text{cluster,avg}} - r_{\text{cov}} , \quad (3.6)$$

Three larger clusters, $\text{In}_{10}\text{P}_{10}$, $\text{In}_{13}\text{P}_{13}$ and $\text{In}_{14}\text{P}_{14}$ have buried atoms with one buried P in $\text{In}_{10}\text{P}_{10}$, and both In and P buried in $\text{In}_{13}\text{P}_{13}$ and $\text{In}_{14}\text{P}_{14}$. Surface atoms in the larger-sized clusters have average CNs ranging from 2.7 to 3.5 for In atoms and 3.0 to 3.3 for P atoms and average In-P nearest neighbor distances of 2.5-2.6 Å, slightly shorter than average In-P bond distance of 2.6-2.8 Å for buried atoms. Overall, while relatively few clusters have a large core of buried atoms, most clusters with more than 18 atoms have a majority of CN=3 or higher atoms, and the few cases with anomalously low energy (e.g. In_9P_9) correspond to a high number such atoms.

3.4.2 Alternative starting configurations

In order to identify how sensitive the final energy and geometric structures of clusters are to the initial configurations, we compare results obtained with three additional initial configurations (see Figure 3-1). Two of the structures are generated from single layer surface models of InP, including: i) a 28 atom layer of InP(011) and ii) a 32 atom layer of InP(001), while the third model is a 26 atom spherical cut of bulk InP. The coordination numbers of the initial structures are highest in the bulk model case ($\text{In}_{13}\text{P}_{13}$) at two to four for both In and P, intermediate and comparable to InP(111) in the $\text{In}_{14}\text{P}_{14}$ model (two to three for In and P), and lowest in the $\text{In}_{16}\text{P}_{16}$ model at one to two for both In and P. The bulk model is the most compact (10.5 Å diameter) while both $\text{In}_{14}\text{P}_{14}$ and $\text{In}_{16}\text{P}_{16}$ are flat, rectangular structures. Comparing AIMD simulations, we observe a shorter time to coalescence (3 ps) for the bulk model than for the InP(111) model, likely owing to shorter initial distances, while for $\text{In}_{14}\text{P}_{14}$ initial average distances are more comparable to InP(111) and the time to coalescence (5 ps) is similar.

Interestingly, energetic and structural properties for the clusters generated from these differing starting structures are quite similar. Final optimized relative energies are within 2 kcal/mol per pair, with the spherical bulk structure slightly lower by 1 kcal/mol per pair with respect to InP(111) and the InP(011) structure slightly higher by 1 kcal/mol per pair. These differences are well within the uncertainty of the choice of other

simulation parameters. As expected from energetic comparisons, average distances are similar, as are average coordination numbers ($\text{In}_{13}\text{P}_{13}$: 3.3 for both In and P in spherical bulk, 3.3 for In and 3.5 for P in $\text{InP}(111)$; $\text{In}_{14}\text{P}_{14}$: 3.1 for both In and P in $\text{InP}(011)$ and $\text{InP}(111)$). Differences in CN arise from formation of a P-P dimer in the $\text{InP}(111)$ -derived $\text{In}_{13}\text{P}_{13}$ cluster. We emphasize here that despite a short coalescence time for the spherical bulk model, the final structure is in fact amorphous in nature and comparable to those obtained from other starting configurations. Overall, differing initial configurations have a limited effect on the final energy and geometry of clusters, emphasizing the robustness of this scheme for sampling low-energy geometries.

3.5 Accelerating cluster structure generation

Thus far, our approach has required 2.5 to 15 ps of AIMD sampling for each cluster size. As an alternative, it may be possible to generate new clusters starting from optimized clusters of a different size. Using the adding approach (Figure 3-5), we generate larger starting clusters for AIMD by identifying In and P atoms with the lowest coordination number at the surface of the cluster. Surface atoms are identified as those with a distance to the center of mass larger than the average radius of the cluster. In some cases (e.g. In_7P_7), there is only one pair of P and In with the minimum coordination number (here, CN=2), while for others (e.g. In_9P_9), several (here, 3) surface sites have the same coordination (here, CN=3), of which one is randomly selected. The additional In (P) atom is placed along the vector between the P (In) site and the center of mass at a distance of 3 Å from the surface. New initial In_4P_4 to $\text{In}_{13}\text{P}_{13}$ configurations from $\text{InP}(111)$ -derived clusters and $\text{In}_{14}\text{P}_{14}$ to $\text{In}_{17}\text{P}_{17}$ from the alternative starting configurations are used as starting points for AIMD runs and subsequent optimizations. The resulting energy of the structures obtained from the adding (also referred to as “single adding”, SA) method is within 3.7 kcal/mol per pair of the results obtained directly from crystal model structures, except for the smallest structure, In_4P_4 . Typically, the energies of structures obtained with the adding method are lower than those obtained directly from rearrangement of crystal-derived models.

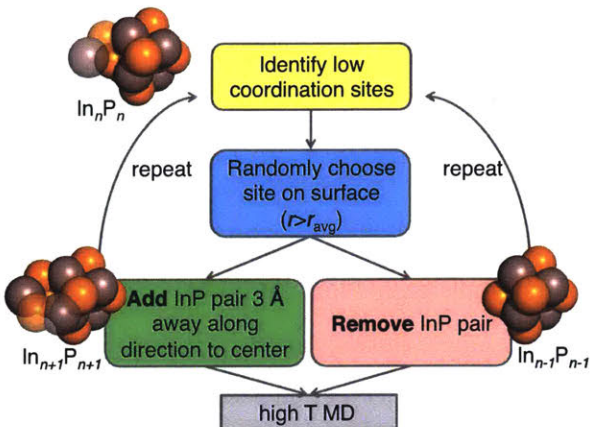


Figure 3-5. Flowchart schematic for adding and removing pairs of In and P to generate new initial structures for *ab initio* molecular dynamics from clusters at a given size. A representative starting structure (In_nP_n) is shown at top with the atoms removed ($\text{In}_{n-1}\text{P}_{n-1}$, bottom right) shown with translucent spheres and the added atoms to the larger cluster ($\text{In}_{n+1}\text{P}_{n+1}$, bottom left) also indicated with translucent spheres. Indium is depicted as an opaque or translucent brown van der Waals sphere, and phosphorus is shown as an opaque or translucent orange van der Waals sphere.

For the generation of larger clusters, we added two atom pairs (“double adding” or DA) to generate In_5P_5 to $\text{In}_{16}\text{P}_{16}$ and $\text{In}_{18}\text{P}_{18}$ from smaller clusters and added three to six atom pairs (multiple adding, “MA”) to generate $\text{In}_{19}\text{P}_{19}$ to $\text{In}_{22}\text{P}_{22}$ clusters. On average, energies per InP pair of the DA structures are slightly higher than those obtained with SA for In_5P_5 to $\text{In}_{15}\text{P}_{15}$ with an average deviation of 1.1 kcal/mol and maximum difference of 4.3 kcal/mol. Energetic differences are a result of differing coordination environment: the SA cluster CN is more uniform with CN=3 for all but one In CN=2 (1;2) and P CN=4 (4;5), while the DA cluster has only two CN=3 In and P atoms and more low-coordinated (CN=2) In (four atoms) or P (three atoms) and high-coordinated (one CN=4 for In, two CN=5 for P) atoms. Interestingly, in both clusters, P-P dimers are observed (1 for SA, 2 for DA). A benefit of the MA approach is the size of clusters we are able to generate low-energy structures for as our 44 atom cluster is 1.5 nm in diameter, on the smaller side of experimental⁴² nanoparticles. For the largest clusters, the average In CN is 2.8-3.3 and P CN is 3.1-3.8, within reasonable agreement to experimental coordination number averages of 3.56 for bulk amorphous InP¹⁵⁴.

In addition to having comparable energetics, the SA, DA, and MA AIMD runs exhibit dramatically shorter coalescence times on the order of 0.5 to 1 ps. For these

approaches, the predominant rearrangement during AIMD is around the site of the newly added atoms. We quantify movements of each atom as the change in distance to the center of mass of the original cluster during the AIMD trajectory. For instance, in the SA trajectory for $\text{In}_{12}\text{P}_{12}$, the change in distance for the four adjacent atoms to the newly added atoms is larger than 0.9 Å, while the movements of other atoms are < 0.5 Å. This limited rearrangement is the source of reduced computational effort for all clusters generated in this manner. Shorter coalescence times with the adding method provide a path toward generating large clusters on the order of the 2-4 nm range generated experimentally⁴² by adding several pairs of atoms at a time and running brief 1 ps dynamics intervals and geometry optimizations for relaxation after each set of atoms has been added. While computational cost of the underlying electronic structure calculations will increase with increasing system size, brief dynamics runs remain feasible for these larger system sizes. Unlike the adding methods, coalescence times from AIMD of InP(111) models increase significantly with increasing system size. By fitting to symmetric InP(111) model coalescence times, we extrapolate that a 2 nm $\text{In}_{52}\text{P}_{52}$ cluster will require 88 ps of coalescence time. While GPU-accelerated electronic structure calculations generally only scale $O(N^2)$ with the number of basis functions¹⁴³, the quadratic scaling of coalescence time with the number of atoms will limit AIMD starting from crystalline models to smaller cluster sizes. Therefore, in order to reach a 2-3 nm cluster size comparable to experimentally synthesized clusters, a sequential adding approach with brief periods of dynamics between each adding step starting from a mid-sized cluster (e.g. ~40 atoms) will greatly reduce the computational cost.

Coordination numbers in clusters generated from all adding methods exhibit a wider range for In (both lower and higher CN) but overall comparable average CN to those obtained from longer MD runs. The SA, DA, and MA clusters have higher average CNs for P due to the increased presence of P-P dimers, with almost all clusters having at least one but as many as nine (in $\text{In}_{22}\text{P}_{22}$). For the larger clusters ($\text{In}_{15}\text{P}_{15}$ - $\text{In}_{22}\text{P}_{22}$), the average CN is between 2.8 to 3.3 (2.1 to 3.0; 3.0 to 3.4) for In atoms and 3.1 to 3.8 (3.0 to 3.2; 3.1 to 4.0) for P atoms compared to a larger range of 2.0 to 3.5 for the average CN and smaller lower limit on the CN (1.9 to 3.2 for In, 2.0 to 3.5 for P; 2.0 to 3.5 for In, 2.0 to 4.5 for P) for the smaller clusters. The overall number of buried atoms also increases,

with the largest model having 5 (4; 5) buried In atoms and 5 (2; 5) buried P atoms.

We also generated new structures by removing pairs of atoms on the optimized clusters (see Figure 3-5) to test whether this approach accelerates generation of comparable, low-energy clusters. As before, we identify pairs of In and P atoms with the lowest CN and now remove them from the cluster. We used an $\text{In}_{13}\text{P}_{13}$ cluster to generate In_3P_3 to $\text{In}_{12}\text{P}_{12}$ and an $\text{In}_{16}\text{P}_{16}$ cluster to generate In_5P_5 to $\text{In}_{15}\text{P}_{15}$ starting structures by repeatedly removing atoms. As with the adding method, coalescence times were significantly reduced, with the longest 2.5 ps time, which was for In_5P_5 generated from $\text{In}_{16}\text{P}_{16}$, likely due to an unfavorable starting configuration from large numbers of removed atoms. The energies of removing method structures were on average within 1.6 kcal/mol per pair of the other methods and comparable to those obtained from crystal models but slightly higher than those obtained from the adding method. The removing approach may be suitable for generating clusters for which no symmetric initial configuration is available. The most elongated InP(111) model required 15 ps for coalescence, while the two structures generated by the removing method coalesced within 0.5-1.5 ps, and final energies agreed within 1.7 kcal/mol for all three structures. Consistent with energetic observations, the overall CNs for the structures generated with the removing method were comparable to those obtained directly and from the adding approach. Phosphorus dimers, which were present in the starting structures, were preserved in many of the new clusters.

3.6 Comparing properties of clusters

Having employed up to five different approaches for a single system size, there are 66 clusters 6-44 atoms in size for which the relative energetics may be directly compared (Figure 3-6). While it was previously noted that the adding approach yields lower-energy structures, there is no single approach that consistently yields the lowest energy structure. The largest energy variation (8 kcal/mol) is observed for In_4P_4 , for which a high-energy structure is characterized by all CN=3 atoms, while the lowest energy structure corresponds to CN=2 for all In and an even mix of CN=3 and CN=4 for P atoms, with the higher CN for P resulting from P-P dimers. The variation in energy per pair from In_5P_5 to $\text{In}_{16}\text{P}_{16}$ between up to five methods is around 1.3-4.3 kcal/mol. As

cluster size increases, the variation in energy of the clusters obtained with the different approaches decreases, and variations narrow considerably for cluster sizes 20 atoms or above. One exception is In_9P_9 , with an energy range of 5.0 kcal/mol across methods, which is larger than the 1.3-2.0 kcal/mol variation for comparably sized clusters (e.g. In_8P_8 , $\text{In}_{12}\text{P}_{12}$, $\text{In}_{13}\text{P}_{13}$). For the 18 atom cluster, higher energy structures have CN=1 and CN=2 In atoms absent from the lowest energy structure.

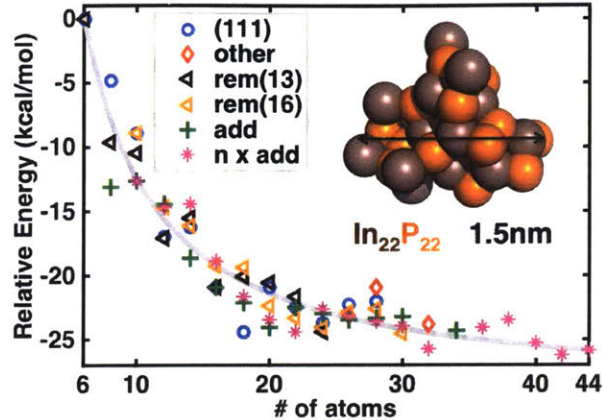


Figure 3-6. Relative energy per pair of InP atoms (referenced against the In_3P_3 cluster) for geometry optimized clusters obtained from *ab initio* molecular dynamics sampling for clusters from 6 atoms to 44 atoms in size. Results are categorized based on the approach for generating the initial structure: from a layer of InP(111) (blue circles); $\text{In}_{13}\text{P}_{13}$ from a spherical cut of bulk (red diamonds), $\text{In}_{14}\text{P}_{14}$ from a layer of InP(011) (red diamonds), or $\text{In}_{16}\text{P}_{16}$ from a layer of InP(001) (red diamonds); using the removing method starting from the $\text{In}_{13}\text{P}_{13}$ cluster (brown triangles); using the removing method starting from the $\text{In}_{16}\text{P}_{16}$ cluster (yellow triangles); using the adding method to generate a structure with $n+1$ pairs from a structure with n pairs (green crosses), and using multiple adding methods with various initial structures (pink stars). A best-fit exponential curve is shown in gray. The resulting structure of one representative cluster ($\text{In}_{22}\text{P}_{22}$, In atoms in brown and P atoms are shown in orange) and its size is provided in the inset.

The size-dependence of relative energies from data on all clusters has a best fit exponentially decaying trend line of the form:

$$E_{\text{per pair}}(n) = 218(2n)^{-1.12} - 29 \quad , \quad (3.7)$$

where the asymptotic relative energy per pair is -29 kcal/mol and clusters $\text{In}_{61}\text{P}_{61}$ or larger are predicted to be within 1 kcal/mol of the asymptote. This trend line is comparable to the one obtained from 6-28 atom InP(111) models, suggesting that cluster properties are converging by around 28 atoms, although this enlarged fit has slightly steeper

dependence on size and a shallower asymptote. The computed energy per pair is relatively flat for all clusters larger than 8 pairs of InP atoms, consistent with the trend line equation that shows the relative energy changes by less than 1 kcal/mol per pair for clusters 18 atoms or larger. Such observations are consistent with previous tight binding calculations by Roy and Springborg¹¹⁹ that also showed similar energetic decreases with increasing system size, though we note in that case geometry optimizations were carried out rather than full AIMD-based rearrangements.

The In-P, In-In, and P-P radial distribution functions (RDF) for all generated clusters (Figure 3-7; In-P bin size 0.13 Å, In-In and P-P bin size 0.24 Å) reveal overall structural characteristics. The In-P RDF is peaked at 2.5 Å, in agreement with experimental¹³⁹ 2.5 Å nearest neighbor distances in the bulk structure, and the RDF first minimum is around 3.1 Å, supporting the distance cutoff choice for coordination number. A broad second shell feature from 4.5 Å to 7 Å is centered around 5.7 Å, which is a larger distance than the experimental¹³⁹ second-sphere distance peak at 4.8 Å. The P-P RDF exhibits a small peak at around 2.1 Å, due to the 116 P-P dimers observed in the clusters. The same behavior is not present in the In-In RDF, where no indium dimers are observed. The same-species RDFs have first non-bonded peaks at 3.6 Å (In-In) and 4.5 Å (P-P), and second peaks centered at 5.8 Å (In-In) and 7.1 Å (P-P). Overall, the P-P RDF peaks are at larger distances than In-In, consistent with earlier observations of differences in average distances in the MD simulations (see Figure 3-2) and in agreement with observations of previous tight-binding geometry optimizations¹¹⁹. These larger P-P distances do not necessarily mean that phosphorus atoms aggregate on the surface. In and P atoms have comparable probabilities in the distance to the cluster center of mass for short and very long distances. While intermediate layers may be segregated with more of one element or the other, core and surface atom numbers are comparable for In and P.

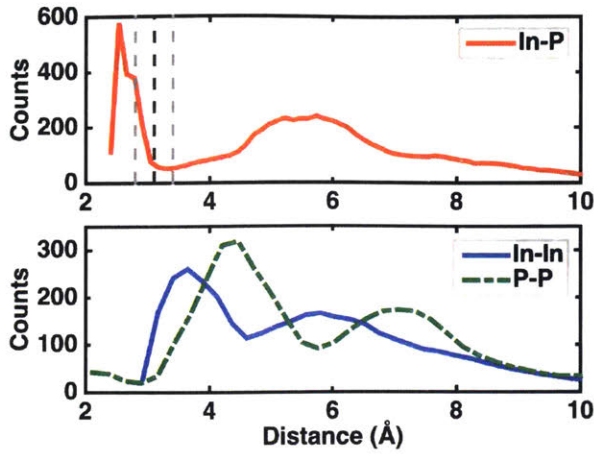


Figure 3-7. The radial distribution functions for (top) In-P distances (red solid line), and (bottom) In-In (blue solid line) or P-P (green dashed line) distances compared over all geometry optimized InP clusters (size range = 6-44 atoms) from all *ab initio* molecular dynamics sampling runs. The nearest neighbor cutoff we define for In-P distances is indicated at top by a black dashed line alongside upper and lower bounds for nearest neighbor cutoffs (gray dashed lines).

Evaluation of overall cluster structural properties reveals high coordination number (CN) around select In and P atoms. Indium CNs range from 1 to 5, with three cases of CN=5 atoms observed in the clusters. The phosphorus atom CNs have a larger range from 2 to 7, with 3 CN=7 P atoms and 6 CN=6 P atoms. We designate short In-P bond distances as $d \leq 2.75$ Å and long In-P bonds as those with $d > 2.75$ Å. A representative CN=7 P (Figure 3-8) is characterized by two short In-P bonds with $d_{\text{avg}} = 2.69$ Å and five long In-P bonds with $d_{\text{avg}}=2.92$ Å, while CN=6 P (Figure 3-8) has three short In-P bonds ($d_{\text{avg}} = 2.67$ Å) and three longer In-P bonds ($d_{\text{avg}} = 2.90$ Å). For CN=5 P, In-P bonds are even shorter with four short $d_{\text{avg}}= 2.59$ Å bonds and one longer 2.77 Å bond, consistent with the presence of long bonds appearing primarily in high CN cases. For a representative CN=5 In, bond distances are similar to the CN=5 P case but with three shorter In-P bonds ($d_{\text{av}}=2.63$ Å) and two longer In-P bonds ($d_{\text{av}}=2.82$ Å). In the crystal structure, In and P are each four-coordinated in a tetrahedral configuration. Our clusters contain a large number of four-coordinated species in two distinct geometries, neither of which perfectly replicate the tetrahedral crystal environment coordination. In the first case, In and P atoms have a quasi-tetrahedral shape (see Figure 3-8) with three short bonds ($d_{\text{av}}=2.60$ Å for In and $d_{\text{av}}=2.64$ Å for P) and one long bond ($d=3.00$ Å for In

and $d=2.85$ Å for P). In the other CN=4 case, the coordinating atoms are all to one side of the likely surface atom, described either by all short bonds ($d_{av}=2.64$ Å for P) or three short ($d_{av}=2.61$ Å for In) and one long bond ($d=3.02$ Å for In).

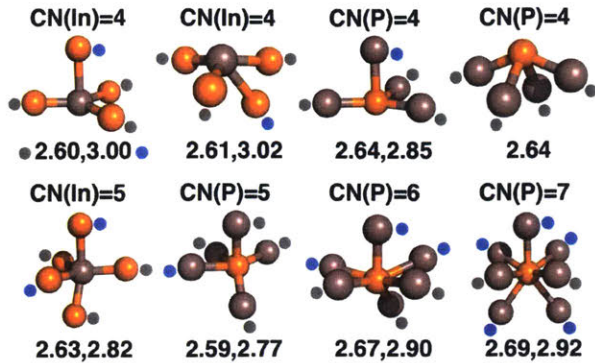


Figure 3-8. Representative configurations of In and P atoms with coordination number (CN) equal to or larger than 4: two In atoms with CN=4 (top left), two P atoms with CN=4 (top right), one In atom with CN=5 (bottom left), one P atom with CN=5 (bottom left), one P atom with CN=6 (bottom right), one P atom with CN=7 (bottom right). Indium atoms are brown and phosphorus atoms are indicated in orange. Short In-P bond distances ($r<2.75$ Å) are indicated by gray dots and long In-P bond distances ($r>2.75$ Å) are indicated by blue dots. Separate averages of the short and long bond distances are shown underneath for each configuration.

Partial charges from NBO analysis demonstrate how coordination environment influences electronic structure (Figure 3-9). As In coordination number increases, the net charge increases from as low as around $+0.75 e^-$ to around $+1.25 e^-$. While there is a variation in charge for different atoms, with the exception of CN=2 In, the distributions are narrow and peaked around one value. At around CN=2, there is a transition between the low-net charge In and high net-charge In, with some CN=2 In charges between these two limits, but for CN>2, the charges are primarily independent of coordination number. Phosphorus charge distributions are complicated by the presence of P-P dimers. For instance, CN=4 P has three peaks: i) at $-1.4 e^-$, corresponding to coordination only by In, ii) at $-1.0 e^-$ for 3 In: 1 P coordination, and iii) at $-0.5 e^-$ for 2 In : 2 P coordinating the central P atom. The reduced net charge in the presence of additional coordinating phosphorus is also apparent for CN=5 and CN=7 (-1.7 - $-1.8 e^-$ vs. -1.1 - $-1.2 e^-$ with P present). Overall, as CN increases, there is also an increase in average net negative charge for both the pure In-coordinated peak and the partially P-coordinated middle

peaks.

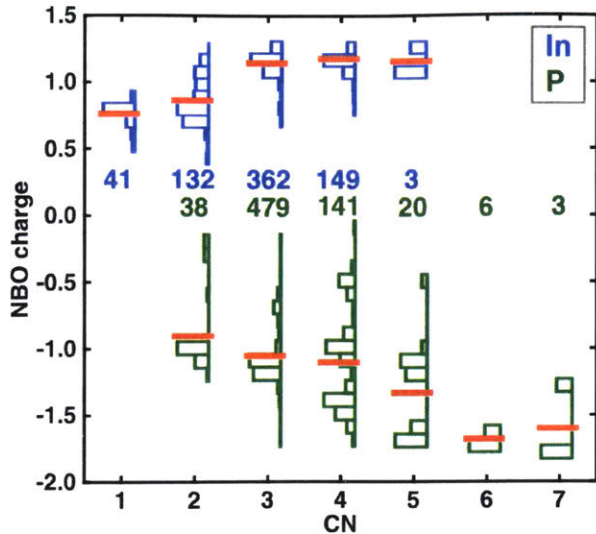


Figure 3-9. The distribution of partial charges for In atoms (blue, top), and P atoms (green, bottom) grouped by coordination number (In: CN from 1 to 5; P: CN from 2 to 7) and averages of each charge distribution (red lines) compared over all atoms from all optimized InP clusters considered. The charge distributions are adjusted so that peaks are at the same height for all distributions, and counts of each coordination number are shown (beneath distributions for In, above distributions for P).

Until now, we have compared energetic trends only amongst the generated amorphous clusters, but a critical question is whether these structures are lower or higher in energy than ordered, crystalline models of the same size. Symmetric models of bulk InP in the studied size range are 14, 24, 26, and 44 atoms, which range from 7.6 Å to 13.3 Å in diameter before geometry optimization, and the largest two have been previously studied¹²¹. For consistency, we do not passivate the surfaces of the ordered clusters, but we do geometry optimize the structures and compare to the amorphous structures (Figure 3-10). Relative energies are evaluated following eqn. 3.4, and, as a result, the smallest 14 atom unoptimized bulk model has a positive relative energy per pair. The unoptimized structures decrease in energy monotonically to a negative value for the largest 44 atom cluster, though these unoptimized structures have relative energies far above the amorphous clusters. After geometry optimization, energies of the ordered models are lowered on average by -15 kcal/mol per pair, with the energy reduction decreasing as the number of bulk atoms increase in the larger clusters. This energy reduction is associated

with rearrangement of atoms that are CN=2 in the initial model to higher-coordinated geometries. Interestingly, the range of relative energies for the amorphous clusters generated previously is consistently below the optimized bulk structures by around 2 to 5 kcal/mol per pair. These energetic observations confirm that we have generated low energy nanostructures of In and P that exhibit coordination environments different from crystalline InP. Such structures may be favored in high-temperature synthesis or with weak ligands that do not direct and slow InP cluster growth. Colloidal quantum dot synthesis is typically directed by strong ligand interactions absent in our simulations, giving rise to an amorphous surface structure and crystalline core. However, structural motifs we have identified are likely candidates for defects and surface structures even in crystalline QDs due to the favorable energetics we have observed. Alternative experimental techniques such as gas phase condensation from laser evaporated materials¹⁵⁵ and more recently microfluidic nebulator technology¹⁵⁶ have both enabled the direct synthesis of amorphous nanoparticle structures. Overall, these observations suggest that this approach for generating amorphous nanostructures might also be applied to study transition-metal phosphide materials that are experimentally already known to have amorphous character¹⁵⁷.

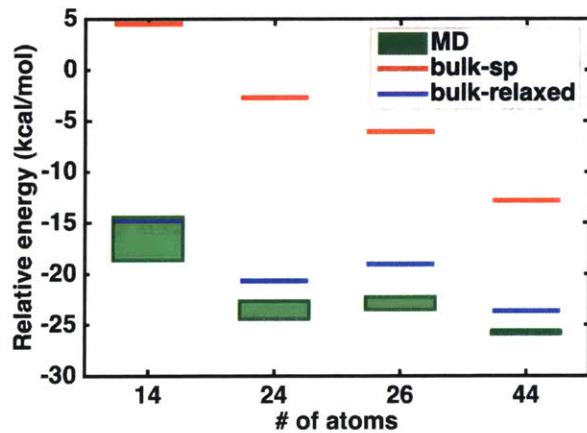


Figure 3-10. Comparisons of relative energy per pair of InP atoms for clusters from *ab initio* molecular dynamics simulations followed by geometry optimizations (green shaded box indicates an energy range from different approaches) with single point energy (red lines) and geometry optimized (blue lines) clusters obtained from spherical cuts of InP bulk (In_7P_7 , $\text{In}_{12}\text{P}_{12}$, $\text{In}_{13}\text{P}_{13}$, and $\text{In}_{22}\text{P}_{22}$). The zero relative energy per pair reference is taken as the energy of the In_3P_3 optimized cluster, as discussed in the text.

3.7 Conclusions

We have introduced a high-temperature *ab initio* molecular dynamics approach for the sampling and discovery of low-energy indium phosphide nanostructures. Starting from open, flat single layer models of crystalline InP, we observed consistent rearrangement to globular, amorphous clusters over a wide size range (8-44 atoms), with exceptions in this trend occurring only for the smallest models considered (6 or 10 atoms). We tracked this rearrangement through observation of a linear decline in average distances in the rearranging cluster that we referred to as coalescence followed by a stabilized regime in which distances fluctuated around constant averages. The time for coalescence depended primarily on the shape of the initial structure and secondarily on system size. When comparing outcomes from differing initial structures, we observed a narrow range in relative energies between clusters. We further identified computational cost reductions in our approach by adding or removing atoms from converged clusters and re-initiating the AIMD step, dramatically reducing the time to coalescence without strongly affecting the final geometric or electronic structure. Accelerated, sequential adding of pairs to grow clusters is likely necessary to study larger clusters in the 2-4 nm range that is more comparable with experimentally synthesized clusters. We note that while coalescence time of direct AIMD simulations from crystalline models grows substantially with system size, sequential adding dynamics relaxation times remain around 1 ps regardless of system size. By harnessing efficiently scaling electronic structure approaches, this efficient rearrangement will enable study of large clusters up to a few hundred atoms as well as efficient screening of properties of a wider array of compounds.

Relative energetics of these structures were strongly size-dependent up to around 20 atoms as average coordination numbers increased dramatically from CN=2 to around CN=3-4. Unusual coordination environments that lowered energy in the clusters included the formation of phosphorus-phosphorus dimers and high-coordination numbers: up to five-coordinated indium and six- or seven-coordinated phosphorus, with alternating short and long bond distances to describe the coordination environment. Although a fair number of four-coordinated In and P were present in the amorphous clusters, few, if any resembled the tetrahedral coordination present in the InP crystal. Despite the unusual

coordination present in these structures, a comparison to bulk models both at experimental geometries and after optimization indicated that the sampled, amorphous structures are consistently lower in energy. Moving forward, our approach is promising for the sampling of low-energy models of amorphous nanostructures, such as those observed in transition-metal phosphides and borides¹⁵⁷.

Chapter 4 Stability of Fullerene Allotropes

This chapter has been published in

Q. Zhao, S. Ng, H. J. Kulik, *J. Phys. Chem. C*, 120 (30), 17035-17045 (2016).¹⁵⁸

4.1 Introduction

Thirty years after the discovery of Buckminsterfullerene (C_{60}) through vaporization of graphite by laser irradiation¹⁵⁹, the excellent properties and potential applications of this unusual carbon allotrope continue to drive considerable scientific inquiry¹⁶⁰. Since their initial discovery, C_{60} fullerenes have found broad technological relevance in polymer-fullerene solar cells¹⁶¹⁻¹⁶⁴, drug delivery¹⁶⁵⁻¹⁶⁶, and proposed hydrogen storage devices¹⁶⁷. The unusual shape and properties of C_{60} have motivated study of its formation mechanism both theoretically¹⁴⁰ and experimentally¹⁶⁸. Soon after the discovery of the carbon-based fullerene, isoelectronic boron nitride fullerenes were synthesized by electron beam irradiation¹⁶⁹ and later with more success through the arc-melting method in a wide size range (B_nN_n , $n=12^{170}$, $24^{171-172}$, 28^{172} , $36^{172-174}$, and 48^{172}). These structures differ from C_{60} in that they are proposed to only have even-membered rings with polar B-N bonds, although transition metal dopants¹⁷³⁻¹⁷⁴ have also been observed to be present due to synthesis conditions. We note that elemental boron, in particular, is well known to produce unusual chemical bonding and allotropes¹⁷⁵⁻¹⁷⁶. Recently, hollow nanocage structures have been made from other elements, including an all boron fullerene¹⁷⁷ and multilayered inorganic $MoS_2^{178-181}$ and $MoSe_2^{178}$ fullerene-like structures.

First-principles simulation can provide valuable insight into the relationship between the unusual geometric structure and associated electronic properties for both fullerenes that have been experimentally isolated and those that may yet still be synthesized. Of all of the binary fullerenes, boron nitride structures have been the primary focus of numerous computational semiempirical¹⁸² and density functional theory (DFT)¹⁸³⁻¹⁹⁰ studies, primarily at sizes commensurate with experimentally characterized BN fullerenes^{182-184, 186-189}, especially $B_{36}N_{36}^{183-184, 186-188}$ allotropes, or slightly larger structures^{185, 190}. Simulations have estimated the 72-atom fullerene to be most stable when 6 four-membered and 32 six-membered rings are present¹⁸³, although there has been some exploration¹⁸⁵⁻¹⁸⁶ of line defects, octagons, decagons and dodecagons or with transition metal dopants¹⁸⁷ and hydrogenated structures¹⁹⁰. Beyond boron nitride, there have been fewer studies of binary compounds comprised of other elements, and typically the focus has been on III-V and II-VI binary A_nB_n fullerenes with light elements¹⁹¹⁻²⁰³ (A =boron,

aluminum, zinc; B=nitrogen, phosphorus, oxygen, sulfur) and small size^{191-192, 195-204} ($n=12$). There are a few exceptions in the literature with heavier elements^{202, 204-206} (A=gallium, cadmium; B=arsenic) and larger sizes^{193-194, 205-206}, and binary IV-IV $\text{Si}_{12}\text{C}_{12}$ ¹⁹² and homogeneous boron fullerenes²⁰⁷⁻²⁰⁸ have also been considered. One notable exception is a study by Beheshtian and coworkers¹⁹¹ who focused on a broader view of the role that element substitution plays in $\text{A}_{12}\text{B}_{12}$ (A=boron, aluminum; B=nitrogen, phosphorus) fullerene properties. In addition to fundamental property studies, some investigations have focused on the potential of binary or ternary III-V²⁰⁹⁻²¹⁰ or II-VI²¹¹⁻²¹³ fullerenes in nanotechnology as gas sensors, for drug delivery²¹⁴, or as hydrogen storage materials²¹⁵⁻²¹⁹.

Despite numerous theoretical studies of structural, energetic, and electronic properties of III-V and II-VI binary fullerenes, a thorough analysis of fullerenes throughout the periodic table has not thus far been carried out in order to identify underlying chemical trends in stable fullerene allotrope candidates. A better understanding of the element-specific rules that govern fullerene allotrope stability will help accelerate identification of potentially synthetically accessible candidates with novel materials properties. Here, we provide a comprehensive study of the relative stability and properties of A_nB_n ($n=28, 30, 36$) fullerenes for 12 III-V materials (A=B, Al, Ga, or In and B=N, P, or As), 4 II-VI materials (A=Zn or Cd and B=S or Se) with some comparison to unary IV C, Si, and Ge structures. In this study, we unearth simple, global descriptors and structural models capable of predicting fullerene stabilities.

4.2 Computational details

First-principles simulations. Calculations were carried out with the graphical-processing unit (GPU)-accelerated quantum chemistry package, TeraChem¹⁴²⁻¹⁴³. Geometry optimizations¹⁴¹ and band gap calculations were performed using DFT with the long-range corrected, hybrid ω PBEh⁹³ exchange-correlation functional ($\omega=0.2$) and the composite LACVP* basis set. The LACVP* basis set corresponds to an LANL2DZ effective core potential basis for the Zn, Cd, Ga, In, As, and Se atoms and 6-31G* basis for the B, Al, N, P, and S atoms.

Structures. We used the $B_{36}N_{36}$ ($B_{28}N_{28}$) fullerene geometry obtained with the CRYSTAL14²²⁰ package as a starting point to generate all other $A_{36}B_{36}$ ($A_{28}B_{28}$) fullerenes. We converted the $B_{36}N_{36}$ ($B_{28}N_{28}$) Cartesian coordinates to internal coordinates in the Gaussian z-matrix format, replaced boron or nitrogen atoms by A or B atoms, respectively, and initially rescaled interatomic distances in the z-matrix based on experimental A-B bond distances in AB crystal structures¹⁴⁸. The optimal bond distances for the starting point of geometry optimizations of $A_{36}B_{36}$ fullerenes were obtained by scanning distances in 0.05 Å increments within ± 0.5 Å of the experimental bond distances. Initial $A_{30}B_{30}$ fullerene configurations were built following the $A_{36}B_{36}/A_{28}B_{28}$ procedure but instead starting from a C_{60} fullerene geometry obtained from the Fullerene Library²²¹. In order to investigate the stability of $A_{36}B_{36}$ fullerenes, we also built unpassivated $A_{36}B_{36}$ spherical nanoparticles (NPs). We obtained experimental parameters of AB crystals from the Crystallography Open Database¹⁴⁸, built supercells of the AB bulk in Avogadro¹⁴⁹, and removed unneeded atoms from the super cells to form spherical NPs. In order to understand stability difference between $A_{30}B_{30}$ and $A_{36}B_{36}$ fullerenes, initial passivated four-, five-, six-membered rings were built using experimental bond distances¹⁴⁸ with Avogadro¹⁴⁹.

Analysis. Coordination numbers (CNs) of individual atoms in fullerenes and NPs are assigned based on rescaled covalent radii of A and B atoms. The cutoff for an A-B bond, $d_{\text{cut}}(A-B)$, was assigned as:

$$d_{\text{cut}}(A-B) = 1.25(r_{\text{cov}}^A + r_{\text{cov}}^B), \quad (4.1)$$

where r_{cov}^A is covalent radius of A atom and r_{cov}^B is covalent radius of B atom. Partial charges of atoms and bonding analysis were obtained from the TeraChem interface with the Natural Bond Orbital (NBO), version 6.0 package²²². NBO calculates the natural atomic orbitals (NAOs) for each atom by computing the orthogonal eigenorbitals of the atomic blocks in the density matrix, and the NBO partial charge on an atom is obtained as the difference between the atomic number and the total population for the NAO on the atom. The Pauling electronegativity difference²²³, which is defined as the dissociation energy difference between A-B bonds and the average of A-A and B-B bonds, was used to analyze the fullerene stability and bonding properties. The projected density of states

(PDOS) was computed for fullerenes by extracting the square of coefficients of atom-centered basis functions of each angular momentum type and applying Gaussian broadening ($\sigma=0.01$ Ha) using an in-house Python script.

4.3 Energetics and electronic properties of $A_{36}B_{36}$ fullerenes

We investigated the energetic properties of $A_{36}B_{36}$ fullerenes from stoichiometric combinations of i) III-V group elements: A = boron, aluminum, gallium, or indium with B = nitrogen, phosphorus, or arsenic and ii) II-VI group elements: A = zinc or cadmium with B = sulfur or selenium. The $A_{36}B_{36}$ structure consists of four- and six-membered rings that contain only A-B bonds and no A-A or B-B bonds, unlike a five-membered-ring-containing binary $A_{30}B_{30}$ model of Buckminsterfullerene (Figure 4-1). The 6 four-membered rings reside on the vertices of the $A_{36}B_{36}$ octahedral structure that also contains 32 six-membered rings.

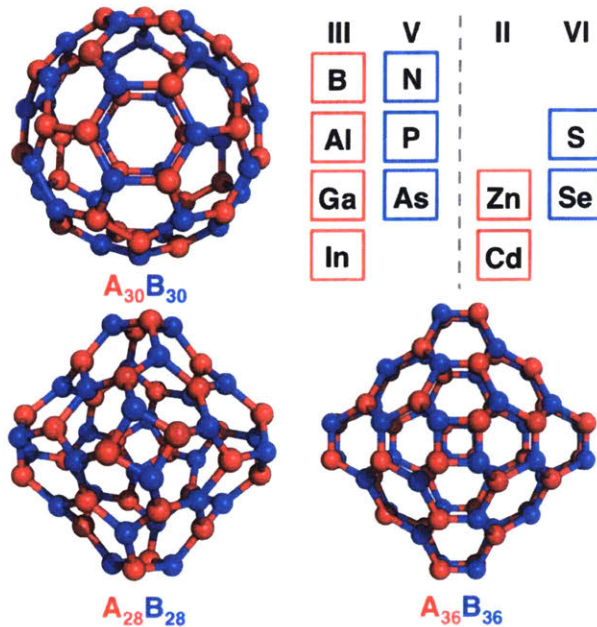


Figure 4-1. Representative ball-and-stick models of $A_{30}B_{30}$ (top left), $A_{28}B_{28}$ (bottom left), and $A_{36}B_{36}$ (bottom right) fullerenes with A atoms shown in red and B atoms in blue. The A and B element choices are shown at top right: A atoms from group III (in red boxes) with B atoms from group V (in blue boxes) or A atoms from group II (in red boxes) with B atoms from group VI (in blue boxes).

Geometry optimization of initial $A_{36}B_{36}$ fullerene structures preserves coordination and qualitative structure with no bond rearrangement. However, the alternating short and long bond lengths in the initial structures become more comparable after geometry optimization. This unchanged coordination indicates that the fullerenes are stable local minima, but comparison to other allotropes is needed to infer global stability. We used nanoparticles (NPs) cut from bulk crystal structures, as is common practice in semiconductor NP studies¹²³⁻¹²⁴, with the same number of atoms as a fullerene in order to provide a candidate low energy reference. For consistency, we geometry optimized these unpassivated NP structures. The average initial CN for the spherical NPs is 3, the same as in a fullerene. NP geometry optimizations result in surface rearrangement, increasing the average CN of each compound to between 3.1 and 3.7. Although we expect the NPs to be more stable than the fullerene structures due to higher average CNs in the optimized NPs, there is a trade-off with some surface atoms (CN < 3) in the reconstructed NPs.

In order to determine the relative stability of $A_{36}B_{36}$ fullerenes, we define a relative energy per pair of A, B atoms in optimized fullerenes ($E(FL)$) with respect to those in the optimized NP ($E(NP)$):

$$E_{\text{per pair}} = \frac{E(\text{FL})}{36} - \frac{E(\text{NP})}{36}, \quad (4.2)$$

We have previously used a similar metric in the analysis of amorphous InP cluster stability¹⁰⁰. Interestingly, the fullerenes are more stable than NPs (i.e., the energy per pair is negative) for almost all materials studied (Figure 4-2). These observations suggest, for instance, that the four-membered rings present in the fullerenes do not induce significant strain, which we will consider in more detail shortly when we compare to other fullerene allotropes that lack four-membered rings. The most stable fullerene (-28 kcal/mol per pair) is $B_{36}N_{36}$, which has already been successfully synthesized experimentally¹⁷²⁻¹⁷⁴. In addition to this well-studied compound, $Al_{36}N_{36}$, $Ga_{36}N_{36}$, $In_{36}N_{36}$, and $B_{36}P_{36}$ fullerenes are all more stable than the optimized NPs by at least 5 kcal/mol per pair. Comparing all element choices, fullerene relative stability decreases when an anion or cation is held fixed and the other species (cation or anion) is substituted with a heavier element. For all 16 compounds considered, we identify only the II-VI $Cd_{36}Se_{36}$ fullerene ($E_{\text{per pair}} = 4$

kcal/mol) as an exception where the NP is more stable. We note, however, that II-VI fullerenes are generally less stable than III-V fullerenes. This trend may be in part due to larger charge separation in the II-VI materials than that of III-V materials. Overall, our observations suggest the following candidates for experimentally stable fullerenes: $\text{Al}_{36}\text{N}_{36}$, $\text{Ga}_{36}\text{N}_{36}$, $\text{In}_{36}\text{N}_{36}$, and $\text{B}_{36}\text{P}_{36}$ in addition to the previously-characterized $\text{B}_{36}\text{N}_{36}$.

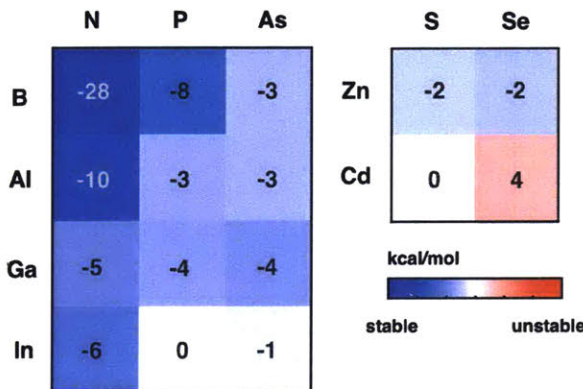


Figure 4-2. Relative energy per pair of AB atoms in kcal/mol of geometry-optimized $\text{A}_{36}\text{B}_{36}$ fullerenes and nanoparticles for different III-V group (left) and II-VI group (right) compounds. The materials for which the fullerenes are most stable are indicated in blue, and those for which the nanoparticles are most stable are indicated in red. The color scale is centered at 0 kcal/mol and saturated values correspond to +/- 15 kcal/mol, as indicated by the inset color bar.

We investigated several candidate descriptors to unearth explanations for these observed trends in $\text{A}_{36}\text{B}_{36}$ fullerene stability. These descriptors included: i) the sum of A and B atoms' atomic numbers, ii) the sum of covalent radii, iii) A-B bond lengths of geometry optimized $\text{A}_{36}\text{B}_{36}$ fullerenes, and iv) electronegativity differences between A and B atoms. We found that no single descriptor correlated sufficiently strongly to stability trends. Instead, we identified a linear combination of properties that describes relative stability trends (Figure 4-3). Our search for a best-fit relationship between relative stability and descriptors reveals a simple functional form ($R^2=0.80$):

$$E_{\text{per pair}} = 30.04 \left[0.31 |\Delta\chi_{\text{B-A}} - 0.75| + 0.69(r_{\text{cov}}^{\text{A}} + r_{\text{cov}}^{\text{B}}) \right] - 53.59 , \quad (4.3)$$

where $E_{\text{per pair}}$ is the relative energy per pair of A and B atoms in kcal/mol, $\Delta\chi_{\text{B-A}}$ is the unitless Pauling electronegativity difference between B and A atoms, $r_{\text{cov}}^{\text{A}}$ and $r_{\text{cov}}^{\text{B}}$ are covalent radii of A and B atoms in Å. This expression suggests that stability is

determined roughly 30% by the electronegativity difference and 70% by the effective size of the substituent elements, which generally increases as we move down the periodic table. The centering of electronegativity differences around -0.75 was based on an analysis of trends in stability versus electronegativity alone.

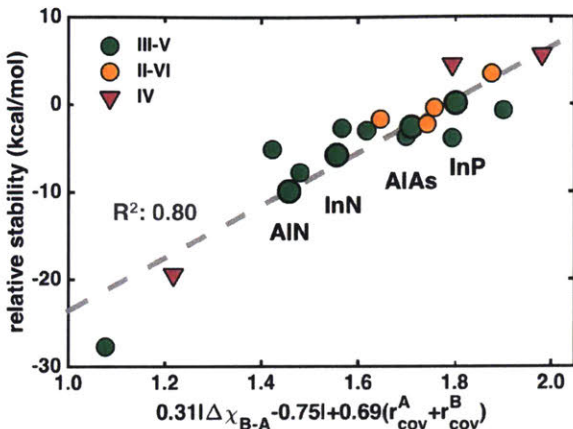


Figure 4-3. Relationship of the relative energy per pair of AB atoms in kcal/mol of $A_{36}B_{36}$ fullerenes referenced against spherical nanoparticles from III-V (green circles), II-VI (orange circles), and IV (magenta triangles) materials with a linear combination of electronegativity difference of B and A atoms ($\Delta\chi_{B-A}$) and sum of covalent radius of A (r_{cov}^A) and B (r_{cov}^B). A best-fit line (gray dashed), which was fit only to III-V and II-VI data, is shown. Selected compounds are labeled and highlighted with bolder symbols.

In order to test the transferability of the observed trend, we investigated whether group IV single-element A_{72} fullerenes (A=C, Si, Ge) stability would follow the same trend as the binary fullerenes. We note here the electronegativity difference is zero ($\Delta\chi_{A-A} = 0$) and the covalent radii are identical ($r_{cov}^B = r_{cov}^A$). Our combined descriptor of electronegativity and covalent radius predicts not only the relative stability of $A_{36}B_{36}$ fullerenes but also that of the homogenous A_{72} fullerenes (Figure 4-3).

We then studied the role that elemental composition plays in determining electronic properties of the $A_{36}B_{36}$ fullerenes. Band gaps may be obtained from total energy differences of cationic, anionic, and neutral species, which is commonly called the D-SCF method^{69,81}, or approximated as the Kohn-Sham gap obtained from the difference in highest-occupied molecular orbital (HOMO) and lowest-unoccupied molecular orbital (LUMO) energies. Generally, the HOMO-LUMO Kohn-Sham gap is known to be quite

close to the fundamental gap for generalized Kohn-Sham methods such as range-corrected hybrids²²⁴⁻²²⁵. We verified the validity of this observation for C₆₀ fullerenes by comparing wPBEh⁹³ HOMO-LUMO (6.0 eV) and D-SCF (5.9 eV) gaps with each other and to the experimental value (4.9 eV). Range-separation parameter (w) tuning to match the negative of the HOMO eigenvalue (-e_{HOMO}) to the ionization potential (IP) has been demonstrated²²⁵ as a strategy to obtaining improved optical properties of materials. Notably, our use of the default w parameter (0.2) yields a difference of only 0.06 eV between the IP and -e_{HOMO}, indicating this value is suitable for the materials studied.

Comparison of geometry-optimized III-V and II-VI A₃₆B₃₆ fullerenes reveals a significant variation from HOMO-LUMO gaps as small as 5.3 eV for heavy elements to as large as 10.8 eV for the lightest element pairings (Figure 4-4). Some A₃₆B₃₆ (B=nitrogen) fullerenes have been previously studied with the PBE functional²²⁶, yielding predicted band gaps of 5.1 eV (A=boron), 2.7 eV (A=aluminum), 2.2 eV (A=gallium) and 0.7 eV (A=indium). The PBE functional is known to underestimate band gaps²²⁶, but focusing on band gap trends indicates a comparable 5 eV difference from the lightest to heaviest fullerenes. This band gap shift is also consistent with the shift observed experimentally for AB crystal structures (from 6.2 eV to 0.42 eV²²⁷⁻²²⁹) with increasingly heavy cation or anion substitutions. Confinement effects in the 0D fullerene structure as well as the slight overestimate of band gaps previously noted for wPBEh explain this difference with respect to the bulk crystal structure. In contrast with overall trends, we note several exceptions to the band gap reduction with increasing mass. Interestingly, these exceptions in our DFT calculations (AlP, GaP > BP and AlAs > BAs) follow trends observed in experimental bulk crystal band gaps.

	N	P	As	S	Se
B	10.8	6.5	6.3	8.0	7.3
Al	7.6	7.1	6.7	7.1	6.5
Ga	7.2	6.7	5.8		
In	5.5	6.0	5.3		

Figure 4-4. HOMO-LUMO gaps (in eV) of geometry-optimized $A_{36}B_{36}$ fullerenes from III-V (left) and II-VI (right) materials obtained with ω PBEh/LACVP*. HOMO-LUMO gaps are color-coded by magnitude from largest (red) to smallest (blue).

In order to compare substitution of A and B elements, we calculated the average change in band gap by keeping the cation (anion) element the same and moving to a heavier anion (cation) element as 1.0 eV and 1.1 eV, respectively, indicating comparable effects in band gaps of substitution of A and B elements. A direct comparison of the dependence of individual HOMO and LUMO eigenvalues with element substitution reveals separate effects of the cation and anion, however. When the cation element is kept the same for III-V or II-VI materials, LUMO eigenvalues show a relatively wider dependence on substitution of different anion elements compared with HOMO eigenvalues, indicating anion elements tend to change the LUMO more. Comparable ranges of HOMO and LUMO shifts are observed by keeping anion the same for III-V materials or II-VI materials, indicating cation elements change HOMO and LUMO equally.

4.4 Comparison of $A_{28}B_{28}$, $A_{30}B_{30}$, and $A_{36}B_{36}$ fullerenes

Thus far, we have studied the energetic and electronic properties of $A_{36}B_{36}$ fullerenes and identified materials that are good candidates to form experimentally stable $A_{36}B_{36}$ fullerenes. A key question that remains is the extent to which $A_{36}B_{36}$ fullerenes may be more stable than the equivalent $A_{30}B_{30}$ Buckminsterfullerene-like allotropes. For $A_{36}B_{36}$ fullerenes, the presence of four-membered rings absent from the Buckminsterfullerenes may introduce strain. On the other hand, the covalent, nonpolar bonds present in the five-membered rings of $A_{30}B_{30}$ fullerenes but absent in $A_{36}B_{36}$ structures may be energetically unfavorable. Therefore, we surveyed energetic properties of the previously studied combinations of III-V and II-VI elements for $A_{30}B_{30}$ models, which have 20 six-membered rings and 12 five-membered rings with 6 nonpolar, A-A bonds and 6 nonpolar, B-B bonds (Figure 4-1). In addition, we investigated a smaller

fullerene model, $A_{28}B_{28}$, which has been experimentally¹⁷² and theoretically^{182, 186} characterized for boron nitride, that contains 6 four-membered rings and 24 six-membered rings (Figure 4-1).

Geometry optimizations of both $A_{28}B_{28}$ and $A_{30}B_{30}$ fullerene structures preserve the coordination with no bond rearrangement. However, the alternating short and long bond lengths in the initial $A_{28}B_{28}$ structures become more comparable. In the $A_{30}B_{30}$ structures, the bond lengths become more disparate, corresponding to the distinct A-B, A-A, and B-B bonds. The lack of change in coordination indicates both $A_{28}B_{28}$ and $A_{30}B_{30}$ fullerenes are stable local minima. In order to compare the stability of these new fullerene structures with that of the $A_{36}B_{36}$ structures, we define a relative energy per pair of A, B atoms in the optimized $A_{28}B_{28}$ fullerene ($E(A_{28}B_{28})$) and $A_{30}B_{30}$ fullerene ($E(A_{30}B_{30})$) with respect to those in the optimized $A_{36}B_{36}$ fullerene ($E(A_{36}B_{36})$):

$$E_{\text{per pair}}(A_{28}B_{28}) = \frac{E(A_{28}B_{28})}{28} - \frac{E(A_{36}B_{36})}{36}, \text{ and} \quad (4.4)$$

$$E_{\text{per pair}}(A_{30}B_{30}) = \frac{E(A_{30}B_{30})}{30} - \frac{E(A_{36}B_{36})}{36}. \quad (4.5)$$

Notably, the $A_{30}B_{30}$ fullerenes are less stable than the $A_{36}B_{36}$ fullerenes for almost all element pairs studied (Figure 4-5). This observation is in stark contrast to carbon-based fullerenes where C_{60} is an exceptionally stable carbon allotrope²³⁰⁻²³¹. Lighter elements, as exemplified by the three nitrogen-containing $A_{30}B_{30}$ fullerenes (A=boron, aluminum, gallium), favor the larger fullerene structure. For instance, these C_{60} analogues are destabilized by more than 11 kcal/mol per A/B atom pairs with respect to $A_{36}B_{36}$ fullerenes. Similarly, the other two aluminum-containing $A_{30}B_{30}$ fullerenes (B=phosphorus, arsenic) are destabilized by more than 5 kcal/mol per A/B atom pair with respect to $A_{36}B_{36}$ fullerenes. For all 16 compounds considered, boron arsenide fullerenes are the only III-V material for which the $B_{30}As_{30}$ structure is more stable than $B_{36}As_{36}$. For II-VI materials, the $A_{30}B_{30}$ fullerenes are destabilized even further by about 10-14 kcal/mol per A/B pair with respect to the $A_{36}B_{36}$ compounds. This energetic trend is not primarily a size effect, as the stabilities of $A_{28}B_{28}$ fullerenes are comparable to $A_{36}B_{36}$ fullerenes, likely due to the presence only of even-membered A-B-alternating rings. One exception to this size-insensitivity is the nitrogen-containing $A_{28}B_{28}$ fullerenes, which

have a relative energy of 2 kcal/mol per A/B pair higher compared to the larger $A_{36}B_{36}$ fullerenes.

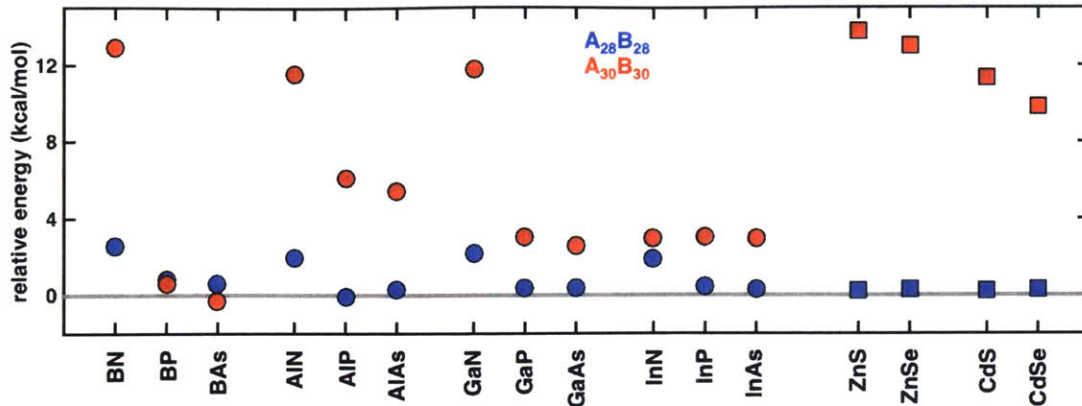


Figure 4-5. Relative energy per pair of A/B atoms in kcal/mol of geometry optimized $A_{28}B_{28}$ (blue) and $A_{30}B_{30}$ (red) fullerenes with respect to $A_{36}B_{36}$ fullerenes from III-V (circles) and II-VI (squares) materials.

We now examine the source of differences in relative stability of $A_{30}B_{30}$ and $A_{36}B_{36}$ fullerenes with quantitative measures derived from the structural and electronic properties of the materials. In order to determine structural effects, we built III-V and II-VI four-, five-, and six-membered rings, passivated the structures with hydrogen atoms, and computed the relative energies of geometry-optimized four- and five-membered rings with respect to optimized six-membered rings (Figure 4-6). These energy penalties (E_{penalty}^4 for four-membered rings and E_{penalty}^5 for five-membered rings) are computed as follows:

$$E_{\text{penalty}}^4 = 2 \left[\frac{E(A_2B_2H_4)}{2} - \frac{E(A_3B_3H_6)}{3} \right], \quad \text{and} \quad (4.6)$$

$$E_{\text{penalty}}^5 = \frac{5}{2} \left[\frac{E(A_3B_2H_5)}{5} + \frac{E(A_2B_3H_5)}{5} - \frac{E(A_3B_3H_6)}{3} \right], \quad (4.7)$$

where $E(A_2B_2H_4)$, $E(A_3B_2H_5)$, $E(A_2B_3H_5)$, $E(A_3B_3H_6)$ are the energies of optimized $A_2B_2H_4$ four-membered ring molecules, $A_3B_2H_5$ or $A_2B_3H_5$ five-membered ring molecules, and $A_3B_3H_6$ six-membered ring molecules. The energy penalties of both four- and five-membered rings decrease with increasingly heavy anion atoms, but the relative stability of four- and five-membered rings varies across the studied materials (Table 4-1).

If bond strain is the largest factor, then four-membered ring energies will always be higher, whereas five-membered rings are expected to be unstable due to the lower favorability of nonpolar bonds with respect to their polar counterparts. The BN, AlN, AlP, AlAs and GaN materials penalize the five-membered ring structures more than four-membered rings, whereas all the other III-V materials show the reverse trend. In previous work¹⁰⁰, we identified P-P bonds to be favorable in amorphous InP clusters, consistent with a lower five-membered ring penalty than four-membered ring penalty in this material (see Table 4-1). The more ionic nature and larger size of the substituents in II-VI materials results in a much larger penalty for the nonpolar bond-containing five-membered ring structures and relatively small penalties for the four-membered rings.

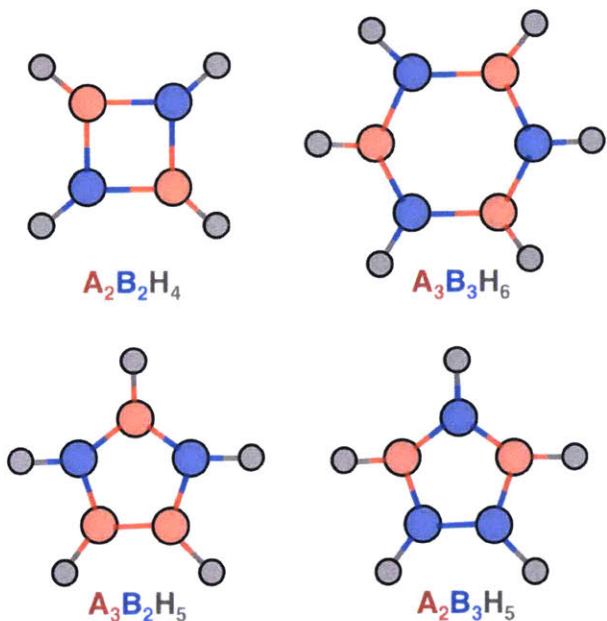


Figure 4-6. Representative ball-and-stick models of hydrogen-passivated four-, five-, six-membered rings: $A_2B_2H_4$ (top left), $A_3B_2H_5$ (bottom left), $A_2B_3H_5$ (bottom right), and $A_3B_3H_6$ (top right) with A atoms shown in red, B atoms in blue and H atoms in gray.

Table 4-1. Relative energy penalties of four-membered (E_{penalty}^4), and five-membered (E_{penalty}^5) rings with respect to six-membered rings in kcal/mol for III-V and II-VI materials.

	E_{penalty}^4	E_{penalty}^5		E_{penalty}^4	E_{penalty}^5
BN	51.1	58.2		GaAs	11.9
					6.0

BP	33.9	18.2	InN	27.1	25.1
BAs	28.4	17.2	InP	19.2	10.6
AlN	29.4	49.8	InAs	17.8	13.9
AlP	19.8	21.8	ZnS	9.2	45.8
AlAs	18.9	20.0	ZnSe	5.4	37.4
GaN	31.0	44.5	CdS	6.8	39.0
GaP	20.7	15.7	CdSe	5.6	35.7

In addition to the relative energy penalty between differing ring structures, the quantity of each ring structure type also matters. In each $A_{30}B_{30}$ fullerene, there are 12 five-membered rings but each $A_{36}B_{36}$ fullerene only contains 6 four-membered rings. Therefore the relative penalties for $A_{30}B_{30}$ and $A_{36}B_{36}$ fullerenes should be calculated as a weighted difference in the number of unfavorable rings on a per-pair of atom basis to maintain consistency as follows:

$$\Delta E_{\text{penalty}} = \frac{12E_{\text{penalty}}^5}{30} - \frac{6E_{\text{penalty}}^4}{36}. \quad (4.8)$$

The relative $A_{30}B_{30}$ to $A_{36}B_{36}$ fullerene energies correlate very well ($R^2=0.92$) with the ring-derived energy penalty differences between the two structures (Figure 4-7). Therefore, our simplified ring model captures all of the underlying differences in chemical bonding that stabilize the $A_{36}B_{36}$ fullerene structures. Although for some heavier III-V materials, five-membered rings are more stable than four-membered rings, the larger (12 vs. 6) number of five-membered rings in $A_{30}B_{30}$ fullerenes with respect to four-membered rings in $A_{36}B_{36}$ means that the 72-atom fullerene is almost always favored. In order to test the transferability of our derived trend, we investigated whether the relative overall stability of group IV elemental A_{60} and A_{72} fullerenes ($A=C$, Si, or Ge) would correlate to the energy penalty differences based on their four-, five-, and six-membered rings. Here, any penalty in the four- and five-membered rings should be derived solely from strain because all bonds are now nonpolar. Heavier A_{60} ($A=Si$, Ge) fullerenes follow the same trend as the heteronuclear materials, but our ring energy penalty metric slightly underestimates the stability of the lighter C_{60} . The difference comes from the

underestimated energy penalty of the hydrogen-passivated four-membered ring because this isolated ring structure assumes an alternating single and double bond structure, but the four-membered rings in fullerenes all have equivalent bond order. For the heavier group IV A₆₀ (A=Si, Ge), the four-membered rings in the fullerene structures are twisted instead of flat, leading to a more representative energetic contribution from the isolated four-membered ring structure.

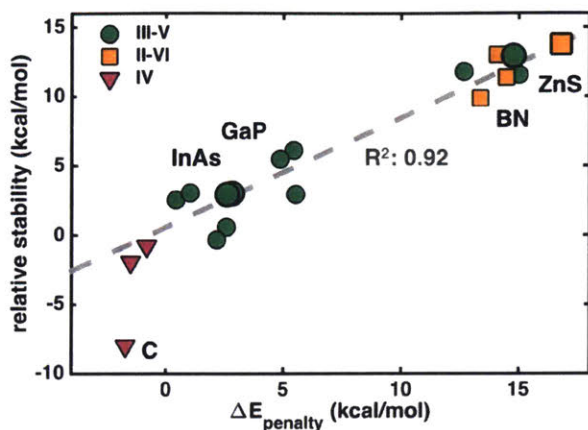


Figure 4-7. Relationship of the relative energy per pair of AB atoms in kcal/mol of $A_{30}B_{30}$ fullerenes referenced against $A_{36}B_{36}$ fullerenes from III-V (green circles), II-VI (orange squares), and IV (magenta triangles) materials with energy penalty differences per pair of AB atoms in kcal/mol between $A_{30}B_{30}$ and $A_{36}B_{36}$ fullerenes. A best-fit line (gray dashed) fit only to III-V and II-VI data is shown. Select labeled compounds are highlighted with bolder symbols.

We also used a reference $A_{36}B_{36}$ spherical nanoparticle to directly compare stabilities of the three different fullerene geometries with respect to substituent cation or anion element changes. We calculate the relative energy per AB pair in three optimized fullerenes $E(A_nB_n)$ ($n=28, 30$, or 36) with respect to those in the optimized $A_{36}B_{36}$ NP ($E(NP)$) as:

$$E_{\text{per pair}}(\text{FL}) = \frac{E(\text{A}_n \text{B}_n)}{n} - \frac{E(\text{NP})}{36} \quad . \quad (4.9)$$

We then examined possible correlations between the relative energies of each fullerene structure with all previously studied materials property descriptors of underlying atoms (e.g., electronegativity or covalent radius) and structure-specific properties (e.g., four- or five-membered rings). From several combinations, we obtained a descriptor, β , which is correlated to the relative stability for all three fullerene structures:

$$\beta = 18.17(r_{\text{cov}}^{\text{A}} + r_{\text{cov}}^{\text{B}}) + \frac{1}{41}(0.19n_4E_{\text{penalty}}^4 + 0.81n_5E_{\text{penalty}}^5) - 0.06n_6, \quad (4.10)$$

where $r_{\text{cov}}^{\text{A}}$ and $r_{\text{cov}}^{\text{B}}$ are covalent radii of A and B atoms in Å, n_4 , n_5 , n_6 are number of four-, five-, six-membered rings in the fullerenes, and E_{penalty}^4 , E_{penalty}^5 are energy penalties of four-, five-membered rings in kcal/mol. The relative stability of each fullerene ($E_{\text{per pair}}(\text{FL})$) is correlated to the descriptor β (Figure 4-8):

$$E_{\text{per pair}}(\text{FL}) = \beta - 43.4, \quad (4.11)$$

where the constant -43.4 kcal/mol depends on the chosen reference structure (an $\text{A}_{36}\text{B}_{36}$ NP). The quantities present in our β descriptor are an intuitive mixture of size- and structure-dependent properties. The relative energy of a fullerene increases with covalent radii of A, B atoms or total energy penalties of four-, five-membered rings, but it decreases with increasing structure size, as indicated by the number of six-membered rings. The instability caused by the energy penalty of five-membered rings is four times larger than that of four-membered rings, as indicated by weights in the final expression and thus this more general correlation indicates that nonpolar bonding is even more destabilizing in the general data set than in our original penalty vs. stability correlation. The size effect corresponding to the number of six-membered rings has a small influence on the fullerene stability, suggesting topology of the fullerene, as described by constituent ring structure energetics, is much more relevant than the size.

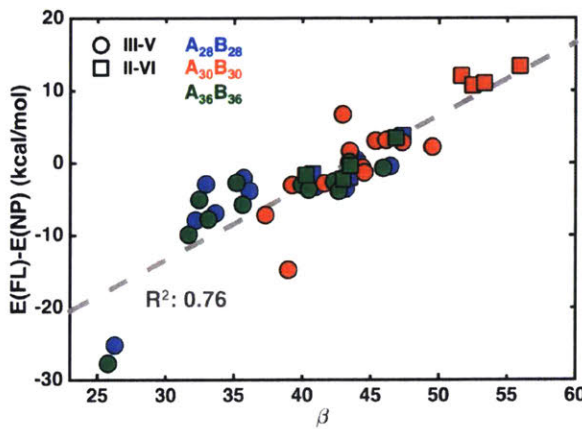


Figure 4-8. Relationship of relative energy per pair of AB atoms in kcal/mol of A₂₈B₂₈ (blue), A₃₀B₃₀ (red), and A₃₆B₃₆ (green) fullerenes referenced against the A₃₆B₃₆ spherical nanoparticles from III-V (circles) and II-V (squares) materials with a descriptor

β which is a linear combination of sum of covalent radius of A and B atoms; total energy penalties of four-, five-membered rings, and number of six-membered rings (the form of β is shown in text). A best-fit line (gray dashed) is also shown.

4.5 Conclusions

We have carried out a systematic study of the role of elemental identity in determining electronic, energetic, and geometric properties of prototypical (i.e., $A_{28}B_{28}$, $A_{30}B_{30}$, and $A_{36}B_{36}$) III-V and II-VI fullerene allotropes. Our use of a nanoparticle reference enabled identification of potentially stable $Al_{36}N_{36}$, $Ga_{36}N_{36}$, $In_{36}N_{36}$, and $B_{36}P_{36}$ fullerenes in addition to the previously-characterized $B_{36}N_{36}$. We found a suitable composite descriptor of electronegativity differences and sum of covalent radii that captured relative fullerene stability in these materials, and, importantly, this descriptor is transferable to group IV A_{72} fullerenes. We observed a shift in band gap with increasingly heavy cation or anion substitutions in the $A_{36}B_{36}$ fullerenes.

We next investigated differences between the 72-atom fullerenes and their $A_{30}B_{30}$ Buckminsterfullerene counterparts, where the latter contain covalent, nonpolar bonds due to the presence of five-membered rings absent in the former, which consists only of polar, alternating A-B bonds in four- and six-membered rings. We expected the four-membered rings of $A_{36}B_{36}$ fullerenes to reduce overall stability due to their large strain energy, but we also anticipated that the nonpolar bonds in $A_{30}B_{30}$ fullerenes might be energetically unfavorable. We found the strain effect to be smaller than the penalty for nonpolar bonding, as $A_{30}B_{30}$ fullerenes were less stable than the $A_{36}B_{36}$ fullerenes for almost all element pairs studied. We also considered size effects by comparison to a smaller $A_{28}B_{28}$ fullerene model, which contains solely four- and six-membered rings and found the energetic trend to not be strongly size-dependent, as the stabilities of $A_{28}B_{28}$ fullerenes are comparable to $A_{36}B_{36}$ fullerenes. In order to understand the energetic difference, we constructed hydrogen-passivated four-, five-, and six-membered rings and computed energy penalties of the strain effect and nonpolar bonds induced by four- and five-membered rings, respectively. We observed a strong correlation between the total relative energy penalties of these substituent ring models to relative fullerene energies. A simple descriptor that consisted only of these penalties and a measure of element size via

covalent radii correlated well to the stabilities of all three fullerene allotropes. Overall, our study has demonstrated a path forward for predicting the relative stability of additional fullerene allotropes of arbitrary shape and size. The strategy presented here should be useful in identifying new stable element combinations and doping strategies in fullerenes.

Chapter 5 Growth Mechanism of III-V Quantum Dots

This chapter has been published in

Q. Zhao, H. J. Kulik, *Chem. Mater.*, 2018, volume just accepted, DOI:
10.1021/acs.chemmater.8b03125.²³²

5.1 Introduction

The unique size-dependent electronic and optical properties²³³⁻²³⁴ of colloidal quantum dots (QDs) make them ideal for applications in photovoltaics,^{37-38, 235} light-emitting diodes,³⁵⁻³⁶ and biological imaging.^{31, 34} Although II-VI CdSe QDs exhibit controllable sizes^{102, 236} and light emission throughout the visible range¹⁰³, III-V InP QDs have emerged as a less toxic¹⁰⁴ alternative²³⁷⁻²³⁸ with even broader emission range.¹⁰⁵⁻¹⁰⁶ Adoption of InP QDs has been limited by difficulties²³⁷ in obtaining optimally narrow QD size distributions and high photoluminescent quantum yields, despite ongoing experimental efforts to understand the QD formation mechanism^{107, 239-243} and tune the growth process.²⁴⁴⁻²⁴⁵ The typical InP synthesis recipe requires high temperatures, employs indium carboxylates^{42, 246-247} that necessitate reactive phosphorus precursors, and long reaction times, making control of size distributions challenging.²⁴⁸

Classical nucleation theory (CNT)²⁴⁹ has been an effective guide for tuning size distributions in more ionic II-VI and IV-VI^{102, 250-251} QDs but nonclassical (i.e., multi-step) nucleation and growth models are needed²⁵² to understand III-V materials.^{240, 253-256} For example, reducing the reactivity of P precursors in accordance with CNT^{244, 257-259} did not improve InP QD size distributions.²⁵² InP magic size clusters (MSCs)^{109, 240} around 1.1²⁶⁰ to 1.3²⁶⁰⁻²⁶¹ nm in size have been observed to be essential intermediates during InP growth, with their size²⁶⁰ and stability²⁴⁰ controlled by In precursor chemistry. InP MSCs have been used as seeds for controlled QD growth²⁴⁰ by decoupling the nucleation and growth stages²⁴². Although MSCs appear an essential key to understanding III-V InP^{240, 253, 261} and InAs²⁶² growth mechanisms, controlled growth of MSCs has also been observed to be beneficial in II-VI materials (e.g., CdS²⁶³, CdTe²⁶⁴, and ternary II-VI alloys²⁶⁵). Indeed, there is increasing consensus that small clusters and MSCs coexist with QDs during growth for a number of materials.^{240, 253, 261-266} The mechanism by which InP QDs form from MSCs remains an open question, with agglomeration unlikely but either dissolution or continued growth at a slower rate both possible.²⁵³

In light of a complex and challenging growth process, precursor variation^{240, 267-268} during synthesis²⁶⁹⁻²⁷² or post-synthetic ligand exchange²⁷³⁻²⁷⁶ on MSCs and QDs have been vigorously pursued experimentally. These efforts have led to discovery of alternate chemistries that can produce unique QD shapes^{269, 273}, size^{237, 267}, stability²⁴⁰,

stoichiometry²⁷⁴⁻²⁷⁵, and quantum yield²⁷⁰⁻²⁷¹, especially through apparent improvements in non-In-passivated surface properties.^{272, 276-277} However, a nanoscale understanding of the QD structure during stages of growth has only been possible in a few cases^{261, 266}, and spectroscopic methods for determining QD structures remain an active area of development²⁷⁸. First-principles simulations have been a valuable complement in understanding the growth mechanism²⁷⁹⁻²⁸⁰ of II-VI and IV-VI QDs. Although properties of amorphous¹⁰⁰, bulk¹¹⁶⁻¹¹⁸, and quantum-confined InP^{100, 120, 133, 158, 281} had been studied in detail, our recent combined *ab initio* molecular dynamics (AIMD) and reaction pathway analysis approach represented the first attempt to discover the growth kinetics and character of early stage intermediates in InP QD synthesis.²⁸² Through AIMD, we observed²⁸² the formation of the earliest stage clusters (ESCs) from isolated precursors in InP QD synthesis. This ESC²⁸² has an indium rich surface surrounding an In₄P tetrahedron with bond lengths and surface carboxylate coordination properties in fortuitously good agreement with simultaneously obtained X-ray crystal structures of InP magic sized clusters^{240, 253, 261}. We also confirmed the paramount importance of In precursors in controlling growth²⁸², and we identified ligand modifications that could provide pathways for low-temperature synthesis²⁸³.

In order to continue to move beyond the limits of CNT, first-principles simulation will provide needed insight to reveal commonalities and variations in the surface chemistry of first-principles ESCs and the experimental MSC structure in order to understand how reactivity changes during QD growth. In this work, we develop a unified electronic structure interpretation of surface reactivity on early-stage²⁸² and magic sized²⁶¹ clusters. We identify high variability of surface site kinetic and thermodynamic properties that depend strongly on nearest neighbor In-In distances in an unexpected manner but can be rationalized through the highly covalent electronic structure at the InP QD surface. This strong relationship between structure and energetics also permits us to interpret and rationalize relative quantities of excess In on the surface of experimentally-characterized²⁶⁶ 3 nm QDs.

5.2 Model curation and computational details

5.2.1 InP clusters

We now review the models we have selected to build up a first-principles understanding of growth from precursors and early-stage intermediates to nm-scale QDs. An early stage cluster (ESC) model was obtained from previous²⁸² high-temperature ab initio molecular dynamics (AIMD) of In and P precursor mixtures. This cluster contains one P atom coordinated tetrahedrally by 4 In precursors along with two complexed In precursors that only coordinate to the neighboring In atoms (Figure 5-1a). The structure²⁸² of this In_4P tetrahedron is similar to the tetrahedral geometry of the zinc blende InP bulk crystal structure²⁸⁴. We perform simulations on the X-ray crystal structure of a magic sized cluster (MSC) that was obtained by growing InP QDs with phenylacetate ligands²⁶¹ (Figure 5-1d). This MSC structure has a surface comprising 16 excess In surrounding a near-1:1 InP core (21 In and 20 P) with geometric properties²⁶¹ similar to the ESC²⁸², albeit with reduced symmetry^{261, 273} in comparison to zinc blende InP²⁸⁴ (Figure 5-1b).

Carboxylate ligands are known^{42, 285} to form multiple binding modes to neighboring indium atoms on surfaces: bidentate carboxylate coordination to a single In center, as is common in isolated $\text{In}(\text{RCOO}^-)_3$ precursors²⁸², or bridging ligands that coordinate multiple In centers in either a symmetric fashion with comparable distance to both In centers or asymmetrically in a manner that supports a partial second bond with one of the two In centers (Figure 5-1e). Monodentate coordination is not observed in equilibrium ESC or MSC structures but is expected to occur transiently during growth steps on the surface. It is useful to classify trends in reactivity and stability by binding mode.

The most common InP QD growth recipe^{109, 239, 241-243, 267, 286} employs myristic acid, a long chain fatty acid, which has comparable electronic properties to shorter chain carboxylic acids, such as acetate or formate²⁸². To manage computational cost, we replace the phenylacetate ligands employed to stabilize the MSC in prior experimental work²⁶¹ with both acetate and formate ligands and we compare to an ESC²⁸² with acetate ligands also replaced by formate (Figure 5-1a,c). We again²⁸² employ PH_3 as our model precursor and discuss the effect of ligand precursor chemistry on our observations.

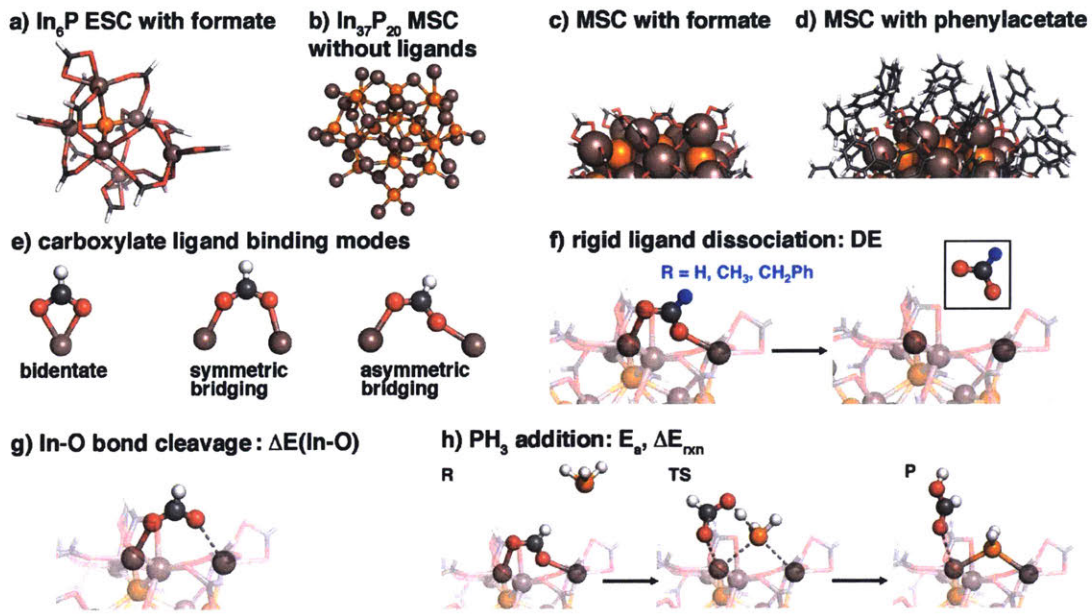


Figure 5-1. Structures of InP clusters and elementary reaction steps studied in this work: a) AIMD-grown InP ESC with formate ligands; b) MSC $\text{In}_{37}\text{P}_{20}$ without ligands; c) the MSC surface with formate ligands; d) the MSC surface with phenylacetate ligands; e) representative models of ligand binding modes; f) MSC rigid ligand dissociation (DE) for formate ($\text{R}=\text{H}$), acetate ($\text{R}=\text{CH}_3$) and phenylacetate ($\text{R}=\text{CH}_2\text{Ph}$); g) MSC In-O bond cleavage ($\Delta E(\text{In-O})$) for formate ligands; and h) PH_3 addition thermodynamics (ΔE_{rxn} , R to P) or kinetics (E_a , R to TS). For all structures, atoms are colored as follows: In brown, P orange, O red, C gray, and H white.

5.2.2 Elementary steps of InP QD Growth

The growth of InP QDs is a dynamic process comprising many individual steps. Prior²⁸² reaction pathway analysis on high-temperature AIMD for ESC formation identified a consistent growth mechanism across reactions of individual precursors and larger ESCs. In both cases, it was observed that for an In-P bond to form, the In center must become undercoordinated through In-O bond cleavage in a coupled or sequential fashion²⁸². A nucleophilic oxygen atom from a carboxylate ligand then abstracts a functional group (here, a proton) from the phosphorus precursor. It is possible for this reaction to occur within a single complex of In and P precursors (i.e., an intracomplex reaction) or through assistance by a neighboring In precursor unit (i.e., intercomplex reaction). Regardless of the nature of the mechanism, In-O bond cleavage energies in

small clusters were identified to be an essential predictor of In-P bond formation reaction energies across a wide range of ligand chemistries²⁸²⁻²⁸³. In-O bond cleavage has also been hypothesized to occur experimentally when InP QDs are exposed to water.²⁶¹ In this work, we investigate the range of surface chemistry and thus reactivity of both our computational ESC and the experimental MSC structures (Figure 5-1). Our goal in this work is to understand the heterogeneity in relative stability or, alternatively, reactivity toward continued growth of sites on model cluster and QD surfaces.

The simplest measure of site- and ligand- (i.e., phenylacetate, formate, and acetate) specific stability/reactivity trends on the surface of a QD model is the rigid ligand dissociation energy, DE_i . We compute the DE by removing the i th ligand from the QD surface and obtaining separate single point energies of the isolated ligand and modified QD for each ligand on the surface (Figure 5-1f).

Given the paramount importance²⁸²⁻²⁸³ of In-O bond cleavage in overall reaction energetics for In-P bond formation, we also compute the energetic cost of cleaving the i th In-O bond, $\Delta E_i(\text{In-O})$, between an In surface site and the carboxylate ligand determined through partial relaxation of the cleaved ligand and comparison to the equilibrium QD energetics (Figure 5-1g). For each ligand, we cleave the weaker In-O bond: the longer of two In-O bonds for chelating bidentate or symmetric bridging ligands and in asymmetric bridging ligands the longer In-O bond for the oxygen that forms two weaker bonds with both In centers (Figure 5-1).

Following In-O bond cleavage, a likely elementary step for continued growth is the addition of PH₃ precursors to the In-rich surfaces (Figure 5-1h). The thermodynamics of this PH₃ addition provides a measure of the likelihood of continued QD growth at various reaction sites on the surface. We do not assume excess P precursor conditions²⁷³ but use the PH₃ addition as a measure of site-specific reactivity. During AIMD, we observed²⁸² rapid formation of In-P(H₂)-In coordination following H abstraction from PH₃. Thus, we model PH₃ addition as the cleavage of an In-O bond at a bridging carboxylate site, proton abstraction by the free anionic carboxylate oxygen, and addition of a PH₂ moiety in the open In···In site (Figure 5-1h). Addition at chelating bidentate sites is also considered with a similar mechanism, although it is energetically less favorable. We report the relative energy of PH₃ addition for each i th site, $\Delta\Delta E_{\text{rxn},i}(\text{PH}_3)$, obtained

from relaxation of the added PH₃ and protonated carboxylate, which typically dissociates from the surface, referenced against the value for an isolated precursor reaction (Figure 5-1).

Although the kinetics of PH₃ addition are important, strong linear free energy relationships (LFERs) between reaction energies and barriers are frequently observed²⁸⁷, including in reactions²⁸³ between PH₃ and In precursors, permitting inference of kinetics from thermodynamic trends. To confirm LFERs on the MSC and ESC models, we compute select approximate transition states (TSes) for PH₃ addition. We compute the *i*th site's relative activation energy, $\Delta E_{a,i}$, on MSCs or ESCs with respect to an isolated precursor pair, where the TS is the highest minimum energy pathway structure obtained during PH₃ deprotonation by the free carboxylate (Figure 5-1h). In total, the steps pursued here are consistent with experimental observations of ligand exchange, and only some hypothesized pathways of MSC decomposition have been neglected.²⁵³

5.2.3 Computational details

Electronic structure calculations were carried out with TeraChem¹⁴²⁻¹⁴³. Geometry optimizations¹⁴¹ and path-based²⁸⁸⁻²⁸⁹ TS searches were performed using density functional theory (DFT) with the hybrid B3LYP^{59, 61, 145} exchange-correlation (xc) functional. The default B3LYP definition in TeraChem uses the VWN1-RPA¹⁴⁶ form for the local density approximation component of the correlation. All calculations were carried out with the composite LACVP* basis set, which corresponds to an LANL2DZ²⁹⁰ effective core potential basis for In and the 6-31G* basis for the remaining atoms. Using a larger aug-cc-pVDZ basis set yields comparable reaction energies for PH₃ addition on representative cases. We validated our choice of xc functional and confirmed that alternative long-range corrected, hybrid ω PBEh⁹³ did not substantially change predicted reaction energies for PH₃ addition on representative cases.

Geometry optimizations were carried out using the DL-FIND¹⁴¹ module in TeraChem with the L-BFGS algorithm in Cartesian coordinates. Default thresholds of 4.5×10^{-4} hartree/bohr for the maximum gradient and 1.0×10^{-6} hartree for the change in energy were employed. For approximate TS searches and minimum energy pathways (MEPs) of PH₃ addition on the MSC and ESC models, initial guesses were provided for

constrained optimizations followed by nudged elastic band (NEB)²⁸⁸⁻²⁸⁹ calculations. Activation energies (E_a) were determined with respect to a reactant in which a PH₃ precursor was 5 Å from the surface. Default NEB thresholds of 4.5x10⁻⁴ or 3.0x10⁻⁴ hartree/bohr for the maximum or root mean square (rms) of energy gradient, and 1.8x10⁻³ or 1.2x10⁻³ for the maximum or rms of the atomic displacement were employed. Twenty initial images were used in NEB, and 10 to 15 images were added after convergence then re-converged to ensure sufficient image density around the TS region. Inclusion of empirical dispersion correction (i.e., DFT-D3²⁹¹) does not change trends for either DEs or DDE_{rxn} values. Incorporation of thermodynamic corrections at 298.15 K does not change DDE_{rxn} values or trends. The 0 K electronic energies are instead reported throughout the main text due to high computational cost of thermodynamic corrections on the 261-924-atom models studied in this work.

The X-ray crystal structure²⁶¹ of the phenylacetate-ligated InP MSC ($\text{In}_{37}\text{P}_{20}(\text{O}_2\text{CCH}_2\text{Ph})_{51}$) was simulated along with acetate- ($\text{In}_{37}\text{P}_{20}(\text{O}_2\text{CCH}_3)_{51}$) and formate- ($\text{In}_{37}\text{P}_{20}(\text{O}_2\text{CH})_{51}$) ligated structures obtained by removing Ph and CH₂Ph, respectively, H-atom capping, optimizing a constrained geometry in which only the H atoms were allowed to move. An acetate-ligated ESC ($\text{In}_6\text{P}(\text{O}_2\text{CH})_{15}$) from previous work²⁸² was studied with formate ligands obtained by removing CH₃, H-atom capping, optimizing only the H atoms. Rigid ligand DEs on the MSC were computed for all three ligand types in bidentate and bridging ligands, whereas the remaining MSC and ESC quantities were computed only with formate ligands. Both a) DE(In-O) cleavage and b) DDE_{rxn} addition energies were computed by i) cleaving one In-O bond, ii) H-capping the anionic O atom, and iii) carrying out a constrained geometry optimization in which only the hydrogenated ligand was free along with PH₂ for b). Model spherical InP nanoparticles were built using the supercell builder function in Avogadro¹⁴⁹ on the experimental bulk InP structure¹⁴⁷ and extracting spheres of target radii using an in-house script.

Atomic partial charges were obtained from the TeraChem interface with the Natural Bond Orbital (NBO) package²²². The Mayer bond order²⁹²⁻²⁹³ was calculated with Multiwfn²⁹⁴.

5.3 Bond cleavage energies

5.3.1 Rigid ligand dissociation energies

As the MSC structure is most relevant to understanding QD growth processes, we first evaluate the rigid ligand DE from an MSC as a probe of surface reactivity and stability in InP QDs. DEs of the phenylacetate ligands on the MSC are both large in magnitude and span a 71 kcal/mol range, with lower DEs for the 12 chelating bidentate ligands (79-116 kcal/mol) than for the 39 bridging ligands (90-150 kcal/mol) regardless of symmetric (5) or asymmetric (34) binding mode (see Figure 5-1). Although coordination mode strongly influences the average DE, the large range of ligand DEs suggests differences in the local surface chemistry of the MSC play the dominant role. Indeed, mapping ligand DEs onto the MSC QD surface reveals heterogeneity in spatial distribution of high and low DE sites: both extrema are surrounded by regions of ligands with intermediate binding energies (Figure 5-2). Although site-specificity was previously suggested in ligand rearrangements on InP QDs²⁶¹, these large variations in energetics are the first quantitative indication of heterogeneous growth rates at different sites on a QD surface.

Qualitative observations for phenylacetate ligands are preserved in small (i.e., formate and acetate) ligands, consistent with observations that In-O bond energies are insensitive to chain length²⁸² (see Figures 5-1, 5-2). Quantitatively, phenyl group bulkiness significantly weakens DEs relative to acetate two outlier cases that give phenylacetate a wider DE range than formate and acetate. Formate and acetate DEs agree to within 5 kcal/mol, although maximum formate DEs are higher due to differences in interligand interactions for differing chain lengths. Thus, we focus throughout this work on formate ligands to mitigate computational cost and expect that energetic and geometric trends inferred should be transferable to other carboxylate ligands, with minor underestimation of stability due to steric bulk in phenylacetate and overestimation of stability for formate (Figure 5-2).

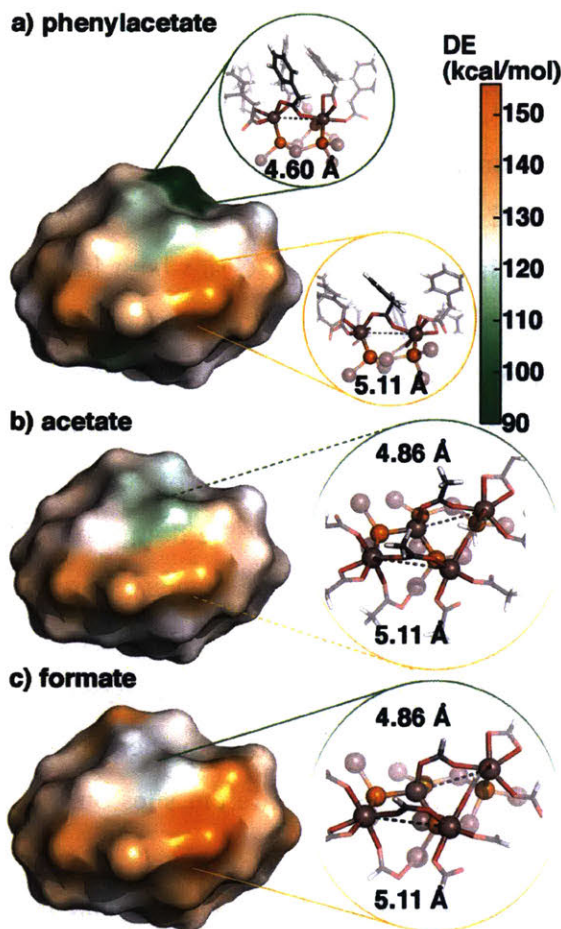


Figure 5-2. Map of the range of 39 bridging ligand rigid DEs on the MSC for a) phenylacetate, b) acetate, and c) formate ligands all shown in the same view. The same inset color bar range is used for all three surfaces, as shown at top right. Representative low (top) and high (bottom) ligand dissociation structures are shown in inset with the In-In separation labeled.

Over the MSC structure, we observe a wide variation in geometric properties: In-In separations range from below 4 Å to nearly 5.5 Å and In-O surface-ligand bond distances vary from 2.08 Å to nearly 2.35 Å, motivating evaluation of possible correlations between energetics and geometry. For the experimentally determined phenylacetate capped MSC, we observe moderate correlations of DEs to geometric properties. Bidentate and bridging ligand types exhibit a single ($R^2=0.48$) correlation between increasing In-O bond length and decreasing DE and weakly positive correlations ($R^2=0.15-0.50$) between increasing In-In separation and increasing DE for bridging ligands. For formate and acetate ligands, these geometric correlations are preserved.

Although we have demonstrated correlations between energetic and geometric properties, we sought to explain the electronic structure origins of surface-ligand interactions by evaluating correlations between energetic and electronic properties. We therefore also evaluated: i) the individual or summed Mayer bond valence (BV) of each In atom coordinated to the ligand, ii) the individual or summed Mayer bond orders of the In-O bonds, and iii) the partial charges of individual and ligand-summed carboxylate O atoms. The In BVs represent the degree of bonding between surface In and any neighboring atoms (i.e., coordinating P in the QD or O from ligands). A wide range of summed In atom BVs (ca. 2.3-2.6) is observed, with average values about half (vs. 6) of what would be expected for purely covalent bonding, consistent with a picture of mixed ionic and covalent bonding²⁶¹. Despite the expectation that the BV is a good indicator of average bonding strength of the In atom to its neighbors, no correlation is observed for individual or summed BVs and DEs.

In contrast to BVs, we observe correlations between the phenylacetate In-O bond order and DEs and summed carboxylate O partial charges. A good correlation between DE and In-O bond order of the weaker of the two cleaving In-O bonds ($R^2=0.68$) is observed, with very weak second bonds corresponding to the lowest DEs. This observation, which extends to acetate and formate ligands as well, suggests a picture in which the weakest interaction determines the overall DE because one weak bond is not compensated by strengthening of the other In-O bond.

Regularized feature selection with LASSO²⁹⁵ confirms observations from univariate correlations: In-O bond distance, O atom partial charges, and the weaker bond In-O bond order are essential features. The multiple linear regression model of the phenylacetate data has enhanced weighting of geometric properties and the formate model has a greater partial charge contribution, but all models have comparable rms errors (RMSEs) of around 5-7 kcal/mol (4-7% of the mean DE). Deviations between ligand types are not detectable from In-O-focused descriptors, which are well-correlated for differing ligands.

Overall, this analysis reveals that in InP QDs, local surface structure and interligand interactions can affect both ionic and covalent contributions to In-O bonds to lead to very large variations (ca. 50 kcal/mol or more) in ligand DEs across the MSC

surface. We next consider the extent to which energetic variations and their electronic structure origins are consistent across lower energy (i.e., more probable) elementary steps in QD growth.

5.3.2 In-O bond cleavage

Single In-O bond cleavage is a more realistic proxy²⁸² for surface-site-specific reactivity, so we next consider whether trends observed for DEs hold for DE(In-O) on the MSC. Although we identified chelating bidentate DEs to be on average lower than the bridging DEs, we focus on DE(In-O) trends for bridging ligands (i.e., 39 of 51 MSC surface ligands). This choice is motivated by the fact that i) continued PH₃ addition likely requires the two available In at bridging sites for PH₂ coordination²⁸² and ii) although DEs were lower for chelating bidentates than bridging ligands, DE(In-O) values are uniformly higher.

As expected, DE(In-O) values are lower than DEs, but, somewhat surprisingly, the two quantities span a comparable range for bridging ligands (29-35 kcal/mol). A good correlation ($R^2=0.59$) is observed between DE(In-O) and DE, and most points fall within a ± 3 kcal/mol range centered around the trendline (Figure 5-3). Mapping DE(In-O) on the InP surface reveals similar labile and stable spots distributed over the QD surface as was observed for DEs, owing to the good correlation of single and double bond cleavage (See Figure 5-2). The lower absolute DE(In-O) values mean that some In-O bonds are twice as strong as others on the MSC surface, and only the weakest bonds are comparable to those (ca. 20 kcal/mol) in isolated precursors²⁸² (Figure 5-3). Thus, most of the MSC is expected to be less reactive than earlier stage clusters.

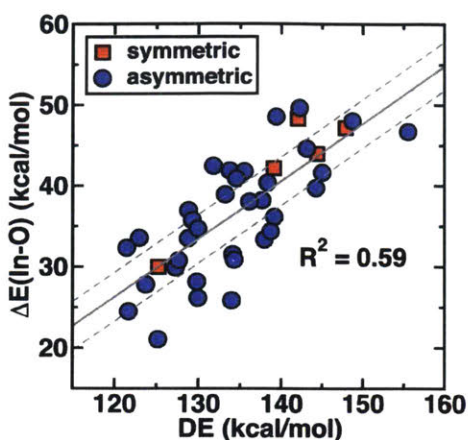


Figure 5-3. Correlation for 39 bridging (34 asymmetric in blue circles, 5 symmetric in red squares) formate ligands on an MSC between In-O bond cleavage ($\Delta E(\text{In-O})$, in kcal/mol) and rigid ligand dissociation energies (DE, in kcal/mol).

Although a good correlation is observed between $\Delta E(\text{In-O})$ and DEs, individual property-energy correlations differ: correlations with the electrostatic O atom partial charges or In-O bond distances are no longer present, whereas correlation to the In-O Mayer bond order is improved. At the same time, a previously observed weak correlation between formate DE and $\text{In}^{\cdots}\text{In}$ internuclear separation is significantly strengthened (for 34 asymmetric ligands from $R^2=0.24$ to $R^2=0.75$), consistent with qualitative observations of short $\text{In}^{\cdots}\text{In}$ separation producing lower $\Delta E(\text{In-O})$ values. Consistent with univariate analysis, feature selection confirms only the In-O bond order and $\text{In}^{\cdots}\text{In}$ separation contribute significantly to determining $\Delta E(\text{In-O})$, with RMSEs for a two-variable linear model as low as 4.5 kcal/mol or around 12% of the mean. Overall, these observations suggest reorganization of the electronic structure on the other In-O bond following single In-O bond cleavage compensates for any electrostatic contribution to the bond cleavage that was observed in DE trends.

5.4 PH₃ addition

5.4.1 Thermodynamics

As with In-O bond cleavage, we observe that relative PH₃ addition reaction energies, $\Delta \Delta E_{\text{rxn}}(\text{PH}_3)$, have a large variation over the MSC surface with labile and stable spots intermingled, although over a smaller range (15 kcal/mol for $\Delta \Delta E_{\text{rxn}}(\text{PH}_3)$ vs. 29

kcal/mol for DE(In-O)) of energies (see Figure 5-4). We previously identified²⁸²⁻²⁸³ that In-O bond cleavage was an essential predictor of In-P bond formation energetics in precursor and ESC reactions. Indeed, this observation holds for the MSC, where we observe a good correlation ($R^2=0.63$) between $DDE_{rxn}(PH_3)$ and DE(In-O). For this reason, energetically unfavorable PH_3 addition at chelating bidentate sites was not pursued.

As would be expected from the close relationship between the two energetic quantities, correlation of $DDE_{rxn}(PH_3)$ to underlying electronic and geometric properties is qualitatively equivalent to trends observed for DE(In-O) (Figure 5-4). That is, $DDE_{rxn}(PH_3)$ correlates well to the In···In separation for symmetric ($R^2=0.99$) and asymmetric ($R^2=0.90$) bridging ligands, with all points falling within a ± 3 kcal/mol range around the trendline in an even stronger correlation than that was observed for DE(In-O) (Figure 5-4). The observation that smaller In···In distances are associated with higher reactivity is at odds with expectations from bulk metal surfaces²⁹⁶, where increasing metal-metal separation is known to make surfaces more reactive, not less so, highlighting unique qualities of covalent, directional bonding in III-V QDs. Given the substantial decline in thermodynamic favorability for $DDE_{rxn}(PH_3)$ with increasing In···In separation, we also considered whether also allowing In sites to reorganize after PH_3 addition, initially neglected from our analysis, might alter our conclusions. For $d(\text{In}\cdots\text{In}) < 5.0 \text{ \AA}$, we observe no change in optimized In···In distance and only modest (ca 0.1 Å) decreases in separation for some of the initial longer separation points. These modest rearrangements suggest the underlying core MSC or QD structure prevents significant changes in In···In separation that would reduce $DDE_{rxn}(PH_3)$ at high $d(\text{In}\cdots\text{In})$ sites.

The only other correlating property observed for $DDE_{rxn}(PH_3)$ is a single correlation ($R^2=0.73$) across both symmetric and asymmetric bridging ligands with the Mayer bond order of the weaker In-O interaction. This correlation is slightly strengthened over that observed for DE(In-O), which is surprising because it may be expected that weakening In-O bonding reduces DE(In-O), whereas PH_3 addition is a competition between In-O bond cleavage and In-P formation.

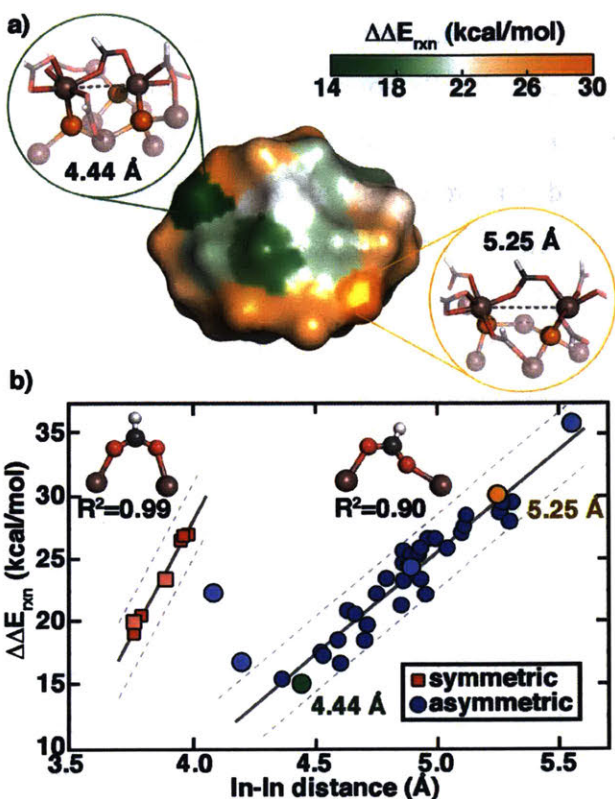


Figure 5-4. a) Relative reaction energies for PH_3 addition ($\Delta\Delta E_{\text{rxn}}$ in kcal/mol) with respect to an In precursor reference for 39 bridging ligands on a surface rendering of the MSC. The energetic range is shown by inset colorbar (green is low and orange is high), and structures with representative highest and lowest reaction energies are shown in the reactant state with relevant In-In distance labeled. b) Correlation of $\Delta\Delta E_{\text{rxn}}$ in kcal/mol versus In-In distance for 5 symmetric bridging bidentate ligand sites (red squares) and 34 asymmetric bridging bidentate ligand sites (blue circles) for the MSC (shown as gray solid lines with R^2 inset). Representative structures from a) are indicated in orange and green. The ESC $\Delta\Delta E_{\text{rxn}}$ for 2 symmetric ligands (light red squares) and 4 asymmetric ligands (light blue circles) are overlaid on top of the MSC correlations. A range of ± 3 kcal/mol from the trendlines is shown in dashed gray.

To confirm the generality of the correlation between In-In separation and $DDE_{\text{rxn}}(\text{PH}_3)$, we also computed PH_3 addition energies for sites on the ESC. Of the 10 bridging ligand sites on the ESC, four (three symmetric, one asymmetric) have lower coordination numbers than observed for any MSC sites and are therefore much more reactive. For the remaining six bridging ligand sites (two symmetric and four asymmetric) on the ESC that have comparable coordination numbers to the MSC, overlaying the ESC energies and distances on the MSC data reveals a consistent relationship (light blue and red symbols in Figure 5-4). As with the MSC, chelating

bidentate ligands have large $DE(\text{In-O})$ values and were therefore not considered for PH_3 addition. These observations suggest that geometrically equivalent MSC and ESC sites are equally reactive, meaning that the subsurface core atoms are not perturbing the electronic structure of the In atoms beyond a nearest neighbor effect, although $\text{In}\cdots\text{In}$ separations sampled in the ESC are in some cases shorter than sampled in the MSC data or sites are more likely to be undercoordinated.

Returning to the fact that across equivalent ESC and MSC sites $DDE_{\text{rxn}}(\text{PH}_3)$ correlates well to both $\text{In}\cdots\text{In}$ separation and Mayer bond order of the cleaving bond, we next considered if there was a strong relationship between these two quantities that could rationalize surface reactivity and stability. Indeed, we observe two good correlations by ligand binding mode (symmetric: $R^2=0.89$, asymmetric: $R^2=0.75$) between increasing $\text{In}\cdots\text{In}$ separation and increasing In-O Mayer bond order. Thus, when In sites are further apart, these surface sites bind ligands more tightly. Since the bond strength in symmetric ligands is higher than in the asymmetric form, two distance-energy relationships are observed, but only one overall energy–bond-order correlation is needed, even across more tightly binding chelating bidentate ligands (see Figure 5-4).

5.4.2 A model for QD-size dependent reactivity

To more directly probe why increasing the $\text{In}\cdots\text{In}$ separation strengthens the weaker In-O bond, we constructed a minimal model of two passivated In atoms and a bridging carboxylate in which we could control $\text{In}\cdots\text{In}$ separation in the asymmetric or symmetric bridging configurations (Figure 5-5). Good correspondence is observed between minimal model bond orders and those in the MSC and ESC, despite differences in chemistry due to the In atoms being isolated instead of on an InP cluster (Figure 5-5). In asymmetric ligands, increasing $\text{In}\cdots\text{In}$ separation above 4.25 Å (i.e., most distances sampled on the MSC) strengthens the weaker of the two In-O bonds because the O atom that was partially bonded to two In centers is now only close enough to the single In center, whereas compression below 4.25 Å increases the Mayer bond order again as the bonding redistributes between the two In centers (Figure 5-5). Conversely, for symmetric bridging ligands, increasing $\text{In}\cdots\text{In}$ separation increases bond order monotonically. These observations explain the higher bond orders observed in short $\text{In}\cdots\text{In}$ separation ESC sites

not sampled on the MSC.

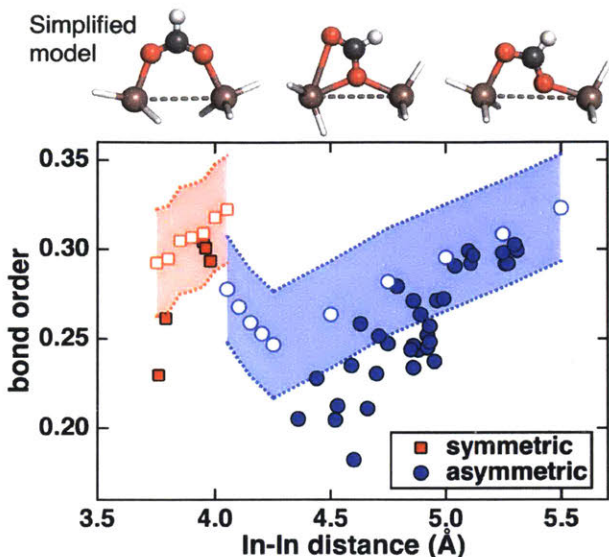


Figure 5-5. In^{···}In separation (Å) versus In-O Mayer bond order for 34 asymmetric (blue filled circles) and 5 symmetric (red filled squares) MSC formate ligands. Bond orders from a simplified model (symmetric and asymmetric shown at top) obtained from constrained variation of In^{···}In separation are shown as white symbols with a ± 0.03 bond order range (shaded region).

Given the strong variations in surface reactivity of MSC sites but consistency with equivalent sites on the even smaller ESC, we next developed a model of how surface morphology is likely to evolve during QD growth. We expect the depletion of reactive surface sites to coincide with the slowing or cessation of QD growth. In addition to the MSC crystal structure, experimental mass spectrometry has quantified²⁶⁶ the number of core and surface In atoms in five QD sizes ranging from 2.42 to 3.28 nm in diameter, which is roughly twice the diameter of the MSC²⁶¹ and a typical size for InP QDs^{240, 255, 266}. These QDs have an In-rich surface with comparable core densities to spherical NPs extracted from bulk crystalline InP.

During growth from an ESC to MSC to QD, the relative excess surface In decreases, increasing average In^{···}In surface separations, $d_{av}(\text{In}^{\cdot\cdot\cdot}\text{In})$ (Figure 5-6). The ESC $d_{av}(\text{In}^{\cdot\cdot\cdot}\text{In}) = 4.13$ Å is the same as that an In-terminated bulk spherical model ($d_{av}(\text{In}^{\cdot\cdot\cdot}\text{In}) = 4.14$ Å), indicating that at the earliest stages of growth the surface is maximally In-rich (Figure 5-6). In comparison, the MSC $d_{av}(\text{In}^{\cdot\cdot\cdot}\text{In}) = 4.75$ Å is already indicative of a less In-rich surface (Figure 5-6). Additionally, a higher ratio of symmetric:asymmetric

bridging sites is observed in the ESC (5 of each, i.e., 1:1) than in the MSC (5:34) (Figure 5-6). We then developed a geometric model of QD surface area to predict $d_{av}(\text{In}^{\cdot\cdot}\text{In})$ in the MALDI-TOF-characterized QDs. The less In-rich surface of QDs leads to an even larger $d_{av}(\text{In}^{\cdot\cdot}\text{In}) = 5.56\text{-}5.77 \text{ \AA}$, with increasing values for increasing QD size.

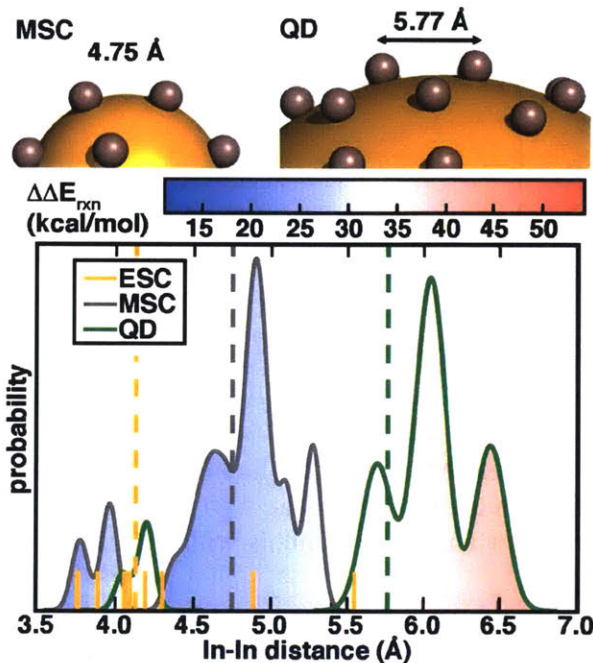


Figure 5-6. Distributions of In-In distances on the ESC, MSC, and a 3.28 nm QD. Normalized and smoothed surface In-In distance distributions are shown for the InP MSC (solid, gray line) and an InP quantum dot (QD) (solid, green line). Each individual surface In-In distance is shown for the ESC (solid, orange, sticks). Average In-In distances in the ESC (dashed, orange), MSC (dashed, gray), and QD (dashed, green) are also indicated. The estimated reaction energies based on the linear best-fit line of reaction energies relative to the $\text{In}(\text{HCOO})_3$ reference are shown with light blue (lowest energy) to light red (highest energy) shaded regions for the MSC and QD distributions, as indicated by the inset color bar. Structural models of average MSC and QD $\text{In}^{\cdot\cdot}\text{In}$ separation are shown at top.

Noting that we have information not just about $d_{av}(\text{In}^{\cdot\cdot}\text{In})$ for the MSC but all $\text{In}^{\cdot\cdot}\text{In}$ separation values on the surface, we smoothed the distribution to show the essential features. Overall, two distinct populations are observed of short $\text{In}^{\cdot\cdot}\text{In}$ separations (3.5-4 \text{\AA}) with symmetric carboxylate ligands and a broader distribution peaked slightly above $d_{av}(\text{In}^{\cdot\cdot}\text{In})$ for the asymmetric ligands (Figure 5-6). As we have seen, increasing $\text{In}^{\cdot\cdot}\text{In}$ separation leads to a rapid decline in favorability for continued PH_3 addition (Figures 5-4 and 5-5). Assuming that the observations of i) decreased reactivity with increasing $\text{In}^{\cdot\cdot}\text{In}$

separation and ii) qualitative features of the MSC distance distribution hold in larger QDs, it should be possible to predict relative surface reactivity of larger (i.e., 3.28 nm²⁶⁶) QDs (Figure 5-6). By taking experimentally-known surface $d_{av}(\text{In}\cdots\text{In})$ and modeling possible distributions of the sites, we observe that the population of thermodynamically favorable addition sites are dramatically reduced in both absolute and relative quantities (only 1.8% or 3 sites should have $\text{DDE}_{\text{rxn}}(\text{PH}_3) < 30 \text{ kcal/mol}$) in comparison to the MSC and ESC (Figure 5-6). This analysis is robust to the approximations we have made such as assuming a continuing increase in ratio of asymmetric bridging to symmetric bridging ligands (from 1:1 in the ESC to 7:1 in the MSC to 10:1 in Figure 5-6). The persistence of the MSCs during growth^{253, 261, 266} is consistent with our analysis and can be understood in terms of a low fraction of most reactive sites. The very persistent (i.e., stable) MSC sizes (i.e., 1.1-1.3 nm²⁶⁰⁻²⁶¹) and stoichiometries observed in InP QD growth²⁶⁶ appear to correspond to configurations that have low concentrations of sterically-accessible and reactive symmetric bridging ligands.

The decreased number of short In \cdots In separation points on the surface of a mature QD can be rationalized by geometric arguments. In the MSC, bridging carboxylate ligands, be they symmetric or asymmetric in their binding, can coordinate two neighboring In sites flexibly for In \cdots In separations ranging from as little as around 3 Å (MSC min. is 3.8 Å) to as high as around 6.5 Å (MSC max. is 5.3 Å) due to the 2.9 Å separation between the carboxylate O atoms. Conversely, a single P precursor must insert between two In atoms for continued growth in a much narrower range (3.6-5.2 Å) of theoretically possible In \cdots In separations. These geometric constraints could rationalize why addition of excess phosphorus precursor to an MSC produces a distinct non-zincblende structure.²⁷³ Therefore, growth should terminate in In-rich surfaces with large In \cdots In separations passivated by bridging carboxylates because any site where a P precursor can attack will be a favorable site for continued In addition. Careful selection of alternate In and P ligand precursor chemistries beyond carboxylates for In precursors should then be expected to change both the nature of growth and of the surface termination.

5.4.3 Kinetics

Thus far, our focus has been on thermodynamic quantities, which are most relevant for slow growth conditions. If strong scaling relationships hold between kinetic (i.e., E_a) and thermodynamic (i.e., ΔE_{rxn}) quantities, then all of the thermodynamic analysis will apply to kinetically limited regimes.^{287, 297-302} We had previously observed²⁸³ good scaling relationships for precursor reactions, but we now test if this relationship holds on larger clusters. We explicitly compute reaction pathways for PH₃ addition on five (i.e., half of all possible) representative bridging ligand sites on the ESC. In comparison to an intracomplex precursor reaction, PH₃ addition on these ESC sites was thermodynamically less favorable for most cases. The minimum energy pathway (MEP) characterization includes i) cleavage of an In-O bond, ii) insertion of PH₃ between two In sites, iii) simultaneous proton abstraction from the substrate, and iv) formation of two In-P bonds. When carried out sequentially, the In-O bond cleavage step comprises most of the full abstraction and In-P bond formation barrier²⁸²⁻²⁸³ (Figure 5-7). Good kinetic correspondence between ESC and precursor pathways is observed for cases where the thermodynamics are comparable (blue versus red lines in Figure 5-7b).

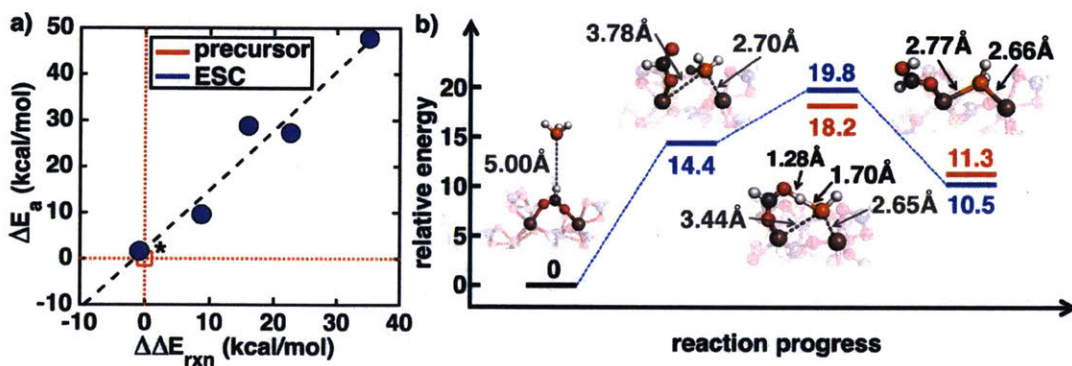


Figure 5-7. a) ΔE_a versus $\Delta \Delta E_{rxn}$ (both in kcal/mol) with respect to an In(HCOO)₃ precursor reference (empty red square) for PH₃ addition on five representative sites on the ESC (blue circles) with a best-fit line (black, dashed) shown. b) Absolute ESC PH₃ addition reaction coordinate shown for case with asterisk indicated in a) in blue compared to absolute intracomplex precursor reaction energetics in red. Relevant structures on the ESC reaction pathway, i.e., In-O bond cleavage and H abstraction, are shown with relevant distances in each step annotated. The exchanged ligand, PH₃ molecule, and associated In atoms are opaque, whereas the neighboring environment is translucent. The energetics of an intracomplex In(HCOO)₃ precursor reaction reference are indicated in red.

For all MEPs, P-H bond shortening and O-H bond elongation is observed

simultaneously as a proton is transferred to the anionic carboxylate oxygen. Higher barriers correspond to cases where the In-P bonds do not shorten significantly or do so only after the abstraction step, whereas low barrier cases exhibit In-P bond formation during proton abstraction (Figure 5-7). The most favorable surface sites for addition enable i) In-O bond cleavage and rotation of the carboxylate away from the surface, ii) alignment of the carboxylate O⁻H⁻P transferring atoms to a near 180° angle, iii) a shortened O⁻ to P separation to enable proton sharing in the TS, and iv) concomitant formation of a shorter (i.e., ~ 2.6-2.8 Å) partial In-P bond for the In site that is no longer bonded to the carboxylate. If In⁻In separation is too large, In-P bonds cannot form during the abstraction process, helping to explain the good scaling relationship between the thermodynamics and kinetics in these systems (Figure 5-7a). Importantly, calculation of the MEPs on three representative MSC sites yields relative E_a s consistent with the scaling relation observed for ESC sites.

Thus, an overall picture emerges in which carboxylate coordination to In sites is more flexible than PH₃ addition, suggesting that both kinetics and thermodynamics are unfavorable for continued addition to the In-rich surface once In sites are fully coordinated and well-separated on the surface. This concept could be used to extend qualitative kinetic growth models²⁵⁵ to directly account for increase in average In⁻In surface separations with continued growth, although we note that instantaneous separations can vary widely as QDs grow.

5.5 Conclusion

We developed first-principles-derived models that unify InP QD formation from the isolated precursor and early stage cluster reactions to 1.3-nm magic size clusters and used these observations to rationalize experimentally observed properties of full sized > 3 nm quantum dots. First-principles modeling on the experimentally characterized, 1.3-nm MSC surface revealed large surface-dependent reactivity for all elementary growth process steps including full ligand dissociation, single In-O bond cleavage, and PH₃ addition. Overall observations revealed that fundamental steps could be as much as twice as energetically costly even between neighboring surface sites. These thermodynamic trends were observed to correlate well to kinetic properties, supporting our assignment of

lable and stable spots from either a thermodynamic or kinetically limited growth perspective.

Correlation of electronic or geometric structural properties to energetics identified surprising sources for these variations in reactivity. Namely, short In \cdots In separation on the surface correlated to the most reactive sites, which was explained by decreasing ligand-surface bond strength in these cases, as judged through bond order metrics derived directly from the In-O bond density. Increasing In \cdots In separation led to more favorable covalent bonding orientation between carboxylate ligands and surface In atoms. This III-V reactivity deviates from typical models for more ionic II-VI QD growth mechanisms. We confirmed that large In \cdots In separation remained favorable for carboxylate binding whereas P precursors were unlikely to favorably add to such sites. This observation was especially surprising because it is at odds with conventional understanding that strain in bulk metallic surfaces increases reactivity. The connection described between structure and reactivity provides a geometry-based method to assess the growth and reactivity of experimentally characterized InP clusters and QDs without further simulation.

The unique constraints of carboxylate or P precursor binding to In atoms rationalized why all sizes of InP clusters and QDs are In-rich but become less so as QDs mature. These observations also point to the importance of the geometric structure of both In and P precursors in considering alternate growth recipes to control both kinetics as well as surface morphology in III-V QDs. In the future, these constraints and energetics could be incorporated into kinetic models to develop a predictive understanding of how to control III-V QD growth through altered ligand chemistries or concentrations.

Chapter 6 Density Localization and Surface Properties in the Solid State

This chapter has been published in

Q. Zhao, H. J. Kulik, *J. Chem. Theory Comput.*, 14 (2), 670-683 (2018).³⁰³

6.1 Introduction

Approximate density functional theory (DFT) is widely used to understand the electronic structure of transition metal-containing molecules and materials. Nevertheless, presently available exchange-correlation (xc) approximations in DFT are plagued by both one- and many-electron self-interaction errors (SIE)^{72, 75, 304-306}, also referred to as delocalization error⁶⁴⁻⁶⁶ (DE), which give rise to well-known problems in dissociation energies⁷⁴⁻⁷⁸, barrier heights⁷⁹, band gaps⁸⁰⁻⁸¹, and electron affinities⁸²⁻⁸⁴. Open shell transition metal complexes and solids are particularly sensitive to imbalances in DE, which leads to strongly xc-dependent predictions of spin-state^{63, 85-89} or magnetic ordering⁹⁰⁻⁹² and thus electronic properties.

DE⁶⁴⁻⁶⁶ has a quantitative energetic definition as the deviation from linearity with respect to exact piecewise linear behavior⁶⁷, which also requires a derivative discontinuity⁶⁸⁻⁷¹, with fractional addition or removal of an electron. The convex deviations⁷²⁻⁷³ of pure xcs in approximate DFT (e.g., local density approximation, LDA or generalized gradient approximation, GGA) from piecewise-linearity³⁰⁷ are manifested in errors in numerous ground state energetic and density properties. HF exchange conversely overlocalizes electrons and exhibits concave deviations⁷²⁻⁷³ from piecewise linearity. These observations have motivated the incorporation of Hartree-Fock (HF) exchange through tuning³⁰⁸⁻³¹⁴ of global or range-separated hybrids^{225, 315-323} in which Janak's theorem³²⁴ is invoked to identify⁹⁸ and eliminate deviations from piecewise linearity.

The limitation of this energetic definition is that as system size increases, the apparent deviation from linearity approaches zero³²⁵⁻³²⁸, making it a less suitable metric in solids. We recently demonstrated⁹⁵ that the DFT+U method³²⁹⁻³³⁰, widely employed for approximately treating SIE in semi-local DFT treatments of transition metal chemistry³³¹, can also recover piecewise linearity. We showed⁹⁵ that this piecewise linearity is not recovered at a calculated self-consistent⁸⁵, linear-response⁹⁶⁻⁹⁷ U but at one determined by the semi-local DFT deviation from linearity⁹⁸.

Although DFT+U and hybrids represent suitable approaches for reduction of energetic DE in transition metal chemistry, the effect on the density of energetic DE corrections remains unclear. It has been known for some time that functionals that

provide good energetics (e.g., B3LYP^{59, 61, 145}) yield poor densities in comparison to accurate references³³², whereas others yield poor energetics and good densities³³³. Correct densities are a necessity for interpreting trends in chemical bonding³³⁴ and associated observable quantities. This importance has been the recent focus of a surge in interest, especially in evaluating density errors of approximate DFT exchange correlation functionals in charged ions and small organic molecules³³⁵⁻³³⁸. Less attention has been paid to how properties of d ³³⁹⁻³⁴⁰ and f ³⁴¹⁻³⁴² valence transition metal complexes and solids are affected. Recently, we showed that global and range-separated hybrids as well as DFT+U universally localize the density away from the metal and onto surrounding ligand atoms in transition metal complexes regardless of metal identity, spin state, ligand electronegativity, or ligand size.^{88,339} These observations were consistent with studies that showed decreased bonding in $3d$ states (e.g., of CuCl³¹⁸ or in a iron octahedral complex³⁴³) and $4f$ states (e.g., lanthanide complexes³⁴¹) with range-separated hybrids. In organic molecules, replacement of approximate DFT densities with ones derived from HF have been demonstrated to yield improved barrier heights³⁴⁴⁻³⁴⁵ and dissociation energies^{64, 346-347}, enabling a separation of energetic- and density-driven delocalization errors⁶⁴. Nevertheless, our recent work showed³³⁹ that at the point of energetic DE elimination in molecules, residual density DE was left behind with respect to accurate correlated wavefunction theory reference densities.

The uniform localization of density away from the metal with all DE corrections was surprising given that the form of the DFT+U potential can either enhance or reduce d state occupations. Within the solid state community, the Hubbard³⁴⁸ and Anderson³⁴⁹ model origins of DFT+U frequently invoke statements regarding electrons being localized onto a metal site, not away from it. It remains an open question whether functional tuning strategies with HF exchange and DFT+U have the same, convergent effect on solid-state properties as they do on transition metal complexes. It is particularly useful to identify if hybrids and DFT+U perform comparably^{339,350-352} due to the increased computational cost of evaluating long range exchange in the solid state. Due to its low computational cost, DFT+U is often employed to open band gaps and recover the correct ground state in studies of transition metal oxides, e.g., with Ce^{90,353-354}, Ti³⁵⁵⁻³⁵⁶, Mn³⁵⁷⁻³⁵⁹, Fe^{357-358, 360-361}, Co³⁵⁷⁻³⁵⁸, Ni³⁵⁷⁻³⁵⁸ in various stoichiometries as well as to correct magnetic

ordering in transition-metal-containing perovskites³⁶². HF exchange, especially in computationally efficient short-range screened hybrids, can be used for similar purposes, e.g., in battery-relevant Ni- and Co-containing transition metal oxides³⁶³ as well as transition metal monoxides³⁶⁴ and di/trioxides^{91, 365-367} and perovskite materials^{92, 368-369}, sometimes with improvement over DFT+U results^{364, 370} for band gaps and structure or magnetic moments that motivate the higher computational cost of hybrids.

Despite the apparently similar effects of DFT+U and hybrids on energetics, few studies have compared how these methods alter the properties of the density in transition metal-containing solids. In this work, we carry out a detailed comparison of the effect of HF exchange and DFT+U on 34 transition metal-containing solids. Over this wide test set, we compare the effects of HF exchange and DFT+U on density in the solid state as we vary electron configuration, substituent size, and coordination environment in order to identify if they behave as similarly as they do in transition metal complexes. Within a subset of open-framework solids, we make direct comparison to isolated molecules through rigid extraction of octahedral complexes from the solid-state environment. Such study is revealing because it sheds light on whether functional tuning effects are transferable from small molecule chemistry, where experimental and accurate wavefunction theory references are abundant, to the solid state.

6.2 Computational details

6.2.1 Hybrid calculations

The effect of exact exchange was investigated by altering^{88, 339} the percentage of Hartree-Fock (HF) exchange in a modified form of the B3LYP^{59, 61, 145} global hybrid functional from as low as 0% (i.e., pure BLYP generalized gradient approximation or GGA) to as high as 50% HF ($a_{\text{HF}} = 0.5$) exchange in increments of 5%, unless otherwise noted:

$$E_x^{\text{modB3LYP}} = E_x^{\text{LDA}} + a_{\text{HF}}(E_x^{\text{HF}} - E_x^{\text{LDA}}) + 0.9(1 - a_{\text{HF}})(E_x^{\text{GGA}} - E_x^{\text{LDA}}) , \quad (6.1)$$

while holding the GGA/LDA ratio fixed to the 9:1 value in standard (i.e., 20% exchange) B3LYP^{59, 61, 145}. Hybrid DFT calculations on solids were performed using the periodic boundary condition (PBC) code CRYSTAL14²²⁰ with a localized basis set (LBS). The

default definition of B3LYP in CRYSTAL employs the VWN5 form for the LDA VWN¹⁴⁶ component of LYP⁶¹ correlation. At least a double- ζ split-valence basis set was used for all atoms, with polarization added in some cases ($3d$ Cr-Ni, and H, N, C, and K), and triple- ζ split-valence basis sets were used for Pt, with polarization added for Ir, as obtained from the CRYSTAL²²⁰ website¹²⁷. Using larger triple- ζ split-valence basis sets yields comparable results on representative cases. All-electron calculations were carried out for all atoms except in the case of Mo, Ir, and Pt atoms where Hay-Wadt³⁷¹ effective core potentials were used, and only the semi-core states of Mo ($4s$, $4p$) or Ir and Pt ($5s$, $5p$) were described explicitly along with the valence electrons.

The atomic positions and lattice parameters of all solids were fully optimized using the BFGS quasi-newton algorithm³⁷²⁻³⁷⁶ with default tolerances of 4.5×10^{-4} hartree/bohr for the maximum gradient and 3.0×10^{-4} hartree/bohr for the root mean squared gradient. Monkhorst-Pack k -point grids were used in all cases to sample the Brillouin zone: $12 \times 12 \times 12$ for MO₂ transition metal oxides, $6 \times 6 \times 6$ for TiX₂ (X= S, Se), and $8 \times 8 \times 8$ for the open-framework solids M(NCNH)₂, M(OH)₂, MCO₃, and K₃M(CN)₆ (M = V-Ni). In order to aid self-consistent field (SCF) convergence, an electronic temperature of 0.005 Hartree was applied. All calculations were spin-polarized and the spin value was assigned to obtain correct atomic spin for ferromagnetic or nonmagnetic states.

Single point energy calculations of iron complexes extracted from open-framework solids with modified B3LYP were performed using the TeraChem¹⁴²⁻¹⁴³ quantum chemistry package with a LBS. The default definition of B3LYP in TeraChem employs the VWN1-RPA form for the LDA VWN¹⁴⁶ component of LYP⁶¹ correlation. Using the CRYSTAL default of LYP correlation (i.e., VWN5) yields unchanged trends with respect to the VWN1-RPA results obtained with TeraChem defaults. Fe was treated with the LANL2DZ effective core potential,^{290,371} and the 6-31G* basis was used for the remaining atoms. Larger aug-cc-pVTZ basis sets yielded unchanged trends on representative cases. High-spin and low-spin iron multiplicities were assigned as quintet and singlet for Fe(II) and sextet and doublet for Fe(III). All calculations were spin-unrestricted with virtual and open-shell orbitals level-shifted³⁷⁷ by 1.0 and 0.1 eV, respectively, to aid SCF convergence to an unrestricted solution.

6.2.2 DFT+U

DFT+U^{329-331, 378} calculations for solids and complexes were performed using the PBC code Quantum-ESPRESSO³⁷⁹, which employs a plane-wave basis set (PWBS). The PBE⁵⁸ GGA was employed with ultrasoft pseudopotentials (USPPs)³⁸⁰ obtained from the Quantum-ESPRESSO website.¹²¹ Plane-wave cutoffs were 35 Ry for the wave function and 350 Ry for the charge density. The atomic positions and lattice parameters of all transition metal solids were fully optimized using the BFGS quasi-newton algorithm³⁷²⁻³⁷⁶ until the maximum residual forces on the atoms were smaller than 1×10^{-3} Ry/bohr (5×10^{-4} hartree/bohr). For solid-state calculations, k -point sampling and smearing values were the same as in the CRYSTAL calculations. All transition metal atoms were given an initial guess of 0.0 starting magnetization for non-magnetic states and 1.0 for ferromagnetic states in spin-polarized calculations.

For transition metal complexes, single point energy calculations were performed with the Martyna-Tuckerman scheme³⁸¹ to eliminate periodic image effects on molecules, and only the Γ point of the Brillouin zone is used in such cases. Cubic box dimensions, chosen to ensure good grid spacing for atomic charges, ranged from 15 to 20 Å were employed depending on the size of the complex. In complexes, all transition metal atoms were given an initial guess of 0.05 starting magnetization for low spin states and 1.0 starting magnetization for high spin states, and total magnetizations were constrained to match the values described in the hybrid calculations on complexes. The simplified DFT+U correction:

$$E^{\text{DFT+U}} = E^{\text{DFT}} + \frac{1}{2} \sum_{I,\sigma} \sum_{nl} U_{nl}^I \left[\text{Tr} \left(\mathbf{n}_{nl}^{I,\sigma} \left(\mathbf{1} - \mathbf{n}_{nl}^{I,\sigma} \right) \right) \right] \quad (6.2)$$

was employed with I corresponding to transition metal atom sites, nl is $3d$ - $5d$, and σ is the spin index. Occupation matrices, \mathbf{n} , are obtained from projections of extended states onto atomic states obtained during pseudopotential generation, as is standard practice³³¹:

$$n_{mm'}^{I,\sigma} = \sum_{k,v} \langle \psi_{k,v} | \phi_m^I \rangle \langle \phi_m^I | \psi_{k,v} \rangle \quad (6.3)$$

The Hubbard U values employed in this work ranged from 0 eV (i.e., pure PBE-GGA) to up to 10 eV in 1 eV increments, unless otherwise noted, following common practice in studies of tuning U effects and typical ranges of U values employed.^{331, 382}

6.2.3 Structure preparation and post-processing

A total of 34 transition metal solids: 8 transition metal dioxides, 1 transition metal disulfide, 1 transition metal diselenide, and 24 open-framework solids were studied in this work (representative structures shown in Figure 6-1). The experimental rutile-type tetragonal structures of transition metal oxides MO_2 ($\text{M} = \text{Ti}, \text{V}, \text{Nb}, \text{Mo}, \text{Ru}, \text{Rh}, \text{Ir}, \text{Pt}$), hexagonal structures of transition metal disulfides/diselenides TiX_2 ($\text{X} = \text{S}, \text{Se}$), trigonal structures of MCO_3 ($\text{M} = \text{Mn-Ni}$) and M(OH)_2 ($\text{M} = \text{Mn}, \text{Co}, \text{Ni}$), orthorhombic structures of M(NCNH)_2 ($\text{M} = \text{Fe-Ni}$), and monoclinic structures of $\text{K}_3\text{M(CN)}_6$ ($\text{M} = \text{Mn-Co}$) were obtained from the Inorganic Crystal Structure Database (ICSD).³⁸³ Analogous MCO_3 ($\text{M} = \text{V, Cr}$), M(OH)_2 ($\text{M} = \text{V, Cr, Fe}$), M(NCNH)_2 ($\text{M} = \text{V-Mn}$), $\text{K}_3\text{M(CN)}_6$ ($\text{M} = \text{V, Cr, Ni}$) structures were built by replacing the metal atom in the closest available experimental structure. All structures were optimized at each level of theory. The structures of extracted Fe(II)(NCNH)_6 , $\text{Fe(II)(CO}_3)_6$, Fe(II)(OH)_6 , and Fe(III)(CN)_6 complexes were generated using the supercell builder function in Avogadro¹⁴⁹ to build large cells from the corresponding fully optimized crystal structures at each tuning parameter and retain only a single octahedral complex. Single point energies of complexes were obtained on the geometries from the solids (i.e., high-spin complex from the ferromagnetic solid, low-spin complex from the non-magnetic solid).

For comparison of partial charges across two tuning procedures for both solids and complexes, we compute real-space Bader atomic charges^{99, 334} using the BADER program³⁸⁴. The grid resolutions were carefully selected to ensure convergence of partial charges and held constant across tuning methods for consistency. Electron density cube files were obtained using the properties postprocessing code for CRYSTAL calculations, the pp.x postprocessing code for Quantum-ESPRESSO calculations, and the Multiwfn postprocessing package²⁹⁴ on Molden files obtained from TeraChem calculations.

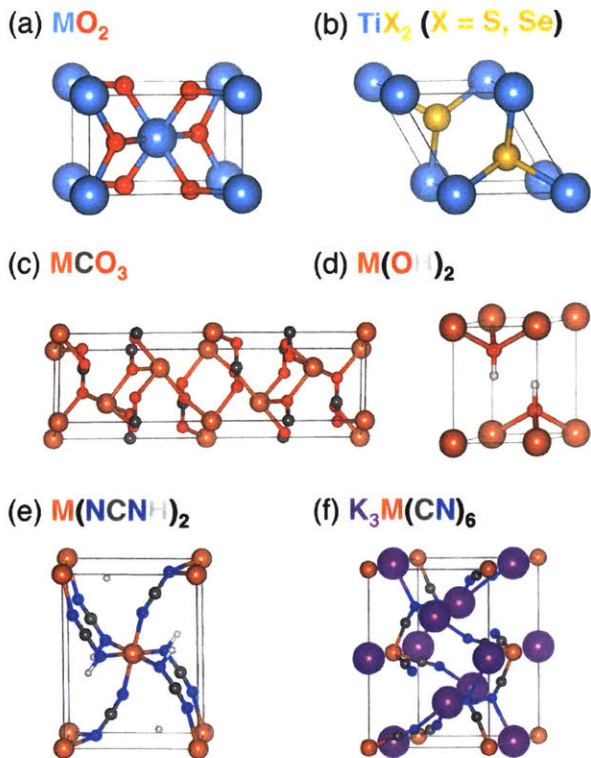


Figure 6-1. Structures of transition metal compounds studied in this work. (a) Transition metal oxides MO_2 ($\text{M} = \text{Ti}, \text{V}, \text{Nb}, \text{Mo}, \text{Ru}, \text{Rh}, \text{Ir}, \text{Pt}$) with a rutile-type tetragonal crystal structure. (b) Transition metal disulfides/diselenides TiX_2 ($\text{X} = \text{S}, \text{Se}$) with a hexagonal crystal structure. Open-framework solids (c) MCO_3 and (d) $\text{M}(\text{OH})_2$ with trigonal crystal structures, (e) $\text{M}(\text{NCNH})_2$ with an orthorhombic crystal structure, and (f) $\text{K}_3\text{M}(\text{CN})_6$ with a monoclinic crystal structure ($\text{M} = \text{V}, \text{Cr}, \text{Mn}, \text{Fe}, \text{Co}, \text{Ni}$).

6.3 Charge localization in transition metal oxides

6.3.1 Transition metal oxides

To determine the effect of DFT+U and HF exchange on densities in the solid state, we selected the frequently studied^{355-356, 385-388} and experimentally available rutile-type transition metal (TM) dioxides (MO_2), in which a metal is surrounded by an octahedral environment of coordinating oxygen anions, producing a non-magnetic (NM) ground state. From eight available structures, we study the effects of varying both d -electron configuration of the neutral metal (d^2s^2 in Ti to d^9s^1 in Pt) and the principal quantum number of the valence electrons (3d: Ti, V; 4d: Nb, Mo, Ru, Rh; and 5d: Ir, Pt). Both tuning strategies have small effects on equilibrium structures: optimizations with

HF exchange decrease lattice parameters slightly (ca. 0.1 Å from GGA to 50% exchange), whereas DFT+U increases lattice parameters for early transition metals (i.e., Ti, V, and Nb, ca. 0.05-0.10 Å for GGA to $U = 10$ eV) and has a smaller effect (ca. 0.02-3 Å) on mid- or late-transition metals.

For the two functional tuning methods, there are slight differences in the GGA reference value: the $U = 0$ eV in DFT+U corresponds to the pure PBE-GGA limit in a plane-wave basis set (PWBS), and the 0% HF point is the pure BLYP-GGA limit in a localized basis set (LBS). Overall, the two GGA references used produce comparable Bader partial charges with small differences in absolute values for early transition metals (ca. 0.04-0.10 e) and slightly larger for late-transition metals (ca. 0.10-0.29 e) (Figure 6-2). Trends of decreasing partial charge with d -filling (i.e., Ti to Pt) and increasing partial charge with increasing principal quantum number (i.e., V to Nb, Rh to Ir) are consistent across the two GGA references (Figure 6-2).

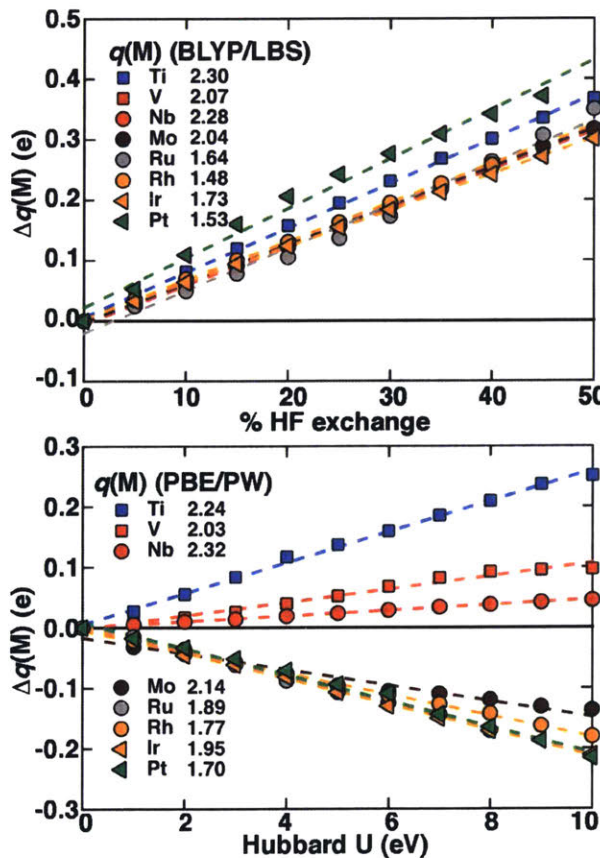


Figure 6-2. Dependence of shift of transition metal (TM) partial charge, $\Delta q(M)$, in e with percentage of HF exchange (top) and U (in eV, bottom) for nonmagnetic rutile-type MO_2

with M = Ti (blue squares), V (red squares), Nb (red circles), Mo (brown circles), Ru (gray circles), Rh (orange circles), Ir (orange triangles), and Pt (green triangles). The GGA partial charge is indicated in the inset, with all curves aligned to have $Dq(M)$ values at zero at the pure GGA value. The dashed lines indicate linear best fit through all data to quantify the partial charge sensitivities to HF exchange or U . Both HF exchange and Hubbard U y-axes span the same 0.6 e range.

Regardless of metal identity, incorporation of HF exchange uniformly increases positive metal partial charges, signifying charge localization away from the metal and onto the surrounding oxygen anions. Increasing U in DFT+U localizes partial charge away from the metal only for early transition metals (i.e., Ti, V, Nb) but onto the metal for mid-row and late transition metals (i.e., Mo, Ru, Rh, Ir, Pt) (Figure 6-2). The increase in metal positive partial charge with incorporation of HF exchange is consistent with our observations on transition metal complexes^{88, 339}, but DFT+U behavior with mid- and late-transition metals diverges from previous observations³³⁹.

Regardless of sign, approximately linear behavior of partial charges with tuning parameter is observed across the range of U and a_{HF} values studied (Figure 6-2). We thus use linear fits as approximations to the M partial charge, q_M , sensitivities (S), i.e. the partial derivatives of q_M with respect to the tuning parameters, p , (i.e., U or a_{HF}):

$$S_p(q_M) = \frac{\Delta q_M}{\Delta p} \approx \frac{\partial q_M}{\partial p} \quad (6.4)$$

The units of U are eV, and we use the unit notation “HFX” to represent the range from 0 to 100% HF exchange. The commonly proposed values of HF exchange in the literature range from around 0%^{386, 389} to at most 40-50%^{363, 368, 390} (i.e., 0.4-0.5 HFX). In comparison, typical ranges of U would be from 0 to around 6 eV.^{363, 389} Throughout the text, we commonly multiply U sensitivities by 10 to compare to HF exchange sensitivities, roughly treating a change in HF exchange from 0 to 100% as equivalent to U variations from 0 to 10 eV, consistent with our prior work³³⁹.

The changes in metal partial charge for rutile-type MO_2 correspond to an approximately 0.3 to 0.4 e loss from the metal with increasing HF exchange from GGA to 50% HF or a sensitivity of around 0.6-0.8 e /HFX (Figure 6-2). Comparing metal-dependent effects, the earliest, TiO_2 , and latest, PtO_2 , are most affected by HF exchange

(ca. 0.4 e loss at 50% HF) with most mid-row TMs reduced to around 0.3 e loss, excluding only RuO_2 . As with electron configuration in the mid-row, principal quantum number dependence is minimal, with comparable behavior for VO_2 and NbO_2 or RhO_2 and IrO_2 . In contrast, for DFT+U with U up to typically applied values of 6 eV, increasing d filling correlates with decreasing electron loss in early transition metals (i.e., Ti, V, Nb) from 0.15 e to 0.03 e , whereas mid-row or late transition metals all gain around 0.10 e to 0.13 e from the oxygen atoms over the same range of U values. The divergent effect of DFT+U means that across the studied transition metal dioxides, DFT+U demonstrates a larger range of charge sensitivities but smaller magnitude than HF exchange.

We can compare charge sensitivities of these transition metal dioxides with $\text{M}(\text{OH}_2)_6^{2+}$ ($\text{M} = \text{Ti}, \text{Fe}, \text{Ni}$), which also have an oxygen-coordinating octahedral environment and are the most-similar complexes in the literature³³⁹. HF exchange had a smaller effect on these molecules than on the solids, e.g. 0.23 e/HFX in $\text{Ti}(\text{OH}_2)_6^{2+}$ vs. 0.8 e/HFX in TiO_2 . In molecules, HF exchange sensitivity increased with increasing d filling, whereas in the transition metal dioxides there is no such trend. With DFT+U, the strong dependence of charge localization on d filling in solids was conversely not observed in complexes³³⁹. For early-row transition metals, where DFT+U sensitivities are positive in both complexes and solids, the sensitivities are higher in the solids, e.g. 0.13 $e/10 \text{ eV } U$ in $\text{Ti}(\text{OH}_2)_6^{2+}$ vs. 0.25 $e/10 \text{ eV } U$ in TiO_2 .

Recalling the slight differences in geometry optimizations with incorporation of HF exchange or DFT+U, we now confirm that differing charge localization trends is not due to differences in each method's equilibrium lattice parameter. We compare sensitivities of the representative early TM TiO_2 and late TM PtO_2 cases at the experimental (expt.) instead of equilibrium (eq.) lattice parameter. Sensitivities are preserved, regardless of structure choice in TiO_2 and PtO_2 .

Visualization of changes in the electron density at fixed lattice parameter with HF exchange and DFT+U confirm the direction of charge localization obtained from partial charge analysis (Figure 6-3). With HF exchange, we observe a spherically averaged loss of electron density from the area directly surrounding the metal (Ti or Pt) center and gain of electron density in the areas surrounding the O atoms. Consistent with observations in

partial charge changes, DFT+U also shows density loss at the Ti metal in TiO_2 , albeit with more d-orbital character to the density loss than the symmetric case for HF exchange. The density difference also confirms clear electron density loss from O atoms and gain at Pt for DFT+U only. Thus, divergent partial charge sensitivities for DFT+U and hybrids on late transition metal oxides are evidence of a qualitative difference in the effect of the two methods that is not sensitive to real-space partitioning in the partial charge scheme or lattice parameter.

We can better understand the influence of the Hubbard U on the density by reviewing the form of the Hubbard potential that is incorporated self-consistently:

$$V^U = \sum_{I,nl} \sum_m \frac{U_{nl}^I}{2} (1 - 2n_{nl,m}^{l\sigma}) |\phi_{nl,m}^I\rangle \langle \phi_{nl,m}^I| \quad (6.5)$$

The potential acts to shift up (i.e., empty) occupied states with weak atomic occupation ($n < \frac{1}{2}$), and it fills occupied states with strong atomic occupation ($n > \frac{1}{2}$).^{95, 97, 331} The potential has the opposite effect on unoccupied states, the efficiency of which was described in our recent work⁹⁵. By reviewing occupation matrices and the potential employed in DFT+U (eqs. 6.2, 6.3 and 6.5), we can thus rationalize the fundamentally different charge localization behaviors between early and late transition metal dioxides. In the non-magnetic states studied here, early transition metals have small fractional occupations that consistently empty with increasing U , whereas the least occupied states are still more than half-filled in late-row transition metals, leading to charge localization onto the metal through the DFT+U potential correction.

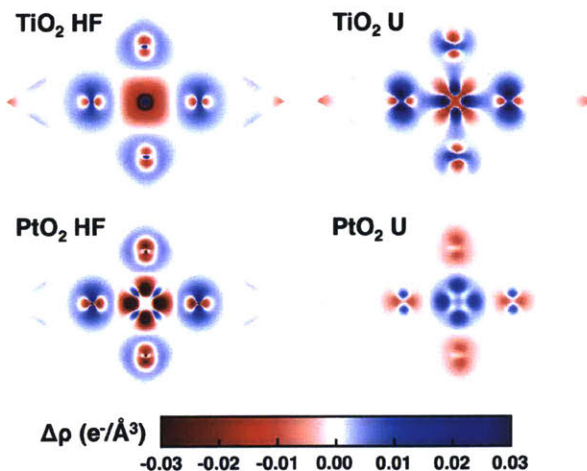


Figure 6-3. Electron density difference between 50% and 0% exchange for the rutile type TiO_2 (top left) and PtO_2 (bottom left), and between $U = 10 \text{ eV}$ and $U = 0 \text{ eV}$ for TiO_2 (top right) and PtO_2 (bottom right). Red and blue colors represent negative (electron density loss) and positive (electron density gain) electron density difference, respectively, as indicated by the inset color bar.

6.3.2 Density of states

Differences in changes in the density of states (DOS) with increasing HF exchange and DFT+U for early (TiO_2) and late (PtO_2) transition metal dioxides can further clarify differences in the two functional tuning strategies (Figure 6-4). Experimentally, TiO_2 and PtO_2 have band gaps of $3.0 \text{ eV}^{391-392}$ and 0.2 eV^{393} , respectively. HF exchange increases the band gap in TiO_2 from its GGA underestimate and introduces a band gap into metallic PtO_2 , whereas DFT+U weakly increases the TiO_2 band gap and maintains a metallic PtO_2 ground state (Figure 6-4 and Table 6-1). Hybrids^{390,394} and DFT+U^{357,395} are often used to open band gaps in GGA metals that are experimentally-known insulators, but the optimal amount of exchange or U is system-dependent. For DFT+U, the largest U studied here (8 eV) increases the gap from the PBE/PWBS GGA reference but still underestimates the experimental value, and the gap in PtO_2 cannot be reproduced. In contrast, HF exchange tuning with high (i.e., 40%) exchange fractions can overestimate the band gaps (Table 6-1). Since the band gaps linearly increase with HF exchange, the optimal HF fraction can be interpolated to be 12-17% (for TiO_2 and PtO_2 , respectively). In the case of TiO_2 , this value can be compared to using the often-recommended inverse of the static dielectric ($1/\epsilon=0.18^{396}$) constant of the material^{369,397},

which would overestimate the experimental band gap by if used directly (Table 6-1).

Table 6-1. Band gaps of TiO_2 and PtO_2 with HF exchange and DFT+U.

	TiO_2	PtO_2
BLYP/LBS	1.91 eV	0.0 eV
40% exchange	5.81 eV	2.72 eV
1/e exchange	3.70 eV	--
PBE/PWBS	1.39 eV	0.0 eV
DFT+U (8 eV)	2.19 eV	0.0 eV
Expt.	3.0 eV ³⁹¹⁻³⁹²	0.2 eV ³⁹³

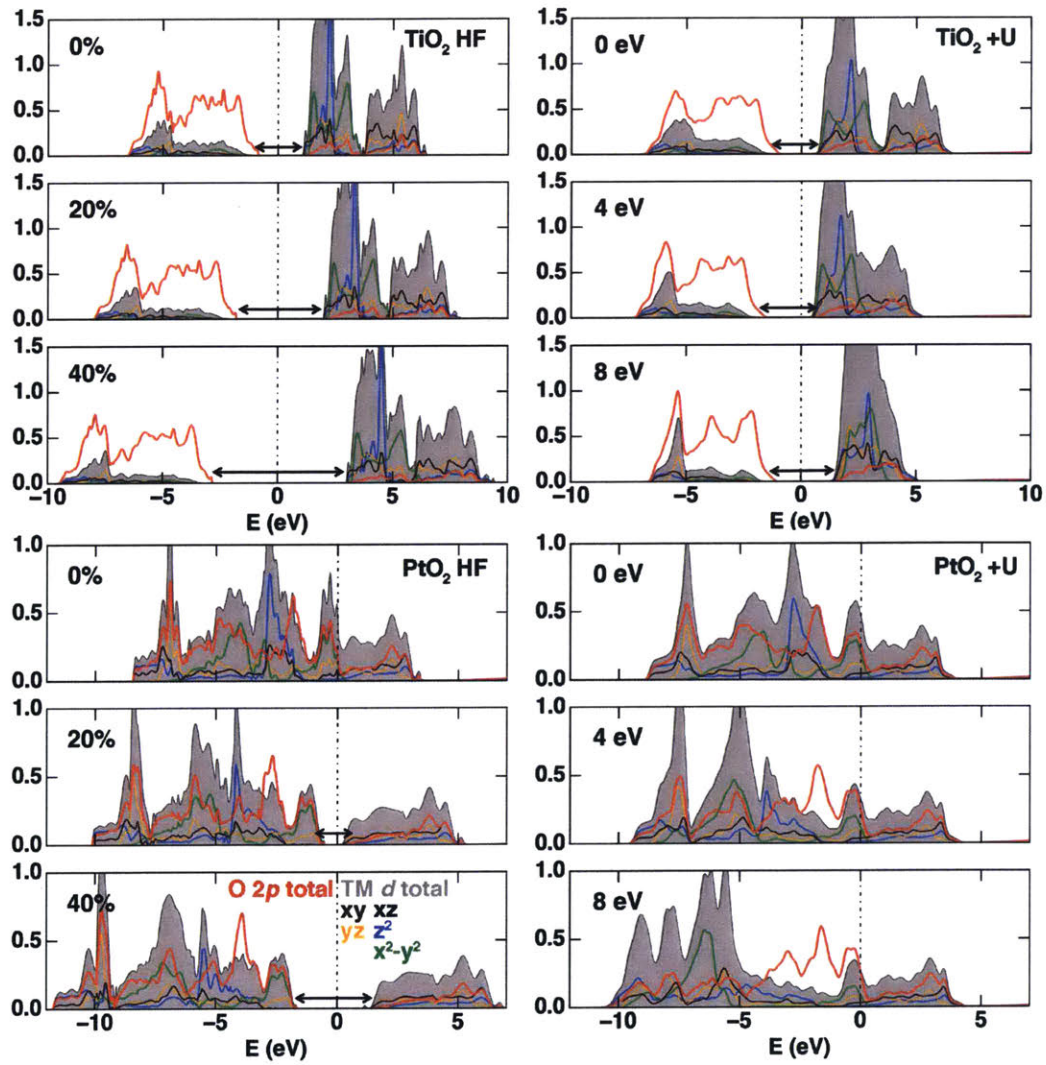


Figure 6-4. Projected density of states (PDOS) of i) non-magnetic TiO_2 (top) or PtO_2 (bottom) d total (gray shaded region) and components: d_{xy} (maroon line), d_{yz} (orange line), d_{xz} (black line), d_z^2 (blue line), $d_{x^2-y^2}$ (green line) and ii) O 2p total (red line). Plots on the left correspond to variation of HF exchange, whereas DFT+U variation is shown at right with values indicated in insets. Arrows indicate the band gap opening with increasing HF exchange percentage and U values around the Fermi level (vertical dashed line). The range in eV of the PDOS is smaller for PtO_2 than for TiO_2 .

Examination of projected density of states (PDOS) features in the valence band (VB) and conduction band (CB) edges also provide orbital-specific information about changes in states that give rise to the observed partial charge sensitivities. Integrating the individual and total d-orbital PDOS for Ti in TiO_2 and Pt in PtO_2 in the VB as HF exchange or U is varied reveals comparable trends to Bader charge analysis and visualization of spatial density differences. HF exchange (50%) in TiO_2 reduces equally occupied d -orbitals with GGA by around 0.2-0.25 e/HFX each and sharpens a sub-VB-edge yz peak. Consistent with observations on the density differences, DFT+U instead selectively decreases the x^2-y^2 orbital occupancy by 0.20 $e/10 \text{ eV } U$ from its GGA value, leaves the xy occupancy unchanged and decreases the occupancy in the remaining orbitals by a more modest amount. In PtO_2 , HF exchange reduces nearly equally occupied d -orbitals by 0.9 e/HFX , which is in excess of the partial charge sensitivity likely due to increasing s occupancy. The previously observed increase in DFT+U partial charges with PtO_2 is reflected in modest increases across all orbitals, except z^2 , by an amount less than the partial charge sensitivity due to simultaneously increasing s occupancy. Other differences evident from the full PDOS include both narrowing of the CB in TiO_2 and a delocalization of the z^2 d state in the VB of PtO_2 with DFT+U that do not occur with HF exchange.

6.3.3 Ligand diffuseness

A commonly invoked explanation of the effect of self-interaction error (SIE) in correlated solids is that typically well-localized $3d$ electrons are more affected by SIE than the more extended bonding states formed by other atoms. It would follow from this argument that SIE should cause the electron density to delocalize from $3d$ states to neighboring atoms. Within molecules, we have recently demonstrated³³⁹ that $3d$ states are

actually relatively delocalized compared to ligand atomic orbitals in $3d$ - $2p$ transition metal coordination environments (e.g., ($3d$: 1.9 Å radius vs. $2p$: 1.7 Å radius for an 0.001 e isosurface)).³³⁹ We also showed³³⁹ that increasing the diffuseness of molecular ligand states (e.g., to $4p$ or larger) with respect to the $3d$ metal-centered orbitals so that $3d$ states are, relatively speaking, well-localized instead increases the degree of delocalization from the metal to the ligand. The differences in transition metal dioxides motivate revisiting the possibility that coordination environment diffuseness could lead to different behavior with functional tuning in solids.

We select rutile TiO_2 as a representative system where both HF exchange and DFT+U localize density away from the metal and onto the surrounding oxygen atoms and examine if replacing oxygen changes charge localization patterns. To study larger-than- $3d$ coordinating atom valence electrons³³⁹ (i.e., $3p$ and $4p$), we calculate properties of TiS_2 and $TiSe_2$ in their experimental hexagonal ground states (Figure 6-5, inset). The structural difference between rutile and hexagonal octahedral environments is a slightly larger asymmetry in the rutile structure compared to more symmetric hexagonal structures (Figure 6-5). The partial charges for the two GGA references (i.e., BLYP/LBS or PBE/PWBS) are relatively close and follow the same trend with increasingly heavy elements (Figure 6-5). With increasing valence orbital diffuseness, the Ti partial charge decreases (i.e., becomes more neutral), consistent with both changes in electronegativity, χ , (Pauling scale – O: 3.4 > S: 2.6 = Se: 2.6) and previously studied transition metal complexes³³⁹ (Figure 6-5).

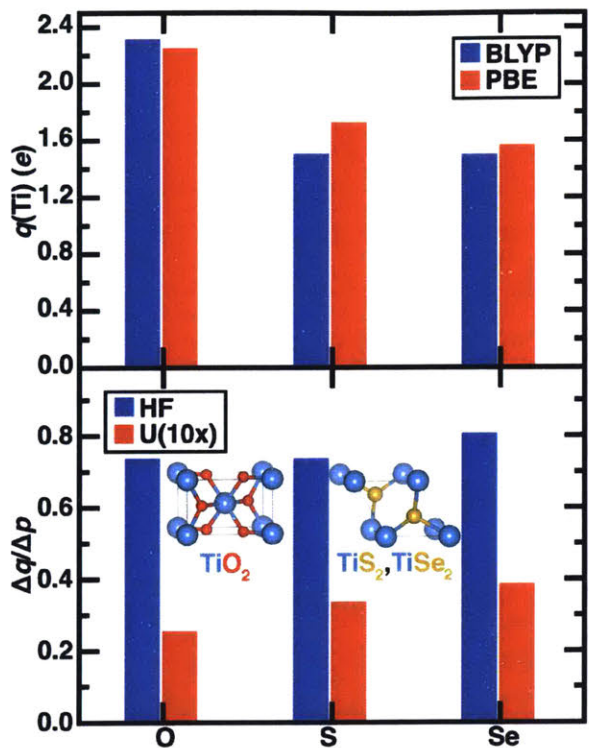


Figure 6-5. (top) Ti GGA reference partial charges in e for U (PBE/PWBS, red bars) or HF exchange (BLYP/LBS, blue bars) without any tuning and (bottom) Ti partial charge sensitivity to changes in U ($e/10$ eV U , as indicated in legend, red bars) and HF exchange (e/HFX , blue bars). Crystal structures for rutile-type tetragonal TiO_2 and hexagonal TiX_2 ($X = S, Se$) are shown in inset.

Importantly, all partial charge sensitivities are positive for the three solids, indicating density localization away from the metal, regardless of functional tuning approach (Figure 6-5). For increasingly diffuse connecting atom valence orbitals (i.e., O to S to Se), the positive sensitivities increase in magnitude for all tuning methods, with monotonic increases for DFT+U and less elemental dependence for HF exchange (Figure 6-5). Thus, unlike, early-to-late transition metal trends in the oxides, metal-to-ligand density localization trends are consistent between DFT+U and hybrids when substituting with increasingly heavy coordinating atoms.

6.4 Charge localization in open-framework solids and extracted transition metal complex analogues

6.4.1 Open-framework solids

The divergent behavior of DFT+U in transition metal dioxides from that previously observed in molecules motivates the study of solids that resemble transition metal complexes and from which isolated octahedral transition metal complexes can be extracted. We thus constructed a test set of 24 open-framework solids, in which early-to-late, first-row transition metals ($M=V-Ni$) are coordinated by ligand-like-moieties of two atoms or more. The four crystal structures have varying oxidation state: $M(III)$ in $K_3M(CN)_6$ and $M(II)$ in $M(NCNH)_2$ or oxygen-coordinating $M(OH)_2$ and MCO_3 (see structures in Figure 6-1). Across these structures, the ligand field strength should nominally vary as $CN^- > NCNH^- > OH^- \sim OCOO^{2-}$. We study all open-framework solids in both their non-magnetic (NM) and ferromagnetic (FM) states to identify the effect of HF exchange or DFT+U on both density-localization trend variations between magnetic states. As in transition metal dioxides, lattice parameters change slightly from GGA reference values with functional tuning: decreasing around 0.1 Å with HF exchange and either increasing or decreasing by around 0.05 Å in a system-dependent fashion with DFT+U.

$M(OH)_2$ most strongly resembles the transition metal dioxides: experimentally, it is a trigonal structure with an octahedral environment of oxygen atoms from hydroxyl groups coordinating the metal. As with the transition metal dioxides, increasing HF exchange consistently increases the metal partial charges in both NM and FM states, regardless of electron configuration of the metal (Figure 6-6). In comparison to sensitivities for the transition metal dioxides, $M(OH)_2$ sensitivities are reduced in both magnetic states (Figure 6-6). These $M(OH)_2$ sensitivities are also more similar to those in transition metal complexes.³³⁹ Examining d -configuration dependence, mid-row TMs have the highest NM sensitivities, whereas sensitivity appears to increase nearly monotonically with d filling in the FM states. Although positive sensitivities are also highest for DFT+U in mid-row Fe for the NM state, negative or near-zero sensitivities are observed for 3 metals (V, Co, Ni) in the NM state and one in the FM state (Cr). This

range of charge sensitivities is comparable to that observed in the transition metal dioxides, and thus additional ligand structure does not eliminate negative partial charge sensitivities with DFT+U. Examining possible underlying correlations across the first row TMs in $M(OH)_2$ reveals no relationship between partial charge magnitudes and sensitivities, unlike previous work on a narrower range of complexes⁸⁸, but sensitivities generally increase with d filling and the magnitudes of the sensitivities are somewhat correlated between DFT+U and HF exchange even when signs differ.

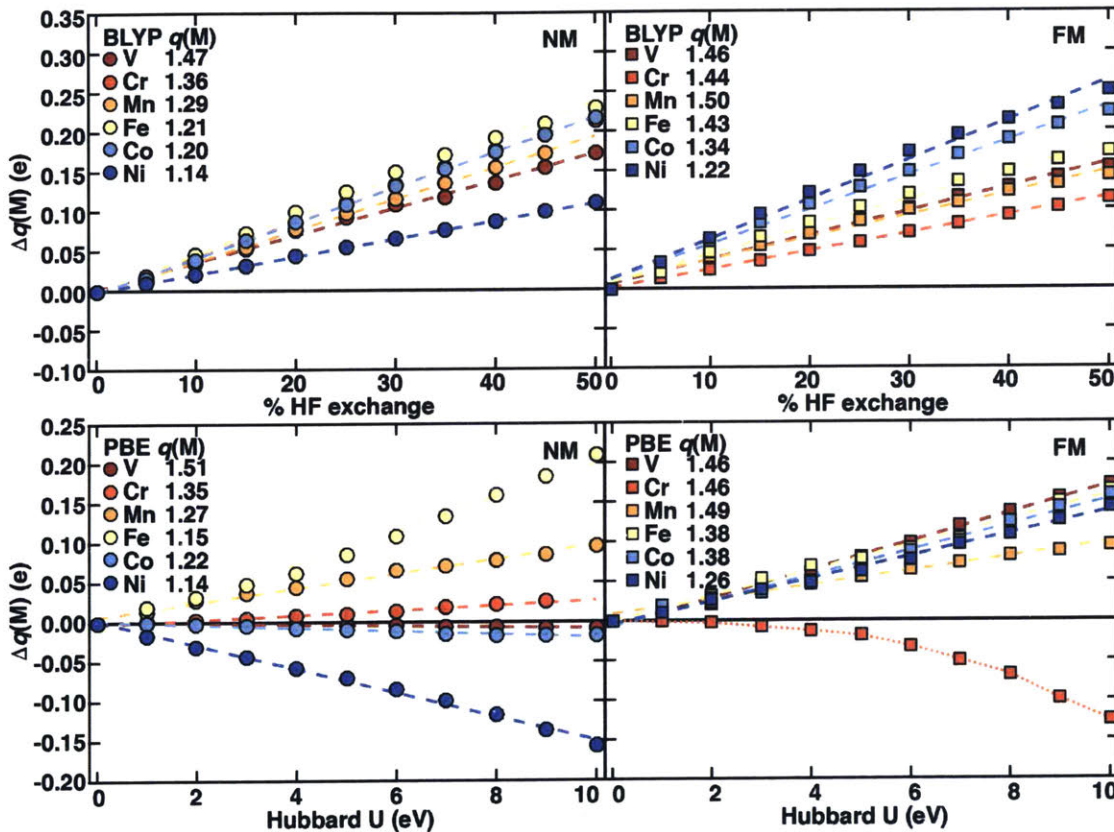


Figure 6-6. Dependence of shift of transition metal partial charge, $Dq(M)$, in e, for non-magnetic (NM) states (left, circle symbols) and ferromagnetic (FM) states (right, square symbols) of $M(OH)_2$ with $M = V$ (maroon), Cr (red), Mn (orange), Fe (yellow), Co (light blue), and Ni (dark blue). The GGA partial charge is indicated in the inset, to allow alignment of the $Dq(M)$ values to zero at 0% HF and $U = 0$ eV. The dashed lines indicate linear best-fit lines to quantify the partial charge sensitivities, and the dotted lines indicate a non-linear fit. All HF exchange and U plots span the same 0.45 e partial charge shift range.

Reviewing sensitivities in the three other open-framework structures (i.e., MCO_3 , $M(NCNH)_2$, and $K_3M(CN)_6$) reveals ligand-dependent effects. Comparable field strength

environments (i.e., MCO_3 vs. M(OH)_2) have similar overall sensitivities, and DFT+U sensitivities are again both positive and negative. Trends of highest sensitivities for late TMs in FM states and highest sensitivities for mid-row TMs in NM states are consistent for MCO_3 and M(OH)_2 solids. Thus, consistent with prior observations in molecules^{63, 88}, the overall crystal structure has limited effect on charge localization as long as the direct ligand atom, and thus field strength, remains the same.

For intermediate-field NCNH^- in M(NCNH)_2 , $S_{\text{HF}}(q)$ values are comparable to the prior two weak-field cases in the NM state, and FM $S_{\text{HF}}(q)$ values are reduced slightly. For DFT+U, negative sensitivities are slightly reduced in magnitude or even change sign (e.g., for FM Cr(NCNH)_2), likely due to greater delocalization of metal density into the more covalent bond that produces lower occupations. Sensitivities of the closest available literature high-spin transition metal complexes with intermediate-field NH_3 ligands³³⁹ are comparable to HF and DFT+U sensitivities in FM states of M(NCNH)_2 .

For the strongest field case considered, $\text{K}_3\text{M(CN)}_6$, the metal is also in a formal M(III) oxidation state. In this case, NM $S_{\text{HF}}(q)$ are reduced with respect to the M(II) compounds, again with highest values for mid-row TMs, whereas values for FM $S_{\text{HF}}(q)$ are comparable to M(II) cases and also consistently increase with *d* filling. Large, uniformly negative sensitivities are observed for DFT+U in both states with NM, highlighting the expected overriding dependence on formal oxidation state rather than on the ligand field strength or magnetic state. Comparing ligand-field-strength trends in partial charge sensitivity with both HF and *U*, subtle ligand-derived trends ($\text{CN}^- < \text{NCNH}^- \leq \text{OH}^- = \text{OCOO}^{2-}$) approximately hold in open-framework solids, in analogy to the trends in transition metal complexes ($\text{CO} < \text{H}_2\text{O} \leq \text{NH}_3$).³³⁹

Having confirmed that DFT+U and HF exchange exhibit diverging behavior across a range of TM solids that was not previously observed in TM complexes, we can quantify how functional tuning will alter the electronic properties of NM and FM states in representative M(OH)_2 solids. Relatively comparable Ni GGA partial charges in NM and FM states differ substantially with DFT+U due to negative NM and positive FM charge sensitivities but remain similar with HF exchange (Table 6-2). In contrast, Cr(OH)_2 charges tuned with HF exchange or DFT+U become even more comparable than predicted with GGA between states but for different reasons: i) with HF exchange,

charges in both magnetic states are tuned in the same direction but with different rates and ii) for DFT+U charge sensitivities have opposite signs in the two magnetic states (Table 6-2).

Table 6-2. Comparison of partial charges at different levels of theory for representative solids.

Method	Ni(OH) ₂			Cr(OH) ₂		
	NM	FM	<i>q</i> (FM-NM)	NM	FM	<i>q</i> (FM-NM)
GGA (PBE/PWBS)	1.14	1.26	0.12	1.35	1.46	0.11
DFT+U (10 eV)	0.98	1.41	0.43	1.37	1.33	-0.04
50% exchange	1.24	1.47	0.23	1.57	1.56	-0.01

Summarizing overall charge sensitivity trends, NM and FM states exhibit differing sensitivities due to differences in delocalization, as was previously observed in isolated molecules. These trends are made more complex by the fact that DFT+U exhibits both positive and negative partial charge sensitivities, whereas HF exchange uniformly localizes density away from metal sites. We also note that GGA functionals have a well-known⁸⁶⁻⁸⁸ preference for low-spin states over high-spin states due to greater delocalization^{331, 339} afforded in low spin states, whereas inclusion of HF exchange⁸⁶⁻⁸⁸ or DFT+U^{85, 351, 382, 398} often reverses this preference. As in the case of diverging behavior of density localization, we also observe unexpected cases (e.g., Fe(OH)₂ for DFT+U and FeCO₃ for hybrids) where nonmagnetic cases are instead stabilized. This unexpected behavior diverges from previous studies on complexes, motivating a more detailed comparison of density and magnetic ordering trends between open framework solids and their inorganic complex analogues.

6.4.2 Extracted transition metal complex analogues

To isolate the role of the crystalline environment in functional sensitivities of energetic and density properties, we constructed transition metal complexes by extracting the octahedral coordination environment from representative Fe-containing open-framework solids. Mid-row Fe was selected because it exhibits divergent behavior in both density and spin-state energetic properties for solids with both HF exchange and

DFT+U. The oxidation state, spin state, and spin-specific metal-ligand bond lengths of these extracted complexes (i.e., $[\text{Fe}(\text{OH})_6]^{4-}$, $[\text{Fe}(\text{CO}_3)_6]^{10-}$, $[\text{Fe}(\text{NCNH})_6]^{4-}$, and $[\text{Fe}(\text{CN})_6]^{3-}$) were kept consistent with the corresponding solids (i.e., $\text{Fe}(\text{OH})_2$, FeCO_3 , $\text{Fe}(\text{NCNH})_2$, and $\text{K}_3\text{Fe}(\text{CN})_6$) (Figure 6-7).

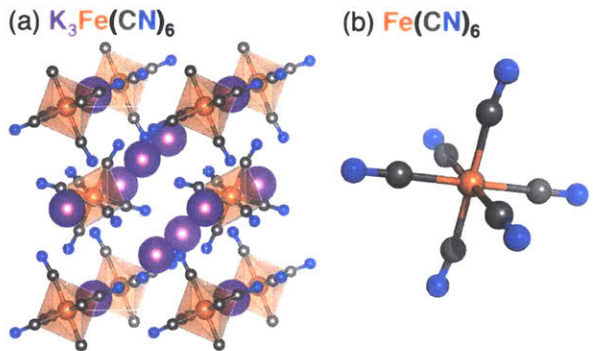


Figure 6-7. (a) Monoclinic crystal structure $\text{K}_3\text{Fe}(\text{CN})_6$ with additional carbon and nitrogen atoms beyond the unit cell boundary to show the octahedral coordination environment of the iron atom (octahedron highlighted in translucent orange) and (b) the structure of transition metal complex $\text{Fe}(\text{CN})_6$ built from the corresponding crystal structure of $\text{K}_3\text{Fe}(\text{CN})_6$. The other transition metal complexes, $\text{Fe}(\text{CO}_3)_6$, $\text{Fe}(\text{OH})_6$, and $\text{Fe}(\text{NCNH})_6$ are built from their corresponding crystal structures in a similar fashion.

We first examine sensitivity of the partial charges in extracted low-spin (LS) and high-spin (HS) complexes (Figure 6-8). Absolute values of partial charges in the extracted complexes are close to those in the solids, especially for the MCO_3^3 structures, and trends in more positive HS/FM partial charges than LS/NM partial charges are consistently preserved. The unusual partial charge sensitivities with DFT+U for solid-state $\text{K}_3\text{Fe}(\text{CN})_6$ are absent from the $[\text{Fe}(\text{CN})_6]^{3-}$ complex in either spin state. For the remaining ligands, the equivalent NM/LS states in solids and molecules have similar sensitivities in both methods. Although the FM/HS directions of charge localization are the same, magnitudes are generally higher in the extracted complexes for both HF exchange and DFT+U (Figure 6-8). Thus, these observations suggest limited transferability of the effect of functional tuning on electron density for representative clusters with respect to behavior in the solid state.

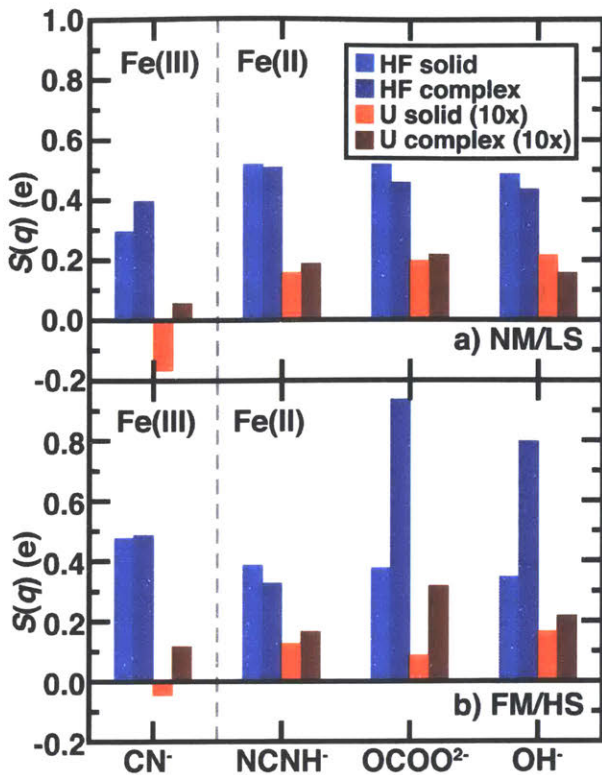


Figure 6-8. Fe partial charge sensitivities to changes in HF exchange (e/HFX) for solids (blue bars) and complexes (dark blue bars), U ($e/10$ eV U, as indicated in legend) for solids (red bars) and complexes (dark red bars) for non-magnetic (NM) or low-spin (LS) states (top) and ferromagnetic (FM) or high-spin (HS) states (bottom) of four ligand environments. All NM/LS and FM/HS sensitivity plots span the same range: 1.2 e/HFX for HF exchange or 1.2 $e/10$ eV U for DFT+U. The vertical dashed line distinguishes that the CN^- ligand environment corresponds to Fe(III), whereas $NCNH^-$, $OCOO^{2-}$, and OH^- ligand environments are Fe(II), as indicated.

Spin-state splitting sensitivities in Fe-containing open framework solids have unexpectedly positive values in $Fe(OH)_2$ with DFT+U or $FeCO_3$ with HF exchange. Computing the HS-LS spin state splitting from single point energies on the extracted complexes can isolate the role of the crystalline environment in these effects. Extracted complexes have very close GGA spin-splittings to the equivalent solids (i.e., within ca. 5-10 kcal/mol). This equivalence is surprising, given that only some solids (e.g., $Fe(NCNH)_2$) exhibit 0.1-0.2 Å increases in the metal-ligand bond length from low-spin to high-spin that would be expected for isolated, equilibrium transition metal complexes. The positive $S_{HF}(DE_{FM-NM})$ for $FeCO_3$ and $S_U(DE_{FM-NM})$ for $Fe(OH)_2$ are negative for the extracted complexes (Figure 6-9). In all cases, HF exchange and DFT+U stabilize HS

states of the isolated complexes, consistent with expectations from previous observations.^{86-88, 399} The $S_{HF}(DE_{HS-LS})$ values in extracted complexes range from -108 to -49 kcal/mol HFX, which is also consistent with typical adiabatic values in fully relaxed transition metal complexes^{88, 399}. The strong ligand-field dependent effects^{63, 88, 399} observed in DFT+U for the solids is reduced in the extracted complexes, which have little variation in $S_U(DE_{HS-LS})$ (Figure 6-9). Thus, these observations highlight that equivalent functionals may differently affect magnetic ordering in the solid state and spin-state ordering in transition metal complexes.

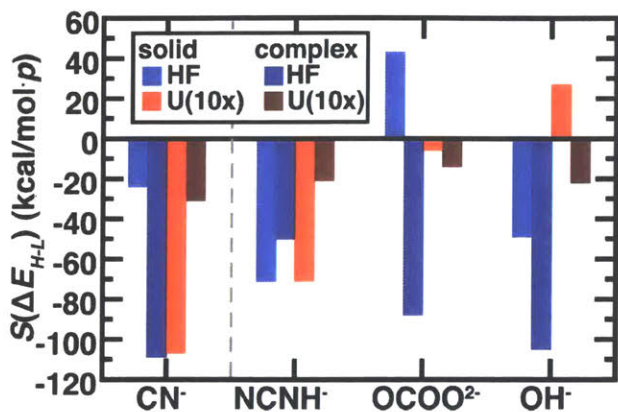


Figure 6-9. Fe magnetic or spin-state ordering sensitivity to changes in HF exchange (kcal/mol HFX) for transition metal solids (blue bars) and complexes (dark blue bars) and U (kcal/mol 10 eV U , as indicated in legend) for solids (red bars) and complexes (dark red bars) of four ligand environments. The vertical dashed line distinguishes the CN^- ligand environment with Fe(III), whereas $NCNH^-$, $OCOO^{2-}$, and OH^- correspond to Fe(II).

6.5 Surface properties in the solid-state

6.5.1 Surface science

Although exchange-correlation functional development remains an active area of research, especially for higher “rung” double hybrid and random phase approximation forms, the majority of heterogeneous catalysis studies are still frequently carried out with pure generalized-gradient approximation (GGA) semi-local DFT (e.g., PBE⁵⁸). In the case of transition metal oxides, well-known shortcomings of semi-local DFT have motivated the inclusion of Hubbard corrections (i.e., DFT+U^{329-331, 378}) or hybrid exchange, frequently in lower cost range-separated hybrids (RSHs, e.g., HSE06⁹⁴) with

exact exchange only in the short range or global hybrids (GHs, e.g., PBE0⁴⁰⁰), albeit at significantly greater computational cost.

In the context of metals, it has been observed that a single GGA or GGA hybrid functional could not reproduce the experimentally-observed surface formation energy (i.e., stability) and binding energy (i.e., reactivity). It was suggested that a single scaling relationship⁴⁰¹ connected all such functionals, creating a trade-off in which either surface formation energies could be improved by being made less stable or adsorbate binding energies could be improved by being made less strong. The fundamental relationship between how many electron self-interaction error (MESIE) and MESIE corrections affect i) surface formation, wherein one bond is lost and metal density reorganizes to the remaining surface atoms and ii) adsorbate binding, wherein an atom or molecule's density is more delocalized when bound to the surface is not yet clear. Inherently, any such MESIE corrections should penalize excess delocalization, but the relationship between energetics and density also remain unclear. A functional tuning approach should be useful in identifying to what extent common approximations are able to simultaneously make surfaces less stable without making them more reactive.

6.5.2 Computational details

Lattice parameters and atomic positions of non-magnetic bulk MO₂ bulk crystals were optimized with DFT functionals using 12×12×12 Monkhorst-Pack *k*-point grids. Using bulk lattice parameters and 4 × 4 × 1 Monkhorst-Pack *k*-point grids, atomic positions in the outermost of four trilayers in 2x1 unit cell models were relaxed for E_{σ} calculations, and atoms in the two topmost trilayers and a single adsorbate were relaxed for ΔE_O calculations. Slab spacing included > 15 Å of vacuum. Hybrid calculations with a LBS were performed using CRYSTAL²²⁰ with default and tuned^{88, 303, 339} PBE0^{400, 402} global hybrid (default: 25% HF; tuned: 0-50% HF in 5% increments) or HSE06^{94, 403} range-separated local hybrid (default: 25% HF, $\omega=0.11$ bohr⁻¹; tuned: HF % as in the GH and ω from 0.0 to 0.4 in 0.1 bohr⁻¹ increments), in addition to the pure BLYP^{61, 404} or PBEsol⁷⁰ GGA functionals. At least a double- ζ split-valence basis set was used for all atoms, triple- ζ split-valence basis sets were used for Pt and Ir, with all basis sets

obtained from the CRYSTAL²²⁰ website³⁷. Hubbard U^{329-331, 378}-corrected semi-local DFT (i.e., with PBE⁵⁸) was carried out with U from 0-10 eV in 1 eV increments using Quantum-ESPRESSO³⁷⁹. These calculations employed a PWBS (cutoffs: 35 Ry for wavefunction, 350 Ry for charge density) with ultrasoft pseudopotentials³⁸⁰ obtained from the Quantum-ESPRESSO website¹⁰⁹. In order to aid self-consistent field (SCF) convergence, an electronic temperature of 0.005 hartree was applied in all spin-polarized calculations. Real-space Bader atomic partial charges^{99, 334} were obtained from the TOPOND package⁴⁰⁵ or the BADER program³⁸⁴, and built-in postprocessing codes were used to obtain electron density cube files. Domain-based local pair natural orbital DLPNO-CCSD(T)⁴⁰⁶ calculations with a localized basis set, aug-cc-pVTZ, on transition metal complexes were carried out using ORCA⁴⁰⁷.

6.5.3 Surface formation energy

We thus examine the relationship between the two most fundamental properties in surface science: i) surface stability through evaluation of surface formation energy, E_o , for the reactive MO₂(110) surface and ii) surface reactivity through calculation of binding energies, ΔE_o , for representative O atom adsorbates in several representative transition metal dioxides both across and down the periodic table from 3d TiO₂ to 5d PtO₂, chosen for their experimentally available crystal structures³⁸³ (Figure 6-10). Rather than carry out an exhaustive survey of each literature definition of various classes of functionals, we extend an approach we have developed for understanding functional sensitivity in density properties^{88, 303, 339}, spin state ordering^{63, 88, 351}, and molecular catalysis³⁵¹, to focus on the sensitivity, S_p , to functional parameter, p (where p is α_{HF} , ω , or U) tuning. As in previous work^{303, 339, 351}, the partial derivative $\partial E_o / \partial p$ or $\partial \Delta E_o / \partial p$ is approximated by finite difference $\Delta E_o / \Delta p$ or $\Delta \Delta E_o / \Delta p$ owing to the near linear dependence of key properties with functional variation. By focusing on S_p values, we minimize difficulties in comparing absolute PBE GGA reference values obtained from plane wave (PW) or localized basis set (LBS) codes, which differ here in accordance with observations in the literature⁴⁰⁸ (Figure 6-11).

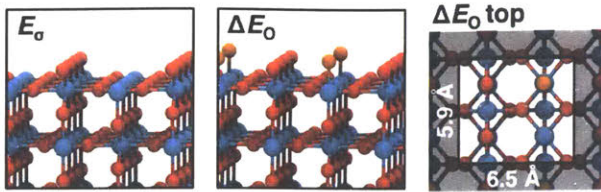


Figure 6-10. MO_2 structures: (left: side-view) pristine 48-atom surface model for calculating E_σ and (middle: side-view, right: top-view) O-atom adsorption in 0.5 ML coverage for calculating ΔE_σ . The unshaded square in the rightmost panel indicates unique atoms in a single unit cell, and representative PBE0 lattice parameters for TiO_2 are shown. Atoms are colored as follows: metal in blue, MO_2 oxygen atom in red, and adsorbate oxygen atom in orange.

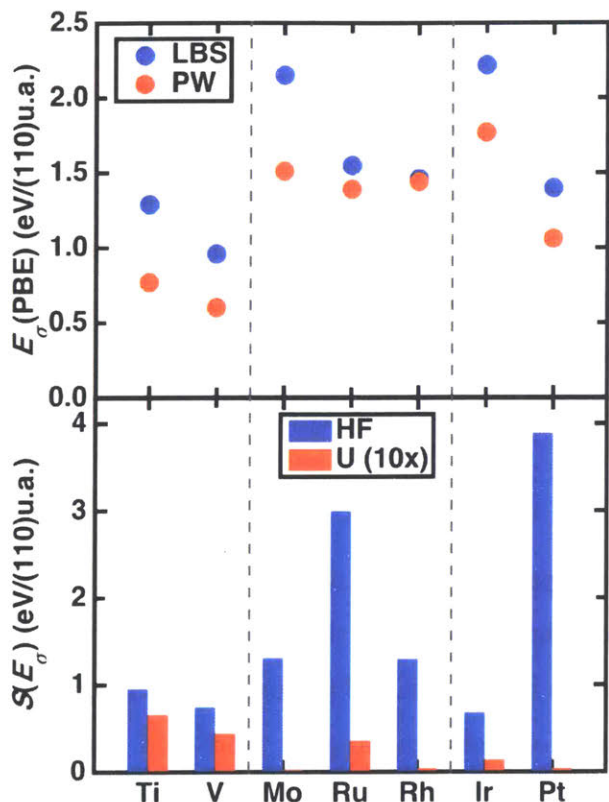


Figure 6-11. (top) $\text{MO}_2(110)$ E_σ in eV/(110) unit area (u.a.) for plane wave (PBE/PW, red circles) or localized basis set (PBE/LBS, blue circles) GGA references. (bottom) Sensitivity of GGA E_σ to tuning U ($E_\sigma/10$ eV U , as indicated in legend, red bars) and HF exchange (E_σ/HFX , where 1 HFX is the range from 0% to 100% exchange, blue bars).

To quantify surface stability with functional tuning, we compute E_σ for the MO_2 (110) surface (Figure 6-10) as:

$$E_\sigma = \frac{E_{\text{slab}} - NE_{\text{bulk}}}{2A} \quad (6.6)$$

the ratio of the difference in energy of the same number of slab and bulk atoms (i.e., E_{slab} and E_{bulk} , N is ratio of the number of atoms in the slab to the bulk) to the surface area, A . Trends in E_σ of more stable early- and very-late TM surfaces (i.e., V<Ti<Pt<Ru~Rh~Mo<Ir) are primarily preserved when comparing PW and LBS GGA values (Figure 6-11). Incorporating +U or HF exchange either uniformly destabilizes surfaces or has no effect, albeit to differing degrees (Figure 6-11). The DFT+U sensitivities, $S_U(E_\sigma)$, are largest for early transition metals (i.e., Ti, and V), decreasing across and down the periodic table for Ru and Ir, and remaining unchanged for the remaining cases (Mo, Rh, and Pt). Conversely, α_{HF} sensitivities are uniformly positive, appearing to increase from early- (Ti, V) to midrow (Ru) before decreasing again only to reach its highest value at Pt. This strong variation in HF sensitivities means that the surface stability ordering in GGA (e.g., Pt<Rh) will change substantially at even moderate 25% exchange (e.g., Rh<Pt). The more modest and comparable DFT+U sensitivities are insufficient to reorder most relative surface stabilities, except for Ti<Pt in GGA becoming isoenergetic at 5eV due to the high $S_U(E_\sigma)$ for TiO_2 .

6.5.4 Adsorption energy

From a fundamental catalysis perspective, higher surface formation energies should correlate to more reactive surfaces, and we have just shown that DFT+U and HF exchange tuning never decrease E_σ and often increases it. Indeed, one interpretation⁴⁰¹ of the limitations of DFT for metal adsorption energies in prior work had been that functionals that destabilized surfaces did so at the cost of making binding too favorable. Thus, we compute the oxygen adsorbate (O^*) binding energy (Figure 6-10):

$$\Delta E_{\text{O}} = E(\text{O}^*) - E(*) - (E_{\text{H}_2\text{O}} - E_{\text{H}_2}) \quad (6.7)$$

where $E(*)$ is the energy of the clean surface, and the gas phase O atom energy is evaluated as in the literature⁴⁰⁹. Trends in ΔE_{O} of stronger binding on early/mid-row- than later- TMs (i.e., V<Mo<Ir<Ru<Rh~Pt<Ti) and stronger binding down the periodic table (i.e., Ir<Rh) are fully preserved when comparing PW and LBS GGA values (Figure 6-

12). Focusing again on the $S_p(\Delta E_O)$, +U and HF exchange corrections either have no effect or otherwise uniformly destabilize ΔE_O , at odds with earlier observations in metals. With the exception of Ti, $S_{HF}(\Delta E_O)$ values nearly monotonically increase with d filling (Figure 6-12). Because ΔE_O becomes less favorable and more sensitive to HF exchange with d filling, $S(\Delta E_O)$ correlates with increasing GGA ΔE_O values, but this trend is not generalizable (i.e., to $S(E_\sigma)$). This more comparable behavior means that no HF exchange fraction reverses the relative reactivity of the oxides. Examination of $S_U(\Delta E_O)$ reveals magnitudes much smaller than the corresponding $S_{HF}(\Delta E_O)$, in contrast with some E_σ cases (TiO_2 and VO_2), meaning that reactivity ordering will remain unchanged regardless of U value (Figure 6-12). Additionally, the precise structures for which $S_U(E_\sigma)$ was highest, i.e., early TMs, are now the cases where $S_U(\Delta E_O)$ is near zero.

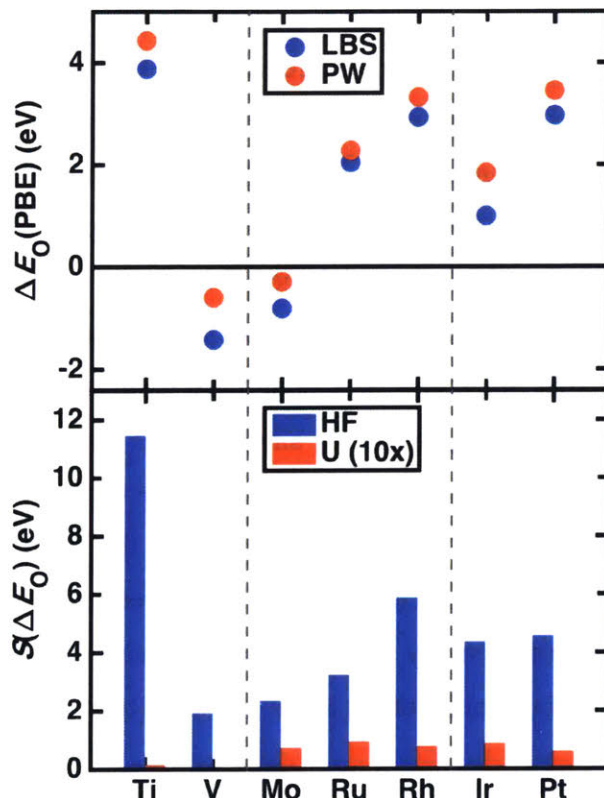


Figure 6-12. (top) $MO_2(110)$ ΔE_O in eV for plane wave (PBE/PW, red circles) or localized basis set (PBE/LBS, blue circles) GGA references. (bottom) Sensitivity of GGA ΔE_O to tuning U ($\Delta E_O / 10$ eV U , as indicated in legend, red bars) and HF exchange ($\Delta E_O / HFX$, where 1 HFX is the range from 0% to 100% exchange, blue bars).

6.5.5 Surface stability vs. reactivity

In the context of metals, it has been observed that a single GGA or GGA hybrid functional could not reproduce the experimentally-observed surface formation energy (i.e., stability) and binding energy (i.e., reactivity). It was suggested that a single scaling relationship connected all such functionals⁴⁰¹, creating a trade-off in which either surface formation energies could be improved by being made less stable or adsorbate binding energies could be improved by being made less strong. For transition metal oxides, modifying the functional from PBE to BLYP or PBEsol can not replicate both surface formation energy and adsorption energy of the more accurate reference calculation with domain-based local pair natural orbital DLPNO-CCSD(T)⁴⁰⁶ method on transition metal complex (Figure 6-13). Since HF exchange tuning can alter stability and reactivity on transition metal oxide surfaces simultaneously, we would like to show the effect on a same plot (Figure 6-13). We indeed observed HF exchange predicting less favorable adsorption energy and less stable surfaces, indicating improvement of both surface formation energies and adsorption energy when compared the more accurate reference.

In addition to global hybrid, we also studied the widely used range-separated hybrid functional in the solid-state community, HSE06, in which the HF exchange is only incorporated in the short range to reduce computational cost (Figure 6-13). By tuning the HF exchange in HSE06 at default separation range $\omega = 0.11 \text{ bohr}^{-1}$, we observed less favorable adsorption energy and less stable surface, indicating similar effect as global hybrid. We also tune the separation range ω from 0 bohr^{-1} to up to 0.4 bohr^{-1} in 0.1 bohr^{-1} increments at default $a_{\text{HF}} = 0.25$. For $\omega = 0 \text{ bohr}^{-1}$, HSE06 is reduced to the hybrid functional PBE0, and for $\omega = \infty$, HSE06 becomes pure GGA PBE. We observed stronger adsorption energy and smaller surface formation energy with increasing ω value due to the decreasing short-range correction, indicating similar effect as HF exchange tuning.

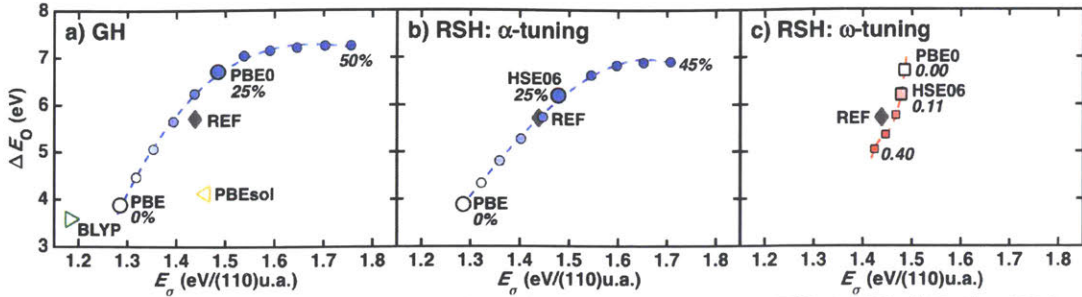


Figure 6-13. $\text{TiO}_2(110)$ E_σ in eV/(110) unit area (u.a.) versus $\text{TiO}_2(110)$ ΔE_0 in eV for a) α_{HF} tuning the PBE0 global hybrid (GH) functional, b) α_{HF} -tuning, or c) ω -tuning the HSE06 range-separated hybrid (RSH) functional. Symbols are colored according to tuning parameters: α_{HF} tuning (circles) from 0% (white) to 50% (blue), ω tuning (squares) from 0.00 bohr⁻¹ (white) to 0.40 bohr⁻¹ (red). The BLYP (empty green triangle) or PBESol (empty orange triangle) result is added for comparison, and the DLPNO-CCSD(T) reference is shown with a gray diamond annotated “REF”, as described in the main text.

6.5.6 Occupation matrix in DFT+U

Returning to the unexpected behavior of DFT+U, it is useful to recall its functional form:

$$E^U = \frac{1}{2} \sum_{I,\sigma} U^I [\text{Tr}(\mathbf{n}^{I,\sigma} (\mathbf{1} - \mathbf{n}^{I,\sigma}))] \quad (6.8)$$

where I is each Hubbard atom (here, metals), σ is a spin index, and \mathbf{n} is the occupation matrix of the relevant Hubbard subshell. In a first order approximation, we have shown how the +U correction has an effect proportional to differences in fractionality, i.e., $\Delta \text{Tr}[\mathbf{n}(1-\mathbf{n})]$ of points being compared, having no effect when fractionality differences approach zero.^{95, 331, 410-411} Thus, we revisit the effect DFT+U has on ΔE_0 and E_σ in the context of theoretical limits on DFT+U corrections.^{95, 331, 410-411} Consistent with observations of DFT+U sensitivities, $\Delta \text{Tr}[\mathbf{n}(1-\mathbf{n})]$ values are higher for $\text{TiO}_2 E_\sigma$ than for ΔE_0 (0.27 vs. 0.08), whereas the ordering is reversed in PtO_2 (0.03 vs. 0.17, Figure 6-14).

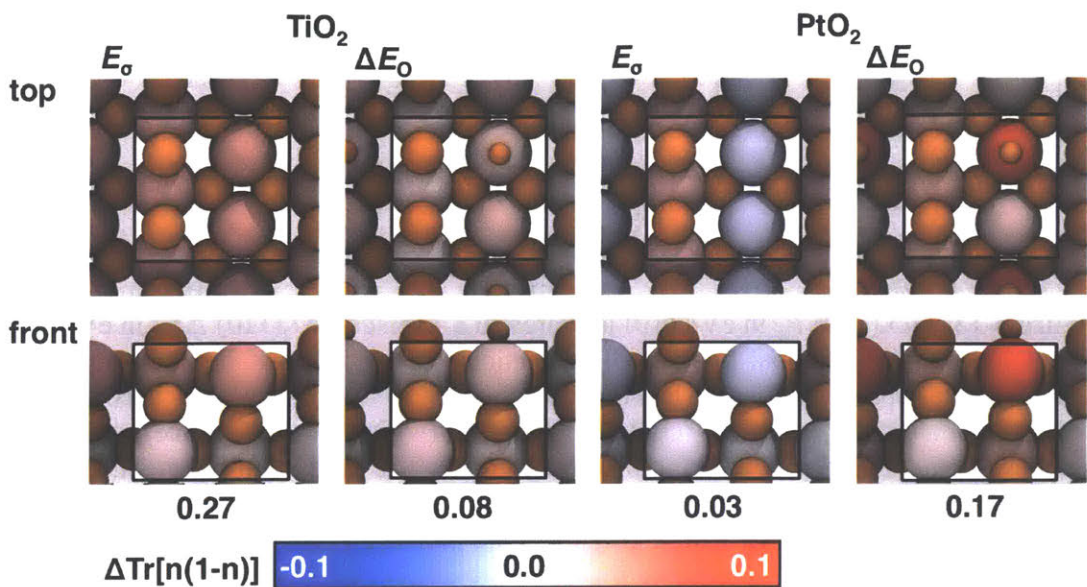


Figure 6-14. Occupation matrix fractionality differences, $\Delta \text{Tr}[\mathbf{n}(1-\mathbf{n})]$, between the pristine surface and bulk structure evaluated in E_0 calculations or between O-atom adsorbed surfaces and pristine surfaces in ΔE_0 calculations for 3d or 5d valence electrons of Ti or Pt shown in both top and front view for TiO_2 (left) and PtO_2 (right). Each metal atom is colored by $\Delta \text{Tr}[\mathbf{n}(1-\mathbf{n})]$ values from -0.1 (blue) to +0.1 (red), as indicated by the color bar at bottom; the oxygen atoms are shown in orange, the largest spheres correspond to metal atoms, and the O-atom adsorbate is distinguished from lattice O atoms by a smaller radius. Unit cell atoms are indicated inside each rectangle, and the overall sum of metal atom $\Delta \text{Tr}[\mathbf{n}(1-\mathbf{n})]$ values in each unit cell are indicated below the respective structures.

In both TiO_2 and PtO_2 , differences between bulk and slab structures for E_0 calculation produce reorganization of M occupations, resulting in $\Delta \text{Tr}[\mathbf{n}(1-\mathbf{n})]$ contributions from all of the 16 M sites in the surface (Figure 6-14). Conversely, for ΔE_0 , the $\Delta \text{Tr}[\mathbf{n}(1-\mathbf{n})]$ arises nearly exclusively from the surface site on which the O atom adsorption occurs (Figure 6-14). For each rehybridized molecular orbital, the maximum theoretical contribution to $\Delta \text{Tr}[\mathbf{n}(1-\mathbf{n})]$ is 0.25, which occurs only in the case that a fully unoccupied or occupied orbital becomes half occupied, a limit typically only achieved in atoms.⁹⁵ Even if two orbitals are invoked in an M=O species for the ΔE_0 calculation, we can thus anticipate at most a contribution of 0.5 to $\Delta \text{Tr}[\mathbf{n}(1-\mathbf{n})]$. In practice, M hybridization with the other five neighboring lattice O atoms can reorganize to lead to more modest effects on $\Delta \text{Tr}[\mathbf{n}(1-\mathbf{n})]$, as is observed for TiO_2 . Conversely, for E_0 , even a small increase in fractionality that is estimated to occur by the formation of a dangling surface bond and addition of excess charge back onto the M centers can be easily

multiplied by eight surface atoms to yield higher $\Delta\text{Tr}[\mathbf{n}(1-\mathbf{n})]$ and thus $S_U(E_\sigma)$ than the theoretical maximum of $S_U(\Delta E_O)$. However, the practical trends in $S_U(E_\sigma)$ arise because excess electron density on the surface can exactly cancel subsurface species in cases where d electron counts are already nearly full, as is observed for the occupation matrices of the late TM compounds.

6.5.7 Electron density

Visualization of changes in the electron density difference between the pristine surface and bulk structure at fixed lattice parameter with HF exchange reveals a electron density loss in the area between surface metal (Ti) center and the coordinating O atoms, indicating less amount of electron density delocalization between atoms in surface, consistent with the observation of less stable surface predicted by hybrid functional (Figure 6-15). The loss of electron density between metal and O atoms leads to electron density gain of δ -orbital character at Ti metal center. In order to simplify and quantify the change of electron delocalization in surface, we applied metal partial charge difference between pristine surface and bulk structure:

$$\Delta q(M) = q(M)_{\text{surf}} - q(M)_{\text{bulk}} \quad (6.9)$$

We observed a more negative metal partial charge difference with incorporation of HF exchange for all metals studied, indicating charge localization onto the surface metal and electron density loss in the region between surface metal and O atoms. Increasing U in DFT+U localizes charge onto surface metal only for early transition metals (i.e., Ti, V), but has negligible effect on electron density for midrow and late transition metals (i.e., Mo, Ru, Rh, Ir, Pt), consistent with divergent effect on surface formation energies for different transition metals.

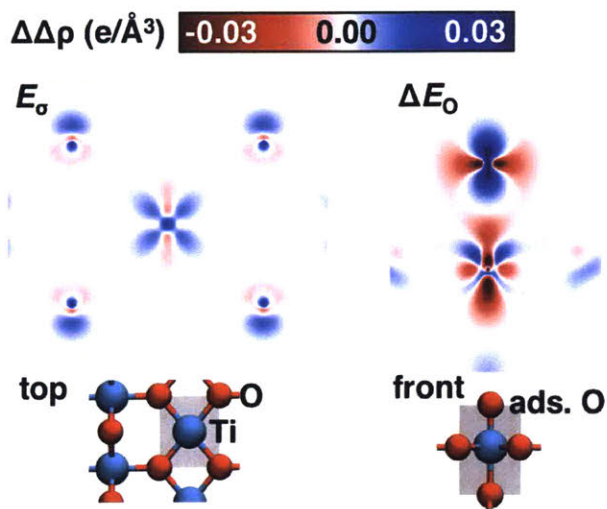


Figure 6-15. Effect of increasing HF exchange from 0 to 50% on the electron density difference of TiO_2 (left) between the pristine surface and bulk structure and (right) between O-atom adsorption and the pristine surface. Red and blue colors represent negative (density loss) and positive (density gain) electron density differences, respectively, as indicated by the color bar at top. The location of the density plane shown is indicated on the bottom inset structures as a shaded gray region.

Examining changes in the electron density difference around the adsorption site between O-adsorbed surface and pristine surface with HF exchange reveals an electron density loss between the oxygen adsorbate and the surface adsorption site, explaining the less favorable adsorption energy with increasing HF exchange (Figure 6-15). To simplify and quantify the effect on electron density loss around the adsorption site, we investigate similar properties, electron density at adsorbate-surface bond critical point and oxygen adsorbate partial charge. The decrease in electron density at adsorbate-surface bond critical point with incorporation of HF exchange is consistent with our observations of less favorable adsorption energies for all transition metal atoms studied. Similarly, the more neutral oxygen adsorbate partial charge also helps demonstrate the electron density loss between adsorbate and surface with HF exchange. DFT+U exhibits diverging behaviors, decreasing electron density at bond critical point and more neutral oxygen adsorbate partial charge with increasing U is only observed in MO_2 with late transition metals, demonstrating the less favorable adsorption energies for Mo, Ru, Rh, Ir, and Pt only.

6.6 Comparison with experimental data

Benchmarking accuracies of the above approximations in DFT with available experimental properties is important to understand the different tuning strategies investigated in this work. Due to the difficulty of obtaining reliable surface properties in experiment, such as surface formation energy and surface adsorption energy, bulk thermodynamic properties are compared and discussed instead, such as bulk formation energies, vibrational properties and band structures.

Metal oxides are important in oxidation and reduction reactions. Previous studies³⁸⁶ have shown that DFT-GGA calculations with PBE functional highly overestimate formation energies of rutile-type transition metal dioxides compared with experimental values obtained from electrochemical series⁴¹²⁻⁴¹⁴, e.g. experimental -4.26 eV vs DFT-PBE result of -4.86 for TiO₂, experimental -2.08 eV vs DFT-PBE result of -2.76 eV for VO₂, and experimental 3.15 eV vs DFT-PBE result of 2.36 eV for RuO₂. Since hybrid functionals with incorporation of HF exchange can reduce electron delocalization between metal atoms and oxygen atoms in both transition metal oxides surfaces and between surface metal active site and oxygen adsorbates as previously observed, the electron delocalization between metal atoms and oxygen atoms in transition metal oxides bulk formation is also expected to decrease with increasing HF exchange through a hybrid tuning. The reduction of electron delocalization in bulk formation will result in a more positive transition metal oxides formation energies, indicating an improvement on the GGA-PBE functional and a better agreement with experimental results. Since DFT+U method shows divergent behavior of electron delocalization regarding different *d* electron configurations, it is expected to show different trends regarding the change of bulk formation energies, and thus it cannot give a consistent result of predicting more positive formation energies as hybrid functionals.

For vibrational properties, GGA-PBE tends to underestimate the vibrational frequency of solids⁴¹⁵⁻⁴¹⁷, e.g., experimental 827 cm⁻¹ vs DFT-PBE result of 774 cm⁻¹ for TiO₂⁴¹⁷. Since there is an observed correlation between bond length change and vibrational frequency shift in hydrogen-bonded complexes⁴¹⁸ and halogen-bonded complexes⁴¹⁹, i.e., increasing in bond length results in decreasing of vibrational frequency and decreasing in bond length results in increasing of vibrational frequency, we can use

our observed change in lattice parameters of rutile-type transition metal dioxides with different tuning strategies to predict the corresponding changes in vibrational properties. Optimizations of rutile transition metal dioxides geometries with HF exchange decrease lattice parameters slightly, indicating increasing of vibrational frequencies and thus better agreement with experimental results. While DFT+U increases lattice parameters for early transition metals and has a smaller effect on mid or late transition metals, which should result in even smaller vibrational frequencies of early transition metals and slightly smaller effect on mid or late transition metals, indicating even larger deviations from experimental vibrational frequencies.

Regarding band structures, GGA is well known to underestimate or even close band gaps. Experimentally, TiO_2 and PtO_2 have band gaps of 3.0 eV³⁹¹ and 0.2 eV³⁹³, respectively. HF exchange increases the band gap in TiO_2 from its GGA underestimate and introduces a band gap into metallic GGA PtO_2 , whereas DFT+U weakly increases the TiO_2 band gap and maintains a metallic PtO_2 ground state. Another problem within DFT is GGA functionals tend to overestimate covalency between metal-oxygen bonds⁴²⁰⁻⁴²¹. We observed that incorporation of HF exchange uniformly increases positive metal partial charges, signifying charge localization away from the metal and onto the surrounding oxygen anions, indicating a decrease of metal-oxygen bond covalency. While increasing U in DFT+U localizes partial charge away from the metal only for early transition metals but onto the metal for midrow and late transition metals, indicating a decrease of metal-oxygen bond covalency for early transition metals and an increase of metal-oxygen bond covalency for midrow and late transition metals. Examination of projected density of states features, especially with integrating the overlap between total metal *d*-orbital and oxygen *p*-orbital PDOS in valence band, also reveals the decrease of metal-oxygen bond covalency for hybrid functionals and divergent behavior for DFT+U calculations with respect to *d*-electron configurations of metal atoms.

6.7 Conclusion

We have compared the effect of two commonly employed strategies for mitigating many-electron self-interaction error within approximate DFT, i.e., DFT+U and global hybrid tuning, on the key nanoscale property, electron densities, and key

observables in heterogeneous catalysis, surface stability and reactivity of a broad set of representative transition-metal containing solids.

We observed HF exchange to consistently localize density away from the metal in solids, as indicated by increasing positive partial charges, in a consistent fashion with behavior previously observed in transition metal complexes. Conversely, DFT+U exhibited both positive (i.e., density loss at the metal) and negative (i.e., density gain at the metal) partial charge sensitivities in an electron-configuration-dependent manner. The individual metal occupation matrices and projected density of states enabled rationalization of these differing charge localization trends between HF exchange and DFT+U for early versus late transition metals. Agreement of hybrids and DFT+U in early TMs and divergence on late TMs was also observed even when the metal's ligand environment was comprised of molecule-like species in open-framework solids. We isolated the role of the crystal environment by rigidly extracting complexes from the octahedral coordination environments of select open-framework solids. Our observations in the solid state of accumulation of charge density on the metal for DFT+U or stabilization of nonmagnetic states with HF exchange or DFT+U were not replicated in these isolated complexes, even though they were held fixed at the solid state equilibrium geometries. This observation confirms the divergent behavior for DFT+U and hybrid exchange is specific to transition metal solids.

For surface stability, we observed incorporation of HF exchange through a hybrid tuning predicts less stable surface for all transition metal atoms we studied, while DFT+U predicts less stable surface for early transition metal oxides only and has no effect for late transition metal oxides. For surface reactivity, hybrid functionals result in a less favorable adsorption in a consistent manner for electron configurations, while DFT+U predicts less favorable adsorption for late transition metal oxides and doesn't change the reactivity for early transition metal oxides. The metal occupation matrices and electron density differences enabled rationalization of these differing behaviors between HF exchange and DFT+U for transition metals with different electron configurations. Observation of divergent behavior between these common approximations in DFT highlights their limited interchangeability in the solid-state community.

Chapter 7 Ionization Potential in Polymer Electrolyte

7.1 Introduction

Polymer electrolytes⁴²²⁻⁴²⁵ in lithium ion batteries are an emerging paradigm for energy storage. Conventional non-aqueous, liquid electrolytes such as carbonates have electrochemical windows less than 5 V, but new high-voltage cathodes⁴²⁶⁻⁴²⁸ necessitate higher electrochemical windows for electrolytes. Many potential energy storage solutions incorporate charged species into polymer matrices to form polymer electrolytes that offer additional advantages over conventional liquid or solid electrolytes through enhanced resistance to variations in volume of electrodes during charge/discharge, flexibility, processability, and longer lifetime^{425, 429}. However, overcoming current limitations of polymer electrolytes necessitates a nanoscale understanding of the oxidation and electron transfer processes by which polymer electrolyte performance may be degraded during charge/discharge cycles. Electronic structure of the salt and solvent composing the electrolyte limit selection of cathode and anode materials with high voltage applications. The electrochemical stability window should be closely related to the oxidation potential of any anions or neutral species (e.g., the polymer) and the reduction potential of any cations or easily reduced species. Thus, widening the electrochemical stability window necessitates increasing oxidation potential of counterions and neutral species in the electrolyte.

Further development of lithium rechargeable batteries is limited by the search for large electrochemical windows of the electrolyte. Accurate computational modeling of oxidation processes in polymer electrolytes is a critical tool in order to continue to optimize materials properties. Although voltage stability of organic electrolytes is not understood in detail, computations of oxidation potentials starting with ionization potentials (IP) have been shown to correspond to voltage measurements of electrochemical decomposition⁴³⁰⁻⁴³¹, thus providing paths forward for computational design. Approximate density functional theory can provide is often the method of choice to provide valuable insight owing to its favorable combination of efficiency and accuracy. However, approximate DFT suffers from well-known errors that make it challenging to directly apply these methods for robust, predictive estimations of ionization potentials and thus the electrochemical stability windows. With the inherent errors for modeling ionization potentials in DFT, alternatives should be sought both for

benchmarking approximate DFT approaches and for avoiding its limitations. Correlated quantum chemistry approaches rigorously introduce electron correlation beyond HF theory and provide more accurate predictions of ionization potentials, but correlated quantum chemistry approaches are less widespread due to its high computational cost and its applications are only limited to small-sized systems. In this work, we carry out a systematic study to efficiently predict accurate ionization potential by using a combination of reduced-scaling, correlated wavefunction theory and density functional theory. First, we identify the most accurate application of reduced-scaling, correlated quantum chemistry methods in gas phase systems where experimental data is available. Next, we tune more efficiently-scaling approximate density functional theory to match such results over both numerous configurations and to reproduce changes in IP of more accurate methods with increasing system size. Finally, we examine the configuration-dependent IP in polymer electrolyte materials and identify the change in IP during ab initio molecular dynamics sampling.

7.2 IP by reduced-scaling correlated wavefucntion theory

The vertical ionization potential (IP) were computed as the difference in the total energies of the netural and cationic molecules,

$$\text{IP} = E_+ - E_0 \quad (7.1)$$

where E_+ and E_0 are the energies of the cationic and neutral states, respectively. The IP may be interpreted as the amount of work to remove an electron. The coupled cluster with single, double excitations and perturbative triples, CCSD(T)⁴³², is the so-called “gold standard” of correlated quantum chemistry, achieving chemical accuracy for most systems of interest. Unfortunately, the computational complexity of conventional CCSD(T) scales as the seventh power of the system size, and the method is therefore only accessible to the small systems. Here, we instead used efficiently reduced-scaling domain based local pair natural orbital coupled cluster, DLPNO-CCSD(T)⁴⁰⁶, method that allows calculations on molecules with hundreds of atoms. However, the various approximations introduced in DLPNO-CCSD(T) method to reach near linear scaling may also introduce inaccuracy in its predicted properties.

We first validate the accuracy of the DLPNO-CCSD(T) method for IP predictions by comparing with more accurate CCSD(T) method and available experimental results for 24 molecules⁴³³ as benchmarks (Figure 7-1). Both DLPNO-CCSD(T) and CCSD(T) calculations are performed with the same basis set, aug-cc-pVDZ. The root mean square error between DLPNO-CCSD(T) and CCSD(T) for the 24 organic molecules is very small, which is only 0.06 eV. The RMSE between DLPNO-CCSD(T) and experimental IP is within acceptable range, 0.27 eV. In addition to the 24 neutral molecules, we also validate DLPNO-CCSD(T) method for 2 anions, bis(trifluoromethane) sulfonamide (TFSI), tetrafluoroborate (BF_4^-), and 2 neutral molecules, dimethoxyethane (glyme), propylene carbonate (PC), which can be used as polymer electrolyte by comparing with more accurate CCSD(T) method (Table 7-1). The RMSE with respect to CCSD(T) is 0.09 eV, and the maximum observed absolute error is 0.16 eV. The benchmarks for 24 organic molecules and molecules for polymer electrolyte validate the accuracy of DLPNO-CCSD(T) method for IP calculations.

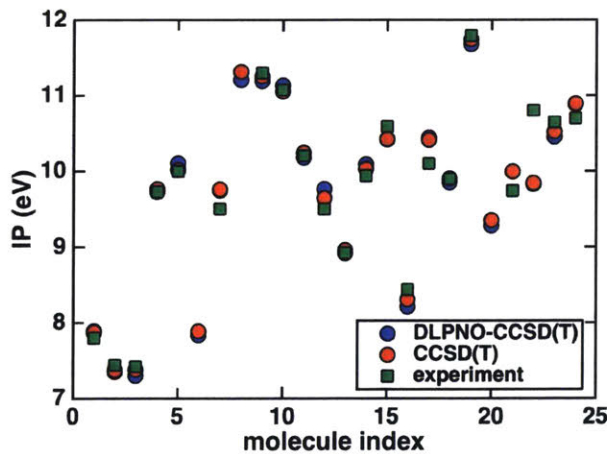


Figure 7-1. Comparison of IP calculated by DLPNO-CCSD(T) method (blue circles), CCSD(T) method (red circles), and experimental values (green squares) for 24 organic molecules.

Table 7-1. Comparison of IP calculated by DLPNO-CCSD(T) method (DLPNO), and CCSD(T) method (CC) for 2 anions and two neutral molecules with up to 4 different configurations.

	TFSI		BF_4^-		glyme		PC	
	DLPNO	CC	DLPNO	CC	DLPNO	CC	DLPNO	CC
1	5.87	5.86	9.73	9.69	8.06	7.90	11.12	11.02
2	5.97	5.94	9.74	9.67	8.25	8.10	10.98	10.88

3	6.23	6.21	9.51	9.50	7.94	7.79	
4			9.65	9.64	7.71	7.60	

7.3 IP tuning in gas phase

We then tune more efficiently-scaling approximate density functional theory to reproduce IP of more accurate DLPNO-CCSD(T) method for both numerous configurations and increasing systems sizes. The DFT exchange correlation functional we used is a long-range corrected hybrid functional, ω PBEh⁹³. Long-range corrected functionals use a standard error function to smoothly separate the Coulomb repulsion term into short-range and long-range contributions, treated by pure GGA and incorporation of HF exact exchange, respectively. The length scale to separate the short range and long range is controlled by the range-separation parameter ω , which we can tune to reproduce DLPNO-CCSD(T) level IP calculations in this work. In order to investigate how ω tuning changes with system size, we built structures of one anion in center and surrounded with different number of neutral species (Figure 7-2). The initial structure of one anion surrounded with 500 neutral species was generated from classical MD simulations, and we extracted our target structures by taking the anion as the center molecule and gradually adding neutral species around the center anion based on their closest distance to the center anion.

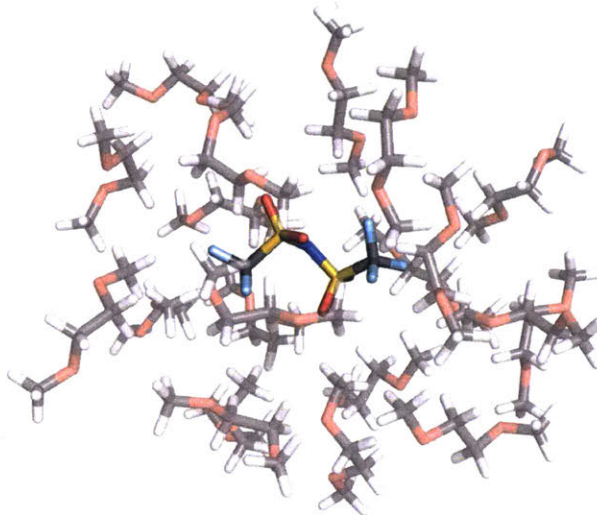


Figure 7-2. Structures of one TFSI anion in center and surrounded with neutral glyme molecules.

The polymer electrolyte materials we studied is bis(trifluoromethane)-sulfonimide (TFSI) anion surrounded by dimethoxyethane (glyme) molecules. The basis set we used for DLPNO-CCSD(T) is aug-cc-pVDZ, while the basis set we used for DFT is 6-31G*. Due to the computation cost, we can calculate IP by DLPNO-CCSD(T) for TFSI with up to 7 glyme molecules. We observed that IP by DLPNO-CCSD(T) increases with number of glyme molecules in the system (Figure 7-3). In DFT calculations with ω PBEh functional, IP shows less size-dependence for small ω values ($0.0 - 0.3 \text{ bohr}^{-1}$), and more size-dependence for large ω values ($0.4 - 0.5 \text{ bohr}^{-1}$), especially when the number of glyme molecules is less than 20. To demonstrate how different range-separation parameters affect the IP error, we computed the RMSE of different ω values with respect to accurate IP by DLPNO-CCSD(T), and $\omega = 0.4 \text{ bohr}^{-1}$ is observed to give the lowest RMSE of 0.32 eV. In addition, we observed that the difference between IP by optimally tuned ω PBEh functional and IP by DLPNO-CCSD(T) keeps constant for different system size.

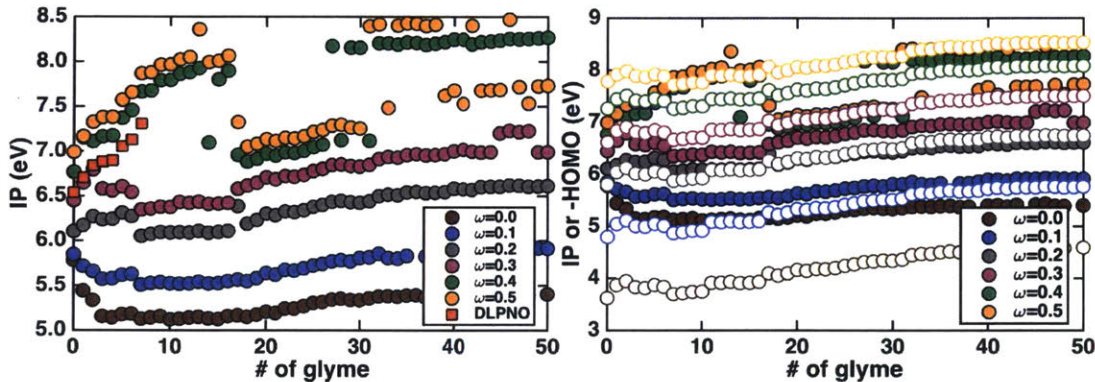


Figure 7-3. (left) Comparison of IP by ω PBEh with different ω values and IP by DLPNO-CCSD(T), and (right) comparison of IP (circles) and $-\text{HOMO}$ (empty circles) by ω PBEh with different ω values for TFSI anion surrounded by different number of glyme molecules in gas phase.

In addition to the optimally tuning ω for accurate IP, we also investigate the optimal ω to enforce Koopmans' theorem (Figure 7-3). When there is no long-range correction ($\omega = 0.0 \text{ bohr}^{-1}$), there is a large difference between IP and $-\text{HOMO}$. When ω reaches 0.2 bohr^{-1} , a good agreement between IP and $-\text{HOMO}$ for different system size is observed, and the mean absolute difference between IP and $-\text{HOMO}$ is 0.10 eV. If ω

keeps increasing to 0.4 or 0.5 bohr⁻¹, difference between IP and -HOMO is large for small systems size and the difference becomes much smaller with increasing system size. We also studied other materials with different neutral species (propylene carbonate) or different anion (tetrafluoroborate). The general tendency keeps the same for different materials.

7.4 IP tuning in polarizable continuum model

In order to study the solvation effect, we examine the IP computation with a polarizable continuum model (PCM). Figure 7-4 shows the comparison of IP and HOMO dependence on number of neutral glyme molecules between in gas phase and in PCM. We used the optimal ω of 0.4 bohr⁻¹ for accurate IP in gas phase and a dielectric constant of 7.2 for glyme. We observed that the variation of both IP and HOMO with different number of glyme vanishes in presence of PCM (Figure 7-4). We then investigate the optimal ω to enforce Koopmans' theorem in PCM (Figure 7-4). We first notice that for all different ω values, both IP and HOMO becomes constant with increasing number of neutral species. The ω PBEh ω value that enforces Koopmans' theorem in presence of dielectric constant is very small due to the good match between -HOMO and IP when there is no long-range correction ($\omega = 0.0$ bohr⁻¹), and the mean absolute difference is 0.07 eV. The difference between -HOMO and IP is dramatically increasing when there is long-range correction. Same results are observed for changing both anions and neutral species.

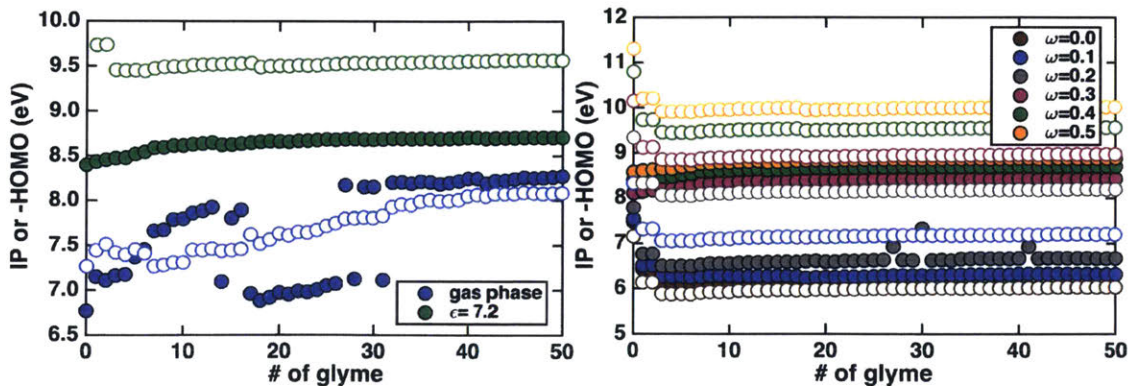


Figure 7-4. (left) Comparison of IP (circles), -HOMO (empty circles) in gas phase (blue) and in PCM (green) by ω PBEh with $\omega = 0.4$ bohr⁻¹, and (right) comparison of IP (circles)

and $-HOMO$ (empty circles) by ω PBEh with different ω values for TFSI anion surrounded by different number of glyme molecules.

In order to perform optimal ω tuning for accurate IP in presence of solvation effect, we also need to quantify the solvation effect in our reference DLPNO-CCSD(T) calculations. Since the open-shell DLPNO-CCSD(T) calculations in PCM is not available in ORCA, we quantify the solvation effect by using MP2 calculations and obtain the difference between MP2 IP in PCM and MP2 IP in gas phase. Therefore, the DLPNO-CCSD(T) IP in PCM is computed as

$$IP_{DLPNO-CCSD(T)}^{PCM} = IP_{DLPNO-CCSD(T)}^{\text{gas phase}} + IP_{MP2}^{PCM} - IP_{MP2}^{\text{gas phase}} \quad (7.2)$$

For TFSI surrounded by different number of glyme molecules, we observed that the optimal ω for accurate IP in PCM is 0.3 bohr^{-1} (RMSE = 0.11 eV), which is smaller than the optimal ω in gas phase (0.4 bohr^{-1}) (Figure 7-5). Similarly to gas phase, the optimal ω for accurate IP is also not size-dependent. In addition to the effect of size on optimal ω , we also studied whether the optimal ω is consistent for different configurations of the system with same size (Figure 7-5). We selected 19 different configurations of TFSI surrounded by 3 glyme molecules, and by comparing with DLPNO-CCSD(T) results, the optimal ω is found to be 0.3 bohr^{-1} with a RMSE of 0.23 eV. Therefore, a single optimal ω in long-range corrected hybrid functional can be used to reproduce accurate IPs from correlated wavfunction theory DLPNO-CCSD(T) for both different systems size and different configurations.

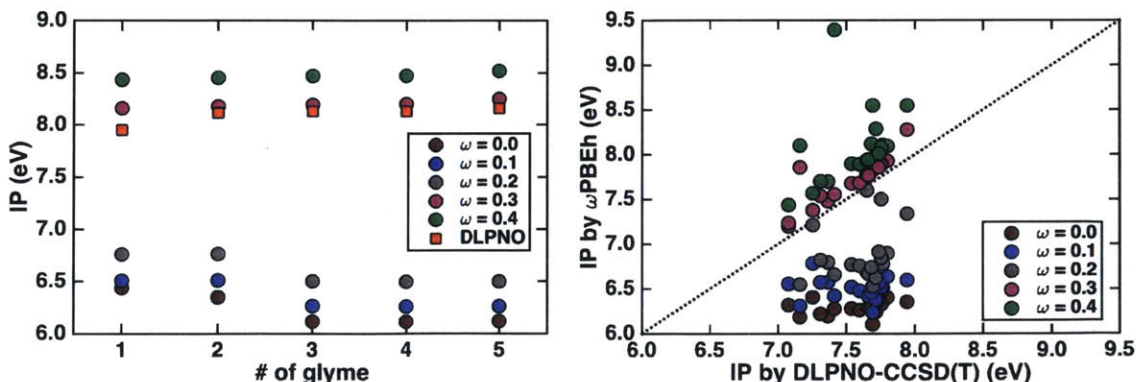


Figure 7-5. Comparison of IP by ω PBEh with different ω values and IP by DLPNO-CCSD(T) for (left) TFSI anion surrounded by different number of glyme molecules, and (right) different configurations of TFSI anion surrounded by 3 glyme molecules in PCM.

7.5 Dynamics of IP sampling

In order to understand the electrochemical stability window of polymer electrolyte, we need to investigate whether there is a large variation in ionization potential dependence on configurations of polymer electrolyte. In order to sample different configurations, we run ab initio molecular dynamics (AIMD) simulations on a widely used polymer electrolyte material, hexafluorophosphate PF_6^- anion covered with glyme molecules (Figure 7-6). We selected this particular system because optimally tuned ωPBEh functional can better enforce Koopmans' theorem (i.e., good correlation between IP and $-\text{HOMO}$), and thus we can use the HOMO printed in AIMD simulations to approximate the changes in IP with configurations. All AIMD simulations were carried out with TeraChem. AIMD simulations were performed with tuned ωPBEh functional with $\omega = 0.3 \text{ bohr}^{-1}$ to reproduce IP from DLPNO-CCSD(T) calculations and the 6-31G* basis set. We employ a 0.5 fs time step and keep a constant temperature of 300 K with a Langevin thermostat. The full trajectory is 20,000 time steps (i.e., 10 ps) in length. We observed a large variation in $-\text{HOMO}$ values, 0.8 eV in the total 10 ps AIMD trajectory (Figure 7-6), indicating a dependence of IP on configurations of polymer electrolyte and providing potential possibilities to alter ionization potential, and thus electrochemical stability window by changing structural properties of polymer electrolytes.

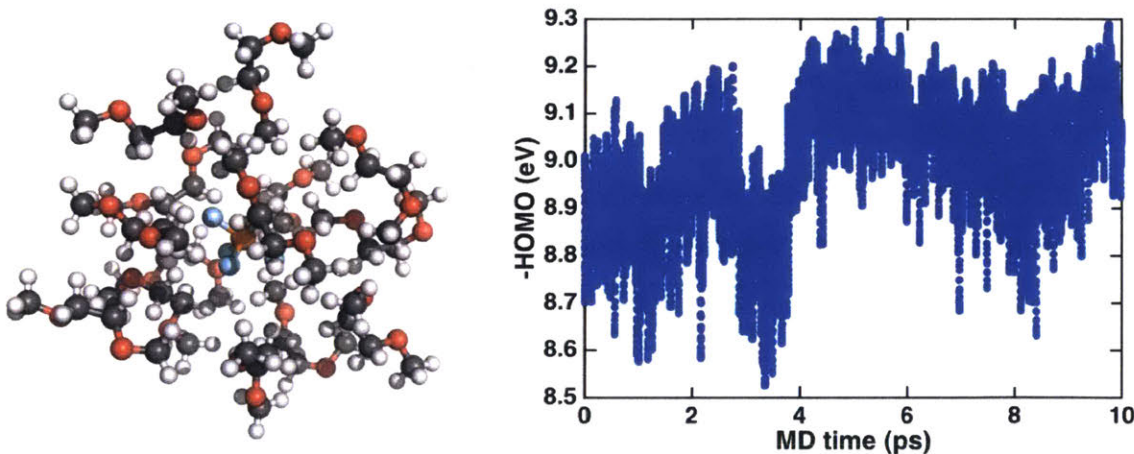


Figure 7-6. (left) Structures of one PF_6^- anion in center and surrounded with 14 neutral glyme molecules. (right) Variations in $-\text{HOMO}$ of PF_6^- anion covered with glyme molecules on different configurations in the 10 ps AIMD sampling.

Interestingly, we observed that there is a good correlation between HOMO of the full configuration, PF_6^- with 14 glyme solvent molecules, and the maximum HOMO of individual 14 glyme solvent molecule at each AIMD snapshot (Figure 7-7). This observation has two significant applications. The first one is that we can alter the ionization potential of a big polymer electrolyte system by tuning the ionization potential of a single polymer molecule, which can potentially have high impact on the development of polymer electrolyte with large electrochemical stability window. The second significance is in theoretically simulations of polymer electrolytes. Instead of simulating a large condensed phase system with many electrons, the system can be broken down to many small molecular systems to highly reduce the computational cost.

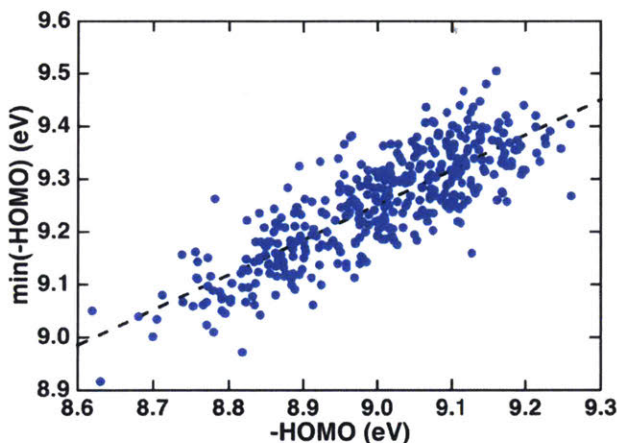


Figure 7-7. Correlation between HOMO of the full configuration, PF_6^- with 14 glyme solvent molecules, and the maximum HOMO of individual 14 glyme solvent molecule at each AIMD snapshot. The AIMD snapshot is selected every 50 time steps (i.e., 25 fs).

This work provides a systematic way to establish multiscale approach to systematically tailor DFT functional choice for challenging condensed phase systems using accurate reference data from higher level correlated wavefunction theory.

Chapter 8 Summary and Outlook

8.1 Summary

Density functional theory provides unique insights into computational materials and catalyst design. In this thesis, we first employed density functional theory to study nanostructured semiconducting materials, where conventional DFT can be expected to perform well. We have established a systematic approach to discover amorphous nanostructures with high-temperature *ab initio* molecular dynamics (AIMD) approach. The sampling approach is robust to initial configuration selection and the generated amorphous structures are even more stable than crystalline structures. This sampling approach can be easily generalized to study amorphous structures of other materials. In addition, we rationalized periodic table dependence in material stability for discovery of low dimensional fullerene materials.

Though DFT performs well in predicting structural and electronic properties of small-sized semiconducting materials, understanding the synthesis process of > nm-scale nanostructures are still very challenging. In this thesis, we bring a surface reactivity perspective to understanding growth processes during material synthesis. We have developed a first-principles-derived model that unifies InP QD formation from isolated precursor and early stage cluster reactions to 1.3-nm magic size clusters, and we rationalize experimentally-observed properties of full sized > 3 nm QDs. Our first-principles study on realistic QD models reveals large surface-dependent reactivity for all elementary growth process steps including In-ligand bond cleavage and P precursor addition. These thermodynamic trends correlate well to kinetic properties at all stages of growth, indicating the presence of labile and stable spots on cluster and QD surfaces. Correlation of electronic or geometric properties to energetics identifies surprising sources for these variations: short In-In separation on the surface produces the most reactive sites, at odds with conventional understanding of strain (i.e., separation) in bulk metallic surfaces increasing reactivity and models for ionic II-VI QD growth. These differences are rationalized by the covalent, directional nature of bonding in III-V QDs and explained by bond order metrics derived directly from the In-O bond density. The unique constraints of carboxylate and P precursor bonding to In atoms rationalizes why all sizes of InP clusters and QDs are In-rich but become less so as QDs mature. These observations support the development of alternate growth recipes that take into account

strong surface-dependence of kinetics as well as the shapes of both In and P precursors to control both kinetics and surface morphology in III-V QDs.

In the solid-state, unique challenges of applying DFT to study transition metal oxides arise from both the strong sensitivities of correlated transition metal oxides on approximations in DFT and the periodic boundary condition. DFT+U and hybrid functionals are two commonly used approaches for approximate delocalization error correction. In the solid-state community, DFT+U is often employed as an efficient alternative to hybrid functionals, owing to the comparable cost of the former to semi-local DFT and the high cost of the latter within periodic, plane wave electronic structure codes. In addition, people tend to assume these two approaches show convergent behavior on solid-state properties. In this thesis, we have observed divergent behavior between DFT+U and hybrid functionals on key nanoscale properties, electron density localization in transition metal oxides. Due to the divergent behavior on density property, it is easily to assume divergent behavior on bulk properties of transition metal oxides. In addition, the divergent behavior of density localization between open-framework solids and extracted transition metal complexes from the solids highlights the limited interchangeability of observed trends between molecular system and periodic system. Following the observations of divergent behavior between DFT+U and hybrids on density properties in solid state, we moved to key observables relevant to heterogeneous catalysis, surface stability through evaluation of surface formation energy and surface reactivity through calculation of adsorption energy. We again observed divergent behavior between DFT+U and hybrids. Incorporating HF exchange can uniformly destabilizes surfaces and destabilizes adsorptions, while incorporating +U can either uniformly destabilizes surfaces or has no effect, and destabilizes adsorptions or has no effect regarding metal atom *d* electron configurations. This work highlights the limited interchangeability of DFT+U and hybrids in the solid-state community.

At the end of this thesis, we introduced a multiscale approach to systematically tailor DFT functional choice for challenging condensed phase systems using accurate reference data from high level correlated wavefunction theory.

8.2 Outlook

Based on the work in this thesis, we propose several future tasks in both theoretical advances and applications. For understanding delocalization error and approximations of DFT in more compelling transition metal oxides, we can compare with embedded correlated wave function scheme⁴³⁴, in which the studied system is broke up into manageable subsystems that may be treated by different computational methods. The most active sites on transition metal oxide surfaces are treated with more accurate correlated wavefunction theory and the remaining atoms in extended surface are treated with more efficient density functional theory. We can better understand the inherent approximations in DFT by comparing and benchmarking with this more accurate embedded correlated wave function theory.

After a better understanding of DFT in the solid-state, we will be more confident to apply DFT to study structure-property relationships of transition metal oxides. We can generalize the approaches we have established to study nanostructured semiconducting materials to study the solid-state. For example, we can generalize the amorphous structure sampling approach to study amorphous transition metal surfaces. In experiment, amorphous materials are frequently prepared or observed and the nature of amorphous structure can make them as more active catalysts in different applications, such as amorphous molybdenum sulfide catalysts for electrochemical hydrogen production⁴³⁵ and amorphous phosphate and cobalt catalysts for water splitting⁴³⁶. However, there is no detailed understanding of correlation between amorphous structure and catalytically active property at atomic level due to the lack of amorphous structure. We can apply high temperature ab initio molecular dynamics to generate amorphous structure and investigate the structure-property relationships.

In addition, the ab initio molecular dynamics simulations can be applied to study other systems, such as to understand surface-liquid interface or study the dynamic process of condense phase system. The systematic approach established in this thesis for understanding synthesis process of semiconducting quantum dots can be generalized to study synthesis of other materials, such as other nanoparticles, including the widely used metal nanoparticles after we have a better understanding of DFT in transition metal-

containing materials. We can use this approach to understand synthesis process of supported catalysts, which requires a demanding synthetic condition.

References

1. Gleiter, H., Nanostructured materials: basic concepts and microstructure. *Acta materialia* **2000**, *48* (1), 1-29.
2. Moriarty, P., Nanostructured materials. *Reports on Progress in Physics* **2001**, *64* (3), 297.
3. Soga, T., *Nanostructured materials for solar energy conversion*. Elsevier: 2006.
4. Goldberg, M.; Langer, R.; Jia, X., Nanostructured materials for applications in drug delivery and tissue engineering. *Journal of Biomaterials Science, Polymer Edition* **2007**, *18* (3), 241-268.
5. Huang, X.-J.; Choi, Y.-K., Chemical sensors based on nanostructured materials. *Sensors and Actuators B: Chemical* **2007**, *122* (2), 659-671.
6. Kuchibhatla, S. V.; Karakoti, A.; Bera, D.; Seal, S., One dimensional nanostructured materials. *Progress in materials science* **2007**, *52* (5), 699-913.
7. Guo, Y. G.; Hu, J. S.; Wan, L. J., Nanostructured materials for electrochemical energy conversion and storage devices. *Advanced Materials* **2008**, *20* (15), 2878-2887.
8. Kim, J.; Piao, Y.; Hyeon, T., Multifunctional nanostructured materials for multimodal imaging, and simultaneous imaging and therapy. *Chem Soc Rev* **2009**, *38* (2), 372-390.
9. Arico, A. S.; Bruce, P.; Scrosati, B.; Tarascon, J.-M.; Van Schalkwijk, W., Nanostructured materials for advanced energy conversion and storage devices. In *Materials For Sustainable Energy: A Collection of Peer-Reviewed Research and Review Articles from Nature Publishing Group*, World Scientific: 2011; pp 148-159.
10. Yu, G.; Xie, X.; Pan, L.; Bao, Z.; Cui, Y., Hybrid nanostructured materials for high-performance electrochemical capacitors. *Nano Energy* **2013**, *2* (2), 213-234.
11. Humplik, T.; Lee, J.; O'hern, S.; Fellman, B.; Baig, M.; Hassan, S.; Atieh, M.; Rahman, F.; Laoui, T.; Karnik, R., Nanostructured materials for water desalination. *Nanotechnology* **2011**, *22* (29), 292001.
12. Han, B. Q.; Lavernia, E. J.; Mohamed, F. A., Mechanical properties of nanostructured materials. *Rev. Adv. Mater. Sci* **2005**, *9* (1), 1-16.
13. Kim, H. S.; Estrin, Y., Phase mixture modeling of the strain rate dependent mechanical behavior of nanostructured materials. *Acta Materialia* **2005**, *53* (3), 765-772.
14. Meyers, M. A.; Mishra, A.; Benson, D. J., Mechanical properties of nanocrystalline materials. *Progress in materials science* **2006**, *51* (4), 427-556.
15. Witkin, D.; Lavernia, E. J., Synthesis and mechanical behavior of nanostructured materials via cryomilling. *Progress in Materials Science* **2006**, *51* (1), 1-60.
16. Minnich, A.; Dresselhaus, M.; Ren, Z.; Chen, G., Bulk nanostructured thermoelectric materials: current research and future prospects. *Energy & Environmental Science* **2009**, *2* (5), 466-479.
17. Zhang, L. L.; Zhao, X., Carbon-based materials as supercapacitor electrodes. *Chem Soc Rev* **2009**, *38* (9), 2520-2531.
18. Szczech, J. R.; Higgins, J. M.; Jin, S., Enhancement of the thermoelectric properties in nanoscale and nanostructured materials. *Journal of Materials Chemistry* **2011**, *21* (12), 4037-4055.
19. Krasheninnikov, A.; Banhart, F., Engineering of nanostructured carbon materials with electron or ion beams. *Nature materials* **2007**, *6* (10), 723.

20. Park, M. S.; Wang, G. X.; Kang, Y. M.; Wexler, D.; Dou, S. X.; Liu, H. K., Preparation and electrochemical properties of SnO₂ nanowires for application in lithium-ion batteries. *Angewandte Chemie International Edition* **2007**, *46* (5), 750-753.
21. Hirst, A. R.; Escuder, B.; Miravet, J. F.; Smith, D. K., High-tech applications of self-assembling supramolecular nanostructured gel-phase materials: from regenerative medicine to electronic devices. *Angewandte Chemie International Edition* **2008**, *47* (42), 8002-8018.
22. Sellmyer, D. J.; Skomski, R., *Advanced magnetic nanostructures*. Springer Science & Business Media: 2006.
23. Tang, B.; Wang, G.; Zhuo, L.; Ge, J.; Cui, L., Facile route to α -FeOOH and α -Fe₂O₃ nanorods and magnetic property of α -Fe₂O₃ nanorods. *Inorganic chemistry* **2006**, *45* (13), 5196-5200.
24. Zhu, Y.; Zhao, W.; Chen, H.; Shi, J., A simple one-pot self-assembly route to nanoporous and monodispersed Fe₃O₄ particles with oriented attachment structure and magnetic property. *The Journal of Physical Chemistry C* **2007**, *111* (14), 5281-5285.
25. Wang, G.; Gao, Z.; Tang, S.; Chen, C.; Duan, F.; Zhao, S.; Lin, S.; Feng, Y.; Zhou, L.; Qin, Y., Microwave absorption properties of carbon nanocoils coated with highly controlled magnetic materials by atomic layer deposition. *ACS nano* **2012**, *6* (12), 11009-11017.
26. Kuwata-Gonokami, M.; Saito, N.; Ino, Y.; Kauranen, M.; Jefimovs, K.; Vallius, T.; Turunen, J.; Svirko, Y., Giant optical activity in quasi-two-dimensional planar nanostructures. *Physical review letters* **2005**, *95* (22), 227401.
27. Jain, P. K.; Huang, X.; El-Sayed, I. H.; El-Sayed, M. A., Noble metals on the nanoscale: optical and photothermal properties and some applications in imaging, sensing, biology, and medicine. *Accounts of chemical research* **2008**, *41* (12), 1578-1586.
28. Liu, L.; Kou, H.-Z.; Mo, W.; Liu, H.; Wang, Y., Surfactant-assisted synthesis of α -Fe₂O₃ nanotubes and nanorods with shape-dependent magnetic properties. *The Journal of Physical Chemistry B* **2006**, *110* (31), 15218-15223.
29. Mao, Y.; Wong, S. S., Size-and shape-dependent transformation of nanosized titanate into analogous anatase titania nanostructures. *Journal of the American Chemical Society* **2006**, *128* (25), 8217-8226.
30. Ray, P. C., Size and shape dependent second order nonlinear optical properties of nanomaterials and their application in biological and chemical sensing. *Chemical reviews* **2010**, *110* (9), 5332-5365.
31. Michalet, X.; Pinaud, F. F.; Bentolila, L. A.; Tsay, J. M.; Doose, S.; Li, J. J.; Sundaresan, G.; Wu, A. M.; Gambhir, S. S.; Weiss, S., Quantum dots for live cells, *in vivo* imaging, and diagnostics. *science* **2005**, *307* (5709), 538-544.
32. Choi, H. S.; Liu, W.; Misra, P.; Tanaka, E.; Zimmer, J. P.; Ipe, B. I.; Bawendi, M. G.; Frangioni, J. V., Renal clearance of quantum dots. *Nature biotechnology* **2007**, *25* (10), 1165.
33. Resch-Genger, U.; Grabolle, M.; Cavaliere-Jaricot, S.; Nitschke, R.; Nann, T., Quantum dots versus organic dyes as fluorescent labels. *Nature methods* **2008**, *5* (9), 763.
34. Parak, W. J.; Gerion, D.; Pellegrino, T.; Zanchet, D.; Michelet, C.; Williams, S. C.; Boudreau, R.; Le Gros, M. A.; Larabell, C. A.; Alivisatos, A. P., Biological applications of colloidal nanocrystals. *Nanotechnology* **2003**, *14* (7), R15.

35. Sun, Q.; Wang, Y. A.; Li, L. S.; Wang, D.; Zhu, T.; Xu, J.; Yang, C.; Li, Y., Bright, multicoloured light-emitting diodes based on quantum dots. *Nature Photonics* **2007**, *1* (12), 717-722.
36. Caruge, J. M.; Halpert, J. E.; Wood, V.; Bulovic, V.; Bawendi, M. G., Colloidal quantum-dot light-emitting diodes with metal-oxide charge transport layers. *Nature Photonics* **2008**, *2* (4), 247-250.
37. Semonin, O. E.; Luther, J. M.; Choi, S.; Chen, H.-Y.; Gao, J.; Nozik, A. J.; Beard, M. C., Peak external photocurrent quantum efficiency exceeding 100% via MEG in a quantum dot solar cell. *Science* **2011**, *334* (6062), 1530-1533.
38. Kamat, P. V., Quantum Dot Solar Cells. Semiconductor Nanocrystals as Light Harvesters. *Journal of Physical Chemistry C* **2008**, *112* (48), 18737-18753.
39. Klimov, V.; Mikhailovsky, A.; Xu, S.; Malko, A.; Hollingsworth, J.; Leatherdale, C.; Eisler, H.-J.; Bawendi, M., Optical gain and stimulated emission in nanocrystal quantum dots. *Science* **2000**, *290* (5490), 314-317.
40. Nanda, J.; Ivanov, S. A.; Achermann, M.; Bezel, I.; Piryatinski, A.; Klimov, V. I., Light amplification in the single-exciton regime using exciton-exciton repulsion in type-II nanocrystal quantum dots. *The Journal of Physical Chemistry C* **2007**, *111* (42), 15382-15390.
41. Selvan, S. T.; Tan, T. T.; Ying, J. Y., Robust, non-cytotoxic, silica-coated CdSe quantum dots with efficient photoluminescence. *Advanced Materials* **2005**, *17* (13), 1620-1625.
42. Cros-Gagneux, A.; Delpech, F.; Nayral, C.; Cornejo, A.; Coppel, Y.; Chaudret, B., Surface chemistry of InP quantum dots: a comprehensive study. *Journal of the American Chemical Society* **2010**, *132* (51), 18147-18157.
43. Yu, P.; Beard, M. C.; Ellingson, R. J.; Ferrere, S.; Curtis, C.; Drexler, J.; Luiszer, F.; Nozik, A. J., Absorption cross-section and related optical properties of colloidal InAs quantum dots. *The Journal of Physical Chemistry B* **2005**, *109* (15), 7084-7087.
44. Moreels, I.; Lambert, K.; De Muynck, D.; Vanhaecke, F.; Poelman, D.; Martins, J. C.; Allan, G.; Hens, Z., Composition and size-dependent extinction coefficient of colloidal PbSe quantum dots. *Chemistry of Materials* **2007**, *19* (25), 6101-6106.
45. Moreels, I.; Lambert, K.; Smeets, D.; De Muynck, D.; Nollet, T.; Martins, J. C.; Vanhaecke, F.; Vantomme, A.; Delerue, C.; Allan, G., Size-dependent optical properties of colloidal PbS quantum dots. *ACS nano* **2009**, *3* (10), 3023-3030.
46. Wang, H.-F.; He, Y.; Ji, T.-R.; Yan, X.-P., Surface molecular imprinting on Mn-doped ZnS quantum dots for room-temperature phosphorescence optosensing of pentachlorophenol in water. *Analytical chemistry* **2009**, *81* (4), 1615-1621.
47. Sheldon, R. A.; Van Bekkum, H., *Fine chemicals through heterogeneous catalysis*. John Wiley & Sons: 2008.
48. Nieuwenhuys, B., Chemistry on single crystal surfaces of Pt and Pd alloys. *Surface Review and Letters* **1996**, *3* (05n06), 1869-1888.
49. Vannice, M., The catalytic synthesis of hydrocarbons from H₂CO mixtures over the Group VIII metals: V. The catalytic behavior of silica-supported metals. *Journal of Catalysis* **1977**, *50* (2), 228-236.
50. Knözinger, H.; Weitkamp, J., *Handbook of heterogeneous catalysis*. Wiley-VCH: 1997; Vol. 1.

51. Topsøe, H.; Boudart, M.; Nørskov, J. K., *Frontiers in catalysis: ammonia synthesis and beyond: Symposium*. Baltzer: 1994.
52. Tan, J. C.; Cheetham, A. K., Mechanical properties of hybrid inorganic–organic framework materials: establishing fundamental structure–property relationships. *Chem Soc Rev* **2011**, *40* (2), 1059–1080.
53. Surnev, S.; Fortunelli, A.; Netzer, F. P., Structure–property relationship and chemical aspects of oxide–metal hybrid nanostructures. *Chemical reviews* **2012**, *113* (6), 4314–4372.
54. Saal, J. E.; Kirklin, S.; Aykol, M.; Meredig, B.; Wolverton, C., Materials design and discovery with high-throughput density functional theory: the open quantum materials database (OQMD). *Jom* **2013**, *65* (11), 1501–1509.
55. Hohenberg, P., P. Hohenberg and W. Kohn, Phys. Rev. 136, B864 (1964). *Phys. Rev.* **1964**, *136*, B864.
56. Kohn, W., W. Kohn and LJ Sham, Phys. Rev. 140, A1133 (1965). *Phys. Rev.* **1965**, *140*, A1133.
57. Senn, H. M.; Thiel, W., QM/MM methods for biomolecular systems. *Angewandte Chemie International Edition* **2009**, *48* (7), 1198–1229.
58. Perdew, J. P.; Burke, K.; Ernzerhof, M., Generalized gradient approximation made simple. *Physical review letters* **1996**, *77* (18), 3865.
59. Becke, A. D., Density-functional thermochemistry. III. The role of exact exchange. *The Journal of Chemical Physics* **1993**, *98* (7), 5648–5652.
60. Burke, K.; Perdew, J. P.; Wang, Y., Derivation of a generalized gradient approximation: The PW91 density functional. In *Electronic Density Functional Theory*, Springer: 1998; pp 81–111.
61. Lee, C.; Yang, W.; Parr, R. G., Development of the Colle-Salvetti correlation-energy formula into a functional of the electron density. *Physical Review B* **1988**, *37* (2), 785–789.
62. Della Sala, F.; Fabiano, E.; Constantin, L. A., Kinetic-energy-density dependent semilocal exchange-correlation functionals. *International Journal of Quantum Chemistry* **2016**, *116* (22), 1641–1694.
63. Ioannidis, E. I.; Kulik, H. J., Ligand-Field-Dependent Behavior of Meta-GGA Exchange in Transition-Metal Complex Spin-State Ordering. *The Journal of Physical Chemistry A* **2017**, *121* (4), 874–884.
64. Kim, M.-C.; Sim, E.; Burke, K., Understanding and Reducing Errors in Density Functional Calculations. *Physical Review Letters* **2013**, *111* (7), 073003.
65. Zheng, X.; Liu, M.; Johnson, E. R.; Contreras-García, J.; Yang, W., Delocalization error of density-functional approximations: A distinct manifestation in hydrogen molecular chains. *The Journal of Chemical Physics* **2012**, *137* (21), 214106.
66. Johnson, E. R.; Otero-de-la-Roza, A.; Dale, S. G., Extreme density-driven delocalization error for a model solvated-electron system. *The Journal of Chemical Physics* **2013**, *139* (18), 184116.
67. Perdew, J. P.; Parr, R. G.; Levy, M.; Balduz, J. L., Density-Functional Theory for Fractional Particle Number: Derivative Discontinuities of the Energy. *Physical Review Letters* **1982**, *49* (23), 1691–1694.

68. Perdew, J. P.; Levy, M., Physical Content of the Exact Kohn-Sham Orbital Energies: Band Gaps and Derivative Discontinuities. *Physical Review Letters* **1983**, *51* (20), 1884-1887.
69. Sham, L. J.; Schlüter, M., Density-Functional Theory of the Energy Gap. *Physical Review Letters* **1983**, *51* (20), 1888-1891.
70. Sagvolden, E.; Perdew, J. P., Discontinuity of the exchange-correlation potential: Support for assumptions used to find it. *Physical Review A* **2008**, *77* (1), 012517.
71. Mori-Sánchez, P.; Cohen, A. J., The derivative discontinuity of the exchange-correlation functional. *Physical Chemistry Chemical Physics* **2014**, *16* (28), 14378-14387.
72. Mori-Sánchez, P.; Cohen, A. J.; Yang, W., Many-electron self-interaction error in approximate density functionals. *The Journal of chemical physics* **2006**, *125* (20), 201102.
73. Vydrov, O. A.; Scuseria, G. E.; Perdew, J. P., Tests of functionals for systems with fractional electron number. *The Journal of Chemical Physics* **2007**, *126* (15), 154109.
74. Ruzsinszky, A.; Perdew, J. P.; Csonka, G. I.; Vydrov, O. A.; Scuseria, G. E., Spurious fractional charge on dissociated atoms: Pervasive and resilient self-interaction error of common density functionals. *The Journal of chemical physics* **2006**, *125* (19), 194112.
75. Ruzsinszky, A.; Perdew, J. P.; Csonka, G. I.; Vydrov, O. A.; Scuseria, G. E., Density functionals that are one- and two- are not always many-electron self-interaction-free, as shown for H₂+, He₂+, LiH+, and Ne₂+. *The Journal of Chemical Physics* **2007**, *126* (10), 104102.
76. Dutoi, A. D.; Head-Gordon, M., Self-interaction error of local density functionals for alkali–halide dissociation. *Chemical Physics Letters* **2006**, *422* (1–3), 230-233.
77. Bally, T.; Sastry, G. N., Incorrect Dissociation Behavior of Radical Ions in Density Functional Calculations. *The Journal of Physical Chemistry A* **1997**, *101* (43), 7923-7925.
78. Zhang, Y.; Yang, W., A challenge for density functionals: Self-interaction error increases for systems with a noninteger number of electrons. *The Journal of Chemical Physics* **1998**, *109* (7), 2604-2608.
79. Johnson, B. G.; Gonzales, C. A.; Gill, P. M. W.; Pople, J. A., A density functional study of the simplest hydrogen abstraction reaction. Effect of self-interaction correction. *Chemical Physics Letters* **1994**, *221* (1), 100-108.
80. Mori-Sánchez, P.; Cohen, A. J.; Yang, W., Localization and Delocalization Errors in Density Functional Theory and Implications for Band-Gap Prediction. *Physical Review Letters* **2008**, *100* (14), 146401.
81. Cohen, A. J.; Mori-Sánchez, P.; Yang, W., Fractional charge perspective on the band gap in density-functional theory. *Physical Review B* **2008**, *77* (11), 115123.
82. Tozer, D. J.; De Proft, F., Computation of the Hardness and the Problem of Negative Electron Affinities in Density Functional Theory. *The Journal of Physical Chemistry A* **2005**, *109* (39), 8923-8929.
83. Teale, A. M.; De Proft, F.; Tozer, D. J., Orbital energies and negative electron affinities from density functional theory: insight from the integer discontinuity. *The Journal of chemical physics* **2008**, *129* (4), 044110.

84. Peach, M. J. G.; Teale, A. M.; Helgaker, T.; Tozer, D. J., Fractional Electron Loss in Approximate DFT and Hartree–Fock Theory. *Journal of Chemical Theory and Computation* **2015**, *11* (11), 5262-5268.
85. Kulik, H. J.; Cococcioni, M.; Scherlis, D. A.; Marzari, N., Density functional theory in transition-metal chemistry: A self-consistent Hubbard U approach. *Physical Review Letters* **2006**, *97* (10), 103001.
86. Ganzenmüller, G.; Berkäine, N.; Fouqueau, A.; Casida, M. E.; Reiher, M., Comparison of density functionals for differences between the high-(T 2 g 5) and low-(A 1 g 1) spin states of iron (II) compounds. IV. Results for the ferrous complexes [Fe (L)(‘NHS 4’)]. *The Journal of chemical physics* **2005**, *122* (23), 234321.
87. Droghetti, A.; Alfè, D.; Sanvito, S., Assessment of density functional theory for iron (II) molecules across the spin-crossover transition. *The Journal of chemical physics* **2012**, *137* (12), 124303.
88. Ioannidis, E. I.; Kulik, H. J., Towards quantifying the role of exact exchange in predictions of transition metal complex properties. *The Journal of chemical physics* **2015**, *143* (3), 034104.
89. Mortensen, S. R.; Kepp, K. P., Spin Propensities of Octahedral Complexes From Density Functional Theory. *The Journal of Physical Chemistry A* **2015**, *119* (17), 4041-4050.
90. Da Silva, J. L.; Ganduglia-Pirovano, M. V.; Sauer, J.; Bayer, V.; Kresse, G., Hybrid functionals applied to rare-earth oxides: The example of ceria. *Physical Review B* **2007**, *75* (4), 045121.
91. Ping, Y.; Galli, G.; Goddard III, W. A., Electronic Structure of IrO₂: The Role of the Metal d Orbitals. *The Journal of Physical Chemistry C* **2015**, *119* (21), 11570-11577.
92. He, J.; Chen, M.-X.; Chen, X.-Q.; Franchini, C., Structural transitions and transport-half-metallic ferromagnetism in LaMnO₃ at elevated pressure. *Physical Review B* **2012**, *85* (19), 195135.
93. Rohrdanz, M. A.; Martins, K. M.; Herbert, J. M., A long-range-corrected density functional that performs well for both ground-state properties and time-dependent density functional theory excitation energies, including charge-transfer excited states. *The Journal of chemical physics* **2009**, *130* (5), 054112.
94. Krukau, A. V.; Vydrov, O. A.; Izmaylov, A. F.; Scuseria, G. E., Influence of the exchange screening parameter on the performance of screened hybrid functionals. *The Journal of chemical physics* **2006**, *125* (22), 224106.
95. Zhao, Q.; Ioannidis, E. I.; Kulik, H. J., Global and local curvature in density functional theory. *The Journal of chemical physics* **2016**, *145* (5), 054109.
96. Pickett, W. E.; Erwin, S. C.; Ethridge, E. C., Reformulation of the LDA+U method for a local-orbital basis. *Physical Review B* **1998**, *58* (3), 1201-1209.
97. Cococcioni, M.; De Gironcoli, S., Linear response approach to the calculation of the effective interaction parameters in the LDA+ U method. *Physical Review B* **2005**, *71* (3), 035105.
98. Stein, T.; Autschbach, J.; Govind, N.; Kronik, L.; Baer, R., Curvature and frontier orbital energies in density functional theory. *The journal of physical chemistry letters* **2012**, *3* (24), 3740-3744.
99. Bader, R. F., *Atoms in molecules*. Wiley Online Library: 1990.

100. Zhao, Q.; Xie, L.; Kulik, H. J., Discovering Amorphous Indium Phosphide Nanostructures with High-Temperature Ab Initio Molecular Dynamics. *Journal of Physical Chemistry C* **2015**, *119*, 23238–23249.
101. Talapin, D. V.; Lee, J.-S.; Kovalenko, M. V.; Shevchenko, E. V., Prospects of colloidal nanocrystals for electronic and optoelectronic applications. *Chemical reviews* **2009**, *110* (1), 389–458.
102. Murray, C. B.; Norris, D. J.; Bawendi, M. G., Synthesis and Characterization of Nearly Monodisperse CdE (E = S, Se, Te) Semiconductor Nanocrystallites. *Journal of the American Chemical Society* **1993**, *115* (19), 8706–8715.
103. Dabbousi, B. O.; RodriguezViejo, J.; Mikulec, F. V.; Heine, J. R.; Mattoussi, H.; Ober, R.; Jensen, K. F.; Bawendi, M. G., (CdSe)ZnS core-shell quantum dots: Synthesis and characterization of a size series of highly luminescent nanocrystallites. *J Phys Chem B* **1997**, *101* (46), 9463–9475.
104. Kirchner, C.; Liedl, T.; Kudera, S.; Pellegrino, T.; Muñoz Javier, A.; Gaub, H. E.; Stölzle, S.; Fertig, N.; Parak, W. J., Cytotoxicity of colloidal CdSe and CdSe/ZnS nanoparticles. *Nano letters* **2005**, *5* (2), 331–338.
105. Yang, X.; Zhao, D.; Leck, K. S.; Tan, S. T.; Tang, Y. X.; Zhao, J.; Demir, H. V.; Sun, X. W., Full Visible Range Covering InP/ZnS Nanocrystals with High Photometric Performance and Their Application to White Quantum Dot Light-Emitting Diodes. *Advanced Materials* **2012**, *24* (30), 4180–4185.
106. Adam, S.; Talapin, D. V.; Borchert, H.; Lobo, A.; McGinley, C.; de Castro, A. R. B.; Haase, M.; Weller, H.; Moller, T., The effect of nanocrystal surface structure on the luminescence properties: Photoemission study of HF-etched InP nanocrystals. *J Chem Phys* **2005**, *123* (8), 084706.
107. Allen, P. M.; Walker, B. J.; Bawendi, M. G., Mechanistic insights into the formation of InP quantum dots. *Angewandte Chemie International Edition* **2010**, *49* (4), 760–762.
108. Gary, D. C.; Terban, M. W.; Billinge, S. J.; Cossairt, B. M., Two-Step Nucleation and Growth of InP Quantum Dots via Magic-Sized Cluster Intermediates. *Chemistry of Materials* **2015**, *27* (4), 1432–1441.
109. Xie, R.; Li, Z.; Peng, X., Nucleation kinetics vs chemical kinetics in the initial formation of semiconductor nanocrystals. *Journal of the American Chemical Society* **2009**, *131* (42), 15457–15466.
110. Karanth, D.; Fu, H., Polarization ratio and effective mass in InP nanowires: Effect of crystallographic axis. *Physical Review B* **2006**, *74* (15), 155312.
111. Schmidt, T., Hydrogen and oxygen on InP nanowire surfaces. *Applied physics letters* **2006**, *89* (12), 123117.
112. Li, D.; Wang, Z.; Gao, F., First-principles study of the electronic properties of wurtzite, zinc-blende, and twinned InP nanowires. *Nanotechnology* **2010**, *21* (50), 505709.
113. Chandiramouli, R., Band structure and transport studies on InP nanotube—A first-principles investigation. *Superlattices and Microstructures* **2015**, *83*, 193–209.
114. Dos Santos, C. L.; Piquini, P., Diameter dependence of mechanical, electronic, and structural properties of InAs and InP nanowires: A first-principles study. *Physical Review B* **2010**, *81* (7), 075408.

115. Shu, H.; Chen, X.; Zhou, X.; Lu, W., Spatial confinement of carriers and tunable band structures in InAs/InP-core–shell nanowires. *Chemical Physics Letters* **2010**, *495* (4), 261-265.
116. Wood, B. C.; Ogitsu, T.; Schwegler, E., Local structural models of complex oxygen-and hydroxyl-rich GaP/InP (001) surfaces. *The Journal of chemical physics* **2012**, *136* (6), 064705.
117. Wood, B. C.; Schwegler, E.; Choi, W. I.; Ogitsu, T., Hydrogen-Bond Dynamics of Water at the Interface with InP/GaP (001) and the Implications for Photoelectrochemistry. *Journal of the American Chemical Society* **2013**, *135* (42), 15774-15783.
118. Wood, B. C.; Schwegler, E.; Choi, W. I.; Ogitsu, T., Surface Chemistry of GaP (001) and InP (001) in Contact with Water. *The Journal of Physical Chemistry C* **2014**, *118* (2), 1062-1070.
119. Roy, S.; Springborg, M., Theoretical study of structural and electronic properties of naked stoichiometric and nonstoichiometric indium phosphide clusters. *The Journal of Physical Chemistry B* **2003**, *107* (12), 2771-2779.
120. Roy, S.; Springborg, M., Theoretical investigation of the influence of ligands on structural and electronic properties of indium phosphide clusters. *The Journal of Physical Chemistry A* **2005**, *109* (7), 1324-1329.
121. Cho, E.; Jang, H.; Lee, J.; Jang, E., Modeling on the size dependent properties of InP quantum dots: a hybrid functional study. *Nanotechnology* **2013**, *24* (21), 215201.
122. Abueela, A. M.; Mohamed, T. A.; Prezhdo, O. V., DFT simulation and vibrational analysis of the IR and Raman spectra of a CdSe quantum dot capped by methylamine and trimethylphosphine oxide ligands. *The Journal of Physical Chemistry C* **2012**, *116* (27), 14674-14681.
123. Isborn, C. M.; Kilina, S. V.; Li, X.; Prezhdo, O. V., Generation of multiple excitons in PbSe and CdSe quantum dots by direct photoexcitation: first-principles calculations on small PbSe and CdSe clusters. *The Journal of Physical Chemistry C* **2008**, *112* (47), 18291-18294.
124. Kilina, S. V.; Kilin, D. S.; Prezhdo, O. V., Breaking the phonon bottleneck in PbSe and CdSe quantum dots: Time-domain density functional theory of charge carrier relaxation. *Acs Nano* **2008**, *3* (1), 93-99.
125. Kim, D.; Kim, D.-H.; Lee, J.-H.; Grossman, J. C., Impact of Stoichiometry on the Electronic Structure of PbS Quantum Dots. *Physical review letters* **2013**, *110* (19), 196802.
126. Woodley, S. M.; Catlow, R., Crystal structure prediction from first principles. *Nature materials* **2008**, *7* (12), 937-946.
127. Zhai, H.; Ha, M.-A.; Alexandrova, A. N., AFFCK: Adaptive Force Field-Assisted ab initio Coalescence Kick Method for Global Minimum Search. *Journal of Chemical Theory and Computation* **2015**.
128. Shen, D.; Kong, C.; Jia, R.; Fu, P.; Zhang, H.-X., Investigate the properties of Mg_n clusters and their hydrogen-storage mechanism: a study based on DFT and a global minimum optimization method. *The Journal of Physical Chemistry A* **2015**.
129. Muz, İ.; Canko, O.; Atış, M.; Kamil Yıldırım, E., Search for the global minimum structures of AlB₃H_{2n} (n= 0–6) clusters. *Journal of computational chemistry* **2014**.

130. Tai, T. B.; Nguyen, M. T., A Stochastic Search for the Structures of Small Germanium Clusters and Their Anions: Enhanced Stability by Spherical Aromaticity of the Ge₁₀ and Ge₁₂₂₋ Systems. *Journal of Chemical Theory and Computation* **2011**, *7* (4), 1119-1130.
131. Assadollahzadeh, B.; Schwerdtfeger, P., A systematic search for minimum structures of small gold clusters Au_n (n= 2–20) and their electronic properties. *The Journal of chemical physics* **2009**, *131* (6), 064306.
132. Rapallo, A.; Rossi, G.; Ferrando, R.; Fortunelli, A.; Curley, B. C.; Lloyd, L. D.; Tarbuck, G. M.; Johnston, R. L., Global optimization of bimetallic cluster structures. I. Size-mismatched Ag–Cu, Ag–Ni, and Au–Cu systems. *The Journal of chemical physics* **2005**, *122* (19), 194308.
133. Johnston, R. L., Evolving better nanoparticles: Genetic algorithms for optimising cluster geometries. *Dalton Transactions* **2003**, (22), 4193-4207.
134. Goedecker, S.; Hellmann, W.; Lenosky, T., Global minimum determination of the Born-Oppenheimer surface within density functional theory. *Physical review letters* **2005**, *95* (5), 055501.
135. Pietrucci, F.; Andreoni, W., Graph theory meets ab initio molecular dynamics: atomic structures and transformations at the nanoscale. *Physical review letters* **2011**, *107* (8), 085504.
136. Kim, H. G.; Choi, S. K.; Lee, H. M., New algorithm in the basin hopping Monte Carlo to find the global minimum structure of unary and binary metallic nanoclusters. *The Journal of chemical physics* **2008**, *128* (14), 144702-144702.
137. Borbón-González, D. J.; Fortunelli, A.; Barcaro, G.; Sementa, L.; Johnston, R. L.; Posada-Amarillas, A., Global Minimum Pt₁₃M₂₀ (M= Ag, Au, Cu, Pd) Dodecahedral Core–Shell Clusters. *The Journal of Physical Chemistry A* **2013**, *117* (51), 14261-14266.
138. Andreeva, N. A.; Chaban, V. V., Global Minimum Search via Annealing. Nanoscale Gold Clusters. *Chemical Physics Letters* **2015**.
139. Hamad, S.; Catlow, C. R. A.; Spano, E.; Matxain, J. M.; Ugalde, J. M., Structure and properties of ZnS nanoclusters. *The Journal of Physical Chemistry B* **2005**, *109* (7), 2703-2709.
140. Chuvilin, A.; Kaiser, U.; Bichoutskaia, E.; Besley, N. A.; Khlobystov, A. N., Direct transformation of graphene to fullerene. *Nature chemistry* **2010**, *2* (6), 450-453.
141. Kästner, J.; Carr, J. M.; Keal, T. W.; Thiel, W.; Wander, A.; Sherwood, P., DL-FIND: An Open-Source Geometry Optimizer for Atomistic Simulations. *The Journal of Physical Chemistry A* **2009**, *113* (43), 11856-11865.
142. Petachem. <http://www.petachem.com>. (accessed Sep 24, 2018).
143. Ufimtsev, I. S.; Martinez, T. J., Quantum chemistry on graphical processing units. 3. Analytical energy gradients, geometry optimization, and first principles molecular dynamics. *Journal of Chemical Theory and Computation* **2009**, *5* (10), 2619-2628.
144. Binkley, J. S.; Pople, J. A.; Hehre, W. J., Self-Consistent Molecular-Orbital Methods .21. Small Split-Valence Basis-Sets for 1st-Row Elements. *Journal of the American Chemical Society* **1980**, *102* (3), 939-947.
145. Stephens, P. J.; Devlin, F. J.; Chabalowski, C. F.; Frisch, M. J., Ab Initio Calculation of Vibrational Absorption and Circular Dichroism Spectra Using Density Functional Force Fields. *The Journal of Physical Chemistry* **1994**, *98* (45), 11623-11627.

146. Vosko, S. H.; Wilk, L.; Nusair, M., Accurate spin-dependent electron liquid correlation energies for local spin density calculations: a critical analysis. *Canadian Journal of Physics* **1980**, *58* (8), 1200-1211.
147. Indium phosphide (InP) lattice parameters, thermal expansion. In *Group IV Elements, IV-IV and III-V Compounds. Part a - Lattice Properties*, Madelung, O.; Rössler, U.; Schulz, M., Eds. Springer Berlin Heidelberg: 2001; Vol. 41A1a, pp 1-9.
148. Gražulis, S.; Daškevič, A.; Merkys, A.; Chateigner, D.; Lutterotti, L.; Quirós, M.; Serebryanaya, N. R.; Moeck, P.; Downs, R. T.; Le Bail, A., Crystallography Open Database (COD): an open-access collection of crystal structures and platform for worldwide collaboration. *Nucleic acids research* **2012**, *40* (D1), D420-D427.
149. Hanwell, M. D.; Curtis, D. E.; Lonie, D. C.; Vandermeersch, T.; Zurek, E.; Hutchison, G. R., Avogadro: An advanced semantic chemical editor, visualization, and analysis platform. *J. Cheminformatics* **2012**, *4* (1), 17.
150. Pyykkö, P.; Atsumi, M., Molecular Single-Bond Covalent Radii for Elements 1–118. *Chemistry – A European Journal* **2009**, *15* (1), 186-197.
151. NBO6.0., E. D. Glendening, J. K. Badenhoop, A. E. Reed, J. E. Carpenter, J. A. Bohmann, C. M. Morales, C. R. Landis, and F. Weinhold, Theoretical Chemistry Institute, University of Wisconsin, Madison. 2013.
152. *The Merck Index - An Encyclopedia of Chemicals, Drugs, and Biologicals*. The Royal Society of Chemistry: 2013.
153. Harmony, M. D.; Laurie, V. W.; Kuczkowski, R. L.; Schwendeman, R.; Ramsay, D.; Lovas, F. J.; Lafferty, W. J.; Maki, A. G., Molecular structures of gas-phase polyatomic molecules determined by spectroscopic methods. *Journal of Physical and Chemical Reference Data* **1979**, *8* (3), 619-722.
154. Glover, C. J.; Ridgway, M. C.; Yu, K. M.; Foran, G. J.; Lee, T. W.; Moon, Y.; Yoon, E., Structural characterization of amorphized InP: Evidence for chemical disorder. *Applied Physics Letters* **1999**, *74* (12), 1713-1715.
155. Tavakoli, A. H.; Maram, P. S.; Widgeon, S. J.; Rufner, J.; van Benthem, K.; Ushakov, S.; Sen, S.; Navrotsky, A., Amorphous Alumina Nanoparticles: Structure, Surface Energy, and Thermodynamic Phase Stability. *The Journal of Physical Chemistry C* **2013**, *117* (33), 17123-17130.
156. Amstad, E.; Gopinadhan, M.; Holtze, C.; Osuji, C. O.; Brenner, M. P.; Spaepen, F.; Weitz, D. A., Production of amorphous nanoparticles by supersonic spray-drying with a microfluidic nebulator. *Science* **2015**, *349* (6251), 956-960.
157. Carenco, S.; Portehault, D.; Boissière, C.; Mézailles, N.; Sanchez, C., Nanoscaled Metal Borides and Phosphides: Recent Developments and Perspectives. *Chemical Reviews* **2013**, *113* (10), 7981-8065.
158. Zhao, Q.; Ng, S. S.; Kulik, H. J., Predicting the Stability of Fullerene Allotropes Throughout the Periodic Table. *The Journal of Physical Chemistry C* **2016**, *120* (30), 17035-17045.
159. Kroto, H. W.; Heath, J. R.; O'Brien, S. C.; Curl, R. F.; Smalley, R. E., C 60: buckminsterfullerene. *Nature* **1985**, *318* (6042), 162-163.
160. Hirsch, A., The era of carbon allotropes. *Nature materials* **2010**, *9* (11), 868-871.
161. Campoy-Quiles, M.; Ferenczi, T.; Agostinelli, T.; Etchegoin, P. G.; Kim, Y.; Anthopoulos, T. D.; Stavrinou, P. N.; Bradley, D. D.; Nelson, J., Morphology evolution

- via self-organization and lateral and vertical diffusion in polymer: fullerene solar cell blends. *Nature materials* **2008**, *7* (2), 158-164.
162. Vandewal, K.; Tvingstedt, K.; Gadisa, A.; Inganäs, O.; Manca, J. V., On the origin of the open-circuit voltage of polymer–fullerene solar cells. *Nature materials* **2009**, *8* (11), 904-909.
163. Price, S. C.; Stuart, A. C.; Yang, L.; Zhou, H.; You, W., Fluorine substituted conjugated polymer of medium band gap yields 7% efficiency in polymer–fullerene solar cells. *Journal of the American Chemical Society* **2011**, *133* (12), 4625-4631.
164. Scharber, M. C., On the Efficiency Limit of Conjugated Polymer: Fullerene-Based Bulk Heterojunction Solar Cells. *Advanced Materials* **2016**, *28*, 1994-2001.
165. Zakharian, T. Y.; Seryshev, A.; Sitharaman, B.; Gilbert, B. E.; Knight, V.; Wilson, L. J., A fullerene-paclitaxel chemotherapeutic: synthesis, characterization, and study of biological activity in tissue culture. *Journal of the American Chemical Society* **2005**, *127* (36), 12508-12509.
166. Shi, J.; Zhang, H.; Wang, L.; Li, L.; Wang, H.; Wang, Z.; Li, Z.; Chen, C.; Hou, L.; Zhang, C., PEI-derivatized fullerene drug delivery using folate as a homing device targeting to tumor. *Biomaterials* **2013**, *34* (1), 251-261.
167. Yoon, M.; Yang, S.; Hicke, C.; Wang, E.; Geohegan, D.; Zhang, Z., Calcium as the superior coating metal in functionalization of carbon fullerenes for high-capacity hydrogen storage. *Physical review letters* **2008**, *100* (20), 206806.
168. Aoyagi, S.; Nishibori, E.; Sawa, H.; Sugimoto, K.; Takata, M.; Miyata, Y.; Kitaura, R.; Shinohara, H.; Okada, H.; Sakai, T., A layered ionic crystal of polar Li@C₆₀ superatoms. *Nature chemistry* **2010**, *2* (8), 678-683.
169. Golberg, D.; Bando, Y.; Stephan, O.; Kurashima, K., Octahedral boron nitride fullerenes formed by electron beam irradiation. *Applied physics letters* **1998**, *73*, 2441.
170. Oku, T.; Nishiwaki, A.; Narita, I., Formation and atomic structures of B_nN_n (n=24–60) clusters studied by mass spectrometry, high-resolution electron microscopy and molecular orbital calculations. *Physica B: Condensed Matter* **2004**, *351* (1), 184-190.
171. Oku, T.; Nishiwaki, A.; Narita, I.; Gonda, M., Formation and structure of B₂₄N₂₄ clusters. *Chemical physics letters* **2003**, *380* (5), 620-623.
172. Oku, T.; Nishiwaki, A.; Narita, I., Formation and atomic structure of B₁₂N₁₂ nanocage clusters studied by mass spectrometry and cluster calculation. *Science and Technology of Advanced Materials* **2004**, *5* (5), 635-638.
173. Oku, T.; Kuno, M.; Narita, I., High-resolution electron microscopy and electronic structures of endohedral La@B₃₆N₃₆ clusters. *Diamond and related materials* **2002**, *11* (3), 940-944.
174. Oku, T.; Narita, I.; Nishiwaki, A., Formation and structures of B₃₆N₃₆ and Y@B₃₆N₃₆ clusters studied by high-resolution electron microscopy and mass spectrometry. *Journal of Physics and Chemistry of Solids* **2004**, *65* (2), 369-372.
175. Ogitsu, T.; Schwegler, E.; Galli, G., β-Rhombohedral Boron: At the Crossroads of the Chemistry of Boron and the Physics of Frustration. *Chemical reviews* **2013**, *113* (5), 3425-3449.
176. White, M. A.; Cerqueira, A. B.; Whitman, C. A.; Johnson, M. B.; Ogitsu, T., Determination of phase stability of elemental boron. *Angewandte Chemie* **2015**, *127* (12), 3697-3700.

177. Zhai, H.-J.; Zhao, Y.-F.; Li, W.-L.; Chen, Q.; Bai, H.; Hu, H.-S.; Piazza, Z. A.; Tian, W.-J.; Lu, H.-G.; Wu, Y.-B., Observation of an all-boron fullerene. *Nature chemistry* **2014**, *6* (8), 727-731.
178. Etzkorn, J.; Therese, H. A.; Rocker, F.; Zink, N.; Kolb, U.; Tremel, W., Metal-Organic Chemical Vapor Deposition Synthesis of Hollow Inorganic-Fullerene-Type MoS₂ and MoSe₂ Nanoparticles. *Advanced materials* **2005**, *17* (19), 2372-2375.
179. Sadan, M. B.; Houben, L.; Enyashin, A. N.; Seifert, G.; Tenne, R., Atom by atom: HRTEM insights into inorganic nanotubes and fullerene-like structures. *Proceedings of the National Academy of Sciences* **2008**, *105* (41), 15643-15648.
180. Albu-Yaron, A.; Levy, M.; Tenne, R.; Popovitz-Biro, R.; Weidenbach, M.; Bar-Sadan, M.; Houben, L.; Enyashin, A. N.; Seifert, G.; Feuermann, D., MoS₂ Hybrid Nanostructures: From Octahedral to Quasi-Spherical Shells within Individual Nanoparticles. *Angewandte Chemie International Edition* **2011**, *50* (8), 1810-1814.
181. Wu, H.; Yang, R.; Song, B.; Han, Q.; Li, J.; Zhang, Y.; Fang, Y.; Tenne, R.; Wang, C., Biocompatible inorganic fullerene-like molybdenum disulfide nanoparticles produced by pulsed laser ablation in water. *ACS nano* **2011**, *5* (2), 1276-1281.
182. Moon, W. H.; Son, M. S.; Hwang, H. J., Theoretical study on structure of boron nitride fullerenes. *Applied surface science* **2007**, *253* (17), 7078-7081.
183. Wu, H.-S.; Xu, X.-H.; Strout, D. L.; Jiao, H., The structure and stability of B₃₆N₃₆ cages: a computational study. *Journal of molecular modeling* **2005**, *12* (1), 1-8.
184. Barone, V.; Koller, A.; Scuseria, G. E., Theoretical nitrogen NMR chemical shifts in octahedral boron nitride cages. *The Journal of Physical Chemistry A* **2006**, *110* (37), 10844-10847.
185. Batista, R. J.; Mazzoni, M. S.; Chacham, H., A theoretical study of the stability trends of boron nitride fullerenes. *Chemical physics letters* **2006**, *421* (1), 246-250.
186. Wu, H.-S.; Cui, X.-Y.; Qin, X.-F.; Strout, D. L.; Jiao, H., Boron nitride cages from B₁₂N₁₂ to B₃₆N₃₆: square-hexagon alternants vs boron nitride tubes. *Journal of molecular modeling* **2006**, *12* (5), 537-542.
187. Batista, R. J.; Mazzoni, M. S.; Chacham, H., Boron nitride fullerene B 36 N 36 doped with transition metal atoms: First-principles calculations. *Physical Review B* **2007**, *75* (3), 035417.
188. Koponen, L.; Tunturivuori, L.; Puska, M. J.; Nieminen, R. M., Photoabsorption spectra of boron nitride fullerene-like structures. *The Journal of chemical physics* **2007**, *126* (21), 214306.
189. Matxain, J. M.; Eriksson, L. A.; Mercero, J. M.; Lopez, X.; Piris, M.; Ugalde, J. M.; Poater, J.; Matito, E.; Solá, M., New solids based on B₁₂N₁₂ fullerenes. *The Journal of Physical Chemistry C* **2007**, *111* (36), 13354-13360.
190. Karttunen, A. J.; Linnolahti, M.; Pakkanen, T. A., Structural Characteristics of Perhydrogenated Boron Nitride Fullerenes. *The Journal of Physical Chemistry C* **2008**, *112* (27), 10032-10037.
191. Beheshtian, J.; Bagheri, Z.; Kamfiroozi, M.; Ahmadi, A., A comparative study on the B₁₂N₁₂, Al₁₂N₁₂, B₁₂P₁₂ and Al₁₂P₁₂ fullerene-like cages. *Journal of molecular modeling* **2012**, *18* (6), 2653-2658.
192. Pokropivny, V.; Ovsyannikova, L., Electronic structure and the infrared absorption and Raman spectra of the semiconductor clusters C₂₄, B₁₂N₁₂, Si₁₂C₁₂, Zn₁₂O₁₂, and Ga₁₂N₁₂. *Physics of the Solid State* **2007**, *49* (3), 562-570.

193. Zope, R. R.; Dunlap, B. I., Electronic structure of fullerenelike cages and finite nanotubes of aluminum nitride. *Physical Review B* **2005**, *72* (4), 045439.
194. Wang, B.; Wang, X.; Chen, G.; Nagase, S.; Zhao, J., Cage and tube structures of medium-sized zinc oxide clusters (ZnO_n ($n=24, 28, 36$, and 48)). *The Journal of chemical physics* **2008**, *128* (14), 144710.
195. Yong, Y.; Li, X.; Hao, X.; Cao, J.; Li, T., Theoretical prediction of low-density nanoporous frameworks of zinc sulfide based on Zn_nS_n ($n=12, 16$) nanocaged clusters. *RSC Advances* **2014**, *4* (70), 37333-37341.
196. Niu, M.; Yu, G.; Yang, G.; Chen, W.; Zhao, X.; Huang, X., Doping the Alkali Atom: An Effective Strategy to Improve the Electronic and Nonlinear Optical Properties of the Inorganic $Al_{12}N_{12}$ Nanocage. *Inorganic chemistry* **2013**, *53* (1), 349-358.
197. Shakerzadeh, E.; Barazesh, N.; Talebi, S. Z., A comparative theoretical study on the structural, electronic and nonlinear optical features of $B_{12}N_{12}$ and $Al_{12}N_{12}$ nanoclusters with the groups III, IV and V dopants. *Superlattices and Microstructures* **2014**, *76*, 264-276.
198. Rad, A. S.; Ayub, K., Ni adsorption on $Al_{12}P_{12}$ nano-cage: A DFT study. *Journal of Alloys and Compounds* **2016**, *678*, 317-324.
199. Lu, P.; Wu, C.; Li, Y.; Yu, Z.; Cao, H.; Wang, S., Investigation on structural, electronic, and magnetic properties of Mn-doped $Ga_{12}N_{12}$ clusters. *Journal of Materials Science* **2013**, *48* (24), 8552-8558.
200. Peyghan, A. A.; Pashangpour, M.; Bagheri, Z.; Kamfiroozi, M., Energetic, structural, and electronic properties of hydrogenated $Al_{12}P_{12}$ nanocluster. *Physica E: Low-dimensional Systems and Nanostructures* **2012**, *44* (7), 1436-1440.
201. Beheshtian, J.; Kamfiroozi, M.; Bagheri, Z.; Ahmadi, A., Theoretical study of hydrogen adsorption on the $B_{12}P_{12}$ fullerene-like nanocluster. *Computational Materials Science* **2012**, *54*, 115-118.
202. Yong, Y.; Song, B.; He, P., Cluster-assembled materials based on $M_{12}N_{12}$ ($M=Al, Ga$) fullerene-like clusters. *Physical Chemistry Chemical Physics* **2011**, *13* (36), 16182-16189.
203. Yong, Y.; Song, B.; He, P., Growth pattern and electronic properties of cluster-assembled material based on $Zn_{12}O_{12}$: A density-functional study. *The Journal of Physical Chemistry C* **2011**, *115* (14), 6455-6461.
204. Ghosh, S.; Sanyal, B.; Das, G., Structural, electronic and magnetic properties of Cr-doped $Cd_{12}S_{12}$ clusters: A density functional investigation. *Journal of Magnetism and Magnetic Materials* **2010**, *322* (6), 734-742.
205. Küskü, S. İ.; Berber, S., Stability of $Ga_xAs_{x\pm4}$ gallium arsenide fullerenes. *Physical Review B* **2009**, *79* (24), 245420.
206. Karamanis, P.; Pouchan, C., On the shape dependence of cluster (hyper) polarizabilities. A combined ab initio and DFT study on large fullerene-like gallium arsenide semiconductor clusters. *International Journal of Quantum Chemistry* **2011**, *111* (4), 788-796.
207. Szwacki, N. G.; Sadrzadeh, A.; Yakobson, B. I., B_{80} fullerene: an ab initio prediction of geometry, stability, and electronic structure. *Physical review letters* **2007**, *98* (16), 166804.

208. De, S.; Willand, A.; Amsler, M.; Pochet, P.; Genovese, L.; Goedecker, S., Energy landscape of fullerene materials: a comparison of boron to boron nitride and carbon. *Physical review letters* **2011**, *106* (22), 225502.
209. Beheshtian, J.; Kamfiroozi, M.; Bagheri, Z.; Peyghan, A. A., B₁₂N₁₂ nano-cage as potential sensor for NO₂ detection. *Chinese Journal of Chemical Physics* **2012**, *25* (1), 60-64.
210. Beheshtian, J.; Bagheri, Z.; Kamfiroozi, M.; Ahmadi, A., Toxic CO detection by B₁₂N₁₂ nanocluster. *Microelectronics Journal* **2011**, *42* (12), 1400-1403.
211. Hadipour, N. L.; Ahmadi Peyghan, A.; Soleymanabadi, H., Theoretical Study on the Al-Doped ZnO Nanoclusters for CO Chemical Sensors. *The Journal of Physical Chemistry C* **2015**, *119* (11), 6398-6404.
212. Baei, M. T.; Tabar, M. B.; Hashemian, S., Zn₁₂O₁₂ Fullerene-like Cage as a Potential Sensor for SO₂ Detection. *Adsorption Science & Technology* **2013**, *31* (5), 469-476.
213. Ghenaatian, H.; Baei, M. T.; Hashemian, S., Zn₁₂O₁₂ nano-cage as a promising adsorbent for CS₂ capture. *Superlattices and Microstructures* **2013**, *58*, 198-204.
214. Ganji, M.; Yazdani, H.; Mirnejad, A., B₃₆N₃₆ Fullerene-like nanocages: a novel material for drug delivery. *Physica E: Low-dimensional Systems and Nanostructures* **2010**, *42* (9), 2184-2189.
215. Li, M.; Li, Y.; Zhou, Z.; Shen, P.; Chen, Z., Ca-coated boron fullerenes and nanotubes as superior hydrogen storage materials. *Nano letters* **2009**, *9* (5), 1944-1948.
216. Venkataraman, N. S.; Belosludov, R. V.; Note, R.; Sahara, R.; Mizuseki, H.; Kawazoe, Y., Theoretical investigation on the alkali-metal doped BN fullerene as a material for hydrogen storage. *Chemical Physics* **2010**, *377* (1), 54-59.
217. Wu, H.; Fan, X.; Kuo, J.-L., Metal free hydrogenation reaction on carbon doped boron nitride fullerene: A DFT study on the kinetic issue. *international journal of hydrogen energy* **2012**, *37* (19), 14336-14342.
218. Wang, G.; Yuan, H.; Kuang, A.; Hu, W.; Zhang, G.; Chen, H., High-capacity hydrogen storage in Li-decorated (AlN)_n (n= 12, 24, 36) nanocages. *International Journal of Hydrogen Energy* **2014**, *39* (8), 3780-3789.
219. Zhang, Y.; Zheng, X.; Zhang, S.; Huang, S.; Wang, P.; Tian, H., Bare and Ni decorated Al₁₂N₁₂ cage for hydrogen storage: A first-principles study. *international journal of hydrogen energy* **2012**, *37* (17), 12411-12419.
220. Dovesi, R.; Orlando, R.; Erba, A.; Zicovich-Wilson, C. M.; Civalleri, B.; Casassa, S.; Maschio, L.; Ferrabone, M.; De La Pierre, M.; D'Arco, P., CRYSTAL14: A program for the ab initio investigation of crystalline solids. *International Journal of Quantum Chemistry* **2014**, *114* (19), 1287-1317.
221. Tomanek, D. T., David <http://www.nanotube.msu.edu/fullerene/fullerene-isomers.html>. (accessed Apr 28, 2016).
222. E. D. Glendening, J., K. Badenhoop, A. E. Reed, J. E. Carpenter, J. A. Bohmann, C. M. Morales, C. R. Landis, and F. Weinhold, NBO, version 6.0. 2013.
223. Pauling, L., The nature of the chemical bond. IV. The energy of single bonds and the relative electronegativity of atoms. *Journal of the American Chemical Society* **1932**, *54* (9), 3570-3582.
224. Kümmel, S.; Kronik, L., Orbital-dependent density functionals: Theory and applications. *Reviews of Modern Physics* **2008**, *80* (1), 3.

225. Kronik, L.; Stein, T.; Refaelly-Abramson, S.; Baer, R., Excitation gaps of finite-sized systems from optimally tuned range-separated hybrid functionals. *Journal of chemical theory and computation* **2012**, *8* (5), 1515-1531.
226. Shevlin, S.; Guo, Z.; Van Dam, H.; Sherwood, P.; Catlow, C. A.; Sokol, A.; Woodley, S., Structure, optical properties and defects in nitride (III-V) nanoscale cage clusters. *Physical Chemistry Chemical Physics* **2008**, *10* (14), 1944-1959.
227. Vurgaftman, I.; Meyer, J.; Ram-Mohan, L., Band parameters for III-V compound semiconductors and their alloys. *Journal of applied physics* **2001**, *89* (11), 5815-5875.
228. NIST. <http://webbook.nist.gov/chemistry/>. (accessed Apr 28, 2016).
229. Madelung, O., *Semiconductors: data handbook*. Springer Science & Business Media: 2012.
230. Wales, D. J.; Miller, M. A.; Walsh, T. R., Archetypal energy landscapes. *Nature* **1998**, *394* (6695), 758-760.
231. Ewels, C. P.; Rocquefelte, X.; Kroto, H. W.; Rayson, M. J.; Briddon, P. R.; Heggie, M. I., Predicting experimentally stable allotropes: Instability of penta-graphene. *Proceedings of the National Academy of Sciences* **2015**, *112* (51), 15609-15612.
232. Zhao, Q.; Kulik, H. J., Electronic Structure Origins of Surface-Dependent Growth in III-V Quantum Dots. *Chemistry of Materials* **2018**.
233. Talapin, D. V.; Lee, J.-S.; Kovalenko, M. V.; Shevchenko, E. V., Prospects of Colloidal Nanocrystals for Electronic and Optoelectronic Applications. *Chemical Reviews* **2010**, *110* (1), 389-458.
234. Alivisatos, A. P., Semiconductor Clusters, Nanocrystals, and Quantum Dots. *Science* **1996**, *271* (5251), 933-937.
235. Chuang, C.-H. M.; Brown, P. R.; Bulovic, V.; Bawendi, M. G., Improved performance and stability in quantum dot solar cells through band alignment engineering. *Nature Materials* **2014**, *13* (8), 796-801.
236. Chen, O.; Zhao, J.; Chauhan, V. P.; Cui, J.; Wong, C.; Harris, D. K.; Wei, H.; Han, H. S.; Fukumura, D.; Jain, R. K.; Bawendi, M. G., Compact high-quality CdSe-CdS core-shell nanocrystals with narrow emission linewidths and suppressed blinking. *Nature Materials* **2013**, *12* (5), 445-451.
237. Tamang, S.; Lincheneau, C.; Hermans, Y.; Jeong, S.; Reiss, P., Chemistry of InP Nanocrystal Syntheses. *Chemistry of Materials* **2016**, *28* (8), 2491-2506.
238. Brunetti, V.; Chibli, H.; Fiammengo, R.; Galeone, A.; Malvindi, M. A.; Vecchio, G.; Cingolani, R.; Nadeau, J. L.; Pompa, P. P., InP/ZnS as a safer alternative to CdSe/ZnS core/shell quantum dots: in vitro and in vivo toxicity assessment. *Nanoscale* **2013**, *5* (1), 307-317.
239. Baek, J.; Allen, P. M.; Bawendi, M. G.; Jensen, K. F., Investigation of Indium Phosphide Nanocrystal Synthesis Using a High-Temperature and High-Pressure Continuous Flow Microreactor. *Angewandte Chemie International Edition* **2011**, *50* (3), 627-630.
240. Gary, D. C.; Terban, M. W.; Billinge, S. J. L.; Cossairt, B. M., Two-Step Nucleation and Growth of InP Quantum Dots via Magic-Sized Cluster Intermediates. *Chemistry of Materials* **2015**, *27* (4), 1432-1441.
241. Gary, D. C.; Cossairt, B. M., Role of Acid in Precursor Conversion During InP Quantum Dot Synthesis. *Chemistry of Materials* **2013**, *25* (12), 2463-2469.

242. Gary, D. C.; Glassy, B. A.; Cossairt, B. M., Investigation of Indium Phosphide Quantum Dot Nucleation and Growth Utilizing Triarylsilylphosphine Precursors. *Chemistry of Materials* **2014**, *26* (4), 1734-1744.
243. Xie, L.; Harris, D. K.; Bawendi, M. G.; Jensen, K. F., Effect of Trace Water on the Growth of Indium Phosphide Quantum Dots. *Chemistry of Materials* **2015**, *27* (14), 5058-5063.
244. Harris, D. K.; Bawendi, M. G., Improved Precursor Chemistry for the Synthesis of III-V Quantum Dots. *Journal of the American Chemical Society* **2012**, *134* (50), 20211-20213.
245. Li, L.; Protière, M.; Reiss, P., Economic Synthesis of High Quality InP Nanocrystals Using Calcium Phosphide as the Phosphorus Precursor. *Chemistry of Materials* **2008**, *20* (8), 2621-2623.
246. Lucey, D. W.; MacRae, D. J.; Furis, M.; Sahoo, Y.; Cartwright, A. N.; Prasad, P. N., Monodispersed InP quantum dots prepared by colloidal chemistry in a noncoordinating solvent. *Chemistry of Materials* **2005**, *17* (14), 3754-3762.
247. Xu, S.; Kumar, S.; Nann, T., Rapid synthesis of high-quality InP nanocrystals. *Journal of the American Chemical Society* **2006**, *128* (4), 1054-1055.
248. Heath, J. R., Covalency in semiconductor quantum dots. *Chem Soc Rev* **1998**, *27* (1), 65-71.
249. LaMer, V. K.; Dinegar, R. H., Theory, production and mechanism of formation of monodispersed hydrosols. *Journal of the American Chemical Society* **1950**, *72* (11), 4847-4854.
250. Hendricks, M. P.; Campos, M. P.; Cleveland, G. T.; Jen-La Plante, I.; Owen, J. S., A tunable library of substituted thiourea precursors to metal sulfide nanocrystals. *Science* **2015**, *348* (6240), 1226-1230.
251. Owen, J. S.; Chan, E. M.; Liu, H.; Alivisatos, A. P., Precursor conversion kinetics and the nucleation of cadmium selenide nanocrystals. *Journal of the American Chemical Society* **2010**, *132* (51), 18206-18213.
252. Franke, D.; Harris, D. K.; Xie, L.; Jensen, K. F.; Bawendi, M. G., The Unexpected Influence of Precursor Conversion Rate in the Synthesis of III-V Quantum Dots. *Angew Chem Int Edit* **2015**, *54* (48), 14299-14303.
253. Cossairt, B. M., Shining Light on Indium Phosphide Quantum Dots: Understanding the Interplay among Precursor Conversion, Nucleation, and Growth. *Chemistry of Materials* **2016**, *28* (20), 7181-7189.
254. Lee, J.; Yang, J.; Kwon, S. G.; Hyeon, T., Nonclassical nucleation and growth of inorganic nanoparticles. *Nature Reviews Materials* **2016**, *1* (8), 16034.
255. Wall, M. A.; Cossairt, B. M.; Liu, J. T., Reaction-Driven Nucleation Theory. *The Journal of Physical Chemistry C* **2018**, *122* (17), 9671-9679.
256. Friedfeld, M. R.; Stein, J. L.; Cossairt, B. M., Main-Group-Semiconductor Cluster Molecules as Synthetic Intermediates to Nanostructures. *Inorganic chemistry* **2017**, *56* (15), 8689-8697.
257. Green, M.; O'Brien, P., A novel metalorganic route for the direct and rapid synthesis of monodispersed quantum dots of indium phosphide. *Chem Commun* **1998**, (22), 2459-2460.

258. Liu, Z.; Kumbhar, A.; Xu, D.; Zhang, J.; Sun, Z.; Fang, J., Coreduction colloidal synthesis of III-V nanocrystals: The case of InP. *Angew Chem Int Edit* **2008**, *47* (19), 3540-3542.
259. Jun, K.-W.; Khanna, P. K.; Hong, K.-B.; Baeg, J.-O.; Suh, Y.-D., Synthesis of InP nanocrystals from indium chloride and sodium phosphide by solution route. *Mater Chem Phys* **2006**, *96* (2-3), 494-497.
260. Ning, J.; Banin, U., Magic size InP and InAs clusters: synthesis, characterization and shell growth. *Chem Commun* **2017**, *53* (17), 2626-2629.
261. Gary, D. C.; Flowers, S. E.; Kaminsky, W.; Petrone, A.; Li, X.; Cossairt, B. M., Single-crystal and electronic structure of a 1.3 nm indium phosphide nanocluster. *Journal of the American Chemical Society* **2016**, *138* (5), 1510-1513.
262. Tamang, S.; Lee, S.; Choi, H.; Jeong, S., Tuning Size and Size Distribution of Colloidal InAs Nanocrystals via Continuous Supply of Prenucleation Clusters on Nanocrystal Seeds. *Chemistry of Materials* **2016**, *28* (22), 8119-8122.
263. Li, J.; Wang, H.; Lin, L.; Fang, Q.; Peng, X., Quantitative Identification of Basic Growth Channels for Formation of Monodisperse Nanocrystals. *Journal of the American Chemical Society* **2018**, *140* (16), 5474-5484.
264. Liu, M.; Wang, K.; Wang, L.; Han, S.; Fan, H.; Rowell, N.; Ripmeester, J. A.; Renoud, R.; Bian, F.; Zeng, J.; Yu, K., Probing intermediates of the induction period prior to nucleation and growth of semiconductor quantum dots. *Nature communications* **2017**, *8*, 15467.
265. Yang, J.; Muckel, F.; Baek, W.; Fainblat, R.; Chang, H.; Bacher, G.; Hyeon, T., Chemical synthesis, doping, and transformation of magic-sized semiconductor alloy nanoclusters. *Journal of the American Chemical Society* **2017**, *139* (19), 6761-6770.
266. Xie, L.; Shen, Y.; Franke, D.; Sebastián, V.; Bawendi, M. G.; Jensen, K. F., Characterization of Indium Phosphide Quantum Dot Growth Intermediates Using MALDI-TOF Mass Spectrometry. *Journal of the American Chemical Society* **2016**, *138* (41), 13469-13472.
267. Battaglia, D.; Peng, X., Formation of high quality InP and InAs nanocrystals in a noncoordinating solvent. *Nano Letters* **2002**, *2* (9), 1027-1030.
268. Tessier, M. D.; De Nolf, K.; Dupont, D.; Sinnaeve, D.; De Roo, J.; Hens, Z., Aminophosphines: A Double Role in the Synthesis of Colloidal Indium Phosphide Quantum Dots. *Journal of the American Chemical Society* **2016**, *138* (18), 5923-5929.
269. Kim, K.; Yoo, D.; Choi, H.; Tamang, S.; Ko, J. H.; Kim, S.; Kim, Y. H.; Jeong, S., Halide–Amine Co-Passivated Indium Phosphide Colloidal Quantum Dots in Tetrahedral Shape. *Angewandte Chemie* **2016**, *128* (11), 3778-3782.
270. Nightingale, A. M., Improving the ensemble optical properties of InP quantum dots by indium precursor modification. *Journal of Materials Chemistry C* **2016**, *4* (36), 8454-8458.
271. Baquero, E. A.; Virieux, H.; Swain, R. A.; Gillet, A.; Cros-Gagneux, A.; Coppel, Y.; Chaudret, B.; Nayral, C.; Delpech, F., Synthesis of Oxide-Free InP Quantum Dots: Surface Control and H₂-Assisted Growth. *Chemistry of Materials* **2017**, *29* (22), 9623-9627.
272. Ramasamy, P.; Kim, N.; Kang, Y.-S.; Ramirez, O.; Lee, J.-S., Tunable, Bright, and Narrow-Band Luminescence from Colloidal Indium Phosphide Quantum Dots. *Chemistry of Materials* **2017**, *29* (16), 6893-6899.

273. Ritchhart, A.; Cossairt, B. M., Templated Growth of InP Nanocrystals with a Polytwistane Structure. *Angewandte Chemie* **2018**, *130* (7), 1926-1930.
274. Stein, J. L.; Steimle, M. I.; Terban, M. W.; Petrone, A.; Billinge, S. J.; Li, X.; Cossairt, B. M., Cation exchange induced transformation of InP magic-sized clusters. *Chemistry of Materials* **2017**, *29* (18), 7984-7992.
275. Gary, D. C.; Petrone, A.; Li, X.; Cossairt, B. M., Investigating the role of amine in InP nanocrystal synthesis: destabilizing cluster intermediates by Z-type ligand displacement. *Chem Commun* **2017**, *53* (1), 161-164.
276. Stein, J. L.; Mader, E. A.; Cossairt, B. M., Luminescent InP quantum dots with tunable emission by post-synthetic modification with lewis acids. *The journal of physical chemistry letters* **2016**, *7* (7), 1315-1320.
277. Baquero, E. A.; Ojo, W.-S.; Coppel, Y.; Chaudret, B.; Urbaszek, B.; Nayral, C.; Delpech, F., Identifying short surface ligands on metal phosphide quantum dots. *Physical Chemistry Chemical Physics* **2016**, *18* (26), 17330-17334.
278. Piveteau, L.; Ong, T.-C.; Walder, B. J.; Dirin, D. N.; Moscheni, D.; Schneider, B.; Bär, J.; Protesescu, L.; Masciocchi, N.; Guagliardi, A.; Emsley, L.; Copéret, C.; Kovalenko, M. V., Resolving the Core and the Surface of CdSe Quantum Dots and Nanoplatelets Using Dynamic Nuclear Polarization Enhanced PASS-PIETA NMR Spectroscopy. *ACS Central Science* **2018**.
279. Puzder, A.; Williamson, A. J.; Zaitseva, N.; Galli, G.; Manna, L.; Alivisatos, A. P., The effect of organic ligand binding on the growth of CdSe nanoparticles probed by Ab initio calculations. *Nano Letters* **2004**, *4* (12), 2361-2365.
280. Manna, L.; Wang, L.; Cingolani, R.; Alivisatos, A. P., First-principles modeling of unpassivated and surfactant-passivated bulk facets of wurtzite CdSe: A model system for studying the anisotropic growth of CdSe nanocrystals. *J Phys Chem B* **2005**, *109* (13), 6183-6192.
281. Eunseog, C.; Hyosook, J.; Junho, L.; Eunjoo, J., Modeling on the size dependent properties of InP quantum dots: a hybrid functional study. *Nanotechnology* **2013**, *24* (21), 215201.
282. Xie, L.; Zhao, Q.; Jensen, K. F.; Kulik, H. J., Direct Observation of Early-Stage Quantum Dot Growth Mechanisms with High-Temperature Ab Initio Molecular Dynamics. *The Journal of Physical Chemistry C* **2016**, *120*, 2472-2483.
283. Kim, J. Y.; Steeves, A. H.; Kulik, H. J., Harnessing Organic Ligand Libraries for First-Principles Inorganic Discovery: Indium Phosphide Quantum Dot Precursor Design Strategies. *Chemistry of Materials* **2017**, *29* (8), 3632-3643.
284. *Handbook Series on Semiconductor Parameters*. World Scientific: 1996; Vol. 1.
285. Margraf, J. T.; Ruland, A.; Sgobba, V.; Guldi, D. M.; Clark, T., Theoretical and Experimental Insights into the Surface Chemistry of Semiconductor Quantum Dots. *Langmuir* **2013**, *29* (49), 15450-15456.
286. Xie, R.; Battaglia, D.; Peng, X., Colloidal InP Nanocrystals as Efficient Emitters Covering Blue to Near-Infrared. *Journal of the American Chemical Society* **2007**, *129* (50), 15432-15433.
287. Gani, T. Z. H.; Kulik, H. J., Understanding and Breaking Scaling Relations in Single-Site Catalysis: Methane-to-methanol Conversion by Fe(IV)=O. *ACS Catalysis* **2018**, *8*, 975-986.

288. Henkelman, G.; Jónsson, H., Improved tangent estimate in the nudged elastic band method for finding minimum energy paths and saddle points. *The Journal of chemical physics* **2000**, *113* (22), 9978-9985.
289. Henkelman, G.; Uberuaga, B. P.; Jónsson, H., A climbing image nudged elastic band method for finding saddle points and minimum energy paths. *The Journal of chemical physics* **2000**, *113* (22), 9901-9904.
290. Hay, P. J.; Wadt, W. R., Ab initio effective core potentials for molecular calculations. Potentials for the transition metal atoms Sc to Hg. *The Journal of Chemical Physics* **1985**, *82* (1), 270-283.
291. Grimme, S.; Antony, J.; Ehrlich, S.; Krieg, H., A consistent and accurate ab initio parametrization of density functional dispersion correction (DFT-D) for the 94 elements H-Pu. *The Journal of chemical physics* **2010**, *132* (15), 154104.
292. Mayer, I., Charge, bond order and valence in the ab initio SCF theory. *Chemical Physics Letters* **1983**, *97* (3), 270-274.
293. Mayer, I., Bond order and valence: Relations to Mulliken's population analysis. *International journal of quantum chemistry* **1984**, *26* (1), 151-154.
294. Lu, T.; Chen, F., Multiwfns: a multifunctional wavefunction analyzer. *Journal of computational chemistry* **2012**, *33* (5), 580-592.
295. Hastie, T.; Tibshirani, R.; Friedman, J. H., *The elements of statistical learning : data mining, inference, and prediction*. 2nd ed.; Springer: New York, 2009; p xxii, 745 p.
296. Mavrikakis, M.; Hammer, B.; Nørskov, J. K., Effect of strain on the reactivity of metal surfaces. *Physical Review Letters* **1998**, *81* (13), 2819.
297. Bligaard, T.; Nørskov, J. K.; Dahl, S.; Matthiesen, J.; Christensen, C. H.; Sehested, J., The Brønsted–Evans–Polanyi relation and the volcano curve in heterogeneous catalysis. *Journal of Catalysis* **2004**, *224* (1), 206-217.
298. van Santen, R. A.; Neurock, M.; Shetty, S. G., Reactivity theory of transition-metal surfaces: a Brønsted- Evans- Polanyi linear activation energy- free-energy analysis. *Chemical reviews* **2009**, *110* (4), 2005-2048.
299. de Visser, S. P., Trends in substrate hydroxylation reactions by heme and nonheme iron (IV)-oxo oxidants give correlations between intrinsic properties of the oxidant with barrier height. *Journal of the American Chemical Society* **2009**, *132* (3), 1087-1097.
300. Usharani, D.; Lacy, D. C.; Borovik, A. S.; Shaik, S., Dichotomous hydrogen atom transfer vs proton-coupled electron transfer during activation of X–H bonds (X= C, N, O) by nonheme iron–oxo complexes of variable basicity. *Journal of the American Chemical Society* **2013**, *135* (45), 17090-17104.
301. Latimer, A. A.; Kulkarni, A. R.; Aljama, H.; Montoya, J. H.; Yoo, J. S.; Tsai, C.; Abild-Pedersen, F.; Studt, F.; Nørskov, J. K., Understanding trends in CH bond activation in heterogeneous catalysis. *Nature Materials* **2017**, *16*, 225-229.
302. Deslahra, P.; Iglesia, E., Reactivity and selectivity descriptors for the activation of C–H Bonds in hydrocarbons and oxygenates on metal oxides. *The Journal of Physical Chemistry C* **2016**, *120* (30), 16741-16760.
303. Zhao, Q.; Kulik, H. J., Where Does the Density Localize in the Solid State? Divergent Behavior for Hybrids and DFT+U. *Journal of chemical theory and computation* **2018**, *14* (2), 670-683.

304. Haunschild, R.; Henderson, T. M.; Jiménez-Hoyos, C. A.; Scuseria, G. E., Many-electron self-interaction and spin polarization errors in local hybrid density functionals. *The Journal of Chemical Physics* **2010**, *133* (13), 134116.
305. Cohen, A. J.; Mori-Sánchez, P.; Yang, W., Insights into current limitations of density functional theory. *Science* **2008**, *321* (5890), 792-794.
306. Schmidt, T.; Kümmel, S., One- and many-electron self-interaction error in local and global hybrid functionals. *Physical Review B* **2016**, *93* (16), 165120.
307. Yang, W.; Zhang, Y.; Ayers, P. W., Degenerate Ground States and a Fractional Number of Electrons in Density and Reduced Density Matrix Functional Theory. *Physical Review Letters* **2000**, *84* (22), 5172-5175.
308. Leininger, T.; Stoll, H.; Werner, H.-J.; Savin, A., Combining long-range configuration interaction with short-range density functionals. *Chemical physics letters* **1997**, *275* (3), 151-160.
309. Toulouse, J.; Colonna, F.; Savin, A., Long-range-short-range separation of the electron-electron interaction in density-functional theory. *Physical Review A* **2004**, *70* (6), 062505.
310. Vydrov, O. A.; Scuseria, G. E., Assessment of a long-range corrected hybrid functional. *The Journal of Chemical Physics* **2006**, *125* (23), 234109.
311. Cohen, A. J.; Mori-Sánchez, P.; Yang, W., Development of exchange-correlation functionals with minimal many-electron self-interaction error. *The Journal of Chemical Physics* **2007**, *126* (19), 191109.
312. Iikura, H.; Tsuneda, T.; Yanai, T.; Hirao, K., A long-range correction scheme for generalized-gradient-approximation exchange functionals. *The Journal of Chemical Physics* **2001**, *115* (8), 3540-3544.
313. Baer, R.; Neuhauser, D., Density functional theory with correct long-range asymptotic behavior. *Physical Review Letters* **2005**, *94* (4), 043002.
314. Tsuneda, T.; Song, J.-W.; Suzuki, S.; Hirao, K., On Koopmans' theorem in density functional theory. *The Journal of Chemical Physics* **2010**, *133* (17), 174101.
315. Livshits, E.; Baer, R., A well-tempered density functional theory of electrons in molecules. *Physical Chemistry Chemical Physics* **2007**, *9* (23), 2932-2941.
316. Stein, T.; Kronik, L.; Baer, R., Reliable Prediction of Charge Transfer Excitations in Molecular Complexes Using Time-Dependent Density Functional Theory. *Journal of the American Chemical Society* **2009**, *131* (8), 2818-2820.
317. Stein, T.; Kronik, L.; Baer, R., Prediction of charge-transfer excitations in coumarin-based dyes using a range-separated functional tuned from first principles. *The Journal of Chemical Physics* **2009**, *131* (24), 244119.
318. Srebro, M.; Autschbach, J., Does a Molecule-Specific Density Functional Give an Accurate Electron Density? The Challenging Case of the CuCl Electric Field Gradient. *The Journal of Physical Chemistry Letters* **2012**, *3* (5), 576-581.
319. Körzdörfer, T.; Brédas, J.-L., Organic Electronic Materials: Recent Advances in the DFT Description of the Ground and Excited States Using Tuned Range-Separated Hybrid Functionals. *Accounts of Chemical Research* **2014**, *47* (11), 3284-3291.
320. Autschbach, J.; Srebro, M., Delocalization Error and “Functional Tuning” in Kohn–Sham Calculations of Molecular Properties. *Accounts of Chemical Research* **2014**, *47* (8), 2592-2602.

321. Gledhill, J. D.; Peach, M. J. G.; Tozer, D. J., Assessment of Tuning Methods for Enforcing Approximate Energy Linearity in Range-Separated Hybrid Functionals. *Journal of Chemical Theory and Computation* **2013**, *9* (10), 4414-4420.
322. Stein, T.; Eisenberg, H.; Kronik, L.; Baer, R., Fundamental gaps in finite systems from eigenvalues of a generalized Kohn-Sham method. *Physical Review Letters* **2010**, *105* (26), 266802.
323. Salzner, U.; Baer, R., Koopmans' springs to life. *The Journal of chemical physics* **2009**, *131* (23), 231101.
324. Janak, J. F., Proof that $dE/dn_i = \epsilon$ in density-functional theory. *Physical Review B* **1978**, *18* (12), 7165-7168.
325. Körzdörfer, T.; Sears, J. S.; Sutton, C.; Brédas, J.-L., Long-range corrected hybrid functionals for π -conjugated systems: Dependence of the range-separation parameter on conjugation length. *The Journal of Chemical Physics* **2011**, *135* (20), 204107.
326. Karolewski, A.; Kronik, L.; Kümmel, S., Using optimally tuned range separated hybrid functionals in ground-state calculations: Consequences and caveats. *The Journal of Chemical Physics* **2013**, *138* (20), 204115.
327. Whittleton, S. R.; Sosa Vazquez, X. A.; Isborn, C. M.; Johnson, E. R., Density-functional errors in ionization potential with increasing system size. *The Journal of Chemical Physics* **2015**, *142* (18), 184106.
328. Vlček, V.; Eisenberg, H. R.; Steinle-Neumann, G.; Kronik, L.; Baer, R., Deviations from piecewise linearity in the solid-state limit with approximate density functionals. *The Journal of Chemical Physics* **2015**, *142* (3), 034107.
329. Anisimov, V. I.; Zaanen, J.; Andersen, O. K., Band Theory And Mott Insulators - Hubbard-U Instead Of Stoner-I. *Physical Review B* **1991**, *44* (3), 943-954.
330. Liechtenstein, A. I.; Anisimov, V. I.; Zaanen, J., Density-Functional Theory And Strong-Interactions - Orbital Ordering In Mott-Hubbard Insulators. *Physical Review B* **1995**, *52* (8), R5467-R5470.
331. Kulik, H. J., Perspective: Treating electron Over-delocalization with the DFT+ U method. *The Journal of chemical physics* **2015**, *142* (24), 240901.
332. Bochevarov, A. D.; Friesner, R. A., The densities produced by the density functional theory: Comparison to full configuration interaction. *The Journal of Chemical Physics* **2008**, *128* (3), 034102.
333. He, Y.; Gräfenstein, J.; Kraka, E.; Cremer, D., What correlation effects are covered by density functional theory? *Molecular Physics* **2000**, *98* (20), 1639-1658.
334. Bader, R. F. W., A quantum theory of molecular structure and its applications. *Chemical Reviews* **1991**, *91* (5), 893-928.
335. Kepp, K. P., Comment on "Density functional theory is straying from the path toward the exact functional". *Science* **2017**, *356* (6337), 496.
336. Medvedev, M. G.; Bushmarinov, I. S.; Sun, J.; Perdew, J. P.; Lyssenko, K. A., Density functional theory is straying from the path toward the exact functional. *Science* **2017**, *355* (6320), 49-52.
337. Brorsen, K. R.; Yang, Y.; Pak, M. V.; Hammes-Schiffer, S., Is the Accuracy of Density Functional Theory for Atomization Energies and Densities in Bonding Regions Correlated? *The Journal of Physical Chemistry Letters* **2017**, *8* (9), 2076-2081.

338. Mezei, P. D.; Csonka, G. I.; Kállay, M., Electron Density Errors and Density-Driven Exchange-Correlation Energy Errors in Approximate Density Functional Calculations. *Journal of Chemical Theory and Computation* **2017**, *13* (10), 4753-4764.
339. Gani, T. Z.; Kulik, H. J., Where Does the Density Localize? Convergent Behavior for Global Hybrids, Range Separation, and DFT+ U. *Journal of chemical theory and computation* **2016**, *12* (12), 5931-5945.
340. Brumboiu, I. E.; Prokopiou, G.; Kronik, L.; Brenna, B., Valence electronic structure of cobalt phthalocyanine from an optimally tuned range-separated hybrid functional. *The Journal of Chemical Physics* **2017**, *147* (4), 044301.
341. Duignan, T. J.; Autschbach, J., Impact of the Kohn–Sham Delocalization Error on the 4f Shell Localization and Population in Lanthanide Complexes. *Journal of Chemical Theory and Computation* **2016**, *12* (7), 3109-3121.
342. Duignan, T. J.; Autschbach, J.; Batista, E.; Yang, P., Assessment of tuned range separated exchange functionals for spectroscopies and properties of uranium complexes. *Journal of Chemical Theory and Computation* **2017**, *13* (8), 3614-3625.
343. Pritchard, B.; Autschbach, J., Theoretical Investigation of Paramagnetic NMR Shifts in Transition Metal Acetylacetonato Complexes: Analysis of Signs, Magnitudes, and the Role of the Covalency of Ligand–Metal Bonding. *Inorganic chemistry* **2012**, *51* (15), 8340-8351.
344. Janesko, B. G.; Scuseria, G. E., Hartree–Fock orbitals significantly improve the reaction barrier heights predicted by semilocal density functionals. *The Journal of chemical physics* **2008**, *128* (24), 244112.
345. Verma, P.; Perera, A.; Bartlett, R. J., Increasing the applicability of DFT I: Non-variational correlation corrections from Hartree–Fock DFT for predicting transition states. *Chemical Physics Letters* **2012**, *524*, 10-15.
346. Kim, M.-C.; Sim, E.; Burke, K., Ions in solution: Density corrected density functional theory (DC-DFT). *The Journal of Chemical Physics* **2014**, *140* (18), 18A528.
347. Kim, M.-C.; Park, H.; Son, S.; Sim, E.; Burke, K., Improved DFT Potential Energy Surfaces via Improved Densities. *The Journal of Physical Chemistry Letters* **2015**, *6* (19), 3802-3807.
348. Hubbard, J., ELECTRON CORRELATIONS IN NARROW ENERGY BANDS. *Proceedings of the Royal Society of London Series a-Mathematical and Physical Sciences* **1963**, *276* (1364), 238-257.
349. Anderson, P. W., Localized Magnetic States in Metals. *Physical Review* **1961**, *124* (1), 41-53.
350. Janet, J. P.; Zhao, Q.; Ioannidis, E. I.; Kulik, H. J., Density functional theory for modeling large molecular adsorbate-surface interactions: a mini-review and worked example. *Molecular Simulation* **2017**, *43*, 327-345.
351. Gani, T. Z. H.; Kulik, H. J., Unifying Exchange Sensitivity in Transition Metal Spin-State Ordering and Catalysis Through Bond Valence Metrics *Journal of chemical theory and computation* **2017**, *just accepted* <http://dx.doi.org/10.1021/acs.jctc.7b00848>.
352. Verma, P.; Truhlar, D. G., Does DFT+ U mimic hybrid density functionals? *Theoretical Chemistry Accounts* **2016**, *135* (8), 1-15.
353. Loschen, C.; Carrasco, J.; Neyman, K. M.; Illas, F., First-principles LDA+ U and GGA+ U study of cerium oxides: Dependence on the effective U parameter. *Physical Review B* **2007**, *75* (3), 035115.

354. Andersson, D. A.; Simak, S.; Johansson, B.; Abrikosov, I.; Skorodumova, N. V., Modeling of Ce O₂, Ce₂O₃, and Ce O_{2-x} in the LDA+ U formalism. *Physical Review B* **2007**, *75* (3), 035109.
355. Shao, G., Red shift in manganese-and iron-doped TiO₂: a DFT+ U analysis. *The Journal of Physical Chemistry C* **2009**, *113* (16), 6800-6808.
356. Hu, Z.; Metiu, H., Choice of U for DFT+ U calculations for titanium oxides. *The Journal of Physical Chemistry C* **2011**, *115* (13), 5841-5845.
357. Rödl, C.; Fuchs, F.; Furthmüller, J.; Bechstedt, F., Quasiparticle band structures of the antiferromagnetic transition-metal oxides MnO, FeO, CoO, and NiO. *Physical Review B* **2009**, *79* (23), 235114.
358. Tran, F.; Blaha, P.; Schwarz, K.; Novák, P., Hybrid exchange-correlation energy functionals for strongly correlated electrons: Applications to transition-metal monoxides. *Physical Review B* **2006**, *74* (15), 155108.
359. Franchini, C.; Podloucky, R.; Paier, J.; Marsman, M.; Kresse, G., Ground-state properties of multivalent manganese oxides: Density functional and hybrid density functional calculations. *Physical Review B* **2007**, *75* (19), 195128.
360. Liao, P.; Carter, E. A., Testing variations of the GW approximation on strongly correlated transition metal oxides: hematite (α -Fe₂O₃) as a benchmark. *Physical Chemistry Chemical Physics* **2011**, *13* (33), 15189-15199.
361. Rollmann, G.; Rohrbach, A.; Entel, P.; Hafner, J., First-principles calculation of the structure and magnetic phases of hematite. *Physical Review B* **2004**, *69* (16), 165107.
362. Hong, J.; Stroppa, A.; Íñiguez, J.; Picozzi, S.; Vanderbilt, D., Spin-phonon coupling effects in transition-metal perovskites: A DFT+ U and hybrid-functional study. *Physical Review B* **2012**, *85* (5), 054417.
363. Seo, D.-H.; Urban, A.; Ceder, G., Calibrating transition-metal energy levels and oxygen bands in first-principles calculations: Accurate prediction of redox potentials and charge transfer in lithium transition-metal oxides. *Physical Review B* **2015**, *92* (11), 115118.
364. Franchini, C.; Bayer, V.; Podloucky, R.; Paier, J.; Kresse, G., Density functional theory study of MnO by a hybrid functional approach. *Physical Review B* **2005**, *72* (4), 045132.
365. Gerosa, M.; Bottani, C. E.; Caramella, L.; Onida, G.; Di Valentin, C.; Pacchioni, G., Electronic structure and phase stability of oxide semiconductors: Performance of dielectric-dependent hybrid functional DFT, benchmarked against GW band structure calculations and experiments. *Physical Review B* **2015**, *91* (15), 155201.
366. Graciani, J.; Márquez, A. M.; Plata, J. J.; Ortega, Y.; Hernández, N. C.; Meyer, A.; Zicovich-Wilson, C. M.; Sanz, J. F., Comparative study on the performance of hybrid DFT functionals in highly correlated oxides: the case of CeO₂ and Ce₂O₃. *Journal of chemical theory and computation* **2010**, *7* (1), 56-65.
367. Pozun, Z. D.; Henkelman, G., Hybrid density functional theory band structure engineering in hematite. *The Journal of chemical physics* **2011**, *134* (22), 224706.
368. He, J.; Franchini, C., Screened hybrid functional applied to 3 d 0→3 d 8 transition-metal perovskites La M O₃ (M= Sc-Cu): Influence of the exchange mixing parameter on the structural, electronic, and magnetic properties. *Physical Review B* **2012**, *86* (23), 235117.

369. Viñes, F.; Lamiel-García, O.; Chul Ko, K.; Yong Lee, J.; Illas, F., Systematic study of the effect of HSE functional internal parameters on the electronic structure and band gap of a representative set of metal oxides. *Journal of Computational Chemistry* **2017**, *38* (11), 781-789.
370. Guo, Y.; Clark, S. J.; Robertson, J., Electronic and magnetic properties of Ti₂O₃, Cr₂O₃, and Fe₂O₃ calculated by the screened exchange hybrid density functional. *Journal of Physics: Condensed Matter* **2012**, *24* (32), 325504.
371. Wadt, W. R.; Hay, P. J., Ab initio effective core potentials for molecular calculations. Potentials for main group elements Na to Bi. *The Journal of Chemical Physics* **1985**, *82* (1), 284-298.
372. Broyden, C. G., The convergence of a class of double-rank minimization algorithms 1. general considerations. *IMA Journal of Applied Mathematics* **1970**, *6* (1), 76-90.
373. Broyden, C. G., The convergence of a class of double-rank minimization algorithms: 2. The new algorithm. *IMA journal of applied mathematics* **1970**, *6* (3), 222-231.
374. Fletcher, R., A new approach to variable metric algorithms. *The computer journal* **1970**, *13* (3), 317-322.
375. Goldfarb, D., A family of variable-metric methods derived by variational means. *Mathematics of computation* **1970**, *24* (109), 23-26.
376. Shanno, D. F., Conditioning of quasi-Newton methods for function minimization. *Mathematics of computation* **1970**, *24* (111), 647-656.
377. Saunders, V.; Hillier, I., A “Level-Shifting” method for converging closed shell Hartree–Fock wave functions. *International Journal of Quantum Chemistry* **1973**, *7* (4), 699-705.
378. Dudarev, S. L.; Botton, G. A.; Savrasov, S. Y.; Humphreys, C. J.; Sutton, A. P., Electron-energy-loss spectra and the structural stability of nickel oxide: An LSDA+U study. *Physical Review B* **1998**, *57* (3), 1505-1509.
379. Giannozzi, P.; Baroni, S.; Bonini, N.; Calandra, M.; Car, R.; Cavazzoni, C.; Ceresoli, D.; Chiarotti, G. L.; Cococcioni, M.; Dabo, I., QUANTUM ESPRESSO: a modular and open-source software project for quantum simulations of materials. *Journal of physics: Condensed matter* **2009**, *21* (39), 395502.
380. Vanderbilt, D., Soft self-consistent pseudopotentials in a generalized eigenvalue formalism. *Physical Review B* **1990**, *41* (11), 7892.
381. Martyna, G. J.; Tuckerman, M. E., A reciprocal space based method for treating long range interactions in ab initio and force-field-based calculations in clusters. *The Journal of chemical physics* **1999**, *110* (6), 2810-2821.
382. Kulik, H. J.; Marzari, N., A self-consistent Hubbard U density-functional theory approach to the addition-elimination reactions of hydrocarbons on bare FeO+. *The Journal of chemical physics* **2008**, *129* (13), 134314.
383. Hellenbrandt, M., The inorganic crystal structure database (ICSD)—present and future. *Crystallography Reviews* **2004**, *10* (1), 17-22.
384. Tang, W.; Sanville, E.; Henkelman, G., A grid-based Bader analysis algorithm without lattice bias. *Journal of Physics: Condensed Matter* **2009**, *21* (8), 084204.
385. Deskins, N. A.; Dupuis, M., Electron transport via polaron hopping in bulk Ti O₂: A density functional theory characterization. *Physical Review B* **2007**, *75* (19), 195212.

386. Martinez, J. I.; Hansen, H. A.; Rossmeisl, J.; Nørskov, J. K., Formation energies of rutile metal dioxides using density functional theory. *Physical Review B* **2009**, *79* (4), 045120.
387. Morgan, B. J.; Watson, G. W., A density functional theory+ U study of oxygen vacancy formation at the (110),(100),(101), and (001) surfaces of rutile TiO₂. *The Journal of Physical Chemistry C* **2009**, *113* (17), 7322-7328.
388. Umebayashi, T.; Yamaki, T.; Itoh, H.; Asai, K., Analysis of electronic structures of 3d transition metal-doped TiO₂ based on band calculations. *Journal of Physics and Chemistry of Solids* **2002**, *63* (10), 1909-1920.
389. Wang, L.; Maxisch, T.; Ceder, G., Oxidation energies of transition metal oxides within the GGA+ U framework. *Physical Review B* **2006**, *73* (19), 195107.
390. Muscat, J.; Wander, A.; Harrison, N., On the prediction of band gaps from hybrid functional theory. *Chemical Physics Letters* **2001**, *342* (3), 397-401.
391. Pascual, J.; Camassel, J.; Mathieu, H., Fine structure in the intrinsic absorption edge of Ti O₂. *Physical Review B* **1978**, *18* (10), 5606.
392. Amtout, A.; Leonelli, R., Optical properties of rutile near its fundamental band gap. *Physical Review B* **1995**, *51* (11), 6842.
393. Strehlow, W.; Cook, E., Compilation of energy band gaps in elemental and binary compound semiconductors and insulators. *Journal of Physical and Chemical Reference Data* **1973**, *2* (1), 163-200.
394. Zheng, X.; Cohen, A. J.; Mori-Sánchez, P.; Hu, X.; Yang, W., Improving band gap prediction in density functional theory from molecules to solids. *Physical review letters* **2011**, *107* (2), 026403.
395. Zhou, F.; Kang, K.; Maxisch, T.; Ceder, G.; Morgan, D., The electronic structure and band gap of LiFePO₄ and LiMnPO₄. *Solid State Communications* **2004**, *132* (3), 181-186.
396. Wemple, S., Optical oscillator strengths and excitation energies in solids, liquids, and molecules. *The Journal of Chemical Physics* **1977**, *67* (5), 2151-2168.
397. Marques, M. A.; Vidal, J.; Oliveira, M. J.; Reining, L.; Botti, S., Density-based mixing parameter for hybrid functionals. *Physical Review B* **2011**, *83* (3), 035119.
398. Kulik, H. J.; Marzari, N., Systematic study of first-row transition-metal diatomic molecules: A self-consistent DFT plus U approach. *J Chem Phys* **2010**, *133* (11), 114103.
399. Janet, J. P.; Kulik, H. J., Predicting electronic structure properties of transition metal complexes with neural networks. *Chemical Science* **2017**, *8*, 5137-5152.
400. Ernzerhof, M.; Scuseria, G. E., Assessment of the Perdew–Burke–Ernzerhof exchange-correlation functional. *The Journal of chemical physics* **1999**, *110* (11), 5029-5036.
401. Schimka, L.; Harl, J.; Stroppa, A.; Grüneis, A.; Marsman, M.; Mittendorfer, F.; Kresse, G., Accurate surface and adsorption energies from many-body perturbation theory. *Nature materials* **2010**, *9* (9), 741.
402. Adamo, C.; Barone, V., Toward reliable density functional methods without adjustable parameters: The PBE0 model. *The Journal of chemical physics* **1999**, *110* (13), 6158-6170.
403. Heyd, J.; Scuseria, G. E.; Ernzerhof, M., Hybrid functionals based on a screened Coulomb potential. *The Journal of chemical physics* **2003**, *118* (18), 8207-8215.

404. Becke, A. D., Density-functional exchange-energy approximation with correct asymptotic behavior. *Physical review A* **1988**, *38* (6), 3098.
405. Gatti, C., TOPOND98 user's manual. *CNR-CSRSRC, Milano* **1999**.
406. Ripplinger, C.; Neese, F., An efficient and near linear scaling pair natural orbital based local coupled cluster method. *The Journal of chemical physics* **2013**, *138* (3), 034106.
407. Neese, F., The ORCA program system. *Wiley Interdisciplinary Reviews: Computational Molecular Science* **2012**, *2* (1), 73-78.
408. Briquet, L. G.; Sarwar, M.; Mugo, J.; Jones, G.; Calle-Vallejo, F., A new type of scaling relations to assess the accuracy of computational predictions of catalytic activities applied to the oxygen evolution reaction. *ChemCatChem* **2017**, *9* (7), 1261-1268.
409. Man, I. C.; Su, H. Y.; Calle-Vallejo, F.; Hansen, H. A.; Martínez, J. I.; Inoglu, N. G.; Kitchin, J.; Jaramillo, T. F.; Nørskov, J. K.; Rossmeisl, J., Universality in oxygen evolution electrocatalysis on oxide surfaces. *ChemCatChem* **2011**, *3* (7), 1159-1165.
410. Kulik, H. J.; Seelam, N.; Mar, B.; Martinez, T. J., Adapting DFT+U for the Chemically-Motivated Correction of Minimal Basis Set Incompleteness. *Journal of Physical Chemistry A* **2016**, *120* (29), 5939-5949.
411. Bajaj, A.; Janet, J. P.; Kulik, H. J., Communication: Recovering the flat-plane condition in electronic structure theory at semi-local DFT cost. *J Chem Phys* **2017**, *147*, 191101.
412. Pourbaix, M., Atlas of electrochemical equilibria in aqueous solutions. *NACEmTX* **1974**.
413. Bratsch, S. G., Standard electrode potentials and temperature coefficients in water at 298.15 K. *Journal of Physical and Chemical Reference Data* **1989**, *18* (1), 1-21.
414. Haynes, W. M., *CRC handbook of chemistry and physics*. CRC press: 2014.
415. Baranek, P.; Lichanot, A.; Orlando, R.; Dovesi, R., Structural and vibrational properties of solid Mg(OH)₂ and Ca(OH)₂-performances of various hamiltonians. *Chemical Physics Letters* **2001**, *340* (3-4), 362-369.
416. Borges, P. D.; Scolfaro, L. M.; Alves, H. W. L.; da Silva, E. F., DFT study of the electronic, vibrational, and optical properties of SnO₂. *Theoretical Chemistry Accounts* **2010**, *126* (1-2), 39-44.
417. Montanari, B.; Harrison, N., Lattice dynamics of TiO₂ rutile: influence of gradient corrections in density functional calculations. *Chemical physics letters* **2002**, *364* (5-6), 528-534.
418. McDowell, S. A.; Buckingham, A. D., On the Correlation between Bond-Length Change and Vibrational Frequency Shift in Hydrogen-Bonded Complexes: A Computational Study of Y⁺ · · · HCl Dimers (Y = N₂, CO, BF). *Journal of the American Chemical Society* **2005**, *127* (44), 15515-15520.
419. Wang, W.; Zhang, Y.; Ji, B.; Tian, A., On the correlation between bond-length change and vibrational frequency shift in halogen-bonded complexes. *The Journal of chemical physics* **2011**, *134* (22), 224303.
420. Szilagyi, R. K.; Metz, M.; Solomon, E. I., Spectroscopic calibration of modern density functional methods using [CuCl₄]²⁻. *The Journal of Physical Chemistry A* **2002**, *106* (12), 2994-3007.

421. Hocking, R. K.; Deeth, R. J.; Hambley, T. W., DFT Study of the Systematic Variations in Metal– Ligand Bond Lengths of Coordination Complexes: the Crucial Role of the Condensed Phase. *Inorganic chemistry* **2007**, *46* (20), 8238-8244.
422. Croce, F.; Persi, L.; Ronci, F.; Scrosati, B., Nanocomposite polymer electrolytes and their impact on the lithium battery technology. *Solid State Ionics* **2000**, *135* (1-4), 47-52.
423. Stephan, A. M., Review on gel polymer electrolytes for lithium batteries. *European polymer journal* **2006**, *42* (1), 21-42.
424. Bruce, P. G.; Scrosati, B.; Tarascon, J. M., Nanomaterials for rechargeable lithium batteries. *Angewandte Chemie International Edition* **2008**, *47* (16), 2930-2946.
425. Tarascon, J.-M.; Armand, M., Issues and challenges facing rechargeable lithium batteries. In *Materials For Sustainable Energy: A Collection of Peer-Reviewed Research and Review Articles from Nature Publishing Group*, World Scientific: 2011; pp 171-179.
426. Amine, K.; Yasuda, H.; Yamachi, M., Olivine LiCoPO₄ as 4.8 V electrode material for lithium batteries. *Electrochemical and Solid-State Letters* **2000**, *3* (4), 178-179.
427. Du, G.; NuLi, Y.; Yang, J.; Wang, J., Fluorine-doped LiNi0.5Mn1.5O4 for 5 V cathode materials of lithium-ion battery. *Materials Research Bulletin* **2008**, *43* (12), 3607-3613.
428. Wang, F.; Yang, J.; NuLi, Y.; Wang, J., Highly promoted electrochemical performance of 5 V LiCoPO₄ cathode material by addition of vanadium. *Journal of Power Sources* **2010**, *195* (19), 6884-6887.
429. Long, L.; Wang, S.; Xiao, M.; Meng, Y., Polymer electrolytes for lithium polymer batteries. *Journal of Materials Chemistry A* **2016**, *4* (26), 10038-10069.
430. Shao, N.; Sun, X.-G.; Dai, S.; Jiang, D.-e., Electrochemical windows of sulfone-based electrolytes for high-voltage Li-ion batteries. *The Journal of Physical Chemistry B* **2011**, *115* (42), 12120-12125.
431. Kazemiabnavi, S.; Zhang, Z.; Thornton, K.; Banerjee, S., Electrochemical stability window of imidazolium-based ionic liquids as electrolytes for lithium batteries. *The Journal of Physical Chemistry B* **2016**, *120* (25), 5691-5702.
432. Scheiner, A. C.; Scuseria, G. E.; Rice, J. E.; Lee, T. J.; Schaefer III, H. F., Analytic evaluation of energy gradients for the single and double excitation coupled cluster (CCSD) wave function: Theory and application. *The Journal of chemical physics* **1987**, *87* (9), 5361-5373.
433. Richard, R. M.; Marshall, M. S.; Dolgounitcheva, O.; Ortiz, J.; Bredas, J.-L.; Marom, N.; Sherrill, C. D., Accurate ionization potentials and electron affinities of acceptor molecules I. Reference data at the CCSD (t) complete basis set limit. *Journal of chemical theory and computation* **2016**, *12* (2), 595-604.
434. Libisch, F.; Huang, C.; Carter, E. A., Embedded correlated wavefunction schemes: theory and applications. *Accounts of chemical research* **2014**, *47* (9), 2768-2775.
435. Benck, J. D.; Chen, Z.; Kuritzky, L. Y.; Forman, A. J.; Jaramillo, T. F., Amorphous molybdenum sulfide catalysts for electrochemical hydrogen production: insights into the origin of their catalytic activity. *Acs Catalysis* **2012**, *2* (9), 1916-1923.
436. Kanan, M. W.; Nocera, D. G., In situ formation of an oxygen-evolving catalyst in neutral water containing phosphate and Co²⁺. *Science* **2008**, *321* (5892), 1072-1075.